High-Resolution X-ray Imaging based on a Liquid-Metal-Jet-Source with and without X-ray Optics

Dissertation zur Erlangung des naturwissenschaftlichen Doktorgrades der Julius-Maximilians-Universität Würzburg

vorgelegt von:
Christian Fella
aus Ulm

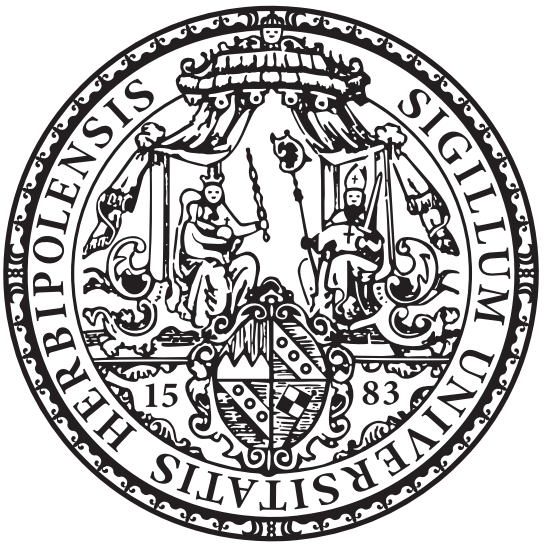

Würzburg 2016

Eingereicht am: 07.07.2016
bei der Fakultät für Physik und Astronomie

1. Gutachter: Prof. Dr. Randolf Hanke
2. Gutachter: Prof. Dr. Peter Jakob
der Dissertation

Vorsitzender: Prof. Dr. Raimund Ströhmer

1. Prüfer: Prof. Dr. Randolf Hanke
2. Prüfer: Prof. Dr. Peter Jakob
3. Prüfer: Prof. Dr. Matthias Kadler
im Promotionskolloquium

Tag des Promotionskolloquiums: 08.03.2017
Doktorurkunde ausgehändigt am:

Abstract

With increasing miniaturization in industry and medical technology, non-destructive testing techniques are an area of everincreasing importance. In this framework, X-ray microscopy offers an efficient tool for the analysis, understanding and quality assurance of microscopic species, in particular as it allows reconstructing three-dimensional data sets of the whole sample's volume via computed tomography (CT).

The following thesis describes the conceptualization, design, construction and characterization of a compact laboratory-based X-ray microscope in the hard X-ray regime around 9 keV, corresponding to a wavelength of 0.134 nm. Hereby, the main focus is on the optimization of resolution and contrast at relatively short exposure times. For this, a novel liquid-metal-jet anode source is the basis. Such only recently commercially available X-ray source reaches a higher brightness than other conventional laboratory sources, $i.e.$ the number of emitted photons (X-ray quanta) per area and solid angle is exceptionally high. This is important in order to reach low exposure times. The reason for such high brightness is the usage of the rapidly renewing anode out of liquid metal which enables an effective dissipation of heat, normally limiting the creation of high intensities on a small area.

In order to cover a broad range of different samples, the microscope can be operated in two modes. In the "micro-CT mode", small pixels are realized with a crystal-scintillator and an optical microscope via shadow projection geometry. Therefore, the resolution is limited by the emitted wavelength of the scintillator, as well as the blurring of the screen. However, samples in the millimeter range can be scanned routinely with low exposure times. Additionally, this mode is optimized with respect to in-line phase contrast, where edges of an object are enhanced and thus better visible.
In the second "nano-CT mode", a higher resolution can be reached via X-ray lenses. However, their production process is due to the physical properties of the hard X-ray range - namely high absorption and low diffraction - extremely difficult, leading typically to low performances. In combination with a low brightness, this leads to long exposure times and high requirements in terms of stability, which is one of the key problems of laboratory-based X-ray microscopy. With the here-developed setup and the high brightness of its source, structures down to 150 nm are resolved at moderate exposure times (several minutes per image) and nano-CTs can be obtained. Thus, the instrument provides an ideal platform to meet the requirements of various industrial and scientific requirements. Therefore, this thesis represents an important step towards establishing high resolution laboratory-based microscopes.

Zusammenfassung

Mit zunehmender Miniaturisierung in Industrie und Medizintechnik werden zerstörungsfreie Prüfverfahren immer wichtiger. In diesem Umfeld bietet Röntgenmikroskopie ein effizientes Instrument zu Analyse, Verständnis und Qualitätssicherung mikroskopischer Proben, insbesondere da sie im Rahmen der Computer-Tomografie (CT) die Aufnahme dreidimensionaler Datensätze des gesamten Probenvolumens ermöglicht.

Die vorliegende Arbeit befasst sich mit Konzeption, Design, Aufbau und Charakterisierung eines kompakten Labor-Röntgenmikroskops im harten Röntgenbereich bei 9 keV, bzw. einer Wellenlänge von 0.134 nm. Im Fokus liegt dabei die Optimierung von Auflösung und Kontrast bei möglichst kurzen Belichtungszeiten. Hierfür bildet die Basis eine neuartige Flüssig-Metall-Anoden Röntgenquelle. Solche erst seit kurzem kommerziell verfügbare Quellen erreichen eine höhere Brillianz als konventionelle Laborquellen, d.h. dass die Anzahl der emittierten Photonen (Röntgenquanten) pro Fläche und Raumwinkel außergewöhnlich hoch ist. Dies ist ein entscheidender Faktor, um nötige Belichtungszeiten zu verringern. Der Grund für die hohe Brillianz ist die Verwendung einer sich sehr schnell erneuernden Anode aus flüssigem Metall. Diese ermöglicht die effektive Abfuhr von Wärme, welche normalerweise die Erzeugung von höheren Intensitäten auf kleinerer Fläche limitiert.

Um ein möglichst großes Spektrum an Proben abzubilden, kann das Mikroskop in zwei Modi betrieben werden. Im „Mikro-CT Modus“ werden kleine Pixel mit Hilfe eines Kristall-Leuchtschirms und einem Lichtmikroskop über das Schattenwurfprinzip erreicht, weswegen dessen Auflösung durch die Wellenlänge des emittierten Lichts und die Unschärfe des Schirms beschränkt ist. Dafür können Proben im Millimeterbereich bei geringen Belichtungszeiten standardmäßig aufgenommen werden. Zudem wurde dieser Modus auf inline Phasen-Kontrast optimiert, bei welchem die Kanten eines Objekts durch Interferenz überhöht dargestellt werden und somit besser sichtbar sind.

Im zweiten „Nano-CT Modus“ kann eine erhöhte Auflösung mit Hilfe von Röntgenlinsen erreicht werden. Deren Herstellung ist aber aufgrund der physikalische Eigenschaften im harten Röntgenbereichs - nämlich starke Absorption und schwache Brechung - technisch extrem schwierig und meist mit einer sehr geringe optischen “Leistung” verbunden. Dies führt in Kombination mit einer geringen Brillianz zu sehr langen Belichtungszeiten und hohen Anforderungen an die Stabilität, was ein Kernproblem der auf Laborquellen basierenden Röntgenmikroskope darstellt. Mit der hier entwickelten Anlage können durch die hohe Brillianz der verwendeten Quelle bei moderaten Belichtungszeiten (wenige Minuten pro Bild) Strukturen der Größe 150 nm voneinander getrennt, sowie Nano-CTs aufgenommen werden. Somit bietet das entwickelte Instrument eine ideale Plattform, um verschiedenste industrielle und wissenschaftliche Anforderungen umsetzen zu können. Aus diesen Gründen stellt diese Doktorarbeit einen wichtigen Schritt zum breiten Einsatz hochauflösender Röntgenmikroskope im Laborbereich dar.

Contents

1 Introduction and motivation

High-resolution imaging techniques provide the most intuitive way to understand systems on a microscopic, and therefore also on a macroscopic scale. As people usually believe in only the things which they directly see, these techniques were - and still are - the key for numerous scientific developments and discoveries. For instance, light microscopy is a very powerful tool in medicine since the pioneering work of van Leeuwenhoek in the 17th century, who imaged for the first time red blood cells and discovered bacteria [1]. However, due to Abbe's diffraction limit [2], conventional light microscopy is not capable of visualizing smaller structures in the nanometer range. Therefore, the inner structure of cells or viruses became only visible in the mid 20th century, when Ruska's electron microscopy revolutionized our world [3]. Besides the fields of medicine or other natural sciences, nowadays basically all industrial branches rely on more and more tiny structures as present in microelectromechanical systems [4]. Therefore, there is a world-wide, continuously growing demand for novel high-resolution imaging techniques.

In general, an image corresponds to a spatially encoded data set of an object's properties in one, two or three dimensions. For this, a probe as well as sufficiently strong interactions of this probe with the sample are needed. Probes can be either particles like electrons, neutrons or ions, or waves like photons or ultrasound. The theoretically achievable *resolution* is thereby proportional to the wavelength λ of the probe [2]; this relationship is not only valid for waves, but also for particles, where λ is the associated de Broglie wavelength $\lambda = h/p$, with the particle's momentum p and Planck's constant h. Therefore, the resolution of conventional light microscopy is limited for blue light to about 200 nm.

Beating the diffraction limit Up to now, this introduction only referred to *conventional* light microscopy. Indeed, nowadays several experimental techniques exist, where the natural diffraction limit is overcome. For instance, in 2014 the Nobel Prize in Chemistry was awarded for the development of super-resolved *fluorescence microscopy* [5]: in the case of stimulated emission depletion microscopy, two laser beams are combined - the first one stimulates fluorescence over a large sample area; the second laser quenches the fluorescence around a nanometer-sized area. Thus, by scanning over the sample, an image with nanometer-resolution can be obtained even

at optical wavelengths. In the case of single-molecule microscopy, the fluorescence of single molecules is turned on and off stochastically. By imaging the same area over a long time interval, a superimposed image contains information on the nanometer range. Thus, in both cases close image points are recorded independently from each other to finally gain a high-resolution image.
In contrast, *near-field* based techniques, which are known since the mid 20th century, take advantage of sub-wavelength structures such as sharp tips or edges to image nearby samples [6]. Here, the resolution is limited technically, for example by the size of the needed auxiliary structures, the achievable scanning step size, and the overall stability of the instrument.

Reducing the wavelength - a simple solution? Instead of improving the concept of light microscopy, an obvious approach to image smaller structures despite Abbe's diffraction limit is to reduce the utilized wavelength. In the case of electron microscopy, the de Broglie wavelength for a setting of 9 kV is only 0.01 nm. In reality, the resolution is limited ultimately for instance due to spherical aberrations. Therefore, typical resolutions are around 1 nm in scanning [7] and 0.1 nm in transmission electron microscopes [8], which is much better than optical microscopy. However, electron microscopy requires conducting, dry and vacuum tight samples and is only surface-sensitive.

In between optical light and electrons, X-rays possess wavelengths in the sub-nanometer range. Therefore, it would be quite logical to utilize X-ray microscopes for imaging nanometer-sized structures. In this regard, one obvious advantage of X-radiation is its high penetration depth, which allows gathering information of the complete volume of a specimen. Moreover, one can separate between different chemical elements by combining the information of refraction and absorption. Furthermore, samples do not need to be prepared specifically, for instance by using contrast agents. However, there are many other technical drawbacks, which limit nowadays operation and particular imaging resolution of X-ray microscopes, as will be discussed in the following.

Progress in X-ray imaging In 1895, Wilhelm Conrad Röntgen discovered X-rays at the "Physikalische Institut der Universität Würzburg" and obtained therefore already in 1901 the first Nobel Price in Physics. Later, with the development of cheaper and more powerful computers, the acquisition of 3D volumes became practicable. Since then, X-ray computed tomography (CT) is widely used in medicine and material inspection, but rather on a macroscopic than microscopic scale. Therefore, one has to pose the question why X-ray microscopy remains limited to only few applications compared to other high-resolution imaging techniques.

One possible approach to set up an X-ray microscope was already presented in 1939 by M. von Ardenne, who proposed to use a nanofocus source in projection geometry to image structures

down to 100 nm. Indeed, Nixon *et al.* successfully implemented this approach already in 1952, proofing that the resolution of X-ray microscopes can be better than that of visible light microscopes [9, 10]. However, the resolved structures were still in the range of hundred nanometers, and thus he could not demonstrate a significant improvement of resolution compared to optical light. Moreover, the low X-ray yield leads to long exposure times and low contrast. Furthermore, the required sample properties are similar to electron microscopy. All this hampered the fast progress of such X-ray shadow microscopes.

In order to overcome these limitations, the number of photons which interact with the X-ray detector needs to be increased. In this regard, the brightness of a source is an important parameter, as it provides a measure of the number of photons which are emitted within a certain time into a certain area and solid angle [11]. Thus, under the assumption of constant brightness, increasing the source size leads to shorter exposure times. However, this also reduces the resolution of nanofocus-based microscopes.

Similar to optical microscopes, an alternative is to construct instruments based on larger sources, for which additional optical elements are used for imaging. Unfortunately, such optical elements show typically a very low efficiency in the X-ray energy range [12]. Therefore, highly brilliant sources are needed for this approach, which became only accessible with the invention of third generation synchrotron sources. As this approach shows nowadays very good results with resolutions well below optical light microscopy, also optical elements are developed further towards higher efficiency and better resolution.

State of the art X-ray imaging By combining highly brilliant synchrotron sources and efficient optical elements, today 2D resolutions in the range of 10 nm can be gained in the soft [13, 14] and hard X-ray range [15, 16]. For three-dimensional imaging, resolutions are slightly higher, *i.e.* in the range of 15-35 nm [17, 18]. Moreover, lensless approaches such as coherent diffractive imaging[1] have shown even better results [20]. Here, the resolution depends only on the system's stability, the utilized wavelength and the detection angle [21]; high-quality optical elements are not needed. Instead, the sample information is reconstructed directly from the diffraction pattern in the Fraunhofer far-field. For such a reconstruction, the phase also needs to be known; one possible way to do this is ptychography: a scanning variant where the phase is reconstructed iteratively, using small - but overlapping - diffraction patterns [22]. However, for this technique fully coherent illumination is needed. Therefore, ptychography only works with sources with high brightness [23], *i.e.* third generation synchrotrons.

In principle, these synchrotron results impressively demonstrate the capability of X-ray micro- and nano-tomography. However, large scale instruments like synchrotrons can never serve a broader audience. Instead, compact setups are needed which can be placed in any laboratory, as it is today standard for good optical and electron microscopes.

[1] First demonstrated by Miao *et al.* [19].

One of the big milestones towards such a development was realized in 2007 by the company *Xradia* (now *Zeiss*), which offers commercially optic-based X-ray microscopes with laboratory sources [24]. In the future, especially the quality of X-ray optical elements needs to be increased, yet technical optimization and affordable prices are requirements to strengthen these X-ray microscopes on the market. Moreover, also novel sources show potential for further improving the image quality of such microscopes [25]; one of these - the liquid-metal-jet source - sets the motivation for this PhD project.

In the framework of this thesis, a microscope in the hard X-ray regime was developed, based on such a highly brilliant source technology invented in 2006 by *Excillum*. In comparison to the commercially available x-ray microscopes, the developed system is a hybrid which works in two different imaging modes. The first one is a lens-less micro-CT mode which uses a high-resolution detector. It is capable of in-line phase contrast, which counteracts the problem of decreasing sample volume, which poses a limit to the signal strength in high-resolution imaging. The second mode is a microscope, which contains an X-ray lens to magnify the sample and reach even higher resolutions.

The thesis itself is structured in five parts. In order to built up an experimental setup, the physical properties of all components need to be well understood. Therefore, chapter 2 gives a broad overview about the underlying physics of X-ray imaging, before chapter 3 describes the experimental setup built in the framework of this thesis. The capability of the instrument is demonstrated in chapter 4 and 5, where the two different modes are presented. Finally, the thesis closes in chapter 6 with a brief outline on further possible experiments, *i.e.* waveguide-based and high-speed imaging, before a general summary and outline follows in chapter 7.

2 Physical properties

In order to built up an experimental setup, the physical properties of all components need to be well understood. Therefore, the following chapter gives a broad overview about the underlying physics of x-ray imaging. Hereby, the structure resembles that of an experimental setup. Starting with an overview of x-radiation itself and the generation of x-rays in section 2.1, the interactions of x-rays with matter are discussed (see section 2.2). This gives a sound basis to understand the challenges for x-ray optics, as discussed in section 2.3. Finally, this chapter closes with an overview about detection methods of x-radiation (see section 2.4).

2.1 X-radiation

Electromagnetic radiation can be described as energy which appears in form of oscillating electric and magnetic fields that propagate as waves. Classically, the coupling between these fields are described by Maxwell's equations [26]. From them, a linear dispersion relation can be deduced, which describes the relation between wavelength λ and frequency ν of the wave:

$$\nu = \frac{c}{\lambda} \tag{2.1}$$

with the speed of light c in vacuum. An alternative description is given by quantum electrodynamics, where the energy is transported by discrete particles called photons, and the relation between the particle's energy E and frequency is given by Planck's equation $E = h\nu$ with Planck's constant h. These two descriptions express the particle-wave duality and can be combined to the relation [27]:

$$\lambda\,[\text{nm}] = \frac{hc}{E} = \frac{1.2398}{E\,[\text{keV}]}. \tag{2.2}$$

As the range of photon energies which might appear is huge, different subclasses of the electromagnetic spectrum are defined. In this thesis, we concentrate on the part of the electromagnetic spectrum with energies between approximately 250 eV and 1000 keV, which is termed X-radiation or X-rays.

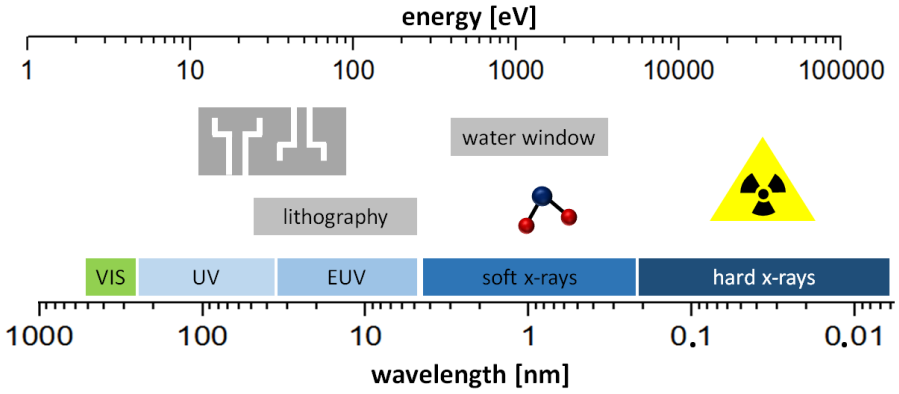

FIGURE 2.1: Excerpt of the electromagnetic spectrum. Between approximately 250 eV and 1000 keV, the energy range is termed X-radiation or X-rays; it can be further separated - for instance by the appearance of water absorption - into soft and hard X-rays. At lower energies, the radiation is called extreme ultraviolet (with its typical application, the lithography), followed by the ultraviolet and the visible range.

Fig. 2.1 depicts this frequency window together with its neighboring ranges. At lower energies than 250 eV, the radiation is called extreme ultraviolet, followed by the ultraviolet and the visible range. For energies above 1000 keV, the photons are often called gamma radiation, which describes X-rays emitted in nuclear decay processes.
X-radiation itself is further subdivided into soft and hard X-rays. However, the separation is not consistently defined in literature and depends especially on the field of application (*e.g.* medicine, imaging or microscopy). In principle, it makes sense to define the transition around 5 keV. Above, it is not necessary to stay in vacuum and 3D-tomography of thicker samples can be done, as materials become more transparent. On the other side, the fabrication of optical elements becomes much more difficult due to higher aspect ratios and the sample's contrast gets lower. Moreover, laboratory sources in the hard X-ray range are often electron-impact tubes with relatively low brightness compared to laser-based plasma sources; these are more common in the soft X-ray region, as here lower laser energies are sufficient for generating X-rays.

2.1.1 Generation of X-radiation

For the generation of X-rays, two main mechanisms are responsible, leading to the characteristic contributions of an X-ray spectrum: the continuous Bremsstrahlung and the spike-like characteristic radiation. The underlying mechanisms are depicted in Fig. 2.2.

The first mechanism is based on the deceleration of fast electrons, which leads to the emission of photons with a continuous spectrum. For laboratory X-ray tubes, this appears as electrons, which are shot towards an anode, change their beam path due to the Coulomb potential of the nuclei. Hereby, the deceleration of the electron and thus the photon energy depends on the closest distance between electron and nucleus. The resulting spectrum is called Bremsstrahlung.

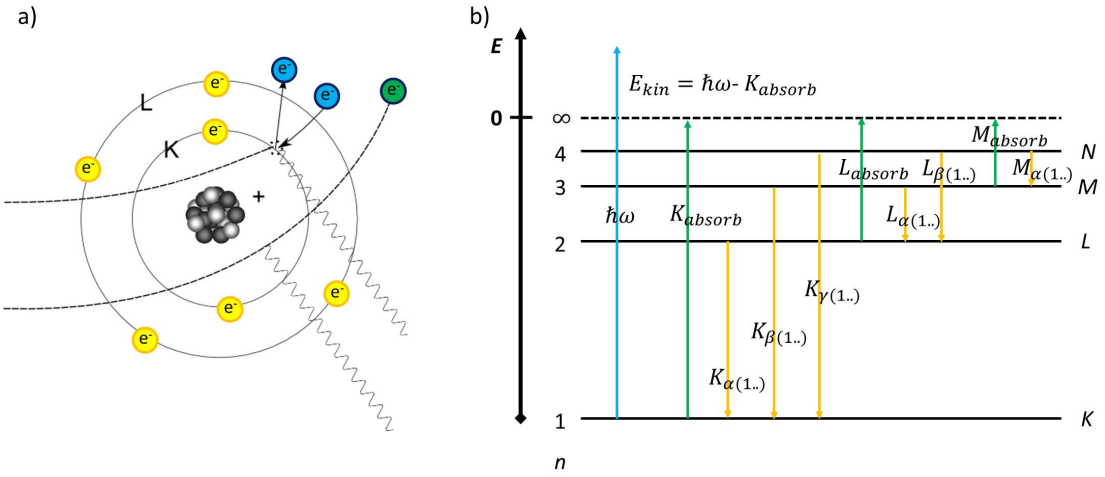

FIGURE 2.2: Schematic drawing of the creation of X-rays [adapted from Ref. [28]]. (a) One process is the deceleration of electrons, for example due to the Coulomb potential of an atomic nucleus (schematically shown for the green electron). Characteristic emission occurs when a bound electron of one of the inner shells of an atom is removed by the collision with a free electron: the hole is filled up by an electron of the next-outer shell, which leads to the emission of an X-ray photon (schematically shown for the blue electrons). (b) Schematic drawing of the core energy levels and allowed transitions, together with the historic line denotations. For this thesis, the mostly relevant lines are K-lines, which result from decay processes involving the $1s^2$-shell.

In synchrotrons or free electron lasers, the deflection of relativistic electrons is achieved by magnets or magnetic arrays, as further described in the next chapter.

Characteristic emission occurs when a bound electron of one of the inner shells of an atom is ionized by the collision with a fast electron: the hole is filled up by an electron of the next-outer shell(s), which leads to the emission of a photon with the energy matching to the energy difference of the involved shells. The core energy levels and allowed transitions are depicted in Fig. 2.2b together with their historic line denotations. Decay processes which involve the $1s^2$-shell are the so-called K-lines. Here, one has to further distinguish between the $K_{\alpha 1}$- and $K_{\alpha 2}$-lines, originating from a decay of the $2s^2$- and $2p^2$-shell, respectively, and the K_{β}-line, which appears due to the decay of a $3s^2$-state.

2.1.2 Properties of X-radiation

In the following, the main properties of X-radiation are defined [29], which allow to describe the differences between sources in the next chapter.

Spatial and temporal coherence Coherence is the ability of waves to create interference patterns, based on well-defined phase and amplitude variations of the X-ray field. Only in the

theoretical limit of a point source, the radiation field would be completely coherent. In reality, only finite coherence exists with respect to time and region.

For a well-defined direction of X-ray propagation, one can decompose the coherence into two components. On the one hand, one has the longitudinal (*i.e.* temporal) coherence l_{long} along the direction of propagation, which gives information about phase relations:

$$l_{\text{long}} = \frac{\lambda^2}{2\Delta\lambda} \tag{2.3}$$

with the spectral width of the source $\Delta\lambda$.
On the other hand, the transverse (*i.e.* spatial) coherence l_{trans} perpendicular to the direction of wave propagation (along the wave front) is related to the size and emission angle of the source, hence to the emittance, and is given by:

$$l_{\text{trans}} = \frac{x\lambda}{2\pi d} \tag{2.4}$$

with the distance from the source x and the source size d.

Spectral brightness, emittance and etendue The brightness B, which is often also called brilliance, describes how many photons N_{ph} with spectral width $\Delta\lambda/\lambda$ are emitted in a certain time interval by a certain area A in a solid angle Ω:.

$$B = \frac{\frac{N_{\text{ph}}}{s}}{A \cdot \Omega \cdot \frac{\Delta\lambda}{\lambda}} \tag{2.5}$$

The factor $A \cdot \Omega$ in the denominator is called emittance, and characterizes the emittance of the source. Closely related to the emittance is the etendue (also called $A\Omega$ product[1]), which is also defined by the product "area times solid angle", but from the whole optical system and not just the source. The etendue remains constant from one plane to another plane along the optical axis, or gets reduced by losses:

$$A_{\text{image}} \cdot \Omega_{\text{image}} \leq A_{\text{object}} \cdot \Omega_{\text{object}}. \tag{2.6}$$

This basic relation can be derived using Liouville's theorem or the lensmaker's equation:

$$\Phi = B(A\Omega)T \tag{2.7}$$

with the photon flux (number of photons per unit time) Φ and the transmittance T. For an optical system, the overall etendue is given by the smallest or limiting etendue; in a real system, this could be for example a wave-guide with area A and acceptance angle Ω. The transmittance in equation 2.7 is the constant that represents losses due to absorption or scattering in the system.

[1]Further descriptions are: acceptance, throughput, light-grasp, collecting power, optical extent and geometrical extent.

Since the brightness in an ideal optical system is a conserved quantity, for a real system it gets always decreased due to these losses, but can not be increased with any optics [11].
For laboratory electron impact sources, as it is used in the framework of this thesis, the brightness can be also defined as:

$$B \sim \frac{P_{\text{ele}}}{A_{\text{area}}} \tag{2.8}$$

with the electronic power P_{ele} and the area of the electron beam A_{area}.

2.1.3 X-ray sources

For X-ray imaging, several X-ray sources are nowadays commonly used. Here, of main interest are X-ray tubes, plasma sources, synchrotrons, and free electron lasers.

X-ray tubes X-ray tubes create X-radiation based on both mechanisms explained in Fig. 2.2. Here, electrons are accelerated in an electrostatic potential difference between a cathode and an anode, with the potential difference being in the kilovolt range for hard X-rays. For an efficient process, the tube has to be evacuated so that the electrons can gain the whole kinetic energy from the potential difference and do not collide with other particles before reaching the anode.

Electrons on the cathode are either created by field emission, thermionic emission or field enhanced thermionic emission [7]. For thermionic emission the cathode has to be heated to around 2800 K for a metal, and to around 1950 K for a LaB_6 crystal, following Richardson's equation [30]. Compared to a tungsten emitter, the LaB_6 cathode has a one magnitude higher electron brightness and a longer lifetime. In field emission cathodes [31], the energy barrier is reduced by an applied field and by having a tip with an extremely small radius, permitting quantum tunneling of electrons through the narrowed barrier into the vacuum.

Further classification of different X-ray tubes results from the type of utlized anode, such as microfocus, nanofocus and rotating anode sources. The former are used when very small spot sizes are needed for direct shadow magnification. In this case, often a transmission target is used, consisting of a thin metal film evaporated on a diamond or beryllium window. The thickness of the metal film and the applied current are usually limiting the minimum spot size. Typical minimum spot sizes for microfocus tubes are smaller than 2 μm [32]. For nanofocus tubes, the spot can be as small as 150 nm [33, 34], however, with very little power.
In rotating anode sources, the anode is rotated with high speed to enlarge the area where the heat is placed. They are widely used for diffraction and small angle scattering, where the high brightness of characteristic lines is needed. In theses cases, up to 1.2 kW are shed on a 0.07 mm circle[2]. With this, a brightness in the order of $4 \cdot 10^9$ photons/sec/mm^2/mR^2 can be reached [35].

[2]The actual size where the power is deposited is larger and appears in the projection of the tilted plane as a circle with a diameter of 0.07 mm.

Moreover, also medical CT scanners use rotating anodes up to 100 kW in order to guarantee short enough exposure times for dynamical processes like the motion of the human heart.

Plasma sources Another efficient possibility to create accelerated electrons and thus X-rays are plasma sources [36]. For the production of the plasma, an ultra-short and intense laser can be focused on a material (typically a metal). However, Tajima and Dawson pointed out in 1979 [37] that the laser can not be only used to create the plasma, but also to create an enormous electric field [38]. For this, the underlying mechanism is based on the ponderomotive force, which causes in an inhomogeneous electromagnetic field a force on charged particles in the direction of low-intensities. As the electrons are very light, they are efficiently forced out of the regions of high laser intensity, while the ions are left behind. The thus created fields are high enough to accelerate electrons up to 1 GeV on a millimeter-scale, leading to the creation of short X-ray pulses.

Synchrotron sources A synchrotron denotes in principle a particle accelerator; in terms of X-ray creation, it is used as a synonym for a storage ring where electrons (or charged particles) travel with relativistic speed at constant energy. Whenever the movement of these electrons deviates from a straight line motion, X-rays are emitted. In contrast to the non-relativistic circular motion of an electron which leads to a dipole-like emission, the synchrotron radiation possesses an opening angle $\sim \gamma^{-1}$ mrad, where γ is the ratio of the electron's relativistic and rest mass (see Fig. 2.3a, [39–41]).

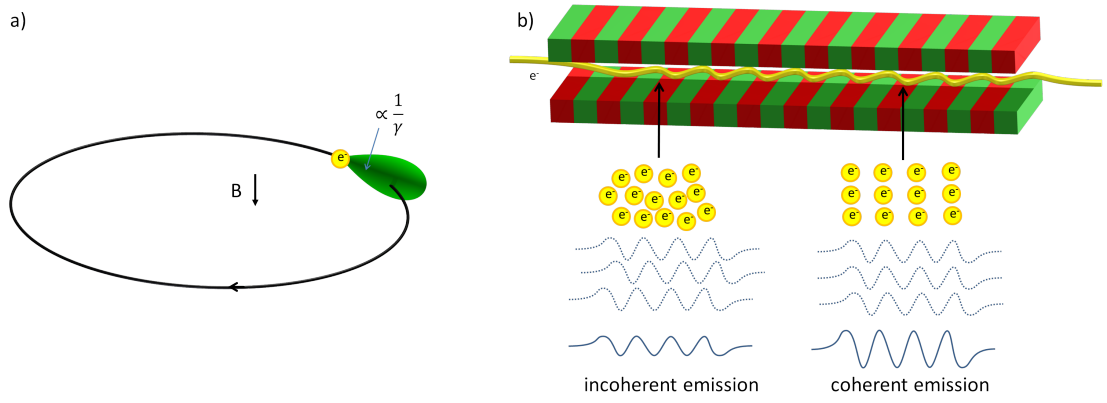

FIGURE 2.3: Principle of synchrotron and free electron laser radiation. a) Whenever the movement of relativistic electrons deviates from a straight line motion, X-rays are emitted. The radiation possesses an opening angle $\sim \gamma^{-1}$ mrad, where γ is the ratio of the electron's relativistic and rest mass. b) Magnets are used to deflect the electron beam and create incoherent synchrotron radiation. In free electron lasers, the electron beam interacts additionally with the electric field of photons, leading to electron density modulations (called microbunching) and coherent emission [adapted from Ref. [42]].

In reality, the ring typically consists of several straight sections, with bending magnets or more complex periodic arrangements of dipole magnets such as wigglers and undulators (see

Fig. 2.3b) which deflect the beam at certain points. Only at these points, highly brilliant X-radiation is emitted. The difference between wigglers and undulators is the so-called K-parameter: $K = 0.934\lambda_u B_0$ with the magnet periodicity λ_u and the magnetic induction B_0; it is approximately one for undulators and bigger for wigglers. While wigglers emit a beam with diameter K/γ, the radiation emitted by an undulator possesses an opening angle compressed by a factor $1/\sqrt{N}$ with the period number N. In general, the geometry of the magnet influences the wavelength of the radiation. In the case of a bending magnet, the wavelength depends on the relativistic energy of the electron and the magnetic field; in the case of an undulator, the periodicity of the magnets additionally plays a role.
Alternatively, a relatively new approach are compact light sources, where the deflection of an electron beam is realized via standing electromagnetic waves in a laser cavity; here, the deflection periodicity λ_u is given by the wavelength of the optical laser and is thus very small [43]. Therefore, the advantage of this approach is that relatively low electron energies and small storage rings are sufficient.

Free electron lasers Free electron lasers are also based on electron accelerators which emit photons when the electrons pass magnetic structures, as typically undulators. However, due to the emission of coherent light, they possess an even higher brilliance than synchrotron sources (see Fig. 2.6). This can appear, if the electron beam interacts with the electric field of the photons (via the ponderomotive force), leading to local energy and electron density modulations; this effect is called microbunching. As the photons emitted by the bunched electrons are in phase, coherent radiation results.

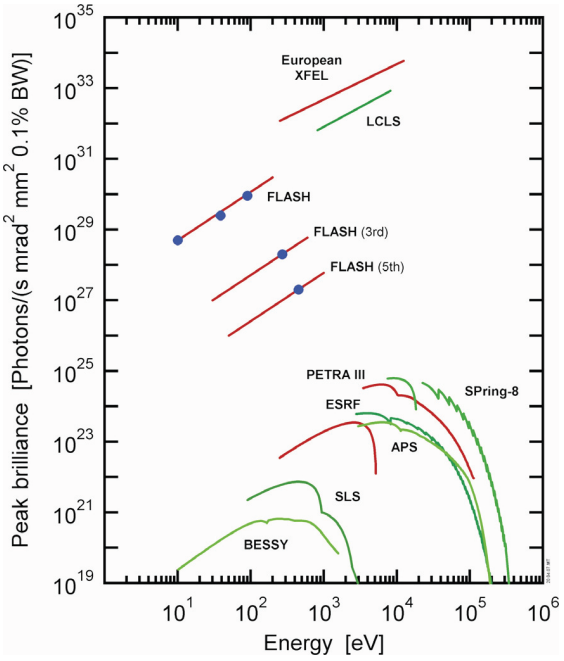

FIGURE 2.4: Comparison of the peak brightness which can be achieved in different electron accelerators [44]. The highest brightness is gained at free electron lasers such as FLASH.

2.2 Interactions of X-rays with matter

In the energy range between 1 and 100 keV, X-rays interact in three ways with electrons in matter: coherent scattering (also called elastic, Thomson or Rayleigh scattering), incoherent scattering (also called inelastic or Compton scattering) and photoabsorption - all depicted in Fig. 2.5. In the first case, the photon's energy is small compared to that of the electron; therefore, the electron's energy stays unaffected and the photon only changes direction. Thus, this process can be abbreviated as "photon in - photon out". For higher energies, inelastic processes can appear, where part of the photon's energy gets transferred to the electron in an "photon in - photon and electron out"-process. As different scattering events are independent from each other due to different states of the electron, the scattered photons do not possess any phase relation to each other and the process is incoherent. An alternative is the photoabsorption, where the complete energy of the photon is transferred to the electron's system in a "photon in - electron out"-process. In the energy range relevant in the framework of this thesis, elastic scattering and photoabsorption are the most important processes and will be discussed in the following in more detail.

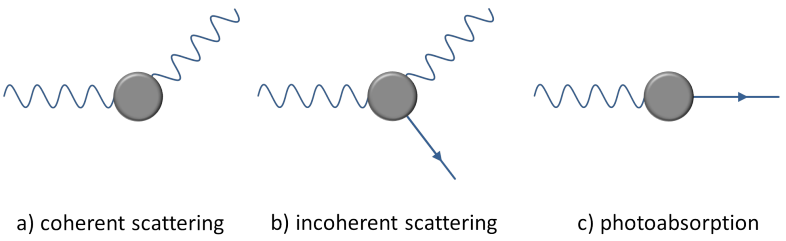

FIGURE 2.5: Schematic drawing of the three ways of interaction between X-rays and electrons in matter between 1 and 100 keV. a) Coherent (*i.e.* elastic scattering) is a "photon in - photon out"-process, where the photon only changes direction, but not energy. b) In contrast, incoherent (*i.e.* inelastic) scattering is an "photon in - photon and electron out"-process and energy is transferred. c) For photoabsorption, the complete energy of the photon is transferred to the electron's system in a "photon in - electron out"-process.

2.2.1 Scattering cross sections and atomic form factors

The cross section of an object gives the probability of its participation in a scattering event per unit area and can be defined as [29]:

$$\sigma = \frac{P_{\text{rad}}}{|\mathbf{S}_{\text{in}}|} \tag{2.9}$$

where P_{rad} is the averaged radiated power to all directions and $\mathbf{S}_{\text{in}}$ the average incident power per unit area represented by the averaged pointing vector:

$$|\mathbf{S}_{\text{in}}| = \frac{1}{2}\sqrt{\frac{\epsilon_0}{\mu_0}}|\mathbf{E}_{\text{in}}|^2. \tag{2.10}$$

Alternatively, the differential cross section $\mathrm{d}\sigma/\mathrm{d}\Omega$ gives the probability of a scattering event into a certain direction per unit solid angle. Thus, it is connected to the total cross section via:

$$\int \frac{\mathrm{d}\sigma}{\mathrm{d}\Omega}\,\mathrm{d}\Omega = \int_0^{2\pi} \mathrm{d}\omega_2 \int_0^{\pi} \frac{\mathrm{d}\sigma}{\mathrm{d}\Omega}\mathrm{d}\omega_1 = \sigma. \tag{2.11}$$

The first classical description of elastic scattering was derived by Thomson for free electrons. For an oscillating electron with acceleration $\mathbf{a} = -\frac{e}{m_\mathrm{e}}\mathbf{E}_\mathrm{in}$, the averaged radiated power is classically:

$$P = \frac{1}{2}\frac{8\pi}{3}\left(\frac{e^2|\mathbf{a}|^2}{16\pi^2\epsilon_0 c^3}\right) = \frac{1}{2}\frac{8\pi}{3}\left(\frac{e^2\left(\frac{e^2}{m_\mathrm{e}^2}|\mathbf{E}_\mathrm{in}|^2\right)}{16\pi^2\epsilon_0 c^3}\right). \tag{2.12}$$

with the elementary charge e, the electron's mass m_e, the vacuum permittivity ϵ_0 and the speed of light c. From this and equations 2.9 and 2.10, the so-called Thomson cross section results [29]:

$$\sigma_\mathrm{T} = \frac{8\pi}{3} r_\mathrm{e}^2 \tag{2.13}$$

with the classical electron radius:

$$r_\mathrm{e} = \frac{e^2}{4\pi\epsilon_0 m_\mathrm{e} c^2}. \tag{2.14}$$

This equation is a good description for the interaction of X-rays with matter far away from any atomic resonance.

However, if this assumption is not valid, one has to consider the case of elastic scattering on bound electrons without ionizing or exciting the atom. It can be well described by a semi-classical model also known as the Lorentz model, where the bound electron is forced by the incident electromagnetic field to oscillate around the atomic nucleus [26]. Of course, the strength of such an oscillation depends on how close the frequency of the incident light is to the resonance frequency of the system ω_res (*i.e.* transitions between atomic states). The differential equation for such an electron is:

$$m_\mathrm{e}\frac{\mathrm{d}^2\mathbf{x}}{\mathrm{d}t^2} + m_\mathrm{e}\gamma\frac{\mathrm{d}\mathbf{x}}{\mathrm{d}t} + m_\mathrm{e}\omega_\mathrm{res}^2\mathbf{x} = -e\mathbf{E}_0 e^{-i\omega t} \tag{2.15}$$

where on the left side the first term describes the acceleration of the electron, the second one the loss of energy due to damping with the damping constant γ, and the third one the restoring force which bounds the electron to the core. The right side of equation 2.15 denotes the force $\mathbf{F}(t) = m_\mathrm{e}\ddot{\mathbf{x}}(t)$ due the electric field of the incident X-rays $\mathbf{E}_\mathrm{in}(t) = \mathbf{E}_0 e^{i\omega t}$; the magnetic force is much smaller and can be therefore neglected.

By assuming the displacement $\mathbf{x}(t) = \mathbf{x}_0 e^{-i\omega t}$ we obtain:

$$\mathbf{x}(t) = \frac{1}{\omega^2 - \omega_\mathrm{res}^2 + i\gamma\omega}\frac{e\mathbf{E}_\mathrm{in}(t)}{m_\mathrm{e}} \tag{2.16}$$

and

$$\mathbf{a}(t) = \ddot{\mathbf{x}}(t) = \frac{-\omega^2}{\omega^2 - \omega_{\text{res}}^2 + i\gamma\omega} \frac{e\mathbf{E}_{\text{in}}(t)}{m_{\text{e}}}. \tag{2.17}$$

Inserting equations 2.10, 2.12 and 2.17 into equation 2.9, one yields the frequency-dependent cross section:

$$\sigma_{\text{L}} = \frac{8\pi}{3} r_{\text{e}}^2 \frac{\omega^4}{(\omega^2 - \omega_{\text{res}}^2)^2 + (\gamma\omega)^2} \tag{2.18}$$

Besides the resonance, one should note that at high frequencies the curve approaches Thomson's scattering cross section (see equation 2.14). At low frequencies (*i.e.* high wavelengths), its slope can be well described by the so-called Rayleigh scattering [29]:

$$\sigma_{\text{R}} = \frac{8\pi}{3} r_{\text{e}}^2 \left(\frac{\omega}{\omega_{\text{res}}} \right)^4 \tag{2.19}$$

which is valid if the radius of a scatterer is much smaller than the wavelength of the incident photon; its most famous usage is the explanation of the sky's blue color.

Up to now, only the scattering on an individual atom was considered. However, a real atom contains many electrons. This can be considered by the atomic scattering factor f, which is in general a complex function of:

- the frequency of the incoming photon,
- the resonance frequencies of the various bound electrons,
- the phase terms which consider the different positions of the electrons within an atom,

and varies the scattering cross section as [29]:

$$\sigma(\omega) = \frac{8\pi}{3} r_{\text{e}}^2 |f|^2. \tag{2.20}$$

For the limit of forward scattering, the scattering factor simplifies to:

$$f(\omega) \approx \sum_i \frac{g_{\text{i}} \omega^2}{\omega^2 - \omega_{\text{res}}^2 + i\gamma\omega} \tag{2.21}$$

with the oscillator strengths g_{i} which give the number of electrons with the same resonance frequency, *i.e.* that belong to the same atomic shell.

As already noted, the form factor is in general a complex and frequency-dependent quantity and can be written for instance as [27]:

$$f(\mathbf{Q}, \omega) = f^0(\mathbf{Q}) + f'(\omega) - if''(\omega). \tag{2.22}$$

with the scattering vector $\mathbf{Q}$; while $f^0(\mathbf{Q})$ is the Fourier transform of the electron density which varies between 0 and Z ($Q \rightarrow 0$), f' and f'' accounts for the fact that electrons are bound, resulting in a frequency-dependent response. In the limit of forward scattering, this equation transforms to:

$$f(\omega) = f_1(\omega) - if_2(\omega). \tag{2.23}$$

These values are tabulated together with the cross-sections element-specifically in the X-ray data booklet [45].

2.2.2 Complex refractive index

The Lorentz model, which describes the response of a bound electron to an incident electromagnetic field, can be further used to derive the refractive index of a wave propagating in a medium [29, 40, 46].

For such an approach, we can derive from equation 2.24 the oscillation velocity of the electron as:

$$\dot{\mathbf{x}}(t) = \mathbf{v}(t) = \frac{1}{\omega^2 - \omega_{\text{res}}^2 + i\gamma\omega} \frac{e}{m_{\text{e}}} \frac{\partial \mathbf{E}(t)}{\partial t}. \tag{2.24}$$

This induces a current density of:

$$\mathbf{J}(\mathbf{r}, t) = -en_{\text{a}} \sum g_{\text{i}} \mathbf{v}_{\text{i}}(\mathbf{r}, t) = -\frac{e^2 n_{\text{a}}}{m_{\text{e}}} \sum \frac{g_{\text{i}}}{\omega^2 - \omega_{\text{res}}^2 + i\gamma\omega} \frac{\partial \mathbf{E}(t)}{\partial t} \tag{2.25}$$

with the atomic number density n_{a}.

Substituting equation 2.25 into the equation for a transverse wave:

$$\left[\frac{\partial^2}{\partial t^2} - c^2\nabla^2\right] \mathbf{E}(\mathbf{r}, t) = -\frac{1}{\epsilon_0} \frac{\partial}{\partial t} \mathbf{J}(\mathbf{r}, t), \tag{2.26}$$

it follows that:

$$\left[\frac{\partial^2}{\partial t^2} - c^2\nabla^2\right] \mathbf{E}(\mathbf{r}, t) = \frac{e^2 n_{\text{a}}}{\epsilon_0 m_{\text{e}}} \sum \frac{g_{\text{i}}}{\omega^2 - \omega_{\text{res}}^2 + i\gamma\omega} \frac{\partial^2 \mathbf{E}(t)}{\partial t^2} \tag{2.27}$$

and finally:

$$\left[\left(1 - \frac{e^2 n_{\text{a}}}{\epsilon_0 m_{\text{e}}} \sum \frac{g_{\text{i}}}{\omega^2 - \omega_{\text{res}}^2 + i\gamma\omega}\right) \frac{\partial^2}{\partial t^2} - c^2\nabla^2\right] \mathbf{E}(\mathbf{r}, t) = 0. \tag{2.28}$$

From this, the refractive index $n(\omega)$ can be defined as:

$$n(\omega) = \left[1 - \frac{e^2 n_{\text{a}}}{\epsilon_0 m_{\text{e}}} \sum \frac{g_{\text{i}}}{\omega^2 - \omega_{\text{res}}^2 + i\gamma\omega}\right]^{\frac{1}{2}} \approx 1 - \frac{1}{2} \frac{e^2 n_{\text{a}}}{\epsilon_0 m_{\text{e}}} \sum \frac{g_{\text{i}}}{\omega^2 - \omega_{\text{res}}^2 + i\gamma\omega}, \tag{2.29}$$

which is consistent with a speed of light in a medium of $c_\mathrm{n} = c/n$. By replacing the oscillator strength with the complex atomic form factors defined in equations 2.21 and 2.23, this leads to the definition:

$$n(\omega) = 1 - \delta + i\beta \approx 1 - \frac{n_\mathrm{a} r_\mathrm{e} \lambda^2}{2\pi} \left[f_1(\omega) - i f_2(\omega) \right] \tag{2.30}$$

with λ being the wavelength in vacuum. Importantly, equation 2.30 links the microscopic oscillator model with the macroscopic description of the refractive index.

Snell's law Macroscopically, the real part of the refractive index is often of interest to determine beam paths at the interface of two non-absorptive media. For this situation, Snell's law applies [47]:

$$\frac{1 - \delta_1}{1 - \delta_2} = \frac{\sin\alpha_2}{\sin\alpha_1} \tag{2.31}$$

with the angles defined with respect to the normal of the interface. Therefore, X-rays entering from air (δ_1 = 0) into a material ($\delta_2 > 0$), leads to refraction with $\alpha_2 > \alpha_1$:

$$\sin\alpha_2 = \frac{\sin\alpha_1}{1 - \delta_2} \tag{2.32}$$

2.2.3 Absorption and phase shift

Empirically, the Lambert-Beer law describes that the absorption of a material grows exponentially with its thickness. In this regard, the transmitted intensity I after a certain thickness d compared to the incoming intensity I_0 can be either expressed using the mass density ρ and the macroscopic absorption coefficient μ of a material:

$$I(d) = I_0 e^{-\rho \cdot \mu \cdot d} \,, \tag{2.33}$$

or dependent on the atomic density n_a and the absorption cross section σ_abs as:

$$I(d) = I_0 e^{-n_\mathrm{a} \cdot \sigma_\mathrm{abs} \cdot d} \,. \tag{2.34}$$

Considering that a plane wave

$$\mathbf{E}(\mathbf{r}, t) = \mathbf{E}_0 \, e^{-i(\omega t - \mathbf{kr})} \tag{2.35}$$

possesses in a material the complex dispersion relation $\omega/k = c/n$, one obtains with equation 2.30:

$$\mathbf{E}(\mathbf{r}, t) = \underbrace{\mathbf{E}_0 e^{-i(\omega t - \mathbf{kr})}}_{vacuum} \underbrace{e^{i(2\pi\delta/\lambda)r}}_{phase-shift} \underbrace{e^{-(2\pi\beta/\lambda)r}}_{absorption}. \tag{2.36}$$

Thus, the wave in the medium has compared to the wave in vacuum a phase shift of

$$\Delta\Phi(r) = \left(\frac{2\pi\delta}{\lambda}\right)\Delta r \tag{2.37}$$

and a smaller amplitude by a factor of $e^{-(2\pi\beta/\lambda)r}$.

Moreover, by comparing the absorption term with the Lambert-Beer law in equation 2.33, it follows:

$$\mu = \frac{2n_{\mathrm{a}}r_{\mathrm{e}}\lambda}{\rho}\, f_2, \tag{2.38}$$

giving a relation between the macroscopic absorption coefficient (which can be easily determined in an experiment) and the imaginary part of the atomic form factor of an atom. Similarly, one obtains with equation 2.34 for the cross section of absorption:

$$\sigma_{\mathrm{abs}} = 2r_{\mathrm{e}}\lambda\, f_2. \tag{2.39}$$

One should note that these absorption coefficients contain all processes discussed in this chapter, and not only the photoabsorption. The photoabsorption itself shows absorption edges, corresponding to a sudden increase of the cross section, as soon as the energy is large enough to access electrons of a higher atomic shell. Despite these edges, the cross section for the photoabsorption decreases with increasing frequency ω and increases with the atomic number Z. This is empirically described by the Bragg-Pierce-law [48]:

$$\sigma_{\mathrm{ph}} \sim \frac{Z^4}{E^{\frac{5}{2}}}. \tag{2.40}$$

2.2.4 Element-dependent interaction processes

Fig. 2.6a depicts the scattering cross sections of different elements for a photon energy of 9.25 keV. Comparing the size of the cross-sections, the photoabsorption process is overall the most relevant contribution. It possesses steps at the element gallium, as it possesses the K_α-line just at 9.25 keV.

Only for very light elements like helium and lithium, Compton scattering dominates. For heavier elements, the cross section of coherent processes is stronger than that of Compton scattering, but much weaker than that of photoabsorption; their increase with Z fits to the expectations when considering equation 2.20 and 2.40. Nevertheless, one should not forget that for many experiments the coherent elastic scattering is very relevant, as refraction, reflection and diffraction are based on it. Moreover, elastic scattering gets especially important in the case of coherent processes, as then the different contributions add up.

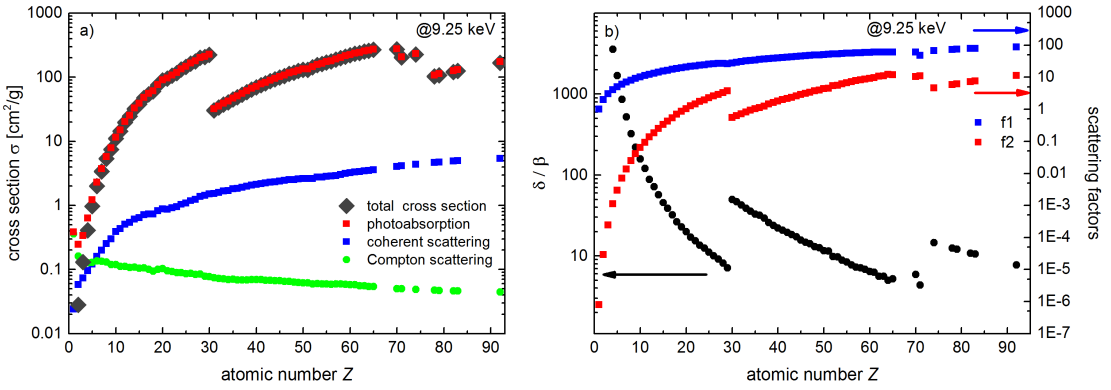

FIGURE 2.6: a) Cross sections as well as b) scattering factors $f_{1,2}$ together with the ratio of the real and imaginary refractive index parts δ/β at 9.25 keV dependent on the atomic Z number. a) The cross sections of photoabsorption, as well as of coherent and Compton scattering are given separately. Despite very light elements, photoabsorption is the most relevant contribution. As expected, the cross section of photoabsorption and coherent scattering increases with Z. b) Absorption processes represented by f_2 and β get more relevant at high Z numbers. In both figures, jumps appear at the element gallium, as it possesses the K_α-line just at 9.25 keV.

Moreover, Fig. 2.6b shows the corresponding scattering form factors together with the ratio of the real and imaginary refractive index parts. As expected, absorption processes represented by f_2 and β get more relevant at high Z numbers.

2.3 X-ray optics

X-ray optics can be split into four different types dependent on the physical origin of their working principle: reflecting, diffractive, refractive and absorbing optics. One should note, however, that there exist also many optics where two or more effects are combined.

An important quantity for optical elements is their numerical aperture, which is defined as:

$$NA = n \cdot \sin\alpha \tag{2.41}$$

with α being half the opening angle which is spanned from the focal point to the edges of the optical element. Thus, the higher the *NA* of an optical element, the larger the angle of the light cone which it can accept or emit.

Moreover, the *NA* is a measure for the possible diffraction limited resolution. For instance, the Rayleigh criterion is based on the definition that two point sources can be still resolved just when the first diffraction maximum of one image coincides with the first minimum of the other one. This leads to the minimum resolved length:

$$d_{\text{min}} = \frac{0.61\lambda}{NA}. \tag{2.42}$$

Thus, the higher the *NA*, the better is the possible resolution with an optical element.

2.3.1 Reflecting optics

From Snell's law (see equation 2.31) it can be easily seen that there exists an angle

$$\alpha_{\mathrm{C}} = \arcsin\left(1 - \delta_2\right) \tag{2.43}$$

where the beam propagates along the air-material-interface. For even larger angles, the light gets totally reflected.

As δ is usually very small for X-rays, this phenomenon appears only close to glancing incidence. Therefore, often an angle θ is introduced, with $\alpha + \theta = 90°$. Approximating $\cos\theta_{\mathrm{C}}$ further with a Taylor expansion, equation 2.43 gets transformed to:

$$\theta_{\mathrm{C}} = \sqrt{2\delta}. \tag{2.44}$$

The critical angle for total reflection can be also approximated as [27, 49]:

$$\theta_{\mathrm{C}}[\mathrm{rad}] = \frac{0.02\sqrt{\rho}}{E} \tag{2.45}$$

with the density ρ in g/cm^3 and the energy E in keV. For quartz glass, the critical angle for 9 keV is about $0.2°$. When higher angles are needed, the glass can be coated with heavier materials like gold or lead. Of course, this can be used to guide X-rays, for instance in mono- or polycapillaries, as explained in the following.

Monocapillaries An ellipse is distinguished by the fact that it focuses light of a point-like source placed in one of its focal points to the other focal point (see Fig. 2.7). Thus, if in one part of the ellipse the angles of incidence stay below θ_{C}, one has the ideal shape to focus light efficiently with a single reflection. Indeed, this concept is used for focusing X-rays via so-called monocapillaries: they are elliptic solids of revolution based on that part of an ellipse, where the condition for total reflection is fulfilled. Since only single reflections appear, their efficiency can be close to 100%. Therefore, monocapillaries are very efficient optics for illumination.

One should note, however, that as a light source is in reality not point-like but has a finite extension, it gets magnified by the monocapillary. For each beam path, the magnification is different and given by the geometric ratio $M = F_1/F_2$, which is shown in Fig. 2.7. From the sum of reflected rays, an average magnification is usually defined. In Fig. 2.8 it is depicted for different capillary lengths, how an average 1:1 magnification is reached if the monocapillary is fully symmetric with respect to the focal points. Moreover, Fig. 2.8 also shows that the

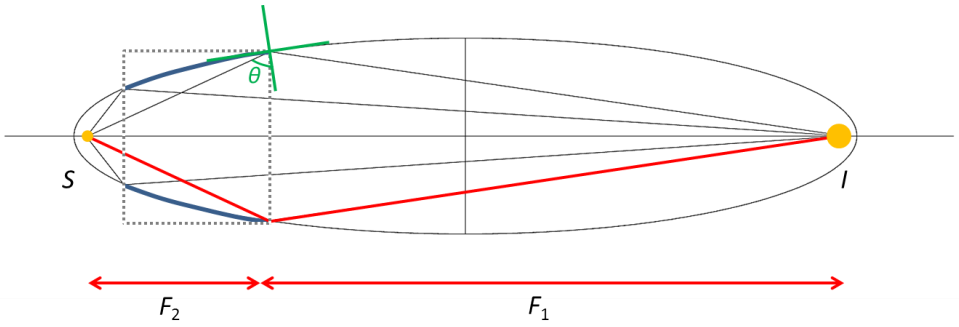

FIGURE 2.7: Schematic drawing to explain the concept of a monocapillary. Light from a source S in the left focal point is imaged by the ellipse wall into the other focal point I, independent from its angle of incidence θ (green). In reality, only a part of the elliptic solid of revolution is fabricated (such as the one marked by the blue wall and gray-dashed box), where the condition for total reflection is fulfilled. As in reality, the source has a finite size, it gets magnified. For each beam path, the magnification is different and given by the geometric ratio $M = F_1/F_2$, as shown exemplarily for the red marked ray.

implemented section of the ellipse defines the maximum light cone; the shorter the length, the smaller the angle of the light cone and thus, the less light is transmitted.

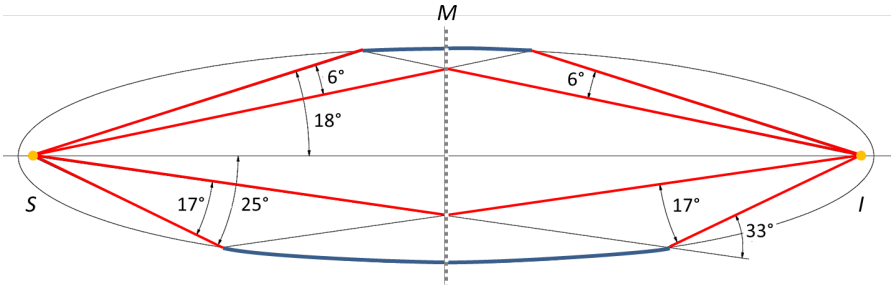

FIGURE 2.8: Schematic drawing of two different monocapillary designs (top and bottom blue sectors) which lead to an average 1:1 magnification, as they are symmetric to the middle axis M (gray dashed line) of the ellipse. They differ by the maximum light cone, which has an angle of 6° for the upper case and 17° for the lower case.

The main challenge for the design of a capillary as a condenser is to match it to the numerical aperture of a zone plate which follows in the beam path. Additionally, also the criteria for total external reflection, the source magnification, the filling factor of the cone and the limits of shape and length due to fabrication challenges have to be taken into account [50, 51]. In order to find an optimal shape, ray tracing programs are needed.

Polycapillaries Larger collection angles can be reached with the concept of multiple reflections, which is the working principle of polycapillaries and was demonstrated for the first time by Kumakhov in 1990 [52] (see Fig. 2.9a).

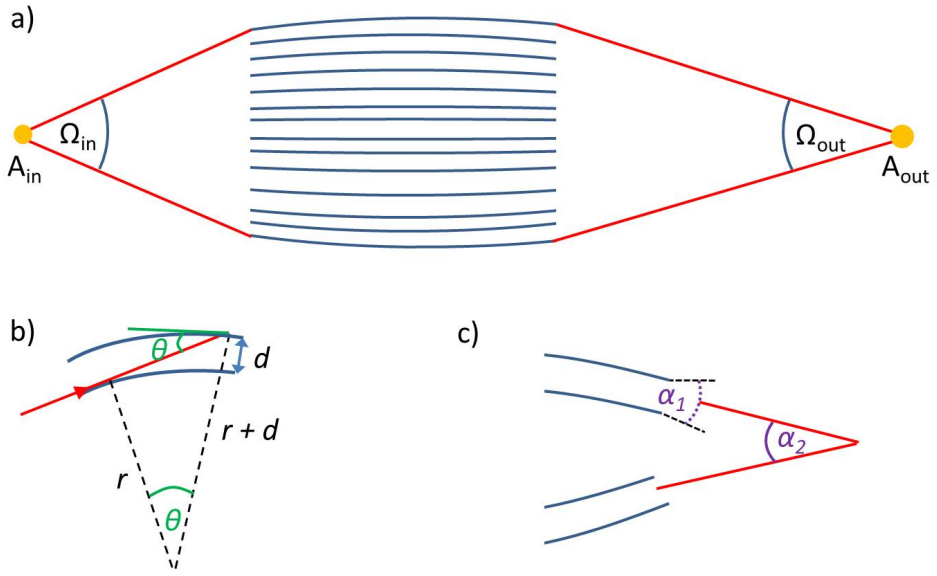

FIGURE 2.9: a) Schematic drawing of a polycapillary with the secondary focus size limited by: $A_{\text{in}}\Omega_{\text{in}} \leq A_{\text{out}}\Omega_{\text{out}}$. b) Dependence of the maximum angle of incidence θ and the bending radius r for a single tube with thickness d. c) Two effects contribute for a polycapillary to the beam divergence. A local divergence α_1 originates from the tube's finite size; a global divergence α_2 arises from the beam geometry. [Adapted from Ref. [53]]

Polycapillaries consist of various bent glass tubes with inner diameters between approximately 2 μm and 50 μm [53]. Each tube possesses a large enough bent radius to keep the reflection angle below the critical angle for total reflection θ_{C}. Indeed, the maximum angle of incidence is given for a tube by its radius r and diameter d (see Fig. 2.9b):

$$\theta = \text{acos}\left(\frac{r}{r+d}\right). \tag{2.46}$$

The transmission efficiency depends strongly on the number of bounces and how strong the optics is bent; therefore, it has a wide spread between 10% and 80% [54]. Indeed, two effects contribute to the beam divergence, as depicted in Fig. 2.9c: besides the global divergence α_2 which arises for optical elements from the beam geometry, an additional local divergence α_1 originates from the tube's finite size.

Concerning the image size produced by a polycapillary, a first approximation can be given by the fact that the etendue stays constant for an optical system or gets reduced due to losses (see equation 2.6). Moreover, it will also depend on the overlap of the spots of the single tubes, as well as the channel sizes, the focus length and the local divergence of the single tubes.

In general, capillaries are broadband optics which work like a low-pass filter, meaning that higher energies than a certain threshold (depending on reflection angles) are damped. Whenever

reflecting optics for a certain wavelength (*i.e.* optics which act like a bandpass filter) are needed, multilayers are the optics of choice - as discussed in the following.

Multilayers Although the reflectivity is in principle low for angles larger than θ_C, in total a high reflectivity can be achieved when many beams reflected by a multilayer system sum up, as depicted in Fig. 2.10. To ensure that the waves of different layers with thickness d interfere constructively, the period of the multilayer has to fulfill the Bragg condition:

$$m\lambda = 2d\,\sin\theta \tag{2.47}$$

with the angle of incidence θ (see Fig. 2.10) and different interference orders $m \in \mathbb{Z}^+$.

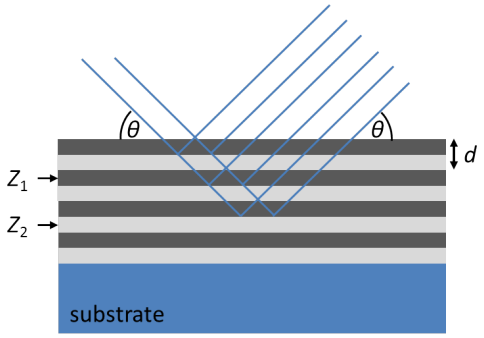

FIGURE 2.10: Schematic drawing of a multilayer. On a substrate, several double-layers of material Z_1 and Z_2 are deposited. Their thickness d needs to be adapted to the angle of incidence θ to fulfill the Bragg condition.

The multilayer can be seen as an artificial crystal made of alternating layers of high and low Z material with a period spacing d. Indeed, the way the wave travels in the material is not negligible: on the one hand, the maximum number of effective layers is limited by absorption effects. On the other hand, refraction has to be considered especially for small grazing angles. Therefore, in order to achieve high efficiencies [55], the spacing in the Bragg equation 2.48 should be adjusted by a refraction correction [56]:

$$d = \frac{m\lambda}{2\sin\theta\sqrt{1 - 2\delta/\sin^2\theta}} \tag{2.48}$$

with the average δ of both layers. As already mentioned, the high-reflection performance is narrow-band. For instance, for the setup constructed in the framework of this thesis, the Ga K_β-line is blocked, when the mirror is designed for the Ga K_α-line (see also chapter 6.1).
In reality, the performance of a multilayer mirror is mostly limited by the surface roughness of the interfaces, as such roughness scatters and reduces the reflectivity. For a good reflectivity, the surface roughness should be below $\sigma = d/10$. A typical value for a Ni/C multilayer with d = 4.0 nm is a reflectivity up to 70% [57].

Similar to capillaries, a multilayer can be also designed for focusing or collimating the beam, if it is shaped elliptically or parabolically. The shape can be produced either by bending the multilayer after deposition or by using a curved substrate. In both cases, the layer periodicity d has to be adopted to still fulfill equation 2.48 in each point of the beam. In reality, often two crossed 1D optics are combined for two-dimensional focusing. When placing the two multilayers perpendicular to each other and side-by-side, this is called Montel-optic.
Moreover, as the Bragg condition can be also fulfilled at large angles, multilayers are well-suited for designing lenses with high numerical apertures. Lenses that fulfill the zone plate law (see next section) and at each zone the local Bragg condition (see equation 2.48) are called multilayer Laue lenses (MLL).

2.3.2 Diffractive optics

Diffractive optics are based on the Huygens–Fresnel principle, meaning that if a wave passes a boundary of an object, every point acts like a new source of a spherical wave.

Fresnel zone plates The so-called Fresnel zone plates are in terms of high resolution imaging the most successfully and most widely used imaging optics. A Fresnel zone plate consists of alternating opaque and transparent radially symmetric rings called zones (see Fig. 2.11). The radii of the zones vary in a way that light transmitted by the transparent zones creates constructive interference at the focal length f [29].

For this, the radii of transparent rings has to be chosen such that the paths x_i of light traveling from neighboring zones to the focal point differs by

$$\Delta x = x_{\mathrm{i}+1} - x_\mathrm{i} = \lambda \tag{2.49}$$

which is the general condition for constructive interference. For the (opaque) zones where this condition is not met, destructive interference occurs. Using for the first zone:

$$x = f + \lambda/2 \tag{2.50}$$

and Pythagoras' theorem, this leads to:

$$f^2 + r^2 = \left(f + \frac{\lambda}{2}\right)^2 \tag{2.51}$$

and thus:

$$r = \sqrt{\lambda f + \frac{\lambda^2}{4}}. \tag{2.52}$$

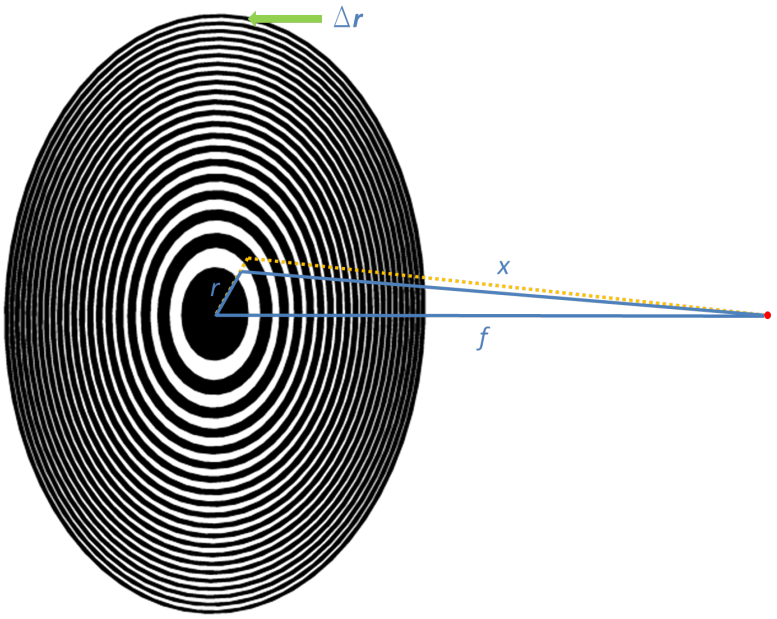

FIGURE 2.11: Schematic geometry of a zone plate, consisting of alternating opaque and transparent radially symmetric rings called zones. The radii r_i of the zones vary in a way that light transmitted by the transparent zones creates constructive interference at the focal length f. For this, the radius of transparent rings has to be chosen such that the paths x_i of light traveling from neighboring zones to the focal point differs by λ. The outer zone is the smallest one with width Δr.

From this, it already follows that the focal length is defined by the diameter of the first zone and the wavelength.

To expand equation 2.52 to all rings, one has to consider in equation 2.50 the zone number n:

$$x = f + n\lambda/2. \tag{2.53}$$

This leads to:

$$r_\mathrm{n} = \sqrt{n\lambda f + \frac{n^2\lambda^2}{4}} \approx \sqrt{n\lambda f} \tag{2.54}$$

where even (n = 0, 2, 4...) and odd zones (n = 1, 3, 5...) contribute waves shifted by $\lambda/2$. Thus, either even or odd zones have to be opaque and the same lens results.

Since for fabrication the smallest structure is the most difficult one, it is useful to express the quantities of interest in dependence of the outermost zone width:

$$\Delta r = r_\mathrm{N} - r_\mathrm{N-1} \tag{2.55}$$

with the total number of zones N. Together with equation 2.54, we can write:

$$r_\mathrm{N}^2 - r_\mathrm{N-1}^2 = Nf\lambda - (N-1)f\lambda = f\lambda \tag{2.56}$$

Inserting the definition of r_{N-1} given in equation 2.55 into equation 2.56 leads to:

$$2r_N\Delta r - \Delta r^2 = f\lambda, \tag{2.57}$$

which can be approximated for $f >> \Delta r$ by:

$$2r_N \approx \frac{\lambda f}{\Delta r} \tag{2.58}$$

This gives a relation between the diameter of the zone plate $D = 2r_N$ and the required smallest zone width Δr.

From equations 2.41 and 2.58, the numerical aperture of a zone lens can be calculated:

$$NA = \frac{r_N}{f} \approx \frac{\lambda}{2\Delta r} \tag{2.59}$$

Using the Rayleigh criterion (see equation 2.42), this leads to a diffraction limited resolution for a zone plate of:

$$d_{\text{min}} = 1.22\ \Delta r \tag{2.60}$$

Up to now, it was neglected that a grating as it appears in a zone plate does not only cause a single interference maximum, but several orders $m \in 0,\ \pm1,\ \pm2....$ Similar to the procedure described above, this leads to focal lengths:

$$f_m = \frac{f}{m}, \tag{2.61}$$

where the zeroth order has the physical meaning of undiffracted light and negative orders represent divergent beams with a virtual focus behind the zone plate. In reality, often only the first order is used. However, since the lens sizes are still the same, higher orders can be used to achieve higher resolutions [58], but with a loss of efficiency (see equation 2.65). Their efficiency η can be calculated by Fourier decomposition of the transmission function of the zone plate [29, 59]:

$$\eta = \begin{cases} 1/4 & m = 0 \\ 1/m^2\pi^2 & m \text{ odd} \\ 0 & m \text{ even} \end{cases} \tag{2.62}$$

Thus, for a binary zone plate (with equal transparent and opaque areas) the highest theoretical efficiency is $1/\pi^2 \sim 10\%$, while 25% pass undiffracted through the zone plate.

Another possibility to enhance efficiency is to replace opaque zones by transparent, phase-shifting zones. In the hard X-ray regime (> 6 keV), practically each zone plate is such a phase zone plate, since thicknesses needed to completely absorb the X-rays are never reached. A phase

shift of $\lambda/2$ with zero absorption would increase the first order efficiency by a factor of four to $\sim 40\%$.

One should note, however, that in reality all materials get absorbing and a solely phase-shifting zone plate does not exist. For such a phase zone plate with absorption, the transmission can be calculated depending on the ratio of δ/β via [12, 60]:

$$\eta = \frac{1}{(m\pi)^2} \cdot \left[1 + e^{\frac{\beta 4\pi t}{\lambda}} - 2e^{\frac{\beta 2\pi t}{\lambda}} \cos\left(\frac{\delta 2\pi t}{\lambda}\right)\right] \tag{2.63}$$

with t being the thickness of the refractive material. From this equation, an optimal phase shift for a certain δ/β-ratio can be calculated. While for $\beta = 0$ the optimum phase shift is as expected π, it decreases continuously with increasing β, for example to 0.73π for $\beta = \delta$.

Moreover, there are also other possible shapes besides binary or phase shift zone plates, for example blazed zone plates (see section 2.3.3) or Gabor phase plates. The latter possesses a sinusoidal modulation of the opacity and thus only three orders (0,1,-1), with a theoretical efficiency of the first order of 34% [12].

Although the zone plate is nowadays probably the most prominent optical element for X-ray imaging, there are still many challenges concerning their production, which should be also briefly discussed. In order to show the limits for the design of lenses, equation 2.58 can be also reshaped to:

$$f = \frac{D\Delta r}{\lambda} = \frac{4N(\Delta r)^2}{\lambda}. \tag{2.64}$$

From this it gets clear that in order to keep f constant for a minimum producible Δr (see chapter 5.2.1), the number of zones N has to be enhanced, which also has an upper fabrication limit.

Moreover, to avoid chromatic blurring and reach full diffraction limited resolution, the condition for the maximum spectral bandwidth:

$$\frac{\Delta\lambda}{\lambda} \leq \frac{1}{N} \tag{2.65}$$

should be fulfilled [29].

Another limit of the above calculations is that so far the zone plate was treated as a flat object without considering any expansion in the beam direction. However, as for high energies the lens has to be thicker, while for large numerical apertures the outermost zone decreases, the combination high energy and large *NA* requires a very large aspect ratio. Therefore, in this case also the Bragg condition needs to be fulfilled (as the outer beams pass several zones and thus layers) and the zones get a wedged shape. These optical elements using a mixture of diffraction and reflection are called multilayer Laue lenses (MLLs) [61]. In reality, the complex

arising shape is often approximated by tilted zones. Moreover, in these cases often two one-dimensional[3] MLLs are combined to focus on a point; however, then the focal planes have to be adjusted to each other. Recently, very high efficiencies and small focal spots were reported for multilayer Laue lenses [62–65].

2.3.3 Refractive optics

Compared to visible light, where the real part of the index of refraction is larger than unity, X-rays possess an index of refraction smaller than one. Therefore, a concave instead of a convex profile is needed to focus radiation.

Compound refractive lenses Since in the X-ray energy range, refraction is very small compared to absorption, a long time it was believed that it is not possible to fabricate efficient refractive X-ray lenses. Indeed, it took roughly 100 years after Roentgen's discovery, until effective refractive lenses were theoretically proposed [66, 67] and experimentally realized [68].

In the following, the focal length of a parabolic X-ray lens is derived [69]. For this, we consider parallel light entering a lens as depicted in Fig. 2.12; refraction induces a direction change of $\Delta\alpha$.

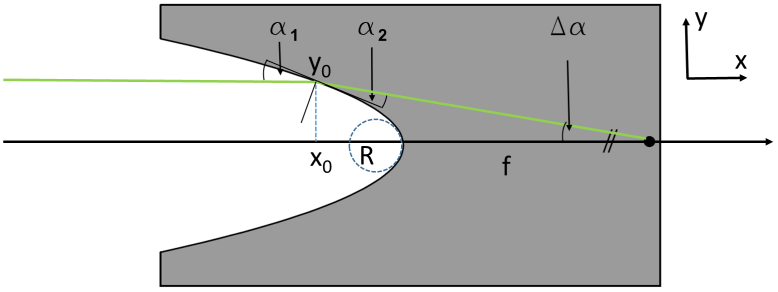

FIGURE 2.12: First part of an X-ray refractive lens with focal length f and opening angle $\Delta\alpha$. A parabola $y(x)$ has its origin at $(0, 0)$; its slope is determined by R. The angle between incoming light (parallel to the x-axis) and the tangent of the lens is α_1; between refracted light and the tangent α_2. Thus, the beam changes direction by $\Delta\alpha$.

From geometrical considerations, one can derive for the shape of the first part of such a focusing lens:

$$\tan(\Delta\alpha) = \frac{y(x)}{f + x_0} \tag{2.66}$$

and

$$\Delta\alpha \approx \frac{y(x)}{f} \tag{2.67}$$

[3] While a standard lens focusses two-dimensionally, *i.e.* on a point, a one-dimensional lens has a line-focus.

with $y(x)$ being the function of the surface and small changes $\Delta\alpha$. In most cases x_0 can be neglected, since it is typically in the range of μm, whereas f is in the range of mm.
With the refraction index $n = 1 - \delta - i\beta$ and Snell's law (see equation 2.31), we get:

$$\frac{\sin(90° - \alpha_1)}{\sin(90° - \alpha_2)} = 1 - \delta. \tag{2.68}$$

with $n = 1$ for air and neglecting the material's absorption. By inserting

$$\Delta\alpha = \alpha_1 - \alpha_2 \tag{2.69}$$

into equation 2.68, it follows that:

$$1 - \delta = \frac{\cos\alpha_1}{\cos(\alpha_1 - \Delta\alpha)} = \frac{\cos\alpha_1}{\cos\alpha_1 \cdot \cos\Delta\alpha + \sin\alpha_1 \cdot \sin\Delta\alpha} \approx \frac{\cos\alpha_1}{\cos\alpha_1 + \sin\alpha_1 \cdot \Delta\alpha}, \tag{2.70}$$

assuming small changes $\Delta\alpha$. Out of the same reason, terms with $\Delta\alpha \cdot \delta$ are negligible, leading to:

$$\Delta\alpha \approx \delta \cot\alpha_1 \tag{2.71}$$

As α_1 is the angle between incoming light and the tangent with the slope $y'(x) = \tan\alpha_1$, we can further combine equations 2.67 and 2.71 to:

$$\delta\frac{1}{y'(x)} = \frac{y(x)}{f} \tag{2.72}$$

By assuming a parabolic shape $y(x) = \sqrt{-2Rx}$ with the derivative $y'(x) = \frac{R}{\sqrt{-2Rx}}$ one finds:

$$\delta\frac{\sqrt{-2Rx}}{R} = \frac{\sqrt{-2Rx}}{f} \tag{2.73}$$

and thus:

$$f = \frac{R}{\delta}, \tag{2.74}$$

meaning that for a parabolic shape, the focal length is independent from the distance off the optical axis y_0.

For a symmetric lens with two parabolic surfaces, the focal length is reduced by a factor of 2; for N thin lenses, it can be shown that the resulting focal length is divided by the number of lenses N [46]:

$$f = \frac{R}{2N\delta} \tag{2.75}$$

Equation 5.6 is only valid for thin lenses, where the total length of the stacked lenses is well below the focal length. For the CLRs used in the framework of this thesis, this is the case.

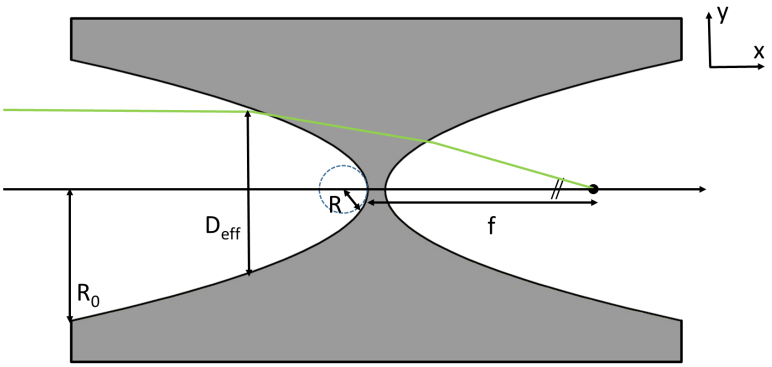

FIGURE 2.13: Schematic drawing of a symmetric compound refractive lens with two parabolic surfaces and focal length f.

One should further note that the strong absorption when X-rays pass a material limit the effective aperture, and thus also the numerical aperture and resolution. In this regard, one can define an effective aperture as [70]:

$$D_{\text{eff}} = 2R\sqrt{\frac{2}{\mu \cdot NR + 2Nk^2\sigma^2\delta^2}} \tag{2.76}$$

where the first term inside the square-root represents absorption due to the material and the second one effects induced by a non-zero surface roughness σ. For many techniques, including X-ray LIGA, the effect of the surface roughness is comparably small and the numerical aperture can be written as [69]:

$$NA = D_{\text{eff}}/2f \tag{2.77}$$

Hence, the CLRs are usually stacks of several lenses with a length L, and the largest possible field of view is limited by a maximum acceptance angle $\sim D_{\text{eff}}/L$. This leads for the thin lens approximation to a field of view:

$$FOV_{\text{CRL}} = \frac{D_{\text{eff}} \cdot g_{\text{object}}}{L} \tag{2.78}$$

with the object distance g_{object}. If the angle is larger, rays passing through the first lens are absorbed in the last one. Moreover, one should also note that besides all the already discussed limits, a suitable illumination has to be ensured for imaging - through each point of the object a ray has to pass through the CRLs.
For the resolution, as D_{eff} is not a sharp aperture (meaning that also above D_{eff}, some radiation is transmitted), the prefactor of the Rayleigh criterion transforms to [56]:

$$d_{\text{crl}} = 0.75\frac{\lambda}{2NA}. \tag{2.79}$$

As already mentioned, the biggest problem for realizing such a lens effectively is the high absorption of X-rays. By using Lambert-Beer's law and integrating along the parabolic shape of the lens, one obtains for a thin lens the transmission:

$$T = \int_R e^{N\beta y(x)} dx \tag{2.80}$$

with the smallest distance d between neighbouring parabola. In order to reduce the absorption, one can investigate which parts of the lens are responsible for refraction. From such studies, it follows that parts inside the lens may be removed without changing the lens' refractive properties. This is shown in Figure 2.14. Starting with a parabolic lens, every time when y reaches a full fraction of λ/δ, material is removed. By rearranging the still present parts an ideal zone plate is created, where the non-absorbed radiation is focused in the first order focus, since the phase shift in each zone is chosen to concentrate in a single focal spot. This is called blazed zone plate. The principle was successfully demonstrated in Refs. [71] and [72]. More generalized, this procedure results in using small prisms to refract the X-ray beam [73].
An ongoing problem is that most high resolution fabrication techniques only work in two and not three dimensions; whereas binary zone plates can be fabricated two-dimensionally, the blazed form requires a three-dimensional technique. Up to now, the only alternative is to use two crossed one-dimensional optics.

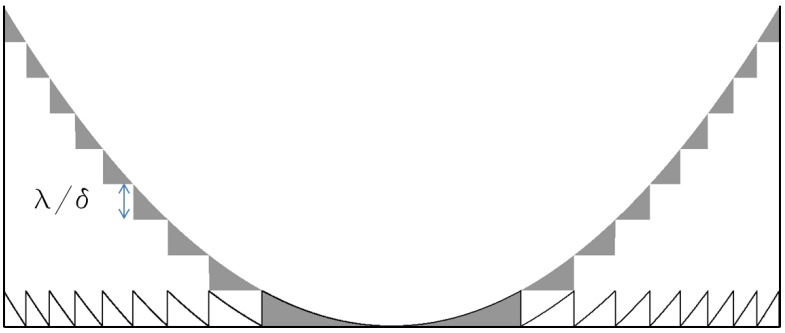

FIGURE 2.14: Drawing of an absorption-optimized CRL, where parts inside the lens are removed without changing the lens' refractive properties. Starting with a parabolic lens, every time when y reaches a full fraction of λ/δ, material is removed. The left-over parts form a blazed zone plate.

2.3.4 Absorbing optics and waveguides

Finally, also absorption can be used to create optical elements. As all absorbing optics are not chromatic, they can be used with any spectrum.

Pinholes The simplest way to improve resolution independent form source or detector (pixel-) size is to use an absorbing pinhole. This creates an inverted image of the object with the magnification $M = (x_0/x_1)$, with the corresponding distances pinhole to object x_0 and pinhole to detector x_1. Although the resolution can reach the aperture's diameter d_p, the big drawback is obviously a very small throughput. While for compound refractive lenses the flux and resolution becomes better with increasing their diameter, for a pinhole the resolution decreases with increasing diameter.
To overcome the limited throughput one can use an array of pinholes (or different shapes), known as coded aperture. In this case, each pinhole produces a shifted image on the detector. With the known positions of the pinholes, the image of the sample can be encoded by image processing [74, 75].

Waveguides Another related optical element whose functionality is based on total external reflection are waveguides. They typically consist of an air channel enclosed with X-ray reflecting surfaces. The reflection between the two surfaces generate transverse standing waves, as the beam propagates along the optical cavity [76]. Waveguides do not act like a lens, but as spatial and coherence filter for a secondary source; thus, the secondary source size does not depend on the input and is usable for in-line phase contrast or holographic imaging [77]. A further advantage is that the production of one-dimensional waveguides in the nanometer range is much easier than that of small pinholes; when they are crossed, two-dimensional focusing is achieved.

2.4 Detection of X-ray photons

Today, mainly two methods are used in X-ray imaging to detect the photons: direct and indirect detection. One possibility for indirect detection is that an intermediate conversion to visible light is done, and this visible light produces an electronic signal. A second type of indirect detection is to use an electronic-optical amplifier, which is also called X-ray image amplifier. Here, X-ray photons are first converted into electrons, which are then accelerated, generating on a scintillator more visible photons; this gives a brighter image but not an improved signal-to-noise ratio. Therefore, due to the high quantum efficiency and low read-out noise of nowadays cameras, in most cases there is no real benefit when using image intensifiers.

Basic properties to compare detectors are efficiency, energy resolution and pixel size (or further the point spread function). For non-photon-counting detectors also the full well capacity (the amount of charges *i.e.* photons a pixel can hold before saturation) and the noise which is produced during an exposure, are relevant. The fraction of these quantities gives the maximum

dynamic range, which is equal to the smallest gray value difference that can be detected; however, in most cases this detector noise does not mainly determine the signal-to-noise ratio, but the photon noise does (see also chapter 3.2). More details about radiation detection is given in the following [56, 78].

2.4.1 Indirect detection

In the case of indirect detection, the X-ray photons are converted by a scintillator to visible photons; this process is called photo-luminescence. Unfortunately, the photo-luminescence process is very complex and many variations exist [79]. Mostly relevant is that the X-ray photon needs to loose energy, before it can be converted into visible light. A model for this energy-loss process in inorganic scintillators can be described as follows: First, an X-ray photon is absorbed and creates a primary photoelectron and the corresponding hole, followed either by the re-emission of a secondary X-ray photon or an Auger secondary electron. While the secondary X-ray photons are cascadically re-absorbed, the fast energetic photoelectrons and Auger electrons create in an avalanche process new secondary electrons, until the energy falls below the ionization threshold [80]. At the end of such a cascade, the electron-hole pairs are thermalized by electron–phonon relaxation to energies in the range of the band gap [81]. Electron-hole clouds (Wannier-excitons) travel through the crystal and recombine at luminescence-centers (*e.g.* defects) by emitting visible light; these are the visible photons which are relayed by a lens system or taper (light guides) to a camera with a pixel array and are finally detected.

From a technical point of view, important scintillator properties are its strength of absorption, its light yield (*i.e.* the conversion efficiency of X-ray photons to visible photons) and the speed of the whole process. In order to guarantee high absorption rates, it is important that the scintillator consists of a high density and high Z material. Moreover, a high speed minimizes the probability for dipole-forbidden recombination processes and long after-glow times. Besides that, technical properties such as the chemical stability, the mechanical strength, as well as the possible thickness and size of the scintillator are important selection criteria. The scintillators used in the setup constructed in the framework of this thesis are listed in chapter 3.2.

2.4.2 Direct detection

Direct detection means that the X-ray photons are directly converted into an electronic signal. When a photon with sufficient energy is absorbed in a semiconductor, an electron is lifted from the valence to the conduction band. As for X-radiation, the kinetic energy of this electron is very high, it produces secondary electrons and thus many electron-hole pairs. Due to an external voltage, these electrons and holes drift in opposite direction, therefore creating a photocurrent. For the next step, one has to distinguish between two different types of detectors, integrating

and single photon detectors. While for the integrating detectors many photons are collected and the electrons are stored in a capacitor before reading, in the single photon detector each X-ray photon is counted separately. To allow this, the current needs to be amplified in each pixel to reach values higher than the noise level [82].

For medical usage, due to the large required size of the detector and rather high X-ray energies (above 25 keV), commonly integrating detectors made of amorphous selenium are used [83]. In the case of imaging smaller samples at lower energies, single photon detectors like the *Medipix*, *Pilatus* or *Pixrad* are used. Since they produce nearly no noise and reach - depending on the energy and thickness of the sensor layer - very high conversion rates (above 99 % at 9 keV for 500 μm Si), they are close to ideal detectors. Although in general dead times between two events have to be considered for these detectors, in latest systems this problem is solved by alternating the readout between two counters. One drawback for high-resolution imaging is that in this case, there are up to now no small pixel size detectors available (below 50 μm).

3 Experimental setup

In this chapter, the experimental setup built in the framework of this thesis is described, starting with a description of the core parts. As the peculiarity of the setup is the extremely bright liquid-metal-jet anode source, the first part focuses on the characteristics of this novel x-ray source (see section 3.1). Afterwards, the utilized detectors are described, concentrating on the home-built ones (see section 3.2). The chapter closes with a description of the whole experimental setup in section 3.3, including a brief overview of the further components and infrastructure.

3.1 The liquid-metal-jet anode source

The liquid-metal-jet anode is an electron impact x-ray tube, where in comparison to common x-ray tubes the solid anode is replaced by a liquid one. This allows a fast dissipation of heat. It was originally developed by the group of Prof. Herz at the *KTH Royal Institute of Technology* in Stockholm [84]. Since 2011, a commercial version is sold by the Swedish Company *Excillum*. Thus, in the here described setup, one of the first series sources is used.

A schematic drawing of the working principle and geometry is depicted in Fig. 3.1. Electrons are created from a lanthanum hexaboride crystal cathode which has a standard diameter of 200 μm, but can be changed to a smaller one (for example 120 μm) if smaller spot sizes are needed. An electron optic focuses them on the jet, creating x-ray photons which pass through a beryllium exit window. The exit window is protected by a thin heated foil from debris; it has an output angle of 13° and is 18 mm away from the focal spot, defining the minimum distance for further optical elements.

3.1.1 The liquid-metal-jet

In general, for an X-ray tube the efficiency for converting electrical P_{ele} into photonic power P_{brems} (without characteristic radiation) is approximately given by [56]

$$\eta = \frac{P_{\text{brems}}}{P_{\text{ele}}} = \frac{1}{2}\, C \cdot Z_{\text{target}} \cdot (\text{e}V_{\text{max}}) \tag{3.1}$$

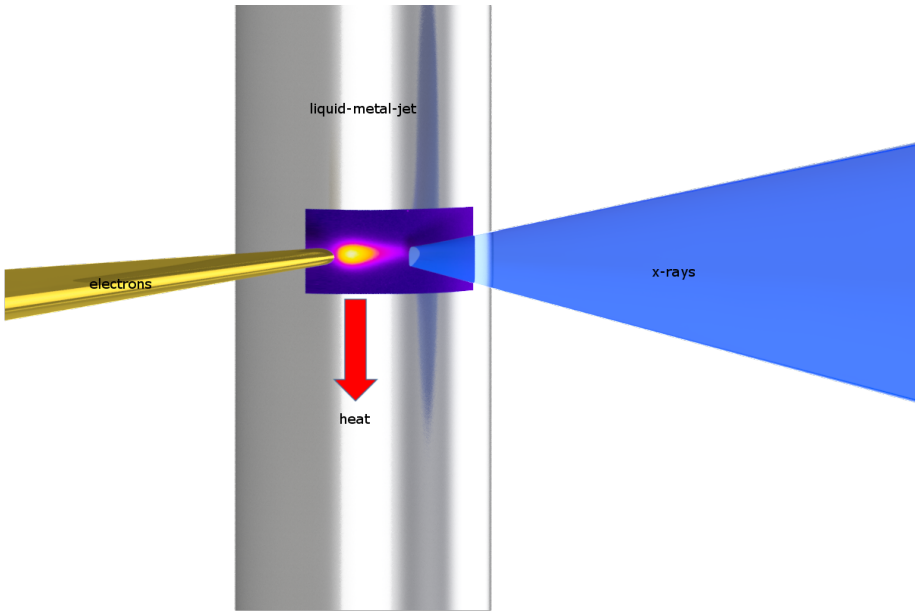

FIGURE 3.1: Schematic drawing which describes the working principle of the liquid-metal-jet anode source. A highly focused electron beam hits a fast traveling jet of a liquid-metal alloy, resulting in the generation of x-ray photons. The major fraction of energy deposited by the electrons is converted into heat, which has to be transported quickly away.

with Kramers' constant $C = 2.2 \cdot 10^{-9}/\text{eV}$, the atomic number of the target material Z_{target}, and the maximum impact energy of an electron $\text{e}V_{\text{max}}$. As in our case, gallium with an atomic number of 31 is used as anode material and the typical tube voltage is 70 kV, ones obtains for the efficiency $\eta = 0.25\%$. Thus, when considering the contributions to the X-ray spectrum (see Fig. 3.6) one can conclude that the totally produced X-ray power (*i.e.* Bremsstrahlung and characteristic irradiation) is below 1 % of the electrical power, meaning that more than 99 % of the energy is deposited into heat. This enormous amount of heat has to dissipate in order to prevent the anode from being destroyed, *i.e.* melting in the case of a standard anode or evaporating in the case of the liquid-metal-jet anode source. Therefore, in the latter case the anode material is continuously replaced by a liquid jet with a very high speed of approximately 75 m/s. This means that a particular gallium volume is only exposed during a very short time period to the electron beam; afterwards, the heat can dissipate to the environment, before the gallium is again exposed to the electrons.

Technically, the high speed of the jet is caused, as a pressure difference between 200 bar and 10^{-8} mbar has to be overcome on a very short distance: on the one side, one has the reservoir, where 250 ml of metal alloy are stored at 29°C in an environmental pressure of 10^{-8} mbar. On the other side, this reservoir creates a hydrostatic pressure which guarantees the functionality of a subsequent membrane pump, equipped with an inlet and outlet check valve. After having passed the pump, the alloy is pressed with 200 bar through a 7 μm particle filter and a nozzle. In the nozzle, a sapphire disc with a 200 μm hole forms the gallium jet with a diameter of 190 μm. Before the jet re-enters the reservoir, the interactions with the electron beam takes place which

generates the X-ray radiation. Afterwards, the jet is slowed down on a tilted ceramic and cooled back to 29°C.

3.1.2 Shape, power loading and stability of the focal spot

When engineering the source, *Excillum* payed particular attention to their calibration system for the size and the shape of the X-ray focus. The reasons are twofold:

- One parameter which is here controlled is the power loading, *i.e.* the power of the electron beam that hits the cathode per square millimeter. This monitoring is extremely important to guarantee a stable emission and avoid a destruction of the cathode or exit window due to overloading. In the latter case, the anode material might evaporate; furthermore, charged ions accelerated towards the cathode are able to destroy it by ion etching. Actually, the latter scenario is still a hot topic of current research by *Excillum* and the *KTH* [85]. They favor now a bent flightpath of the electrons. Like this, any collision of charged ions with the cathode material can be excluded, as the ions do not longer hit the cathode due to the different mass-charge ratio compared to electrons.
- Secondly, the shape of the focal spot has severe influence on the imaging properties. In the case of imaging without X-ray optics, it affects the resolution (see chapter 4); when optical elements are used, it causes differences in the intensity (see chapter 5). Thus, it is in any case beneficial to know the actual shape of the focus in order to optimize the recording time and resolution.

Calibration The calibration is done whenever source settings are changed, as well as typically in a 24 hours cycle. In principle, the built-in calibration system of the source controls the electron optics and thus the focal spot. Technically, the size of the electron jet gets characterized by electrons which hit an electron beam dump and thus generate an electric current; in between electron source and beam dump, the liquid-metal-jet is situated. Thus, by scanning the electron beam over the edge of the jet, one can determine the extension of the beam. This is done on the one hand by scanning in the horizontal plane via deflector coils. For the vertical dimension, the electron beam is rotated and the size is determined in the same way. Certainly, the obtained results depend on the original calibration of the deflector coils, but it allows to adjust changes in jet position and size.

Spot settings While the direction of incoming electrons is always orthogonal to that of the emitted X-ray photons (see also Fig. 3.1), the exact shape of the X-ray spot depends delicately on the horizontal point of impact on the anode. This horizontal shift dx is freely adjustable.

A second parameter which has influence on the X-ray spot size is the interaction depth of the electrons with the anode material, which is simulated and discussed in Ref. [86].

For an experiment, several spot diameters of the electron beam can be freely chosen between 5 μm and 120 μm. In the most cases, elliptically shaped spots are used, because according to the operation recommendations by *Excillum*, the safe power loading scales with a factor of 2.5 times the horizontal direction and 10 times the vertical direction, as well as linear with the maximum acceleration voltage. As a rule of thumb, as in the case of bigger spots neighboring area is also heated, a higher brightness can be reached with a smaller spot; however, the overall flux decreases with decreasing spot size.

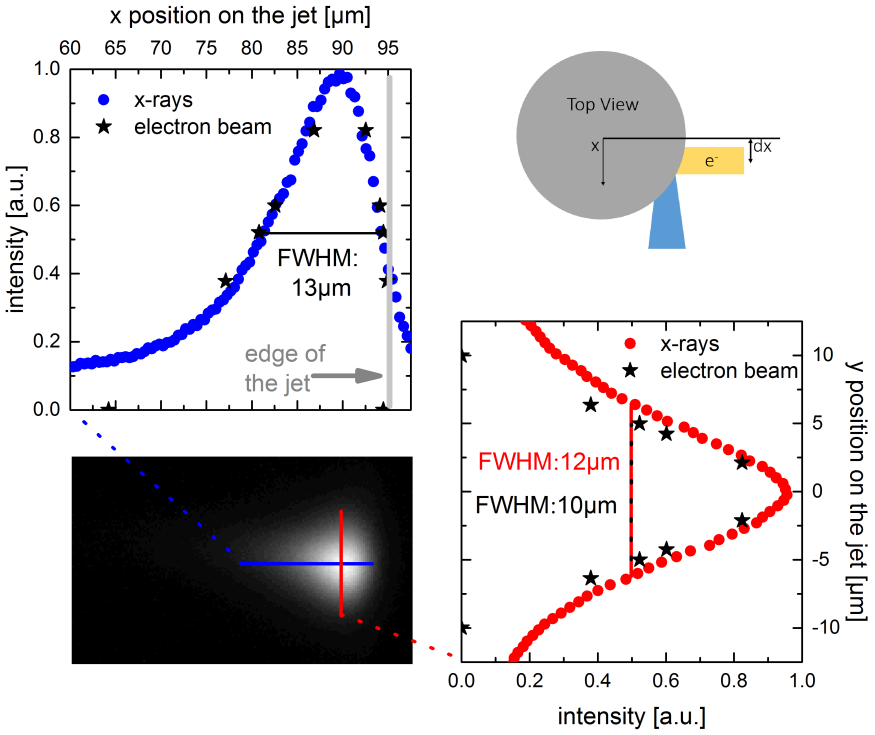

FIGURE 3.2: Image of the X-ray spot shape and corresponding line profiles of the liquid-metal-jet source in horizontal (top) and vertical (right) direction compared to the electron beam size. The set spot size of the incoming electron beam was 10 μm $\times$ 40 μm, orthogonal to the plane of the figure, with a horizontal shift of $dx = 30\,\mu$m (see scheme in upper right corner). The image was magnified by a factor of 1.5 with a zone plate on the detector. The detector pixel sampling was chosen as 619 nm for an exposure time of 30 s. In the horizontal direction, the extension of the electron beam and X-ray spot match pretty well. For the vertical direction, the full width at half maximum (*FWHM*) differs by $\sim 2\,\mu$m.

In the framework of this thesis, several spot sizes were tested in order to optimize the performance of the setup. In order to visualize the extension of the focal spot, images of the source were made using a zone plate. In contrast to the usually taken images via a pinhole camera, this has the advantage of a higher resolution at shorter exposure times. One should note that the zone plate works for the design energy around 9 keV; therefore, the images only show the source

distribution for this energy. However, this is for most experiments done at the setup described in this thesis the most relevant energy.
Fig. 3.2 shows exemplarily such a spot image for a nominal electron beam setting of $10\,\mu$m $\times$ $40\,\mu$m. One should note that these settings refer to the size of the incoming electron beam, which is orthogonal to the created X-ray beam. In the figure, the line profiles of the electron and X-ray beam are compared for the direction orthogonal to the incoming electron beam. While in the horizontal direction, the extension of the electron beam and X-ray spot match pretty well, for the vertical direction, the *FWHM* differs by $\sim 2\,\mu$m, which corresponds to the resolution of the calibration.

Further characteristic examples for typically used spots are given in table 3.1 and Fig. 3.4. It should be noted that the here given area is not the area of the incoming electron beam (defined by the FHMW), but that of the corrugated area on the surface of the jet, where the electron beam is projected. While the maximum powerloading of rotating anode sources is $\sim 7\,$kW/mm^2 (1.2 kW on $70 \times 700\,\mu$m^2 with 6° take-off angle), the liquid-metal-jet source reaches values which are approximately a factor of ten higher. For both source types, an elliptic shape of the electron beam is used to hold the apparent X-ray spot smaller than the heat collecting area. Therefore, the power density is sometimes calculated with the smaller projected area, leading to larger values than given in table 3.1.
From the experience gained in the framework of this thesis, when following the safety recommendations for stable operation the highest brightness can be gained for a spot size of $40\times10\,\mu$m^2 (see Fig. 3.3d). If the recommendations are slightly passed over, a higher brightness can be reached (see Fig. 3.3c). Although this may reduce the lifetime of the cathode, a stable operation can be observed over many weeks. It can be also seen in table 3.1 that the background intensity represents the total flux and scales more or less with the power independent from source size; slight deviations result from electrons placed on the quarter of the jet not oriented to the detector, especially in the case of larger spots (see Fig. 3.3a).

	spot size [μm^2]	shift [mm]	power [W]	area [μm^2]	powerloading [kW/mm^2]	background [counts]	signal [counts]	signal relative
a)	80×20	30	200	5640	58	1550	10920	0.61
b)	10×10	64	25	429	35	210	4280	0.24
c)	46×16	35	200	2648	75	1050	21710	1.21
d)	40×10	30	100	1375	71	600	18010	1
e)	30×30	55	100	3679	27	600	5193	0.28

TABLE 3.1: Characteristic values of typically used spots which are also displayed in Fig. 3.3. The input values: spot size (horizontal × vertical diameter), horizontal shift of the spot away from the jet center dx, electronic power of the X-ray tube, resulting nominal beam area, and the corresponding powerloading (power × area) are listed for an electron acceleration voltage of 70 kV. The last columns show the resulting background and the maximum signal (absolute as well as relative to the signal gained in d), which are corrected by the camera offset (1000 counts). The table shows experimentally that the brightness scales with powerloading.

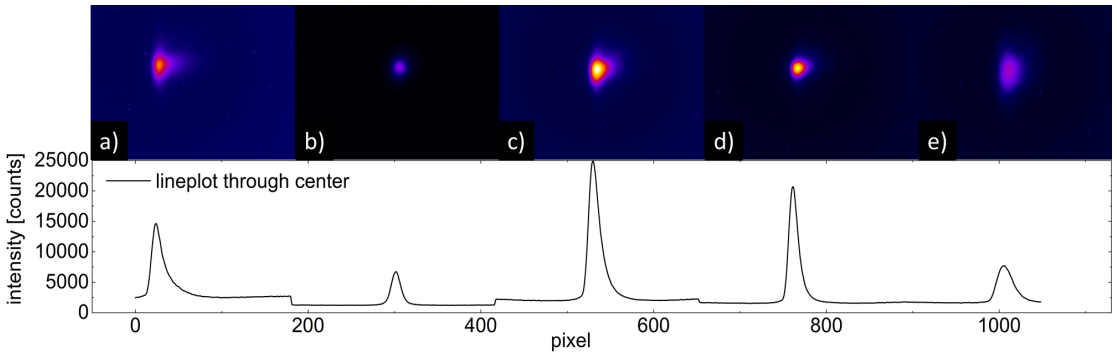

FIGURE 3.3: (Top) Images of the source spots for different power settings and electron beam sizes described in table 3.1. (Bottom) Additionally, the lineplots through the center of the images in horizontal direction are shown. From these plots, the values for the background and maximum signal are taken for table 3.1.

It is very intuitive that the flux scales linearly with input power, as also demonstrated in Fig. 3.4. However, brightness is also influenced by the focal area, as can be seen when comparing Fig. 3.3d and e: while the total flux is more or less the same (corresponding to the same electronic power of the X-ray tube and the same background), the resulting brightness is much higher for higher powerloading. Indeed, this proves experimentally the relation given in equation 2.8, *i.e.* that brightness scales linearly with power at a fixed spot area. This relation only holds as long as the density of the target material does not change (*e.g.* by evaporating), as such a change would influence the penetration depth of the electrons and the self-absorption.

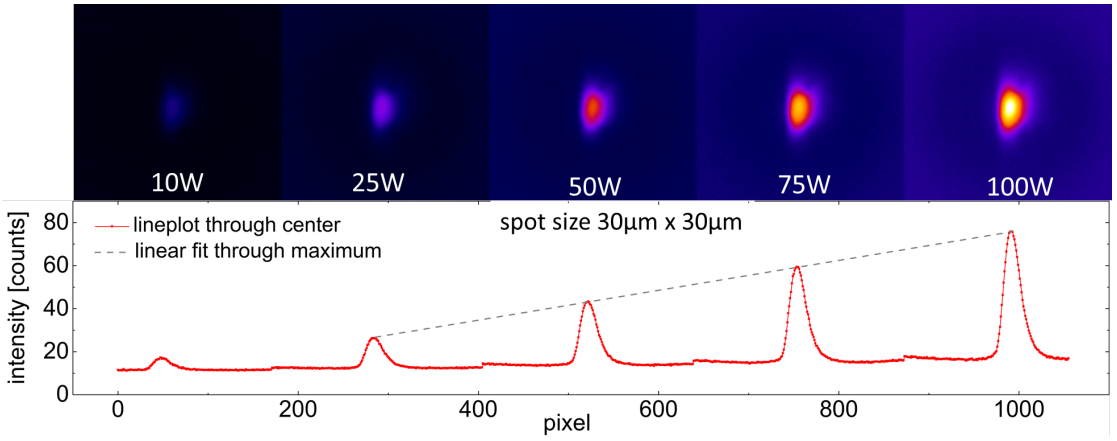

FIGURE 3.4: (Top) Images of the source spot at different power-settings, but with constant source size. (Bottom) Additionally, the lineplots through the center of the images in horizontal direction are shown. The fit shows that the maximum signal increases linearly with power.

Stability Spot-stability is an important parameter which has to be guaranteed for a measurement, since a movement of the spot causes a blurred image in case of imaging without optical elements and an intensity variation for imaging with magnifying optics. For the first case, the constructed setup is not very sensitive to small movements of the spot, as the spot is much larger

than the pixel size (*e.g.* 20 μm source and 1μm pixel size). However, such a movement could still cause errors when reconstructing CT volumes.

Figure 3.5a displays the position of the center of mass of the focal spot, after the source was initially switched on. A clear movement can be observed for about two hours. The movement originates from heating up the whole source-head and mount with 200 W to around $0.6°$C above the room temperature. After heating up, the movement is well below 1 μm per hour and randomly distributed, as can be seen in Fig. 3.5b.
In principle, to guarantee a stable operation the source can be kept on over a long time by using a shutter. However, since this shutter increases the minimum accessible distance of the source to $\sim$ 24 mm, it is not used in the here-described setup. Instead, the time needed for heating up is always considered; it can be used for alignment or less sensitive measurements.

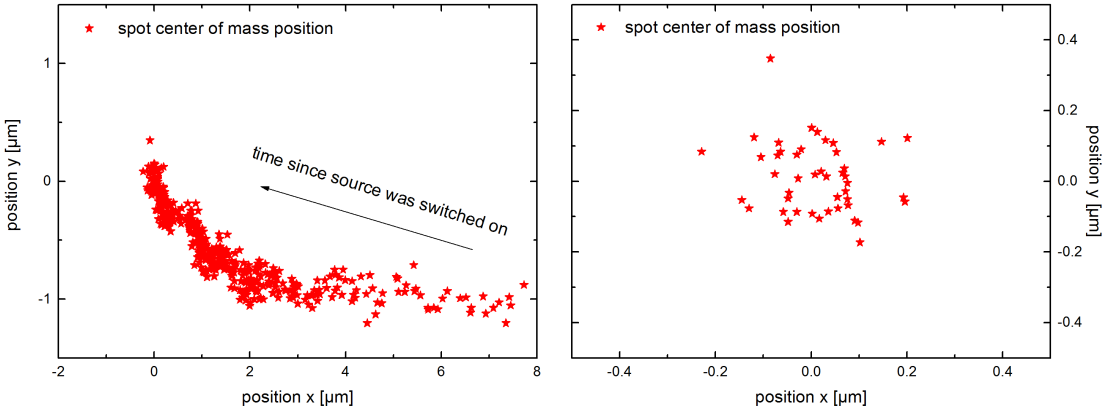

FIGURE 3.5: a) Tracing of the spot center of mass over a time period of 2 hours after the source was switched on. A clear movement appears due to the heating up of the source-head and mount. b) When the source and its mount have reached thermal equilibrium, the spot possesses a stable position. Deviations are then within the sub-micrometer range.

3.1.3 Material of the anode and spectrum

Whenever X-rays are emitted due to the collision of accelerated electrons with an anode, the spectrum is a superposition of two contributions. One is the continuous contribution called Bremsstrahlung, the other is the spike-like characteristic radiation. The resulting spectrum is shown in Fig. 3.6.

The shape of the Bremsstrahlung is in principle a triangle, starting at the energy which corresponds to the acceleration voltage of the electrons. However, self-absorption is damping the intensity especially at lower energies. The resulting shape depends on the atomic number of the anode material, the penetration depth of the electrons and the acceleration voltage; it can be numerically assessed by Monte Carlo simulations [86, 87]. The characteristic radiation results as described in 2.1.3.

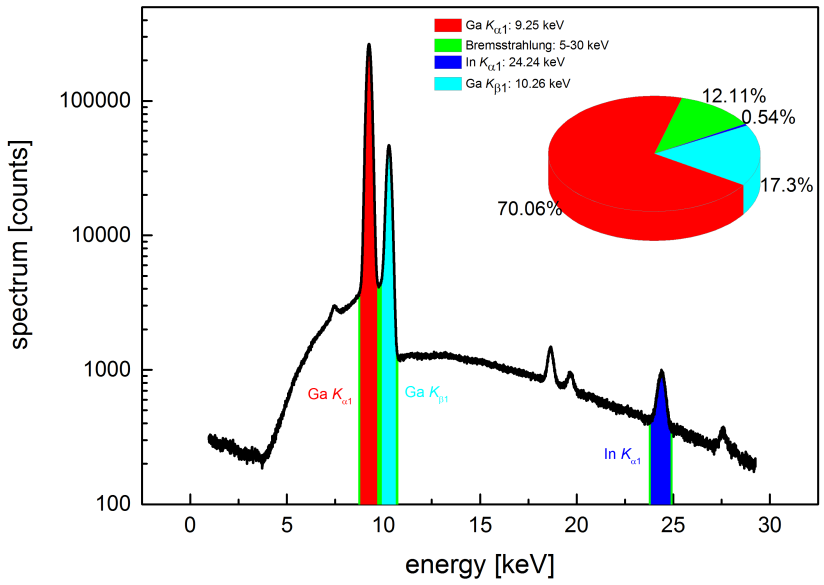

FIGURE 3.6: Measured X-ray spectrum of a Ga-In alloy with 5% In content, together with an overview of the intensity distribution of the most prominent contributions. The distance between source and spectrometer was set to 500 mm. For the measurement, an *Amptek X-123 Si-PIN* spectrometer was used and the beam was collimated with a 200 μm tungsten pinhole.

The ratio of characteristic radiation to Bremsstrahlung can be important if "relative" monochromatic radiation is needed, *e.g.* when working with magnifying optics (see chapter 5). While the number of photons included in the characteristic radiation is proportional to $(V_{\text{tube}}/V_{\text{min}} - 1)^{1.2}$, the number of photons contained in the Bremstrahlung is proportional to the power of two (see equation 3.1). Moreover, V_{min} depends on the atomic Z number of the target. From this, it can be estimated that the highest ratio [56] is reached for low-voltage tubes ($< 100\,\text{kV}$) at 6-7 times the characteristic energy, *i.e.* at 60 kV for gallium. However, photon flux of both contributions increases above this voltage. By integrating the measured spectrum depicted in Fig. 3.6 in the range between 5-30 keV, the contribution of the Ga $K_{\alpha1}$ line to the overall intensity is approximately 70 %.

Filtering can be achieved by using filter foils of different materials. When a relative monochromatic spectrum is needed, absorption edges can be used to selectively damp characteristic lines. With a zinc filter of 8 μm thickness, the K_β line at 10.26 keV is damped about 80%, whereas the relative loss for K_α used for imaging is only 20%. When for thicker samples low energies would be completely absorbed, the spectrum can be shaped by filters made of copper or aluminum to avoid beam hardening by the sample. Additionally, varying the maximum voltage and filters can be used to do dual energy computed tomography with a single source [88].

Choice of the anode material For liquid-jet anodes, besides the existence of an optimum atomic number for a desired spectrum, the anode also has to be fluid at a technical accessible

temperature and a low vapour pressure. First experiments were done with non-metallic materials like water and alcohol, suitable for the generation of soft X-rays. First hard X-ray sources were realized by using a melted alloy of 63% Sn and 37% Pb with a melting point of $183°$C [89]. At this time, the source had no continuous metal cycle, thus it was not able to generate X-rays over a long time. A summary of the development of the jet source technology can be found in Ref. [90].

For the commercial liquid-metal-jet source, today two non-toxic alloys are commonly used. The first one contains 95% gallium and 5% indium with a melting point of $26°$C (see also Fig. 3.6). The emission spectrum is close to that of widely used rotating copper anode sources. Therefore, these can be replaced by the liquid-metal-jet source with higher brilliance. The second commonly used alloy is galinstan, a composite of gallium, indium and tin with a melting point of $-19°$C (see also Fig. A.2). Here, the In K_α-line is suitable to replace silver anode sources; in this regard, successful low dose propagation-based phase-contrast microangiography using the 24 In K_α-line was demonstrated in Ref. [91]. As in the present setup the priority is set on high resolution, mainly the 9 keV Ga K_α emission line is explored (see section 3.2).

In principle, there exist also low-melting materials with higher Z needed to use hard X-ray liquid-jet technology in medical imaging. Some examples are non-toxic Field's metal (containing bismuth, tin, indium; melting point $T_\mathrm{m} = 62°$C), Rose's metal (containing bismuth, lead, tin; $T_\mathrm{m} = 98°$C) and toxic Wood's metal (containing bismuth, lead, tin, cadmium; $T_\mathrm{m} = 70°$C). Recently, *Siemens* announced together with Prof. A. Olivo of the *University College London* [92] in a press release that they are working on a new source based on a lithium-jet with $5\,\%$ heavy elements such as bismuth or lanthanum. However, so far there is no data published which shows the powerloading of such a source.

3.2 Detectors

One way of detecting X-rays are scintillators, which convert the X-rays to visible green light, recordable with an optical camera (see chapter 2.4). In the framework of this thesis, three such indirect detectors were built to meet different requirements regarding the field of view, pixel size and acquisition speed. Table 3.2 summarizes the different properties of the detectors. One can distinguish between a microscope, a macroscope and a high-speed detector. Besides this, for some tasks a *Medipix2* with six detector elements and a *Rad-icon* flatpanel detector were used.

Microscope and macroscope were further combined in one housing as shown in Fig. 3.7. This is the mostly used detector (see also chapter 4 and 5). Dependent on the desired resolution, one can choose between two different objectives via a rotating attachment. While the macroscope

Detector Camera	Pixelsize [μm]	*FOV* [mm]	Pixel $n \times m$	Scintillator normally used	Speed fps max
Microscope					
Zyla sCMOS	0.619	1.58×1.33	2560×2160	LSO	100
FLI CCD	0.66	2.04×2.04	3056×3056	LSO	0.1
Macroscope					
Zyla sCMOS	3.095	7.92×6.68	2560×2160	LUAG/CWO	100
FLI CCD	3.33	10.19×10.19	3056×3056	LUAG/CWO	0.1
High-speed					
Zyla sCMOS	26	49.92×28.08	1920×1080	Gadox Al coated	200
Medipix2	55	28.16×42.24	512×768	direct	5
Rad-icon	48	49.15×49.15	1024×1024	Gadox	10

TABLE 3.2: Properties of the used detectors. Besides the home-built detectors (microscope, macroscope and high-speed detector), also a *Medipix2* and a *Rad-icon* flatpanel detector were used.

contains a linear axis piezoelectric stage for moving the scintillator inside the focus of the objective, the microscope needs a three-axis piezoelectric stage to place the scintillator in the focal plane of the objective. Due to the combination of a thin scintillator and the small focus depth of the objective, only in this way a homogeneous image sharpness can be achieved over the whole image. Behind the objective, a low-pass filter blocks wavelengths above 640 nm, so the red light used as illumination for the monitoring cameras in the hutch is kept outside the detector. Afterwards, two mirrors deflect the light either on a sCMOS camera or a CCD, which are described in more detail in section 3.2.3.

For "high-speed-imaging" (see chapter 6.2), another detector was built in a separate housing. The difference to the microscope / macroscope detector is the larger pixel size with 26 μm, so the optics demagnifies in this case. The design configuration is very similar to the above described one; instead of two objectives, only one is used. The detector is a fast sCMOS camera with 10-Tap camera link connection, capable to record constantly 16 bit dynamic range and 200 frames per second with full-HD resolution. Since normal hard discs are not able to write at these data rates, a fast enough memory (*e.g.* PCIe SSD, RAM) is needed in the computer.

3.2.1 Scintillators and optics

For a detector, the pixel size on the scintillator has to match with its point spread function, or at least should not be much larger. A higher pixel size causes oversampling, which does not improve the resolution but decreases the signal-to-noise ratio.

In terms of energy and resolution, three reasonable material forms are available for scintillators: columnar or structured materials [93], powders and crystals. One example for the first option is CsI, where the columnar structure guides the light. Therefore, resolution and thickness are not

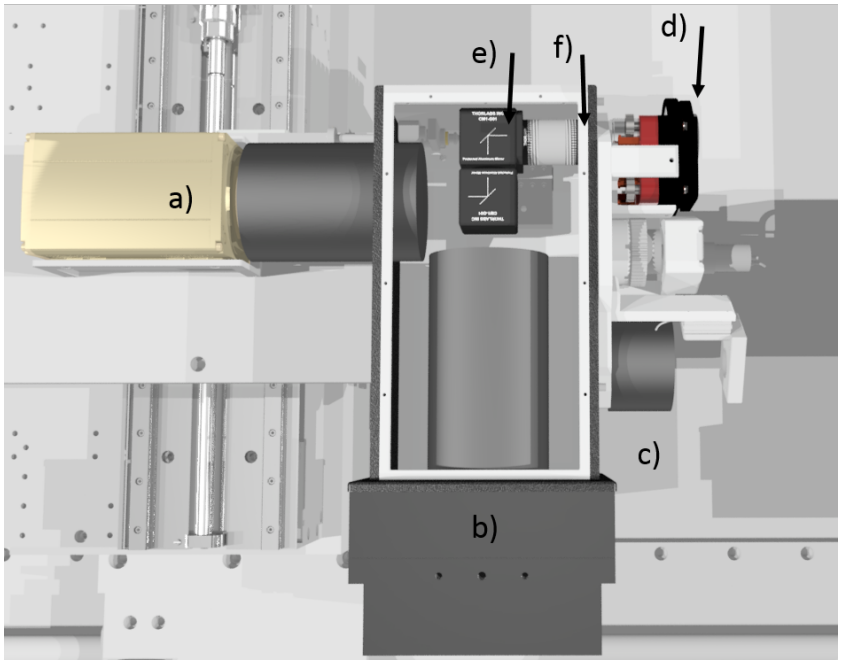

FIGURE 3.7: CAD rendering of the combined microscope / macroscope detector. (a) *Andor Zyla* sCMOS or (b) *FLI PL0900 CCD* are illuminated either by a (c) macroscope or (d) microscope objective with scintillator and focusing unit. (e) The camera can be chosen via movable mirrors. (f) A filter blocks wavelengths above 640 nm, in order to keep light which does not originate from the scintillator outside the detector.

directly coupled. However, CsI is not used in the present setup, as for commercially available scintillators the resolution is well above 3 μm and thus too coarse for our purposes [94]. An alternative are powder-screens, which act like Lambertian sources [95]. Here, the resolution is limited by the thickness and size of the grains. The Lambertian source characteristics help to improve the efficiency of the optical coupling, especially for low aperture optics. However, the achievable resolution based on 3% *MTF*[1] is limited approximately by $R_{\mathrm{L}} = 500/z$ (in lp/mm), with z being the thickness in μm [96]. Another disadvantage is that the density of the material is reduced to half the density of the bulk.

For these reasons, crystal scintillators are often the best choice. In the case of transparent crystal scintillators, the resolution is diffraction limited and thus defined for self-illuminating objects by the numerical aperture NA and the wavelength λ as: $d = 0.61\lambda/NA$, if the crystal is thinner than the focal depth of the lens. Both, manufacturing techniques and the finite thickness of the scintillator prevent reaching the optical resolution limit, and raise the resolution to typically 1-2 μm.

Further details on how the resolution is influenced by the properties of the crystal scintillator are described in Refs. [97–99]. Usually, the main limitation is a blurring due to light created outside the focus of the objective, as the scintillator is often thicker than the focus depth. In

[1] Modulation transfer function, see chapter 4.1.3.

contrast, simulations show that the effect of scintillation relocated from the impacted of the X-ray photon is usually negligible. The achievable resolution based on the 10% *MTF* criterion can be described as:

$$R = \sqrt{\left(\frac{0.34\mu\text{m}}{NA}\right)^2 + (0.036 \cdot x \cdot NA)^2}, \tag{3.2}$$

dependent on the numerical aperture of the objective NA and the scintillator thickness x; the constants were taken from Ref. [98]. While the first term lowers the resolution in the case of low-numerical objectives, the second term considers the thickness of the scintillator.

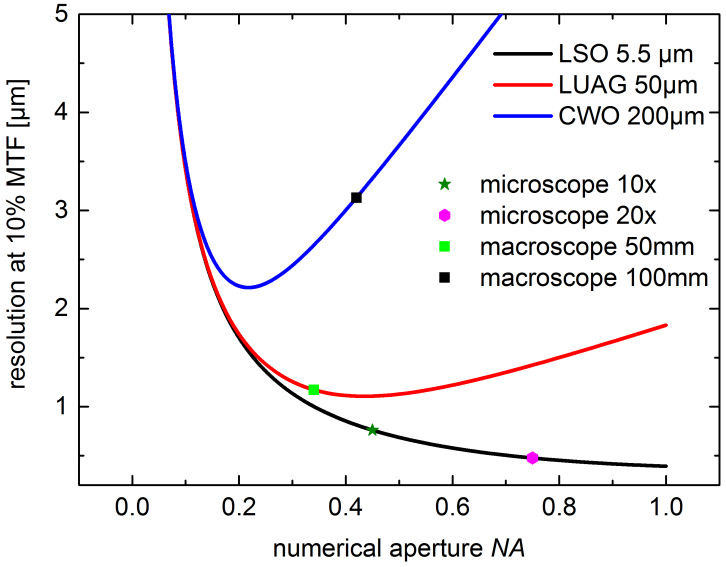

FIGURE 3.8: Theoretically achievable detector resolution dependent on the numerical aperture of the objective for several cerium doped scintillators with an emission wavelength of 550 nm. Used combinations in the setup are marked with points.

Additionally, spherical aberration in the substrate of the scintillator can further lower the resolution. In the case of the 5.5 μm LSO scintillator, the substrate thickness is chosen as 170 μm, because commercially available microscope objectives are matched to this thickness. In contrast, the Gadox scintillators are placed on a 1 mm quartz glass without any correction, lowering the resolution. This problem does not appear for LUAG, as here the scintillator itself has a thickness of 50 μm and is therefore free-standing.

In general, one should note that the measured resolution is always slightly lower than the theoretically achievable one, as further discussed in chapter 4.

3.2.2 Detective quantum efficiency of the detectors

Detective quantum efficiency (*DQE*) describes how effective a detector can produce an image. An ideal detector would have a *DQE* of 100%. Lower *DQE* will add noise to the image and reduce the signal-to-noise ratio, as further discussed in chapter 4.1.1.

Name Formula	diameter [mm]	thickness [μm]	structure grain	light yield [ph/keV]	absorption at 9.25 keV	density [g/cm^3]
Gadox $Gd_2O_2S:Tb$	30×20	5	powder 1-2 μm	60 [100]	0.62	7.3
Gadox $Gd_2O_2S:Tb$	80×60	50	powder 4-5 μm	60 [100]	0.999	7.3
LSO:Tb $Lu_2SiO_5:Tb$	10	5.5	crystal	52 [101]	0.55	7.4
LUAG:Ce $Lu_3Al_5O_{12}:Ce$	20	50	crystal	20 [102]	0.999	6.76
CWO $CdWO_4$	50	200	crystal	15	1	7.90

TABLE 3.3: List of utilized scintillators. One has to distinguish powder (Gadox) and crystal scintillators (LSO, LUAG and CWO). The thinner the scintillator, the higher the achievable resolution. However, this gain in resolution is on the expense of absorption, *i.e.* efficiency. Moreover, crystal scintillators have a lower light yield, meaning that less photons are produced per keV X-ray radiation.

In general, the detective quantum efficiency is a function of spatial frequency and defined as [103]:

$$DQE = \frac{SNR^2_{\text{out}}(u)}{SNR^2_{\text{in}}(u)} \tag{3.3}$$

with the in- and out-coming signal-to-noise ratio SNR_{in} and SNR_{out}, respectively, both depending on the spatial frequency u in the Fourier space.

For a detailed description, the used indirect detector can be modeled as a cascaded system, consisting of a scintillator, a lens-system and a camera [104]. In this case, the detection process can be separated into five stages: incident stage (*i.e.* photon which should be detected), absorption of an X-ray photon in the scintillator, yield of optical light, optical relay (*i.e.* the lens system) and the optical detection at the camera's sensor[2]. For such a stage cascaded system, where every input is Poisson distributed (which is valid for an X-ray system), one obtains [105]:

$$DQE = \frac{1}{1 + \sum_{i=0}^{N} \frac{1+\epsilon_{\text{i}}}{g_1 \dots g_{\text{i}}}} \tag{3.4}$$

with the gain at the i^{th} stage g_{i} and the Poisson excess term ϵ_{i} which compensates for deviations from non-Poisson distributed stages.

One should note that equation 3.4 is only valid for zero spatial frequency. In general, a frequency-dependence has to be taken into account, as the scintillator changes noise level by stochastic spreading. Therefore, equation 3.4 has to be extended by multiplying each gain g_{i} with the *MTF*. By this, also the Poisson excess term changes to $\epsilon_{\text{i}} = \epsilon_{\text{i}-1} \cdot MTF(u)$, assuming that the spreading is small. In the following, however, we only consider the case of zero frequency,

[2]Electronic and thermal noise of the camera are considered in the next section 3.2.3.

which corresponds to the case that a secondary quantum always has the same location as the primary one.

Figure 3.9 shows a quantum accounting diagram which displays the products of different gains (g_1, $g_1 \cdot g_2$...) contributing to equation 3.4. For each stage, the actual number of quanta is displayed, starting with one photon at the input. When the number of quanta gets below one or the input number of the *DQE* is strongly decreased, such a stage is called "quantum sink". From the diagram one can conclude that for the here considered detectors only the second stage (*i.e.* the absorption) is below 1, while all other stages have higher values. Thus, no big losses occur, meaning that there is no further optimization possible.
It is important to note that taking a very bright scintillator with high light yield as displayed in stage 3 does not provide a high *DQE* if any other stage is much below one, such as the absorption at stage 2; this can be directly deduced from equation 3.4. This is exemplarily shown in Fig 3.9 for a thin LSO scintillator: while the absorption for 9 keV is reasonably good with a *DQE* of approximately 54%, it decreases drastically for higher energies, *e.g.* to approximately 9% at 24 keV. Moreover, image intensifiers widely used in the past became useless when the camera's quantum efficiency (*QE*) got high enough (see stage 5).

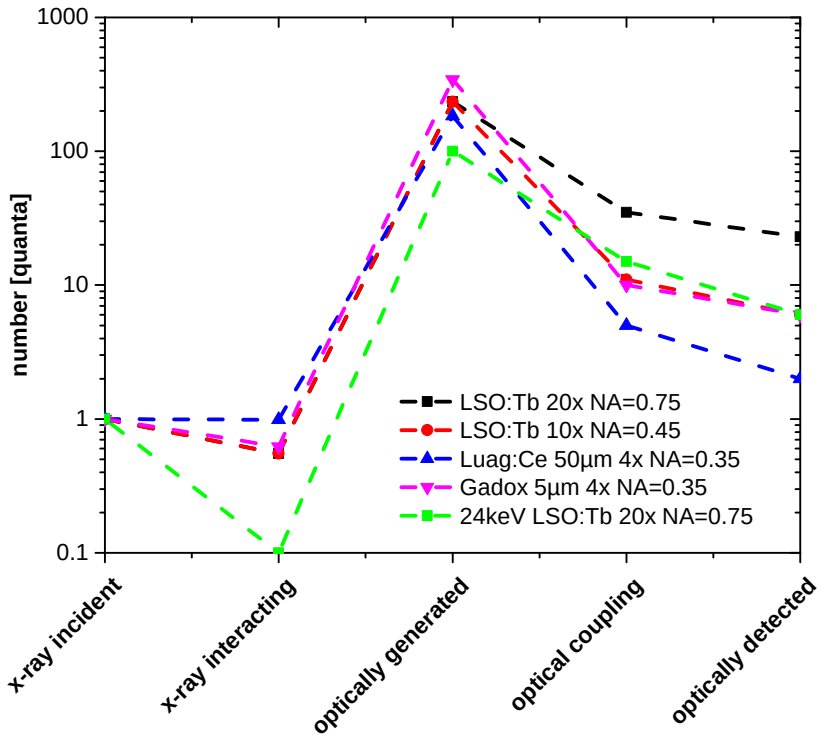

FIGURE 3.9: Quantum accounting diagram of indirect detectors, showing the amount of quanta (*i.e.* photons) at each stage, starting with one at the input. Values below 1 indicate quantum sinks, where the *DQE* and the *SNR* are strongly reduced. For the built detectors values below 1 only occur at stage 2, which is a non-avoidable trade-off to reach high resolutions.

The efficiencies for the relay optics utilized in the framework of this thesis are summarized in table 3.4. For microscope and macroscope, two objectives are used in infinity configuration:

	objective focal length	objective *NA*	tubus lens focal length	efficiency	magnification
Microscope	10 mm	0.75	105 mm, 180 mm	$\sim$15%	10.5×, 18×
Microscope	20 mm	0.45	105 mm, 180 mm	$\sim$4.8%	5.25× , 9×
Macroscope	50 mm	0.34	105 mm, 180 mm	$\sim$2.6%	2.1× , 3.6×
Macroscope	100 mm	0.42	105 mm, 180 mm	$\sim$4.1%	1.05×, 1.8×
High-speed	17.5 mm	0.52	-	$\sim$1.4%	0.25×

TABLE 3.4: Properties of the used detectors optics. The efficiencies are calculated with a transmission of 0.9 through the objective and a refractive index $n \sim 1$ for air.

the scintillator is the focal plane of the objective; thus, the optical light path is parallel between scintillator and lens, and gets focused on the sensor. For such a configuration, the collected flux is proportional to the squared numerical aperture and the collecting efficiency can be calculated as [106]:

$$\eta_{\text{collect}} = \frac{1}{2} \cdot \left(1 - \sqrt{1 - \frac{NA^2}{n^2}}\right) \cdot T_{\text{L}} \tag{3.5}$$

with the transmission of the objectives glass T_{L} and its refractive index n. For the high-speed detector, a single-lens estimation is done.

3.2.3 Optical Cameras

Optical cameras are used to record the image. Since there is anyway a big market for high-end cameras, *e.g.* in life science, over the last decades a lot of effort was put on the development of area sensors.

The quantum efficiency gives the probability whether a photon which hits the sensor gets converted into an electron-hole pair. It depends strongly on the wavelength; its spectral shape can be influenced by coatings. Good back-illuminated CCDs reach a *QE* of more than 95%.
Figure 3.10 shows the quantum efficiency of our two cameras and the emission of the two mainly used crystal scintillators. It is important that the emission and the region of maximum *QE* match; this requirement is met in both cases.

The two utilized cameras differ in the sensor readout technology. While the *FLI Proline 9000* is a CCD camera [107], the *Andor Zyla* is an sCMOS.
In a CCD ("charge-coupled device") camera, a charge created in a photodiode (pixel) is transferred through the other pixel within a line to an output node; there, the voltage is measured, amplified and converted into a digital signal. The *FLI Proline 9000* is a front-side-illuminated full-frame CCD with a mechanical shutter [109]. To prevent blooming which may occur when an X-ray photon interacts with the sensor and saturates the pixel, the sensor is equipped with drain structures to avoid spreading over to other pixels.
In a CMOS ("complementary metal-oxide-semiconductor") camera each pixel is read separately.

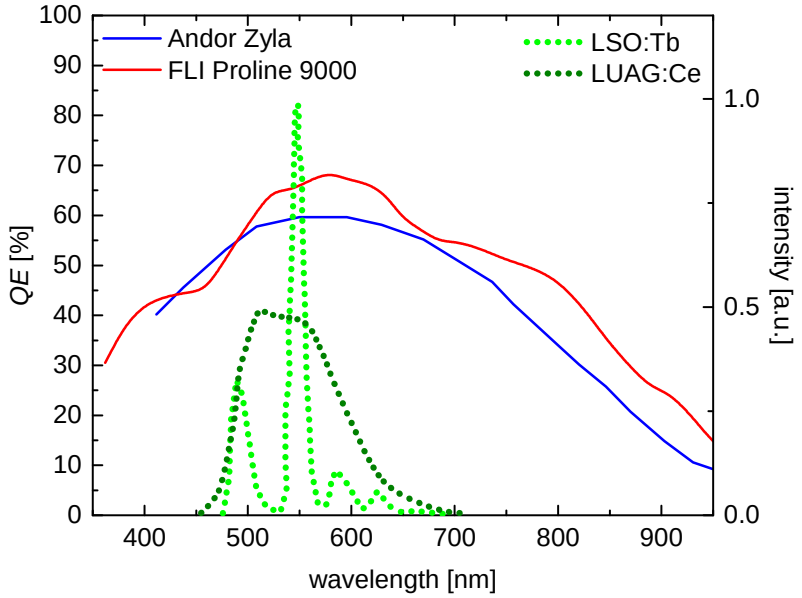

FIGURE 3.10: Wavelength-dependent quantum efficiency of the cameras *FLI Prolin 900* [107] and *Andor Zyla* [108], together with the spectra emitted by the scintillators.

The *Andor Zyla* uses an sCMOS sensor (s: "scientific"). Here, dual-level amplifier with low and high gain are separately converted by analog-to-digital converters with 11 bit. Both 11 bit signals are merged to a 16 bit output [108], resulting in an ultra-low readout noise. It can be used either with a global or a rolling shutter; a micro-lens array guarantees high quantum efficiencies.

Due to these differences, the field of applications differs for the two cameras. On the one hand, the *Andor Zyla* provides a very low readout noise, no relevant readout time and the ability to record pictures up to 100 fps. However, the maximum exposure time is 30 s and binning, *i.e.* combining several pixel to one, is not possible. On the other hand, the readout noise of the *FLI Proline 9000* is with 10 electrons rms higher, but it possesses a better quantum efficiency and supports binning. Thus, for short exposure times the *Andor Zyla* is the camera of choice, whereas for long exposure times the *FLI* becomes the better option due to its lower dark noise. To quantify this statement, the following equation can be considered [110]:

$$SNR = \frac{DQE\, N_{\text{visible}}}{\sqrt{DQE \cdot N_{\text{visible}} + N_{\text{dark}}(T,t) + N_{\text{read}}}} \tag{3.6}$$

with the *DQE* of the camera, the number of visible photons at stage 4 in the quantum accounting diagram in Fig. 3.9 N_{visible}, the dark noise N_{dark} dependent on temperature T and time t, and

the squared readout noise N_{read}.
To reach the point where readout noise becomes a negligible factor the condition:

$$N_{\text{visible}} \gg \frac{N_{\text{read}}}{DQE} \tag{3.7}$$

has to be fulfilled, *i.e.* $N_{\text{visible}} \gg 150$ photons per pixel for the *FLI CCD*, and $N_{\text{visible}} \gg 2.5$ photons per pixel for the *CMOS Zyla*. However, as for good images typically many X-ray photons are needed, in most cases the higher readout noise of the CCD does not disturb the image quality. The different dark noise of the cameras is especially important for low-flux geometries and very long exposure times, *e.g.* 1 hour exposure time at high magnification.

Name	max exposure	readout noise	dark noise electrons/s	pixel size	full well capacity	digitization
FLI CCD	∞ s	10 e^- at 1 MHz	0.02 at -35°C	12 μm	110000 e^-	16 bit
Zyla sCMOS	30 s	1.2 e^-	0.1 at 0°C	6.5 μm		2×11 bit

TABLE 3.5: Summary of the technical data of the utilized cameras, the *FLI Proline 9000* and the *Andor Zyla*. Besides the camera type, also the maximum exposure time, the readout noise, the dark noise, the pixel size, the capacity and the digitization are compared.

3.3 Infrastructure

The following section describes the general infrastructure of the setup. It includes the temperature management, the mechanical system and the software control.

3.3.1 Temperature stability

Since imaging in the spatial space depends - in contrast to other techniques such as small angle scattering in Q-space - on the relative position of sample and detector, their distance has to be extremely stable. In more detail, the resolution is directly limited by the position stability, *i.e.* for a CT scan, the position variations need to be smaller than the aimed resolution for a complete set of exposures. However, if some tracking features (like high Z material with a size comparable to one pixel) are available and the noise level is small enough, the images can be corrected.

In the beginning of the construction work, the setup was equipped with a standard air conditioning system. It turned out that at 25°C, this produces a periodic temperature oscillation with an amplitude of 1.6°C. However, this temperature drift causes considerable length variations of the mechanical stages, which are nearly all made of aluminium: for example, a 100 mm aluminium part expands by 3.8 μm when heated up from 25.0°C to 26.6°C.

In order to overcome this problem, a custom temperature control system was developed. Besides an overall higher stability, it also keeps the temperature in the pumpbox of the source at 30°C to prevent the alloy from freezing and keep it highly viscous. Therefore, the system now consists of two independent cooling cycles, depicted schematically in Fig. 3.11. The cooling water of the reciprocator chiller has (7 ± 1)°C. This is linked to two secondary cooling cycles with high precision chillers: one for cooling the source head, the other to climatize the pumpbox and remove heat from several motors and piezoelectric controllers. This is done by cold plates with fans running at low speed. Fresh air is provided by the house air-conditioning, which has a large enough volume to cause only slow variations and can be switched off if very high stability is needed. When the door of the experimental hutch is opened, the time to re-stabilize is about 5 to 10 minutes, *i.e.* less than the source needs to warm up. The temperature is monitored at four points with Pt100 sensors: at the detector stage, the sample stage, the air and the source head. Air temperature measurements show a typically achieved stability within ± 0.1°C over a short time frame of half an hour and ± 0.16°C over 20 hours (see Fig. 3.12). The more relevant temperature of the bulk material of the stages oscillates for half an hour less than ± 0.02°C, for 20 hours $< \pm 0.04$°C.

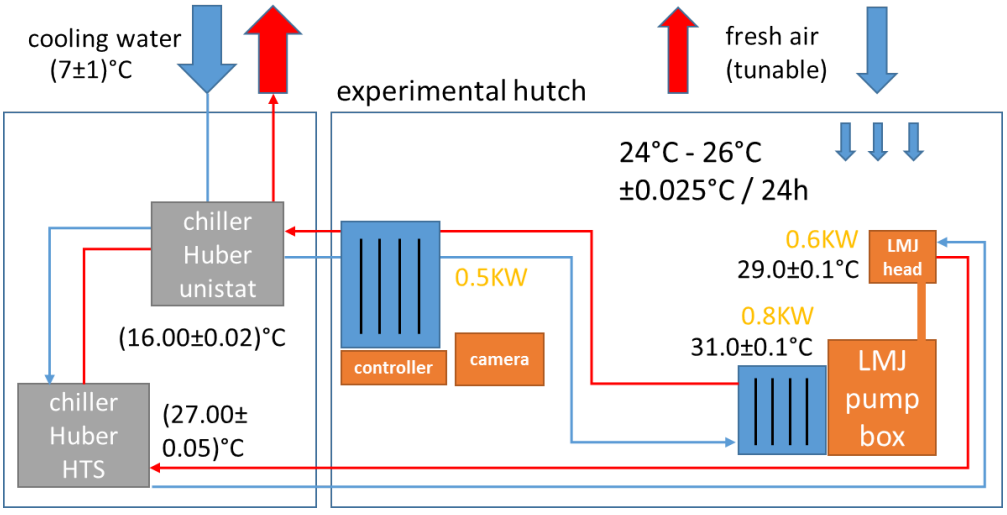

FIGURE 3.11: Drawing of the temperature control system of the experimental hutch. The cooling water of the reciprocator chiller has (7 ± 1)°C. It is linked to two secondary cooling cycles with high precision chillers (*Chiller Huber unistat* and *HTS*), which cool the source head and other elements in the hutch. Fresh air can be provided by the house air-conditioning. The temperature is monitored at four points with Pt100 sensors.

3.3.2 Mechanical system and radiation protection

Figure 3.13 shows a rendering of the current mechanical system. The vertical distance between the center of the beam and the table is relatively large, as this large distance is needed to work with large detectors and large directly driven air bearing rotation stages which are needed for

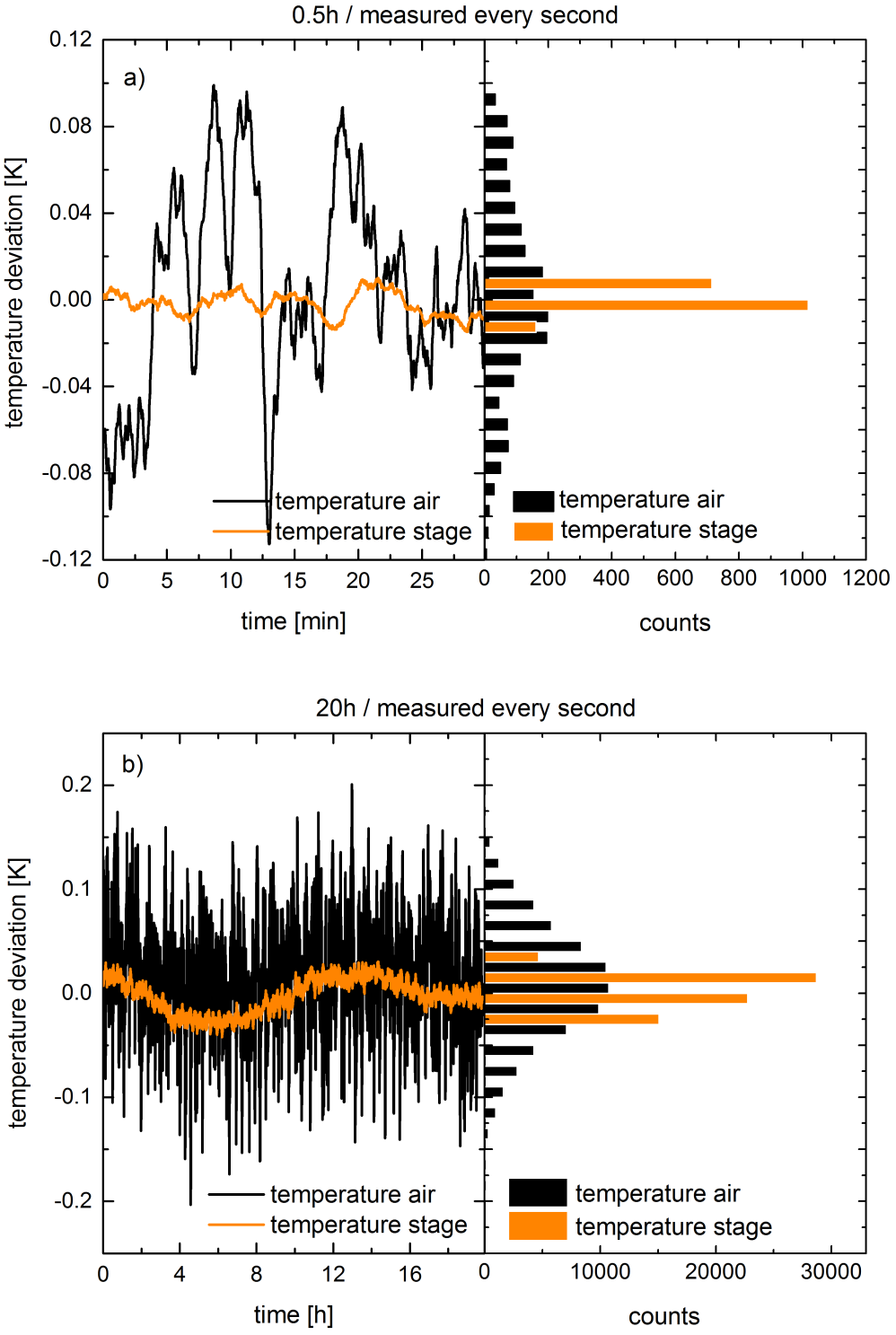

FIGURE 3.12: Temperature stability inside the experimental hutch (a) for 30 min and (b) for 20 h with the improved air-conditioning system. The charts show a typical temperature course when the source is on and the light is switched off, measured with Pt100 sensors. The orange chart is measured with the sensor in thermal contact with the sample stage; the black curve displays the air temperature. The temperature deviation (a) measured is below ± 0.1°C for the air and around ± 0.02°C for the stage. For the longer time period (b) it is $\sim \pm 0.16$°C for the stage and ± 0.04°C for the air.

high speed CT (see chapter 6.2). For high resolution imaging, the big stage structures are actually counter-productive in terms of vibration and stability.

The major components of the setup can be described as followed:

- The whole setup is mounted on an approximately two tons granite block which is placed on passive air dampers to isolate the components from vibrations above 5 Hz. In total, the table length is 2100 mm, resulting in a maximum source-detector distance of 1500 mm.
- The detector is positioned on a three axis *xyz*-stage. To access many positions, the detector is further placed on a long arm. This is especially needed to use the setup with as well as without X-ray optics: while small distances are required for the first option, long distances are needed for the second one. Furthermore, this long arm allows to record images at all positions along the optical path of the X-ray beam.
- The object and manipulator stage is placed on a long *xy*-stage for variable distances.
- The source is fixed on a non-movable steel structure. Below the source, the source pump box and the liquid-metal high pressure pump can be found.
- Optionally, the beam path can be evacuated by a tube (not displayed in the rendering) with 20 μm PET windows which can be placed between detector and zone plate, since for long distances the absorption due to air becomes noticeable (54% absorption in 1 m air for 9.25 keV).

In order to get a better impression about the complexity of the setup, Fig. 3.14 displays the CAD rendering of the object and optics manipulator stages in more detail. It contains:

- a 7-axis manipulator for the condenser alignment (1 translation + 6 axis hexapod),
- a 6-axis sample stage (3 translation + 3 rotation),
- a 3-axis manipulator (3 translation) and two 6-axis manipulators (3 translation + 3 rotation) which can be used for gratings, a beam stop, lenses or pinholes,
- and a slit-system for beam shaping.

Most stages are piezoelectric driven slip-stick devices; only vertical stages are driven by stepper motors, because the force provided by piezoelectric engines would be too small. Compared to the other axes, the rotation stage for tomography is larger and has better bearings to minimize wobbling. Most axes have encoders and run in closed loop configuration.

The whole instrument table is placed inside a hutch of 2.8 m $\times$ 3.6 m, which is shielded with 6 mm lead. This is enough shielding to guarantee radiation protection for 160 keV X-ray tubes.

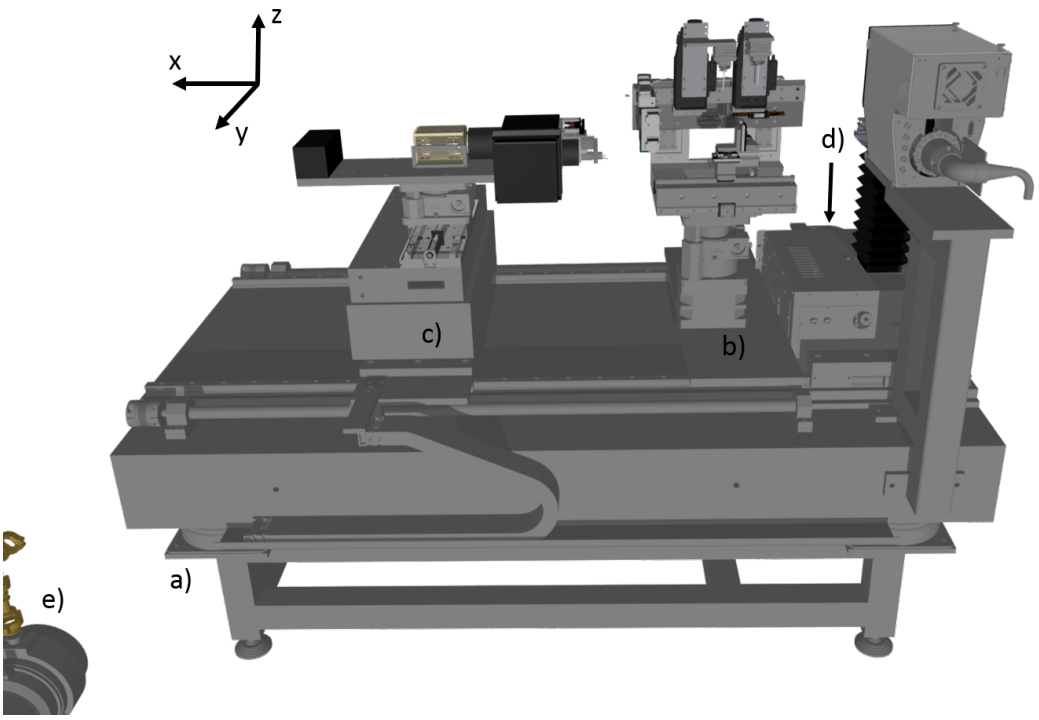

FIGURE 3.13: CAD rendering of the positioning stages. a) Air damped granite table, b) object and optics stage, c) detector stage, d) source and source pumpbox, as well as e) scroll vacuum pump for evacuating the beampath.

The door is double interlocked, turning off the high-voltage of the source and the heating of the cathode immediately when the door is opened. To further ensure that nobody is inside the hutch when the radiation is switched on, an alarm signal marks the start-up of the source and the room is cctv monitored.

3.3.3 Control software

The whole instrument can be operated via *Labview* from *National Instruments*. This includes the camera and detector readout, the control of the source, the control of the 31 axes, as well as the regulation of light and focus of the monitoring camera. Additionally, it is capable to log many data like temperature and all values which are measured by the source (*e.g.* emission current or vacuum pressure). A more detailed description of the software is given in the appendix A.2.

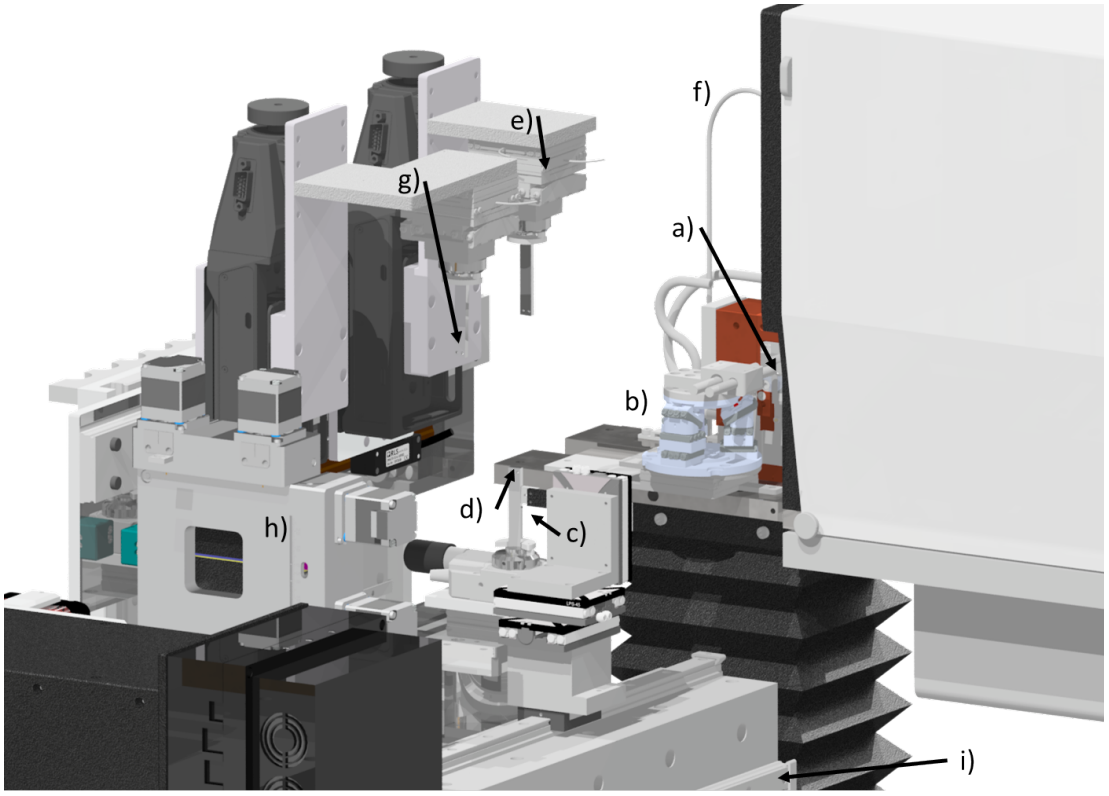

FIGURE 3.14: CAD rendering of the setup, together with its close environment. (a) Exit window of the source, (b) 7-axis manipulator for the condenser alignment (1 translation + 6 axis hexapod), (c) 3-axis manipulator for a pinhole (3 translation), (d) 6-axis sample stage (3 translation + 3 rotation), (e) 6-axis manipulator for a beam stop or grating (3 translation + 3 rotation), (f) high-pressure line where the alloy is transported, (g) 6-axis manipulator for a zone plate or grating (3 translation + 3 rotation), and (h) slit-system for beam shaping.

4 Imaging and micro-CT in shadow projection geometry

In this chapter, the imaging capability of the instrument for the case of using only source and detector (with no further x-ray optics) is described. As a major requirement for the setup was to work as a micro-CT scanner, the chapter focuses on the resolution in the region of one micrometer with good (phase) contrast for weakly absorbing samples at scan times in the order of 1-5 hours for 3D volumes. After introducing the peculiarities of the acquisition geometry (see section 4.1), the setup is characterized by examining its typical noise level and contrast (see section 4.1.1), its practicability for inline phase contrast measurements (see section 4.1.2), as well as the achieved resolution (see section 4.1.3). Moreover, the typical measurement (see section 4.2.1) and analysis procedure is described (see section 4.2.2), before selected examples of successfully performed micro-CTs are presented (see section 4.2.3).

4.1 Acquisition geometry and image properties

When working in shadow projection geometry, due to geometric blurring the achievable resolution is roughly given by the smallest size of either the source or the detector pixels. Today, the design of conventional micro-CT instruments is based on large magnifications combined with small tube spot sizes of 1-2 μm and large detector pixel sizes in the range of 50-200 μm (see Fig. 4.1a). This means that the source-object distance (*SOD*) is small in comparison to the object-detector distance (*ODD*), leading to a high magnification $M = SDD/SOD$ (with the sample-detector distance $SDD = SOD + ODD$). An alternative approach utilizes a larger source of 5-30 μm and a smaller pixel size of 1-5 μm, as depicted in Fig. 4.1b. This leads to an inverted ratio of *SOD* and *ODD* and magnifications lower than $M = 2$. Therefore, this geometry resembles more that of synchrotron beamlines with low divergence and magnifications close to one.

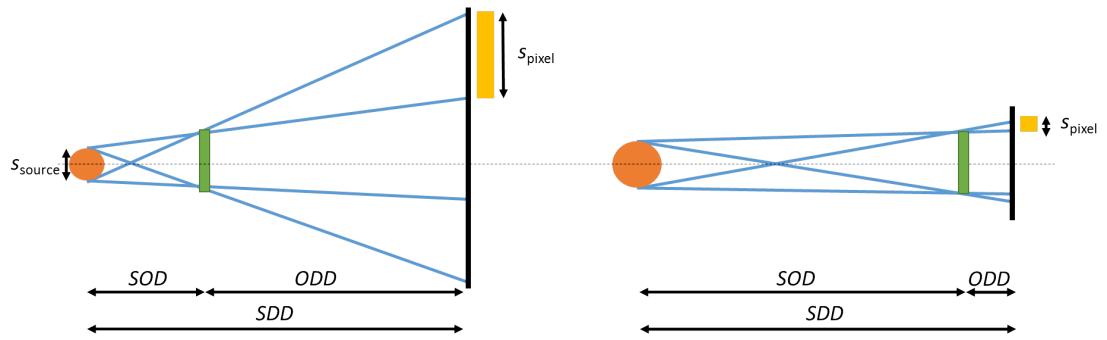

FIGURE 4.1: Schematic drawing of the different geometries for laboratory-based micro-CTs dependent on the source-object distance (*SOD*), the object-detector distance (*ODD*) and the sample-detector distance $SDD = SOD + ODD$ which define the magnification $M = SDD/SOD$. a) Conventionally, small sources and large detector pixel sizes are combined with large magnifications. b) Alternatively, the same resolution can be gained if large sources and small detector pixel sizes are combined, yielding small magnifications. The latter approach is realized in the setup constructed in the framework of this thesis.

Both approaches have their respective advantages and disadvantages. For comparing the different geometries, one has to consider aspects like achievable spatial resolution, desired energy, exposure times and fabrication costs:

- Starting with the resolution, it is either limited by the smallest possible detector pixel or by the focal spot size. In principle, the pixel size of a scintillator-based detector is limited by the wavelength of the emitted light, which is typically larger than the source spots that can be created by focused electrons [33]. However, in the context of micro-CT with reasonable exposure times, both approaches reach similar resolutions below one micrometer with a sufficient signal-to-noise ratio; hence, this limitation does not play a big role (see chapter 5.4).

- At typical CT energies, large detector pixels enhance the *DQE* of detectors, since the layer which absorbs the x-rays can be made thicker; especially for energies above 50 keV, this makes the low magnification approach not suitable. Although one may argue that for small spot sizes also thin anodes are needed, due to the low penetration depth of electrons (compared to that of x-ray photons in the scintillator), this is usually negligible.

- Typical exposure times can be estimated via the photon flux through a voxel in the sample. In the following, it is shown that the exposure time can be the same for both geometries. While for the low magnification geometry the fraction of cone used is smaller than in the high magnification geometry, the resulting lower flux can be compensated by the higher power of the source which covers a bigger target area. Indeed, the compensation of the two effects is perfect when the brightness remains constant for different source sizes. In order to clarify this, Fig. 4.2 shows the product of the solid angle and the source power for a constant pixel sampling of the object with 0.97 μm voxel edge, dependent on the

sample-detector distance *SDD* for a 1 W source. While the red line represents different source sizes but a fixed detector pixel size of 1 μm, for the green lines the source size is fixed at 1 μm and the detector pixel size varies. Moreover, black arrows are depicted, corresponding to the factor needed to gain for the low magnification geometry the same flux as for the standard geometry. Indeed, the needed factor corresponds exactly to the ratio of source areas. Thus, in the case that the brightness is constant and independent of the source size, the power gain due to a larger source exactly compensates the smaller solid angle and both geometries get equal in performance. Moreover, Fig. 4.2a shows that the photon flux can be increased if the length of the complete setup is shortened. However, in reality this distance is limited since the sample has a non-negligible spatial extent and therefore, the sample-object or object-detector distance cannot become too small (also plotted in Fig. 4.2a). Finally, it can be deduced that either a large source or pixel size leads to an enhanced flux without compromising on the resolution.

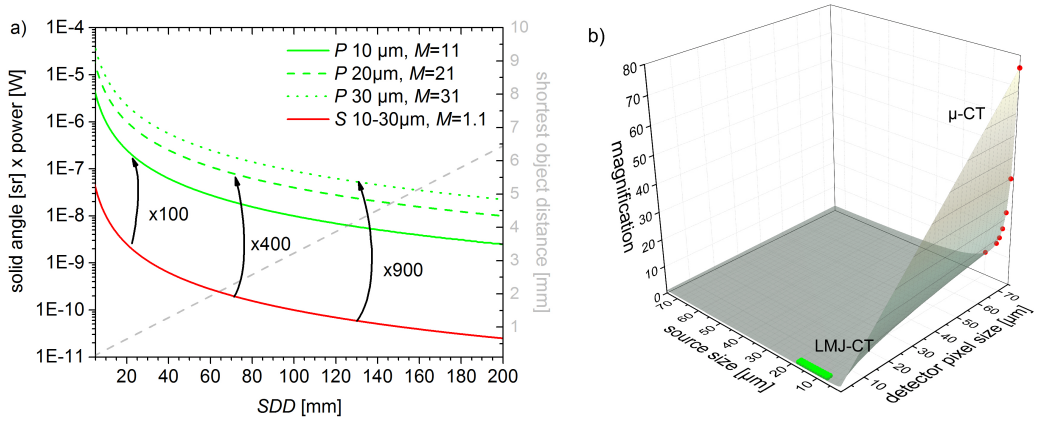

FIGURE 4.2: Considerations for building up a laboratory-based micro-CT. a) Solid angle $\times$ power $\propto$ photon flux through a voxel in the sample with voxel edge length 0.97 μm dependent on the sample-detector distance *SDD* for a 1 W source. While the green lines denote curves with different pixel size P (of the detector) between 10 μm and 30 μm at constant source size $S = 1\,\mu$m, the red line corresponds to different S at constant $P = 1\,\mu$m. For each case, the magnification was adapted to the fixed voxel size (*i.e.* the same resolution). The flux rapidly increases with decreasing *SDD*, as the solid angle increases. However, the shortest distance to source or detector limits the size of *SDD*, as shown exemplarily for P or $S = 30\,\mu$m (gray dashed line, right axis). The arrows show how a smaller solid angle can be compensated by a higher source power (> 1 W). In the case that the brightness is independent of the source size, the power gain due to a larger source exactly compensates the smaller angle (*i.e.* a factor of 100 scales the $S = 10\,\mu$m spot on the $P = 10\,\mu$m curve). b) Ideal magnification dependent on source and detector pixel size. The *Fraunhofer sub-μ-CT* and the setup described in this thesis are marked with red and green points, respectively.

Thus, from these points of view, mainly the higher *DQE* favors the standard geometry which uses high magnifications. Nevertheless, the setup built in the framework of this thesis was designed based on the low magnification approach (see Fig. 4.2b) out of the following reasons:

- As it is shown in the next section, the small source and pixel sizes allow for inline phase contrast measurements with a compact setup.
- While the high magnification geometry is very sensitive to movements of the source spot, the low magnification geometry is more sensitive to movements of the sample versus the detector. This can be an advantage, since the detector is not heated like the anode and therefore, it is easier to keep it thermally stable.
- Moreover, a small pixel detector is more suitable and flexible for the combination with x-ray optics (see chapter 5).

	LMJ-micro-CT	*Sub-μ-CT Fraunhofer*
typical source size [μm $\times\mu$m]	20	1
pixel size [μm $\times\mu$m]	0.62	75
typical magnification *M*	1.1	76
acquisition settings	(see Fig. 4.3)	
SDD [mm]	136	460
SOD [mm]	128	6.95
solid angle/voxel [sr]	$8.35 \cdot 10^{-11}$	$3.50 \cdot 10^{-8}$
sampling [μm]	1.16	1.13
power [W]	200	2
exposure time/projection [s]	8	8

TABLE 4.1: Comparison of the *Sub-μ-CT* located at the *Fraunhofer EZRT* and the *LMJ-micro-CT* constructed in the framework of this thesis, representing high and low magnification setups, respectively. The values given for the systems are useful values for best resolution (*e.g.* more power with larger spots is always possible). The acquisition settings were chosen as similar as possible to allow a comparison.

Table 4.1 and Fig. 4.3 show a comparison of the here-built *LMJ-micro* setup with a CT scanner named *Sub-μ-CT* located at the *Fraunhofer EZRT*, which uses high magnifications. However, any comparison is difficult, as the spectra differ due to different anode materials - tungsten and gallium. From the energy range, the sapwood chosen here as sample is more suitable for the *LMJ-micro* setup. Furthermore, the required relatively long scans (8 s $\times$ 1200 projections) brings the high magnification geometry to its limits, which can be clearly seen in Fig. 4.3b:

although in principle, the resolution which can be reached with the *Fraunhofer Sub-μ-CT* is higher than with the *LMJ-micro* setup, only in the former case the image is blurred due to a lack of focal spot stability. In this regard, the smaller pixel size detector of the *LMJ-micro* plays an important role to reduce the sensitivity to artificial movements.

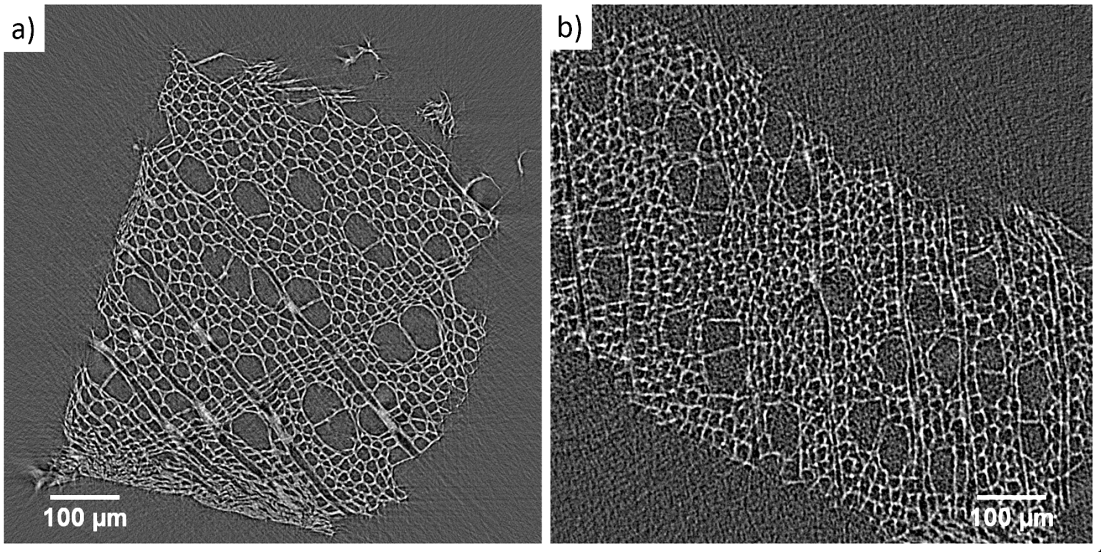

FIGURE 4.3: Comparison of two CT scans of a low absorbing sapwood sample, taken a) with the liquid-metal-jet based *LMJ-micro* setup and b) the *Fraunhofer Sub-μ-CT*. For both scans, the exposure time was set to 8 s and the object sampling to $\sim$1 μm. The liquid-metal-jet based setup leads to a better contrast, while the *Sub-μ-CT* scan severely suffers from focal drift blurring.

4.1.1 Noise and contrast

Noise in images can be seen as an unwanted random part overlying the real signal, resulting in a variation of the intensity not correlated to the object. For an observer, this reduces the visibility of image features. There are several sources of noise, which can be separated by their origin either in quantum noise of x-rays, or system noise from the detector (see chapter 3.2.2). Quantum noise possesses an uncorrelated Poisson distribution with random spatial and temporal variation [111]. Thus, in this case a signal of N photons possesses a photon noise of $\sqrt{N}$. From this, the signal-to-noise ratio can be expressed [104]. In the photon limited case, read-out and dark noise are negligible, and equation 3.6 simplifies to:

$$SNR = \frac{DQE \cdot N}{\sqrt{DQE(E) \cdot N}} = \sqrt{DQE \cdot N} \tag{4.1}$$

This can be used as a good approximation for normal exposure conditions, where the relevant source of noise is given by the statistical distribution of the x-rays. Thus, with knowing the detective quantum efficiency of the detector $DQE(E)$ and the measured *SNR* of the image,

one can directly draw a conclusion about the number of photons with a certain energy which create the image. Since the x-ray photons are information carriers, it is essential to have such knowledge.

Practically, the *SNR* is determined by using a flat-field image (*i.e.* an image without object) and normalizing this for slow intensity variations and a fixed pattern of noise (*e.g.* dirt on the scintillator). This is done by dividing the flat-field image by the average of many other flat-fields (depending on the exposure time, usually 50); before, the dark image (*i.e.* image, where the x-ray source is switched off) is subtracted from all images. It is assumed that the noise level in the averaged image is small enough that it does not influence the result. Then, the standard deviation of the photon count is calculated by:

$$\sigma_{\text{noise}} = \sqrt{\frac{1}{N-1}\sum_{i=1}^{N}(I_i(x,y) - \bar{I})^2}, \tag{4.2}$$

where the difference to the median intensity $\bar{I}$ is squared and summed up over all pixel N. From this, the *SNR* can be calculated as:

$$SNR = \frac{\bar{I}}{\sigma_{\text{noise}}}. \tag{4.3}$$

This procedure can be repeated for any detector distance and source setting. In the following, it is exemplarily presented for 200 W source power and a source-detector distance *SDD* of 136 mm. In combination with the microscope CCD detector and 2×2 binning, this allows for relatively short CT scans of about 2-3 hours and is therefore a "standard" setting. The distribution of the resulting pixel counts for the corrected flat-field is shown in Fig. 4.4 for different exposure times. One can easily see that the distribution gets broader for shorter exposure times, and it looks Gaussian-like. In order to prove that the noise is dominated by the Poisson process of the x-ray photons, Fig. 4.4b depicts the *SNR* measured out of images with different exposure times. As the data points can be well described by equation 4.3, the assumption of photon noise being the dominant source of noise is justified. Moreover, from the fit the (minimum) number of photons which created the image can be calculated. Under the assumption that N grows linearly with time, the resulting number of photons are also added to the graph as a straight line.
The same procedure was also done with the sCMOS. Since the distances were adapted for a nearly equal object sampling (with the identical *SOD*), the resulting values directly reflect differences of the cameras: the sCMOS counts less x-ray photons, reflecting mainly the lower *DQE* of the camera (see chapter 3.2.3).

On the other side, the procedure gives a conversion factor between counts (camera output) and detected photons. With the approximation that only monochromatic 9.25 keV radiation is detected, the conversion factor is 0.9 counts/photon for the CCD, and 0.8 counts/photon for the sCMOS. The difference to the values given in Fig. 3.9 (about 20) results on the one hand from

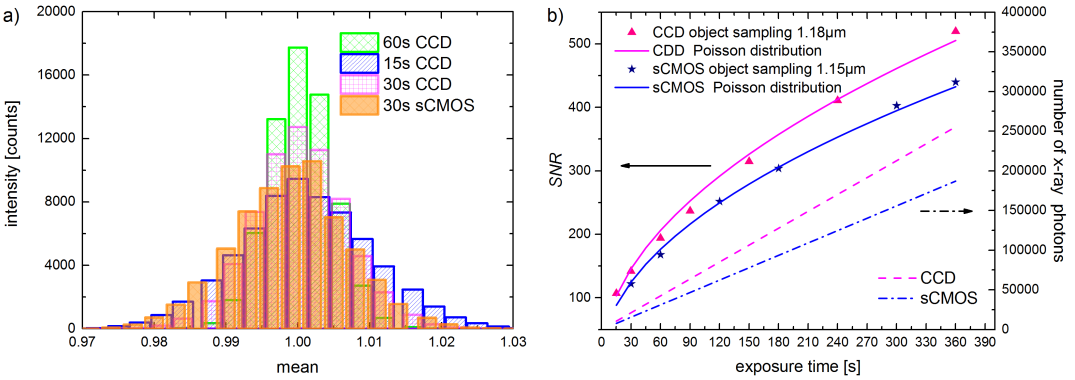

FIGURE 4.4: *SNR* of the micro-CT setup determined by dividing a flat-field image by averaged flat-field images. a) Histogram of the intensity distribution for different exposure times (15 s, 30 s and 60 s) and different cameras (CCD and sCMOS). b) *SNR* of the CCD and sCMOS camera dependent on the exposure time; for the sCMOS, images were summed up to gain a longer exposure time. The data points are directly extracted from the images. From the fit, the number of photons per pixel obtained from the first image (data points) can be extracted.

the internal conversion factor of the cameras (approx. 0.6 counts/photon). Additionally, either the scintillator emits less visible photons than reported in literature or the optical system is less efficient than calculated.

In the following, the influence of the *SNR* on the perception of a feature's contrast C is briefly discussed. In absorption contrast, the Lambert-Beer law gives the transmission through an object with known μ and thickness x:

$$C = \frac{\Delta I}{\bar{I}} = 1 - e^{-\mu x}. \tag{4.4}$$

with ΔI as depicted exemplarily in Fig. 4.5. From this, a so-called contrast-to-noise ratio can be defined as a product of *SNR* and contrast:

$$CNR = \frac{\Delta I}{\sigma_{\text{noise}}} = C \cdot SNR \tag{4.5}$$

This simple relation points out the connection between *SNR* and contrast. In the Rose model, a *CNR* of 5 is defined as a limit where a feature can be reliably identified [112]. It should be noted that this definition only holds for weak absorption. Otherwise, instead of the flat-field *SNR*, the *SNR* of the region of the image which is not obscured by the object has to be used.

To visualize the influence of different noise levels, Fig. 4.6 shows an image sequence of the same object with several simulated *SNR*s. The absorption object has two areas with a transmission of 0.85 and 0.90, as well as a smaller feature with a transmission of 0.90 inside the 0.85 area.
From this, it can be clearly seen that also the size of an object influences its visibility: although the smaller object has the same transmittance as the bottom part, only the smaller feature is

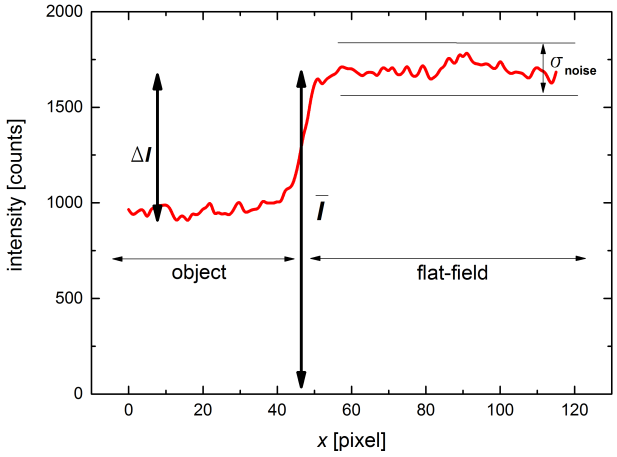

FIGURE 4.5: Definition of the signal properties such as the averaged intensity $\bar{I}$, the noise σ_{noise} and the intensity difference between object and flat-field ΔI.

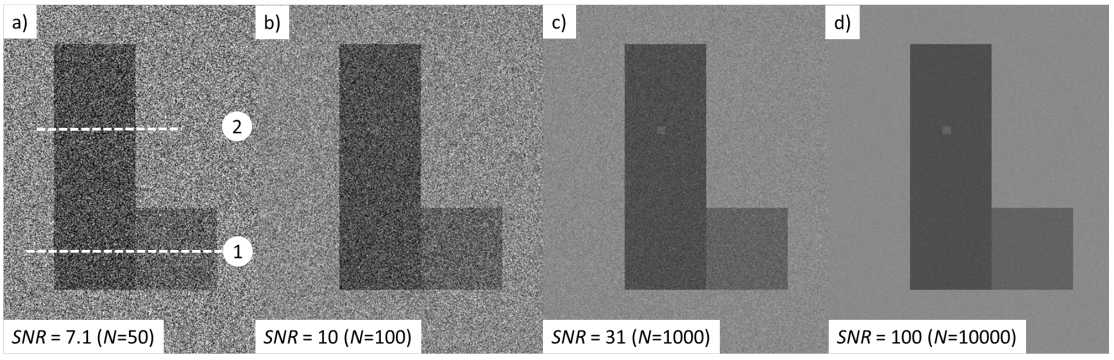

FIGURE 4.6: Image sequence of an absorption object with two areas with a transmission of 0.85 (left) and 0.9 (bottom), as well as a smaller feature with a transmission of 0.90 inside the 0.85 area. From a)-d), the *SNR* is increased.

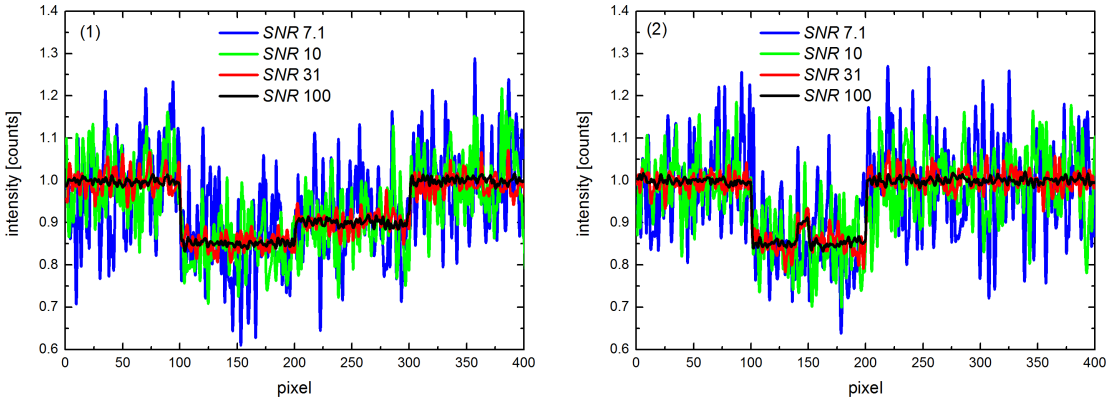

FIGURE 4.7: Exemplarily lineplots along the lines 1 (left) and 2 (right) of Fig. 4.6. From this, it can be understood why the smaller feature can not be seen for a *SNR* of 10.

barely visible at low signal-to-noise ratios. This can be also understood from the lineplots in Fig. 4.7, which were exemplarily taken for the lines 1 and 2 marked in Fig. 4.6.

4.1.2 Inline phase contrast

By passing through an object, X-rays are damped with $e^{-\mu x}$ and refracted due the real part of the refractive index δ. Since available detectors can only detect the intensity, *i.e.* the square of the amplitude of the incoming wave, in general the phase is not measured. However, it will be explained in the following, under which conditions phase contrast can play an important role in imaging.

Whenever X-rays hit an interface where δ changes abruptly, refraction appears, *i.e.* the propagating direction of their wave front with phase $\phi(x)$ changes by an angle θ:

$$\theta = \frac{\lambda}{2\pi} \frac{\partial \phi(x)}{\partial x}. \tag{4.6}$$

Such an interface can be either geometrical (like in a CRL, see chapter 2.3.3), or due to a variation of electron density (see Fig. 4.8).

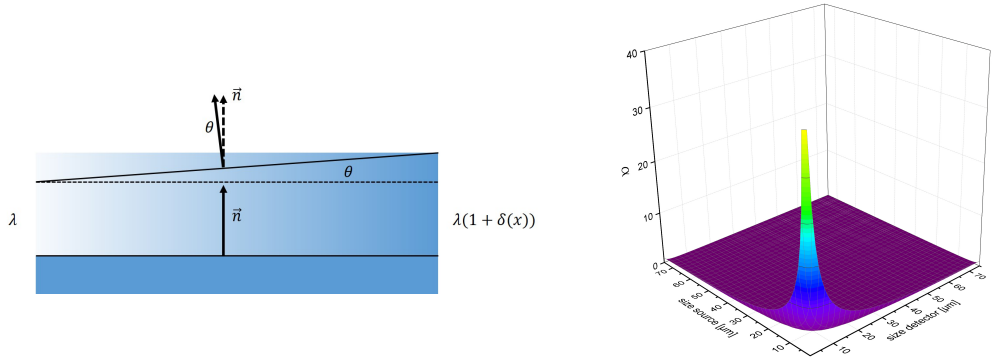

FIGURE 4.8: a) Angular deviation θ of the wave front due to an electron density gradient; measuring phase contrast requires to resolve θ. A wave front passes an interface from the bottom. The material above the interface possesses an electronic gradient (left: vacuum, right: finite electron density), as schematically depicted by the color gradient. b) Plot of the propagator argument α dependent on the source and pixel size with a *SDD* of 200 mm. For small source and detector pixel size, α increases dramatically, leading to a better phase contrast.

In order to use the phase contrast for imaging, one has to detect the resulting angular deviation θ, which is typically quite small for X-rays. In principle, three methods are commonly used: inline phase contrast using free space propagation, grating interferometry using the Talbot effect, and analyzer-based methods [113]. In the here described setup, the first two methods are implemented. As grating-based interferometry is a topic of a different project and further described in Ref. [114], we concentrate in the following on inline phase contrast. It convinces by its simplicity, since no additional elements (such as analyzer or gratings) are needed and shows

up in images as interference fringes at interfaces and boundaries inside the sample.
To quantify under which conditions a setup is in general able to record inline phase contrast images and how strong the phase contrast is, one can derive from the Fresnel-Kirchhoff integrals a so-called propagator formalism. There, the wave field at the detector plane $u_\mathrm{d}(r)$ is expressed as a product of the incoming wave field u_inc and the complex transmission function T of the object, convoluted with the propagator $P_\mathrm{r} = \frac{1}{i\lambda r} e^{(\frac{ik}{2r}(x^2+y^2))}$:

$$u_\mathrm{d}(r) = ([u_\mathrm{inc} \cdot T] * P_\mathrm{r}). \tag{4.7}$$

Assuming source and detector pixel sizes σ_s and σ_p, respectively, which are described by a Gaussian function due to blurring effects, one can derive (as shown in our manuscript, Ref. [114]) an equation for the argument in the Fourier transform of the propagator:

$$\alpha = \frac{\lambda \cdot \mathit{ODD}}{4\pi} \frac{\mathit{SDD}/\mathit{SOD}}{\sigma_\mathrm{p}^2 + (\sigma_\mathrm{s} \cdot \mathit{ODD}/\mathit{SOD})^2}. \tag{4.8}$$

In a first approximation, the larger α, the stronger the phase contrast. Thus, the visibility of phase contrast depends on the distances between object, source and detector, as well as on source and detector pixel size. Of course, this does not take into account whether the sample has interfaces at all - being the prerequisite for having any phase contrast - but it is still a useful parameter to evaluate CT-scanners for their phase contrast capability.

In Fig. 4.8a, the propagator argument α is plotted for a fixed wavelength and setup length *SDD*. One can easily recognize that it dramatically increases when source and detector size get smaller. Comparing Fig. 4.8 with the magnification plot in Fig. 4.2, it gets clear why the inline phase contrast is large for the here-described setup: both - source and detector pixel size - are small. Thus, this is already a very good geometry for inline phase contrast. An even better geometry is realized at synchrotron beam lines, were the *SDD* can reach more than 50 m, combined with small source ($< 100\,\mu$m) and detector pixel sizes ($< 5\,\mu$m) [115, 116].
In contrast, most medical and laboratory micro-CT scanners are built in a way that the phase contrast is small. This is mainly because the argument α is small due to large pixel or source sizes; the only way to compensate this would be a very large *SDD*, which is normally not the case. However, in the hard X-ray regime above 5 keV, δ exceeds β; therefore, using δ for imaging bears the potential to reduce the irradiation dose. Thus, as low doses are very important for many biological samples including medical scanners, it would be very interesting to use the additional image information from phase contrast.

Figure 4.9 shows phase contrast for a fiber-reinforced injection molding. To visualize the influence of the sample-detector distance, the *SDD* was step-wise shortened for a fixed *SOD*. Indeed, this reduces the phase contrast significantly, although the total flux through an object voxel remains the same. The second observation which can be made from this example is that phase

contrast can also reduce the resolution for certain parameter sets; the reason for this effect are overlapping interference fringes (see Fig. 4.9a).

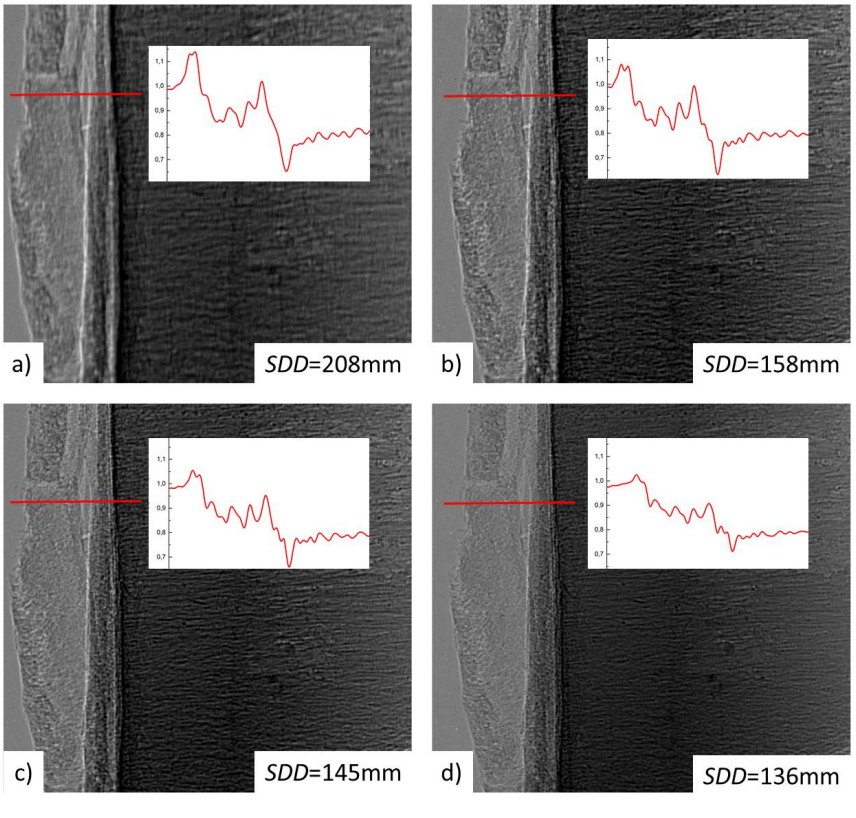

FIGURE 4.9: Phase contrast for a fiber-reinforced injection molding. From a-d), the sample-detector distance *SDD* is step-wise decreased for a fixed *SOD* = 128 mm. The inset show a lineplot through the normal of the interface. In principle, the phase contrast and thus also the resolution get reduced with decreasing *SOD*. However, overlapping interference fringes may also reduce the resolution, as shown in a).

To use the additional information of the fringes, the phase can be retrieved to calculate a contrast enhanced absorption image from the interference fringes. In this process, first the thickness of the object is recalculated from the image via the phase. In a second step, the hereby induced blurring is deconvolved.

Figure 4.10 shows a typical retrieval in two steps. This example was processed using the program *ANKA phase* by Weitkamp, Haas and Rack [117], where a retrieval based on Paganin *et al.* [118] is implemented. For the 3D volumes presented in section 4.2.3, an in-house implementation by M. Ullherr [119] was utilized, where the phase retrieval is applied to the 3D volume and not to 2D projections.

In the used phase retrieval algorithm by Paganin *et al.* [118], the thickness of a sample is retrieved for an image with a single *SDD*. The algorithm is derived from the transport-of-intensity equation and gives the thickness:

$$T(\mathbf{r}) = -\frac{1}{\mu}\ln\left[\mathcal{F}^{-1}\left(\mu\frac{\mathcal{F}(I)/I_0}{d\,\delta\,k^2+\mu}\right)\right] \tag{4.9}$$

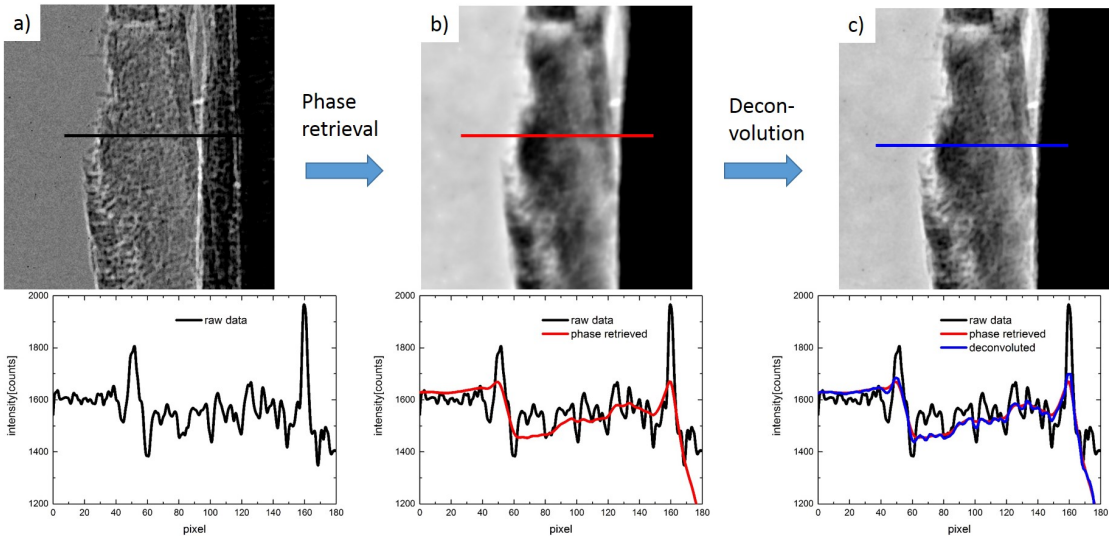

FIGURE 4.10: Example for a phase contrast retrieval for the fiber-reinforced injection molding shown in Fig. 4.9. From a) the image, b) the thickness of the object is recalculated via the phase. c) Afterwards, the thus induced blurring is deconvoluted.

dependent on the recorded image intensity I, the wavelength $1/2\pi k$, the refraction index δ, and the absorption μ; $\mathcal{F}$ and $\mathcal{F}^{-1}$ denote Fourier and inverse Fourier transformations and d the propagation distance, corresponding to *ODD* for a parallel beam and *SOD*×*ODD*/*SDD* for a point source.

It should be noted that this retrieval is in principle only valid for a single materials interface, as well as for a sufficiently thin object, where the phase shift is proportional to the thickness. However, it can be also utilized for other cases, where an effective μ and δ are estimated. An overview of more non-iterative phase retrieval methods, together with a discussion about which method is the best choice for a certain condition, is given in Refs. [119, 120].

4.1.3 Resolution

The resolution of an imaging system denotes the smallest distance between two features of an object which can be still separated in an image. Thus, the resolution can be determined by investigating small features of a well-defined object.

The underlying reason that two point-like objects can not be separated any more in an image are their broadened intensity distributions, which get superimposed. If the objects come too close, the superposition does not longer allow to recognize separate objects. Mathematically, this object broadening in the image is described by the point spread function (*PSF*).

As an example, Fig. 4.11 shows the answer of an imaging system to a focused X-ray beam with a diameter less then 100 nm. The image was recorded at the *BESSY BAMline* with a pixel

sampling of 430 nm and a 50 μm thick CWO screen. Compared to the system's resolution, the original beam diameter corresponds to a point object. Thus, it gets strongly broadened in the image, representing the point spread function of the system. The *PSF* possesses a *FWHM* of about 1.6 μm - 1.9 μm, depending on the direction.

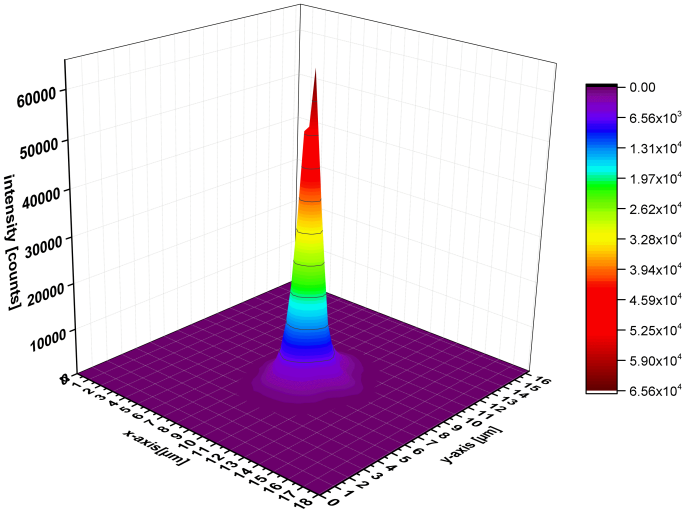

FIGURE 4.11: Image of a focused X-ray beam with a diameter smaller than 100 nm, taken at the *BESSY BAMline* with a pixel sampling of 430 nm and a 50 μm thick CWO screen. The resulting *PSF* is slightly anisotropic with a *FWHM* of about 1.6 μm to 1.9 μm.

A common way to describe the resolution mathematically is the modulation transfer function (*MTF*). It is defined as the magnitude of the 2D Fourier transform of the *PSF*:

$$MTF(u,v) = |\mathcal{F}(PSF(x,y))| \tag{4.10}$$

The *MTF* is a function which reproduces how strong the contrast is damped by an imaging system at a certain spatial frequency, with the spatial frequency being usually given in line pairs per millimeter. For a nearly isotropic 2D *MTF*, radial averaging leads to the 1D *MTF*. On the other hand, the 1D *MTF* can be described as the ratio of image and object contrast:

$$MTF(f) = \frac{C_{\text{image}}(f)}{C_{\text{object}}(f)}. \tag{4.11}$$

As mentioned in the previous section, if no optics are used, the resolution is limited by the source or the pixel size. The exact relation is plotted in Fig. 4.12a: a high resolution (*i.e.* a small σ_{res}) can be achieved either for small detector or small source size. If both are small, the resolution is further enhanced. Assuming no blurring effects for the detector pixel and source sizes, for a detector pixel size of 1 μm and a source size of 10 μm, a resolution of 0.9 μm results; the same resolution results for a detector pixel size of 10 μm and a source size of 1 μm. For an equal source and detector pixel size of 1 μm, the resolution can be optimized to 0.5 μm. For a Gaussian

distribution of detector pixel and source sizes, the resolution slightly increases. Measurements show that the exact resolution values are in between the two curves, but closer to the Gaussian approximation.

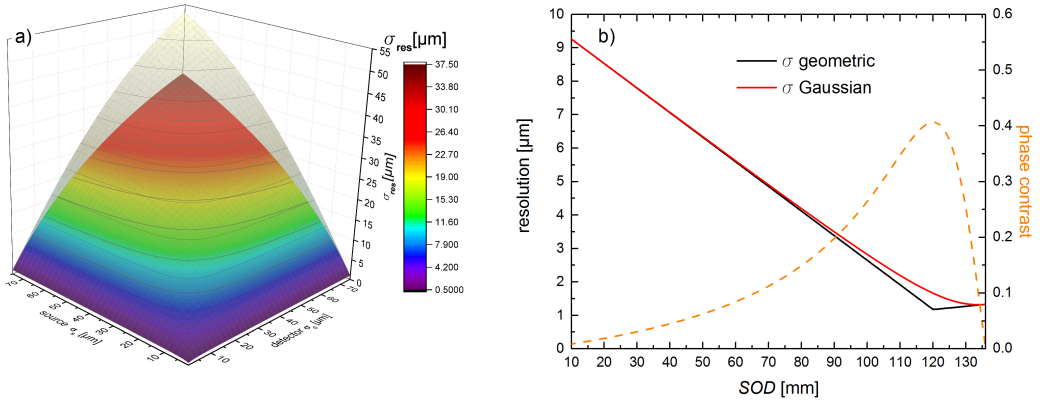

FIGURE 4.12: a) Reachable resolution dependent on the source and detector pixel size. The colored surface represents a rectangular source and detector pixel size; the gray shaded one a Gaussian distribution. b) Resolution for 20 μm source *FWHM* and 1.33 μm pixel sampling. The black curve represents a rectangular, non-blurred source and detector pixel size, the red one a Gaussian distribution with the standard deviation σ corresponding to the source and pixel sizes. For the Gaussian distribution, the optimum resolution is shifted closer to the smaller σ, here to the detector. Additionally, the phase contrast is plotted (orange curve). Its maximum coincides with the highest resolution of the black curve.

Before determining the system resolution, the geometrical parameters should be further considered. To reach the values from Fig. 4.12a, the object has to be also placed in the right position between source and detector. This dependence is shown in Fig. 4.12b for typical acquisition settings: an overall *SDD* of 136 mm, a source size of 20 μm and a pixel sampling of 1.33 μm. For these parameters, one finds the best *SOD* at 120 mm, assuming a rectangular, non-blurred source and detector pixel size; at this position, the blurring induced by the source corresponds to the size of one pixel.

The most direct and intuitive way to determine experimentally the *MTF* of a system is to plot the modulation:

$$m = C/2 = \frac{I_{\max} - I_{\min}}{I_{\max} + I_{\min}}, \tag{4.12}$$

of bar patterns with different sizes, corresponding to different spatial frequencies. Figure 4.13a shows the X-ray image of such a resolution target together with significant lineplots. The target was fabricated by cutting defined bars in a 1 μm thin gold foil with focused ion beam; the gold layer was sputtered on a 200 nm SiN_3-membrane. The horizontal and vertical bars have the widths of 4 μm, 3 μm, 2 μm, and 1 μm (from left to right). Figure 4.13b shows how the modulation decreases for higher spatial frequencies.

While such a resolution target delivers only the modulation for discrete spatial frequencies, a continuous distribution can be deduced from measuring the 1D response of an edge. From the

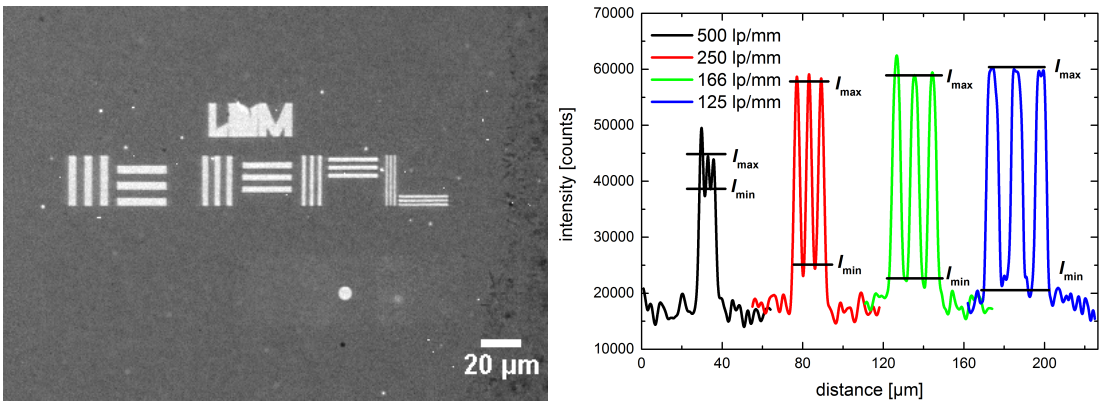

FIGURE 4.13: a) Resolution target with vertical and horzontal bars, decreasing from 4 to 1 μm line width. The target is made of a Au film and ion beam lithography. Exposure time was 60 s for a pixel sampling of 0.630 μm. b) From the lineplots through the bars, the contrast modulation at different spatial frequencies can be deduced. One can clearly see how the modulation becomes weaker for smaller bars, *i.e.* higher spatial frequencies.

edge spread function (*i.e.* the lineplot through the edge), the line spread (*LSF*) function can be calculated as its derivative. Furthermore, the 1D Fourier transform of the *LSF* delivers the 1D *MTF*.

Experimentally, similar to the resolution target, the edges have to be well-cut. Therefore, the edges were also fabricated with focused ion beam. Figure 4.14a depicts line profiles through such an edge, exemplarily shown for the combination of the microscope detector with the FLI CCD. The Fourier transform of this profile, *i.e.* the resulting *MTF*, is depicted in Fig. 4.14b, together with the single data points obtained from the bar patterns in Fig. 4.13. The slight discrepancies result from the fact that the resolution target should in principle have sinusodial structures, and not rectangular ones. This leads to a slight overestimation of the resolution.

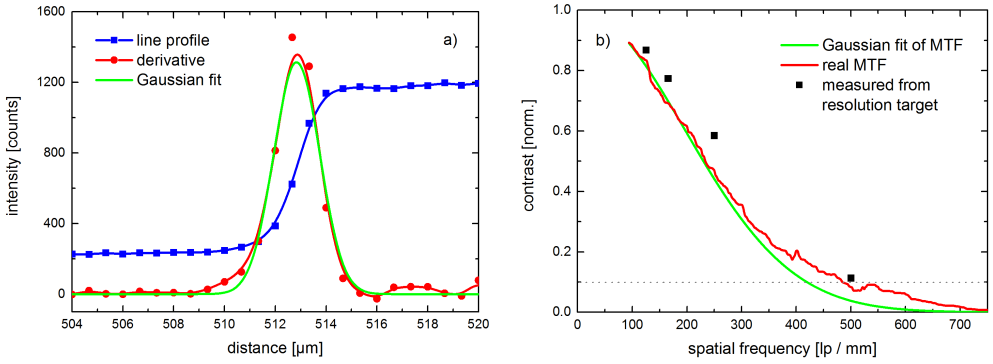

FIGURE 4.14: Exemplarily determination of the *MTF* for the microscope detector with the FLI CCD. a) Edge profile together with its derivative which can be fitted with a Gaussian. From its Fourier transform, the b) *MTF* results. Additionally, data points obtained from the bar patterns in Fig. 4.13 are depicted. The gray dotted line depicts the 10% *MTF* criterion.

The Rayleigh resolution corresponds to 9% contrast in the *MTF*. Beside this, also values of 10%, 5% or even 3% are used when people determine their resolution. This can be justified in some situations, as the human eye is able to detect features well below 10% *MTF*, and is further influenced by other parameters like the noise present in an image.

Table 4.2 summarizes for the here described setup the best measured resolutions of different detectors, using the 10% *MTF* criterion. From the determined spatial frequency which corresponds to this criterion, the resolvable line width was determined by:

$$w_{\text{line}} = \frac{1000}{2R} \tag{4.13}$$

with the line width w_{line} in μm and the spatial frequency R in lp/mm.

	sampling [μm]	*MTF* at 10% [lp/mm (μm/line)]	*MTF* at 10% Gaussian [lp/mm (μm/line)]	features [μm]
Microscope sCMOS	0.589 M=1.05	500 (1)	410 (1.22)	0.8
Microscope CCD	0.634 M=1.05	490 (1.02)	420 (1.19)	0.8
Macroscope CCD	3.1 M=1.05	110 (4.54)	110 (4.54)	$\sim$4
High-speed sCMOS	13 M=2	-	-	$\sim$10

TABLE 4.2: Determined system resolution in projection imaging. For the first three detectors the resolution is limited by the detector, because the magnification factor M is close to unity. When dividing the magnification by the detector's pixel size, one obtains the object sampling (first column). From edge measurements, the spatial frequency is determined by following the scheme given in Fig. 4.14. The last column named "features" gives smallest bars which were resolved with resolution targets.

A comparison of the values given in table 4.2 with the theoretical resolution in Fig. 3.8 shows that the resolution reached in reality for the microscope is about half of the theoretically achievable value. This can be explained by the idealized theoretical model, which does not consider the point spread function of the CCD itself, as well as imperfections of the optical system (stray-light and quality of the tube lens) and of the scintillator. On the other hand, other mechanisms in the X-ray path such as scattering or refraction can influence the resolution measurement. For the macroscope, the larger resolution was accepted to reach a larger field of view.

4.2 Computed tomography

The method to obtain three-dimensional volume data of an object is called "computed tomography" (CT). For this, the sample needs to be rotated, while two-dimensional images are recorded from different directions. The thus obtained images are "projections"; they can be arranged in a

two-dimensional array, called "sinogram". From the sinograms, the object can be virtually reconstructed with the help of a computer and be visualized three-dimensionally or via horizontal cuts through the volume, which are called "slices".
Besides the data recording, a CT-scan consists of several steps, as depicted in 4.15, and explained in the following in more detail.

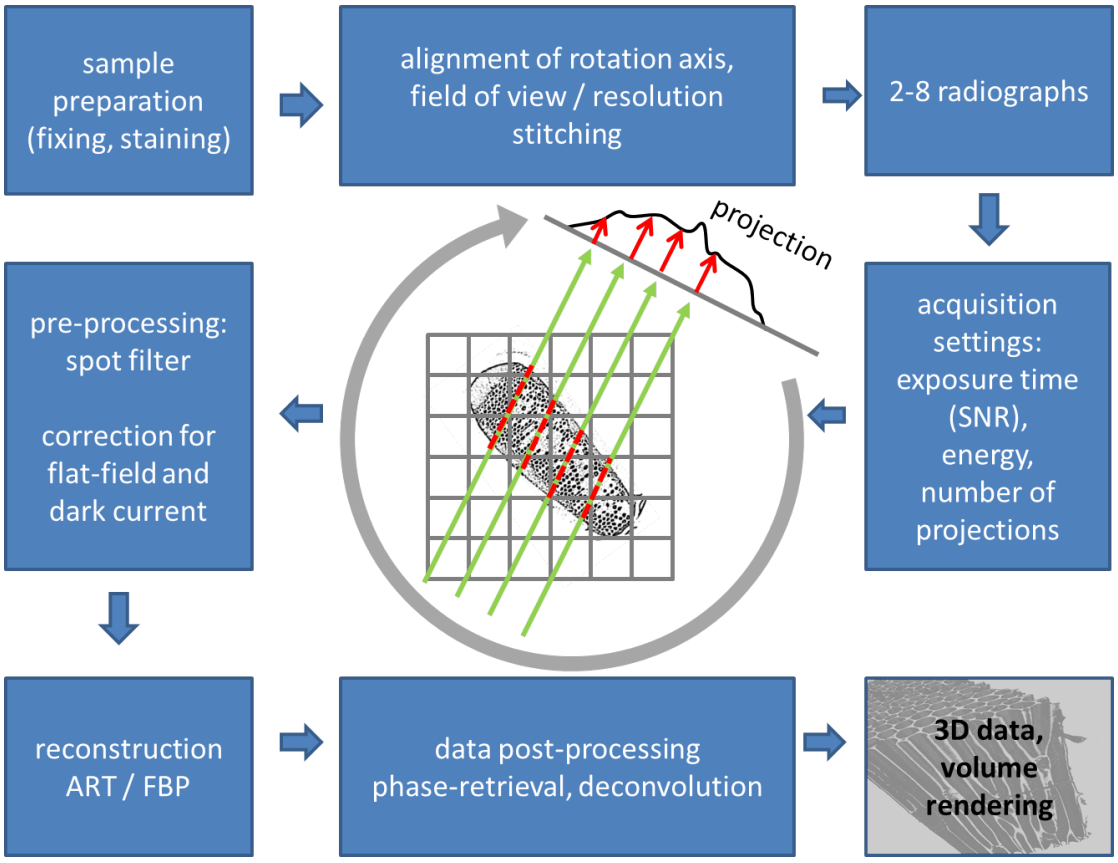

FIGURE 4.15: Usually performed steps to record a three-dimensional object via computed tomography. After the sample preparation, the rotation axis needs to be aligned and the resolution as well as the field of view are determined. If the sample is too big, stitching can be considered. Afterwards, some test radiographs are performed. From these, the acquisition settings are chosen - such as the exposure time (determining the signal-to-noise ratio), the energy and the number of projections - and the data acquisition can start. After all projections were taken, several pre-processing steps such as filtering, corrections for flat-field and the dark current or position changes are performed, before the CT is reconstructed via algebraic reconstruction techniques (ART) or filtered back projection (FBP). Finally, a data post-processing - such as phase-retrieval or deconvolution - typically marks the last step, before the data are visualized three-dimensionally.

4.2.1 Setting up a measurement

Sample preparation Carrying out a CT-scan starts with preparing the sample. For this, one has to ensure that during the data acquisition, the sample does not move more than the desired resolution. Usually, the sample is therefore glued on a rod, which is then clamped onto the rotation stage. The glue has to be hardened completely to avoid slow flowing. For hot glue it turned

out that this is reached after some minutes; for super-glue an additional activator should be used, with a waiting time of at least 15 minutes. In addition to the mounting of the sample, for wet or biological materials the most critical risk is drying and the corresponding change of shape. Therefore, for biological samples, proper **fixation** or a cell with constant humidity is needed. Samples enveloped in paraffin wax showed not the required leakproofness, but the drying process was slowed down sufficiently to provide a time window for short scans (1-2 hours). Objects embedded in agarose gel are more long-time stable, but the gel also decreases the contrast and the sample may change due to the heating during the preparation. Thus, the best way to prevent mechanical changes is probably cryocooling by liquid nitrogen, but this is also the most complicated method; it was first demonstrated for soft X-ray microscopy by Schneider *et al.* [121] to allow higher radiation strengths, but was also used for fixation in micro-CTs [122].
For some samples **staining** with a contrast agent is necessary. A typical example is inter-tissue contrast, where the difference in absorption between two phases is often very small. Suitable staining is done for example with iodine; the staining process to image the vascular structure of mouse hearts is described in Ref. [123].

Setup preparation Before the experiment can start, also the setup needs to be prepared. The **axis of rotation** has to be aligned parallel to the detector surface and orthogonal to a pixel row. In order to do so, the axis is adjusted with a yaw and tilt goniometer below the rotation stage. To find the optimum position, a small sphere is rotated while recording images. If all images are summed up, an ellipse results for a non-aligned rotation axis. The tilt angle of the ellipse can be directly used to adjust the tilt angle of the goniometer; from the opening of the minor axis, the yaw angle can be derived. After proper re-adjusting, the summed up images show the sphere.
The **resolution** and the **field of view** are correlated by the limited number of the camera's pixels. In principle, the sample has to be smaller than the field of view of the detector, because the part outside the field of view is included in only some projections; these additional data decrease the reconstruction quality. To overcome this limitation, the measured field can be enlarged by taking several shifted images at each projection, and by assembling these images afterwards together. An example of such a **stitched** image of 25 single images is shown in Fig. 4.16. For the experiment, this means that the time for a single combined projection grows quadratically, while the required number of projections grows linearly with the width of the projection. A compromise for this approach is to merge a large field of view image with low resolution and a small field of view image with high resolution. This delivers a high resolution volume of interest with minimized reconstruction errors.

Test measurements to derive acquisition settings The **exposure time** is always a compromise between total scan time and image quality. Its value is mainly determined by the size of the features and the material. Furthermore, it is also influenced by the full-well capacity of the

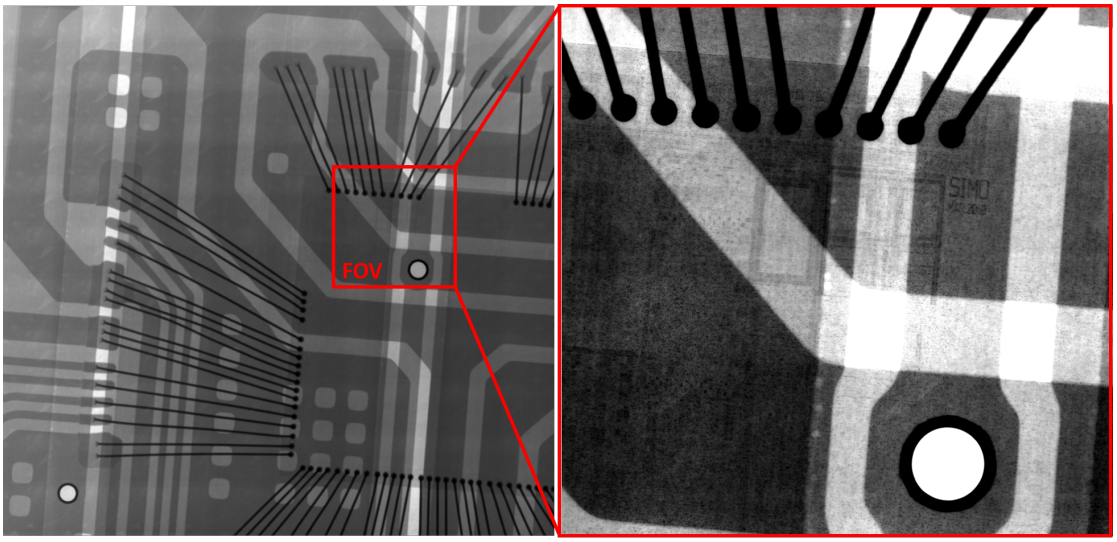

FIGURE 4.16: Radiography of a microchip on a circuit board with bond wires. The image is stitched from an array of 5×5 images to extend the field of view. The red border marks a single field of view of the detector with 2048×2048 pixels, witch each having an edge length of 0.66 μm; this results in a single field of view of 1.36 mm. The combining process was done by aligning the images with 2D autocorrelation and linear interpolation.

sensor and the stability or radiation hardness of the sample. From test scans taken prior to the full CT, one can obtain a roughly needed signal-to-noise ratio and estimate the exposure time for a single projection.

However, the resulting noise level in a CT scan also depends on the **number of projections**. To outline this, Fig. 4.17 shows a set of reconstructions done with different numbers of projections - all from the same measurement data. The whole data set consists of 720 projections over equally spaced 360°[1]. Each projection was acquired within 15 s with a pixel sampling of 1.33 μm. From the lower line plots (black and red) on the right side one can see the change in visibility due to an increased signal-to-noise ratio. Each measurement delivers N (number of pixel in a row) measurements points. By interpreting a slice as solution of linear equations, N^2 measurements are needed to calculate the slice. However, for most scans less projections are recorded, since the sample does not completely fill the volume. This breaks down when the system becomes underdetermined. Coming back to Fig. 4.17, one can see that the basic shape and strong features can be estimated already for about 110-210 projections. For more projections, smaller features and fibers become visible, until at a certain point the additional projections "only" reduce noise. From this, it can be deduced that the required number of projections depends simultaneously on the geometry of the sample (*e.g.* diameter of fibers), but also on the *SNR* of a single projection.

In the particular case of the here described setup, the maximum acceleration voltage is in most cases set to 70 kV, which determines the **energy setting**. It turned out that lower voltages do not effectively provide any advantage, since the spectrum's center of mass does not move to lower

[1]While for a parallel beam and a low magnification factor also a scan over 180° would be sufficient, for a high magnification geometry a 360° scan is always required. For the latter case, the number of projections should be odd to ensure that on the second half, different angles are recorded and additional data is acquired.

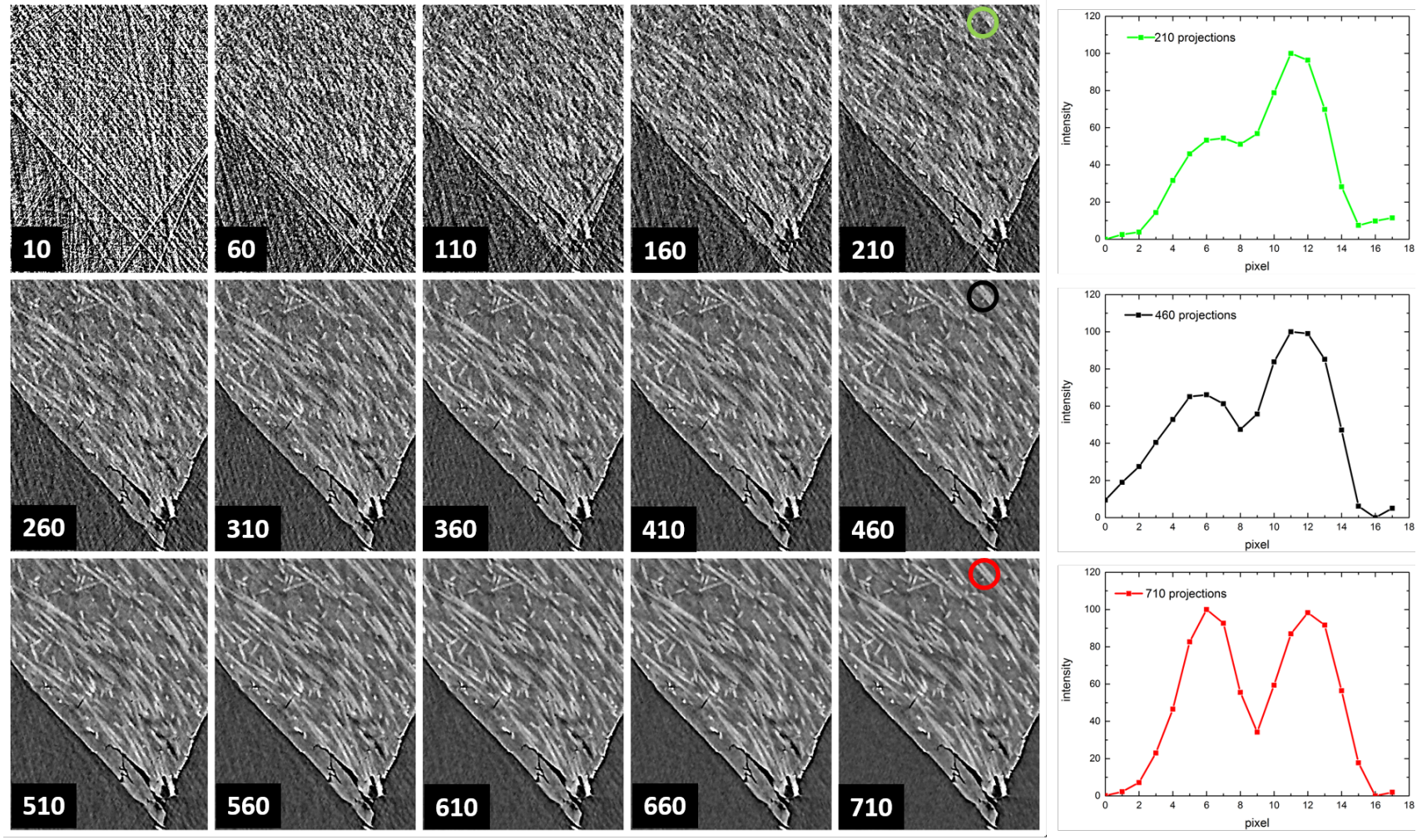

FIGURE 4.17: Slice of a fiber-reinforced plastic reconstructed with different numbers of projections between $n = 10$ and 710, as well as corresponding line profiles of a double-fiber feature for $n = 210$, 460 and 710. Each projection was acquired within 15 s with a pixel sampling of 1.33 μm. While the basic shape of the object can be estimated already for about 110-210 projections, for more projections, smaller features and fibers become visible (as seen in the lineplot) and the signal-to-noise ratio gets improved.

energies; instead of this, only flux is lost.
Finally, before starting the acquisition, also **dark** images (with the source turned off) and **flat-field** images (without sample) are recorded, with an averaging which is high enough not to introduce additional noise.

4.2.2 Pre-processing, reconstruction, artifacts and post-processing

Pre-processing After the measurements, the projections need to be corrected. On the one hand, **spikes** are filtered. These spikes have their origin in scattered X-rays which directly hit the image sensor without interacting with the scintillator. They can be removed by filtering with a selective median filter which is only applied when a pixel deviates from the surrounding pixel by a certain threshold. Moreover, a **flat-field and dark correction** is done by dividing the image by the flat-field image I_{flat}, both corrected by the dark image I_{dark}:

$$I_{\text{corr}} = \frac{I_{\text{im}} - I_{\text{dark}}}{I_{\text{flat}} - I_{\text{dark}}}. \tag{4.14}$$

These corrected images are further normalized so that in the region where no sample is present the mean value is one. This is done to compensate intensity fluctuations of the source during a scan. The intensities measured at the *LMJ-source* fluctuate around 2-3$\%$ for shorter 1-2 hour scans, and 5-7$\%$ for scans longer than 24 hours.

Reconstruction The reconstruction is mathematically an inverse problem, *i.e.* the measurements are results and the causes have to be calculated. Directly solving the linear equations simultaneously is practically not doable due to computation time and noise. In reality, mainly two principles are used for fast calculations, namely back-projection and iterative methods.
Filtered back projection (FBP) is the commonly used standard reconstruction technique [124]. Here, each projection is smeared back into the image with distributing the complete absorption equally along its ray path in the reconstructed image. From this, the error of the method is obvious, as the absorption was in reality not constant along the whole ray path. Thus, a single point object smears out, because intensity is back-projected in surrounding regions. In order to understand how this problem can be overcome with a filter, a mathematical description needs to be considered. For this, one should note that the whole idea of smearing is based on the Radon transformation, meaning that each two-dimensional object property can be described by an infinite number of line integrals; an example is that the space-dependent absorption $\mu(x, y)$ can be defined via the projections $p_\theta(s)$, with $x,\ y$ being Cartesian coordinates and $\theta,\ s$ being Polar coordinates. This, however, does not answer *how* one can exactly use the measured projections $p_\theta(s)$ to determine the function $\mu(x, y)$. For this, also the Fourier slice theorem is needed, which describes the relation of a function $f(x, y)$ to its Fourier transform $F(u, v)$ via

the projection $p_\theta(s)$ of $f(x, y)$ and its Fourier transform $P_\theta(w)$; it follows from the theorem that $P_\theta(w)$ describes the values of $F(u, v)$ along the radial direction through the origin which is defined by the angle θ. Thus, by measuring many projections $p_\theta(s)$ and adding up their Fourier transforms $P_\theta(w)$, one can construct the two-dimensional $F(u, v)$ and thus by inverse Fourier transformation the unknown function $f(x, y)$. For such a calculation, also the transformation from Polar to Cartesian coordinates needs to be considered; this causes a radial factor $|w|$ in the integration, corresponding to the fact that in Polar coordinates the values of low frequencies (*i.e.* large details in real space) are more densely distributed than those of high frequencies (*i.e.* small distances in real space). Such a multiplication in the Fourier space corresponds to a filter or convolution in the real space, coining the name *filtered* back projection. For the here presented images, in most cases the commercially available software *Octopus* from *InCT* was used, as well as in some cases in-house developed FBPs.

Further alternatives are **iterative** techniques such as the simultaneous algebraic reconstruction technique (SART) [125, 126], the simultaneous iterative reconstruction technique (SIRT) [127], as well as the iterative least squares technique (ILST) [128]. As an example, the ART algorithm works as explained in the following: at first stage, all pixels are set to an arbitrary value (or zero). Then, the values in the pixel array are compared with each measurement and changed accordingly; if the sum measured along a ray is higher than the sum written in the array, all pixel values are increased. When this process was done with all projections, the reconstructed image is usually still not the correct, since changes done with the n^{th} projection might also change values which were correct before. Therefore, the process needs to be repeated for many iterations, with the aim that the error becomes smaller and the reconstruction convergences to the correct solution.
In principle, iterative techniques provide more flexibility [129], as well as allow to use prior knowledge of the used geometry and sample, which either improves the image quality or reduces the exposure time or dose. An example where iterative methods are advantageous compared to FBP is the compressed sensing implementation [130], where the information density of the sample is smaller than the sum of reconstructed data points (voxel).

Artifacts Structures that occur in reconstructed data which do not belong to the object are called "artifacts". Main artifacts are beam hardening artifacts, motion artifacts and ring artifacts. In the latter case, **rings** appear in the reconstructed data. The origin of these rings is either an irregular sensitivity of the different pixels, dust on the scintillator or an insufficient flat-field correction due to intensity variations. This results in straight vertical lines in the sinogram, and circles in an image. To avoid ring artifacts, software filters can be used. An alternative is a technique called "MaxShift" [131], where the detector is moved pixel-wise between the projections; thus, the same point of an object is imaged by different pixels (at different projections).
Moreover, **motion** artifacts originate from the unwanted motion of an object in the beam path

between the projections. Therefore, although the reconstruction assumes uniform angle steps, they differ in the measurement due to mechanical inaccuracy and wobble errors of the bearings. To overcome this problem, in the beginning highly accurate air-bearing rotation stages were used for the here-described setup. However, as these require more space, they were replaced by a smaller mechanical stage when the setup got more complex. Their motion can be partially corrected by an auto-correlation algorithm.

Another challenge are **beam hardening** artifacts which occur for polychromatic radiation, as the lower energies of the spectrum are more attenuated than the high-energy part. In this case, the overall transmission does not follow the simple absorption law (see equation 2.33. However, when only the characteristic radiation is used for imaging adequate samples (with low Z), the spectrum and detector response leads to nearly monochromatic imaging and beam hardening does not play a role.

A special artifact which is not only related to beam hardening, but also to edge effects, is a **metal artifact**. It causes in the reconstructed volume streaks from high Z metals. To correct metal artifacts in an iterative algorithm, an obvious approach is to replace the metal pixel with forward projected values from the previous iteration and reconstruct the metal pixel separately. This method has the disadvantage that the resolution of the surrounding material is also reduced. Thus, whenever it is possible, one should separately scan parts of an object with high and low Z material, as it was for instance done in Fig. 4.22.

Visualization For three-dimensional visualization, *Avizo Fire* from the *FEI Visualization Sciences Group* and *Volume Graphics VGStudio MAX* was used. These softwares include 3D rendering, image processing and segmentation; moreover, *Avizo Fire* possesses additional toolboxes for quantification and analysis in material science. Furthermore, both programs support surface mesh generation for exports to applications like computer aided design (CAD) or simulation tools like finite element method (FEM).

4.2.3 Selected examples

In the following, some selected micro-computed tomography scans are shown, in order to demonstrate the typical capabilities and restrictions of the instrument which does not rely on X-ray optics.

Stemming from the spectrum of the source (see section 3.1), a natural limit for the sample diameter is simply given by its absorption. Indeed, an upper as well as a lower absorption limit exists for X-ray imaging: on the one hand, an absorption of a sample of 95% and above is too high for imaging, as basically no photons can pass the sample and reach the detector; on the other hand, the absorption of a sample should not be lower than roughly 5% to still provide a reasonable absorption contrast of sub-structures. To outline the implication of this, Fig. 4.18 displays this

absorption range of 5%-95% for different organic and inorganic materials dependent on their thickness for 9.25 keV and 30 keV photon energy; these energies are chosen as they correspond to the characteristic Ga K_α-line, as well as to the average energy of the setup's Bremsspectrum.

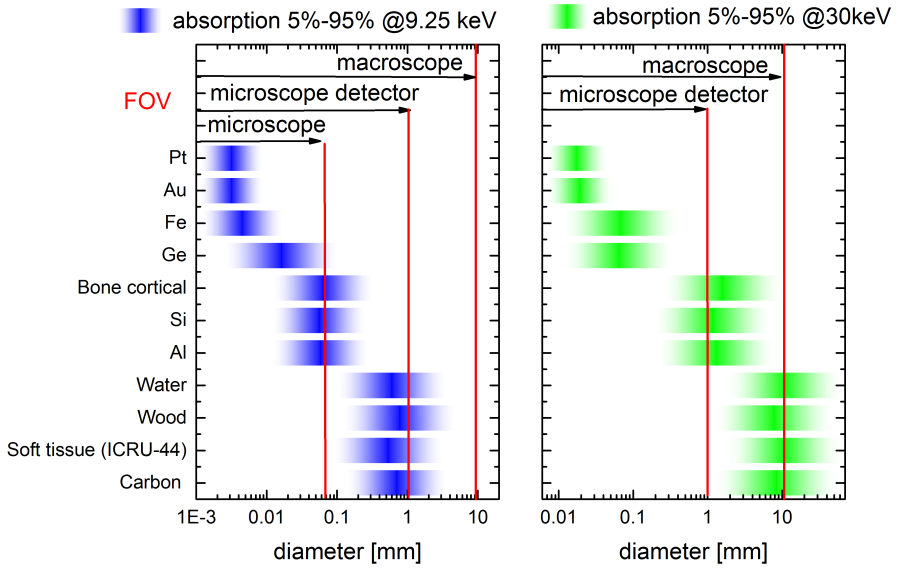

FIGURE 4.18: Absorption range of 5%-95% for different organic and inorganic materials dependent on their thickness for 9.25 keV (corresponding to the Ga K_α-line) and 30 keV photon energy (corresponding to the average energy of the setup's Bremsspectrum). Vertical red lines mark the field of view (*FOV*) of the different detectors (microscope and macroscope), as well as of the microscope. Whenever the *FOV* matches an absorption range, the material is suitable for imaging with the corresponding detector and photon energy. For instance, carbon-based materials can be nicely imaged with the microscope detector and the Ga K_α-line, as well as with the macroscope detector and the Bremsspectrum.

From this, we can make a rough estimate which sample (concerning its size and material) is suitable for a given spectrum and resolution. Concentrating for instance on the Ga K_α-line, one notes that all listed samples which fill the field of view of the macroscope detector have an absorption above 95%. Thus, the macroscope detector is not suitable for imaging with the characteristic 9.25 keV line, unless the material has a high porosity (*e.g.* foams). In contrast, it can be used for imaging with the Bremsspectrum materials such as wood, water, soft tissue and carbon. Smaller samples of these materials can be ideally imaged with the microscope detector in combination with the Ga K_α-line. Finally, materials like silicon or bones should be investigated using a 9.25 keV microscope with further optical elements, as will be discussed in chapter 5.

In the following, selected examples are shown for the different absorption ranges. On the one hand, low Z-materials such as organics and carbon-based materials are imaged with the microscope detector and the Ga K_α-line; on the other hand, as an example for a high Z-material, a cochlear implant is imaged with the macroscope detector and the Bremsspectrum.

Wood The first example presented here is sapwood. Although it is one of the most extensively used materials, there exist still many open questions in the field of wood technology and tree physiology. One of these questions is how to optimize the drying process. For this, the so-called "pits" play an important role, which are parts of the wood cell wall that work as small valves to regulate the exchange of fluids. In this regard, the here presented setup was used to investigate how many pits are closed or opened for a special drying procedure. As shown in Fig. 4.19, the cell structure of the wood can be perfectly imaged.

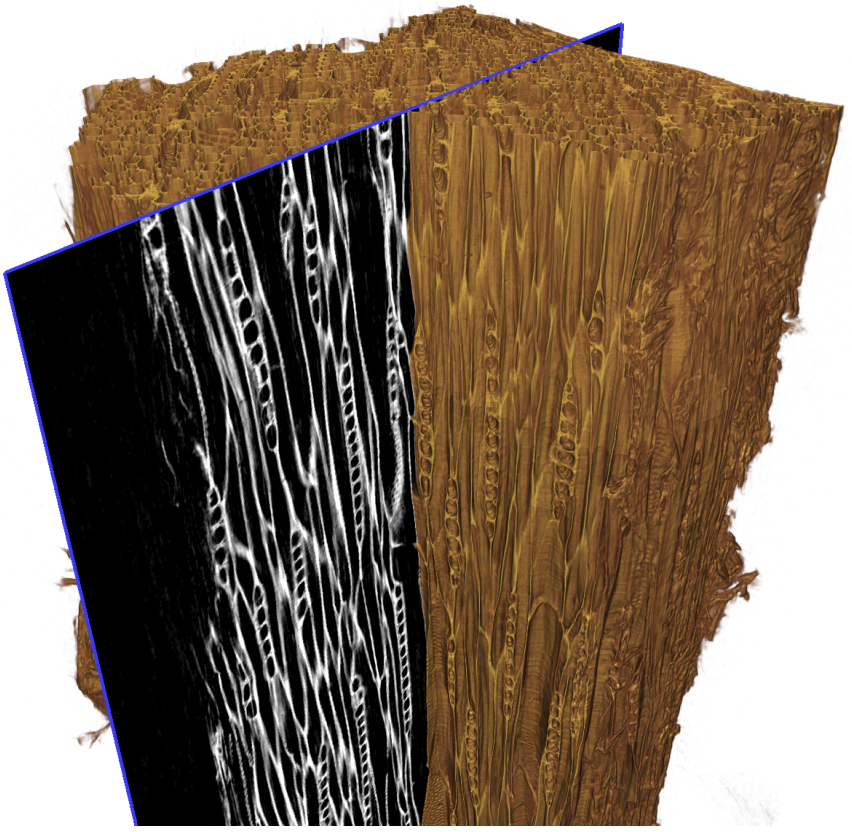

FIGURE 4.19: Three-dimensional rendering of a sapwood. For imaging, a voxel sampling of 0.57 μm was used; the diameter of the horizontal cut corresponds to 800 μm. 1400 projections were taken with an acquisition time of 30 s per scan. One clearly observes the cell structure of the wood and even details inside the cell wall.

With a common composition of 50% carbon, 43% hydrogen and 6% nitrogen, the transmission through a 1 mm thick wood sample with a density of 0.7 g per cm^3 is around 80% at 9.25 keV. The rendering shown in Fig. 4.19 was taken within approximately 12 hours. However, a reduction to a voxel sampling of 1.33 μm leads to a recording time of around 1 hour with basically the same signal-to-noise ratio. This results, as the resolution without using optics is anyway at least 1 μm; therefore, the loss in resolution is small compared to the time saved. Anyway, if time is not limited, the longer scan for sure delivers a sightly better result. The signal-to-noise ratio in the unfiltered flat-field image is in the range of 90-120.

Carbon fiber-reinforced objects Fiber-reinforced plastic plays an important role in lightweight design. In future, this role will further increase due to the need of energy efficiency in automotive and aircraft industry. Investigating this sample class by computed tomography has either the goal of damage inspection or to verify the distribution of the fibres after production [132]. The latter is especially interesting in the case of injection molding, as for this fabrication method it is not clear how the fibers are oriented at edges and whether they are broken. However, both uncertainties substantially influence the strength of an object. Knowing the exact orientation of the fibers allows a comparison with numerical calculations, as well as further optimization.

In comparison with other techniques such as optical or electron microscopy, micro computed tomography delivers a three-dimensional data set instead of two-dimensional slices [133, 134]. Therefore, the here-presented setup was also used to investigate fiber-reinforced plastic samples, as shown in Fig. 4.20. As can be clearly seen, the fibers can be separated from the matrix. Moreover, segmentation of a sub-volume allows to optimize the visualization of different fibers and their orientation.

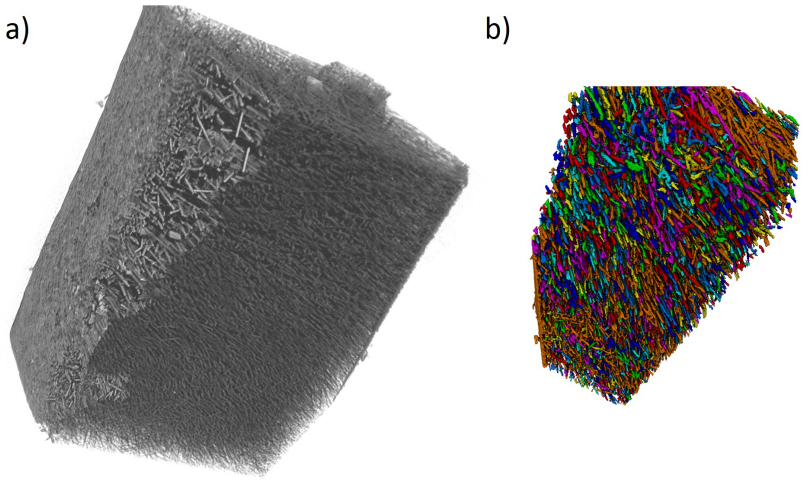

FIGURE 4.20: a) Three-dimensional rendering of a fiber-reinforced plastic, with b) a segmented sub-volume to further show details. For imaging, a voxel sampling of 1.2 μm was used; the fiber diameter is approximately 6 μm. 720 projections were taken with an acquisition time of 15 s per scan. The segmentation was done using a standard threshold for binarisation and further a watershed filter to separate the fibers, which are clearly visible in the image.

Batteries Another important mass product which is suitable for investigations with the Ga K_α-line of the here-presented setup is the graphite electrode of a lithium-ion battery. Currently, large efforts are made to enhance their efficiency, as there exists world-wide a high demand for better batteries. The volume shown in Fig. 4.21 was taken within the framework of Lukas Gold's master thesis [135] about the cycling behavior of lithium-ion batteries, including altering and hysteresis effects. In this thesis, high-resolution micro-CTs were used to investigate the

geometry changes between charged and uncharged batteries.

The graphite anode depicted in Fig. 4.21 was prepared out of a pouch cell, in order to have the sample smaller than the field of view and to avoid attenuation due to highly absorbing material around the anode. One observes Graphite particles, which have a size in the order of 7-12 μm. The volume was sampled with 0.54 μm and an exposure time of 20 s per projection, as well as 4 times averaging; for the whole volume 1600 projections were recorded. Thus, in comparison to the wood and fiber scan shown above, the exposure time is much longer. The reason for this is that the source voltage was reduced to 25 keV (instead of 70 keV) to reduce the high energy Bremsstrahlung and enhance the absorption. Indeed, it turned out that in contrast to common tungsten sources, setting even lower voltages does not enhance the contrast anymore; indeed, it only increases the scan time, as also the Ga K_α-line is weakened. This result is in good agreement with the discussions in chapter 3.1.3, where the relationship between characteristic radiation and Bremsstrahlung is explained.

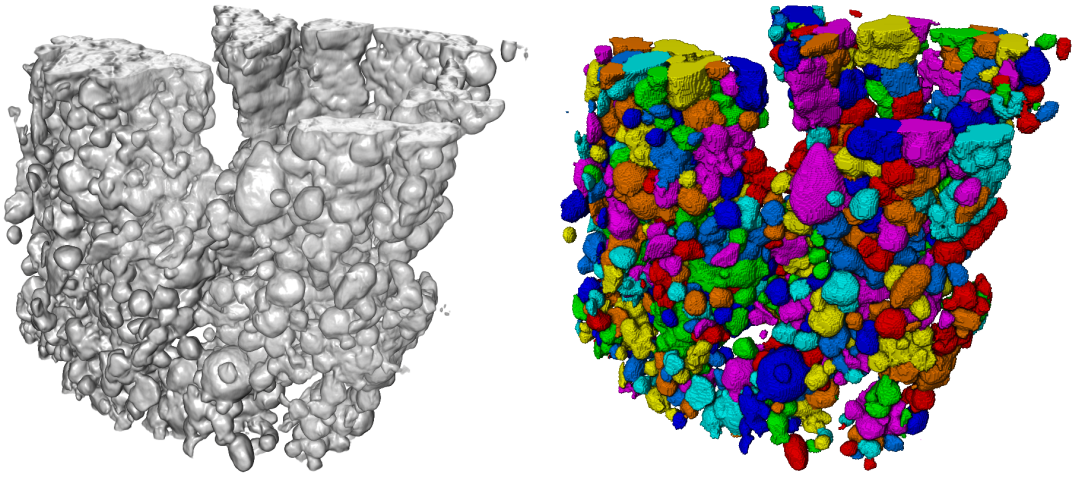

FIGURE 4.21: Graphite electrode of a lithium-ion battery. For imaging, a voxel sampling of 0.53 μm was used. 1600 projections were taken with an acquisition time of 20 s per scan, four times averaged. One observes Graphite particles, which have a size in the order of 7-12 μm.

Medical implants So far, the presented samples were all low-contrast materials based on carbon; thus, the imaging is mainly produced by the absorption and refraction of the Ga K_α-line. However, for thicker samples and higher Z material the transmission at this energy is negligible. Nevertheless, the remaining intensity of the Bremsstrahlung can be still used for a CT scan, with a loss of acquisition speed. To outline this, a scan of a cochlea implant is depicted in Fig. 4.22, showing not only the rendering of the implant itself, but also the surrounding soft tissue and bone in a mouse ear. The implant consists of four platinum electrodes and wires coated with latex.

One reason for deafness could be the damage of sensory hair cells in the cochlea. Implants can replace the function of the sensory hair cells by electrical stimulation [136]. Although the implants allow patients to hear again, the quality is only sufficient to understand voices in a quiet

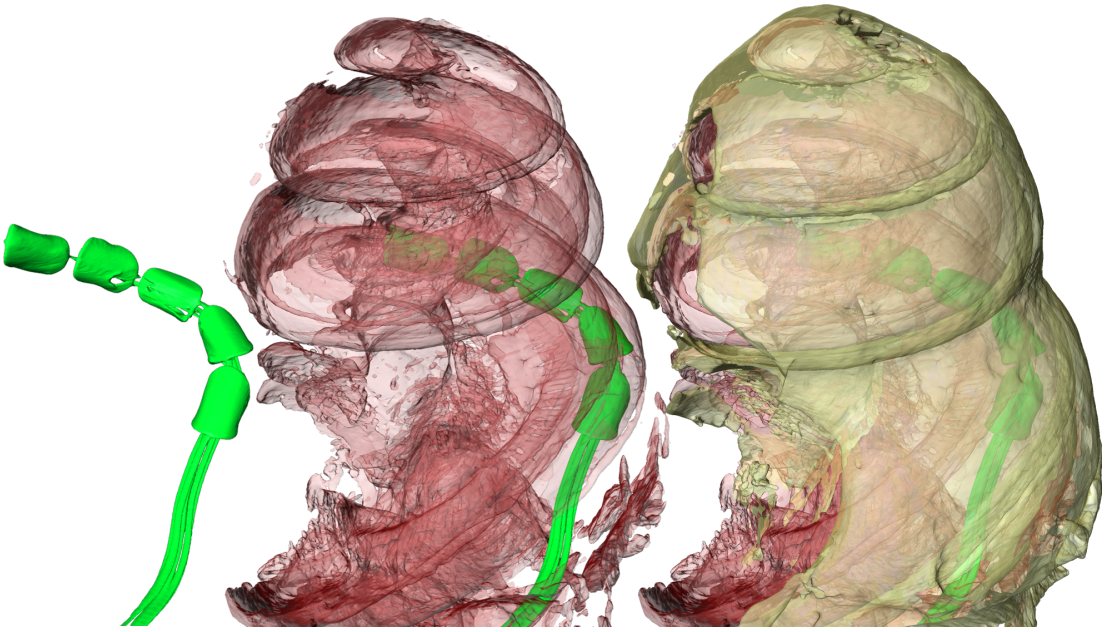

FIGURE 4.22: Cochlear implant in a mouse ear, without environment (left), with surrounding soft tissue (middle) and additional surrounding bones (right). For imaging, a voxel sampling of 2.3 μm was used; the diameter of the middle turn of the cochlea is 2.2 mm. 1500 projections were taken with an acquisition time of 20 s per frame. To increase the resolution, the implant and its environment were imaged separately.

environment. Thus, further research is urgently needed. For this reason, it is important to know the position where an implant exactly sits and which region is stimulated. To answer the latter question, micro computed tomography is the perfect tool, as depicted here for a sample provided by Armin Wiegner from the *Comprehensive Hearing Center Würzburg*.

5 Imaging by magnifying x-ray optics

X-ray microscopy using optical elements can be divided in full-field and scanning techniques [25]. On the one hand, full-field transmission x-ray microscopy (TXM) corresponds to visible light bright-field microscopy (see Fig. 5.1a). In this case, a sample is illuminated from the backside with a condenser and forms a transmission x-ray image, which is further magnified by an optical element onto the detector. As the detector possesses a pixel array, the complete spatial sample information is acquired simultaneously. On the other hand, in scanning transmission x-ray microscopes (STXM), x-rays with a high degree of spatial coherence are focused on a small spot (see Fig. 5.1b). The sample is scanned in two dimensions over this spot and the signal of each scanning step is recorded with a fast detector which does not possess a pixel array. To guarantee that only the focused beam hits the sample, a central beam stop and an aperture are placed between optics and sample.

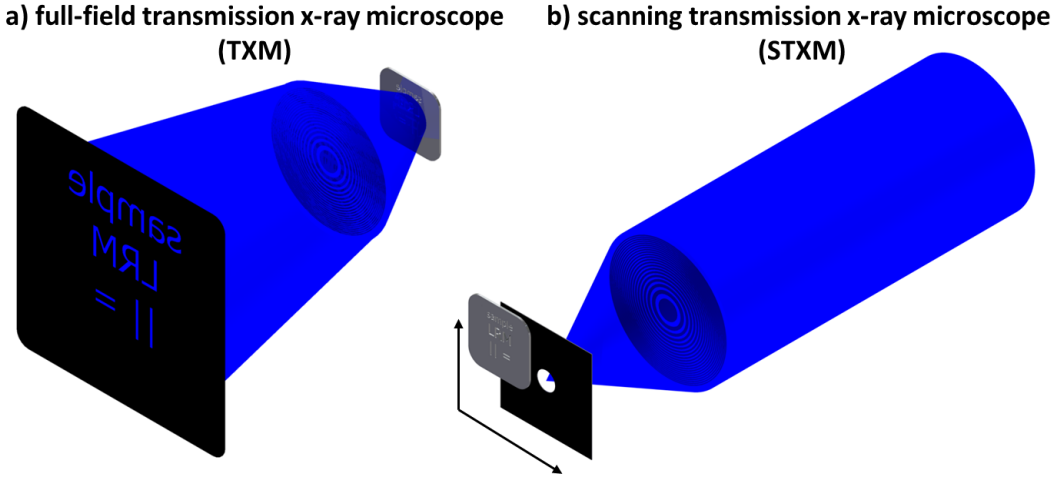

FIGURE 5.1: Schematic drawing depicting the working principle of a) a full-field transmission x-ray microscope (TXM) and b) a scanning transmission x-ray microscope (STXM). a) In the case of TXM, a sample is illuminated from the backside with a condenser and transmits x-rays, which are further magnified by an optical element on the detector. b) In STXM, x-rays with a high degree of spatial coherence are focused on a small spot, which is scanned in two dimensions over the sample.

A major advantage of STXM is that lower doses are needed, because the inefficient x-ray optical element is not placed between sample and detector. Moreover, STXM allows spectroscopy and therefore, quantitative chemical mapping. On the other hand, TXM provides shorter acquisition times, although (besides the condenser) a rather inefficient zone plate is used as optical element. In order to understand the reason for the shorter acquisition time, one should first recall equation 2.7, stating that the flux on a detector is always given by the brightness of the source and the etendue $A\Omega$ of the system. As the latter is conserved within the beam path, the optical element with the smallest etendue limits the flux through the system. In a real x-ray microscope, typically the numerical aperture of the zone plate limits the solid angle Ω and the resolution determines the smallest area A. This is true for both microscopes, STXM and TXM. Thus, in one acquisition step, for both microscopes the same flux hits one pixel on the detector. Therefore, it results that for STXM the total acquisition time is higher, as many scanning steps are necessary for one image.
This can be also understood as followed: for the TXM, while the photons are distributed over the whole sample area, also light from a larger solid angle of the source is collected. In contrast, for the scanning microscope only a very small fraction of the sample is illuminated, corresponding to one pixel. For this, the source-optic distance needs to be large and only light from a small solid angle can be collected. In other words, while a high degree of spatial coherence is required for STXM, TXM also uses the incoherent light for the simultaneous acquisition of all pixels. Therefore, TXM is a faster acquisition technique.
In the case of a very bright source such as a synchrotron, the acquisition time of a single scan can be very short. This limits the use of STXM exclusively to synchrotron or XFEL sources, because for the brightness of a laboratory source, the exposure time would be unreasonably high. A similar argument holds for spatial beam filtering ($e.g.$ with waveguides): although it provides the required coherence for scanning and allows for a compact setup, the combination with laboratory sources also entails long exposure times (see also chapter 6.1).

In the following, first general considerations for designing an x-ray microscope with a laboratory source are discussed (see section 5.1). Afterwards, the here-built microscope based on zone plates is presented (see section 5.2), before also results with refractive lenses are shown (see section 5.3). Finally, the chapter closes with a comparison of nanofocusing setups (see section 5.4).

5.1 General considerations for designing a laboratory microscope

In order to obtain good images with a microscope, enough photons have to interact with each voxel of a sample. In other words, for maximizing the amount of photon flux transferred from source to detector, we have to consider the optical path of photons between source and detector

and understand which of the given optical parameters define the photon flux through a voxel. For this, the suitable approach is basic radiometry.

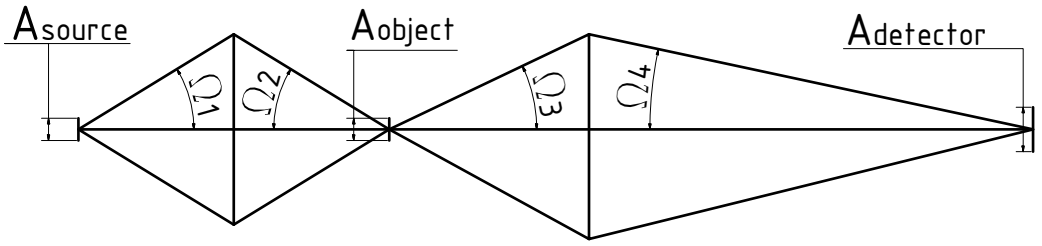

FIGURE 5.2: Drawing of the $A\Omega$-product for a system of source (with area A_{source}), condenser, object (with A_{object}), zone plate and detector (with A_{detector}). For an ideal system, $A \times \Omega$ remains constant throughout the beam path.

In the following, for an ideal loss-less system a single pixel in the sample on the object plane A_{object} is considered; it is illuminated by a source via a condenser, and detected by a detector via a zone plate (see Fig. 5.2). The Fresnel zone plate magnifies the area A_{object} according to the thin lens equation $1/f = 1/q + 1/p$ (with f: focal width, q: image distance, p: object distance) to the detector plane with the area A_{detector}. For this, the object is not positioned in the focal plane of the zone plate, but further away. Thus, the numerical aperture of the imaging process is:

$$\Omega_3 \sim NA^2_{\text{working}} = \sin^2\left(\tan^{-1}\left(\frac{\tan\left(\sin^{-1}(NA)\right)}{1/m+1}\right)\right) \tag{5.1}$$

were m is the magnification $m = q/p$. For high magnifications, NA_{working} is equal to the normal *NA* of the zone plate.

The condenser is illuminating the object plane at an angle Ω_2. It can be easily understood that Ω_2 should be equal to Ω_3: if it is larger, photons will not be collected by the zone plate and are lost; if it is smaller, the zone plate is not fully illuminated and flux as well as resolution are reduced.

With these constrains $\Omega_2 = \Omega_3$ and a certain pixel size which defines the area A_{object}, one can check which parameters we have for optimizing the flux. For this, we reconsider equation 2.7 that defines the flux Φ on the detector (with all losses taken into account by a factor T), from which one obtains:

$$A_{\text{source}} \cdot \Omega_1 = A_{\text{object}} \cdot \Omega_3 = A_{\text{detector}} \cdot \Omega_4 = \text{const.} \tag{5.2}$$

and therefore:

$$A_{\text{source}} \cdot \Omega_1 = A_{\text{object}} \cdot \Omega_2. \tag{5.3}$$

Thus, enhancing A_{source} (*i.e.* the area of the focal source spot which radiates photons with a given brightness to A_{object}) does not help to enhance the flux, as also discussed in the following on the basis of typical examples. For this, the starting point is a symmetric condenser, where $p = q$ and thus also $\Omega_1 = \Omega_2$ as well as $A_{\text{source}} = A_{\text{object}}$. If we now take a larger source which gets demagnified to A_{object}, it is intuitive from geometrical optics and also given by equation 5.3 that Ω_1 gets decreased - while the flux stays constant. For a smaller source which gets magnified to A_{object}, obviously the opposite happens - Ω_1 gets enhanced - while the flux also stays constant. Thus, for a constant brightness, simply changing the area of the source does not change the detected flux. This also means that a small source can be magnified on a large object size without loosing flux.
Let us now consider the flux in one pixel of the microscope detector. In reality, its limiting etendue $A\Omega_{\text{lim}}$ is given by the NA^2 of the zone plate and the pixel size. However, the size of the pixel has to be kept small for high resolutions. Thus, the *NA* of the zone plate is the "bottleneck" of the whole x-ray microscope. Therefore, optical properties of the condenser can never overcome the bottleneck given by the zone plate.

Thus, to improve the photon flux, only three possibilities are available:

1. Higher brightness of the source. The total power of the source is independent of the flux through a pixel, and only depends on the source brightness.
2. Enlarge the limiting etendue, *i.e.* higher *NA* of the zoneplate.
3. Enlarge the efficiency of all optical elements T, which is the product of the individual efficiencies η_{i} of condenser, zone plate and absorption in air or filters.

Unfortunately, for zone plates the latter two points are antagonistic, regarding what is technically possible. For binary zone plates, the efficiency depends on the thickness (*i.e.* height of the structure, see equation 2.63), yet the numerical aperture depends on the width of the outermost zone (see equation 2.59). In the fabrication process, there is a maximum possible aspect ratio between thickness and zone width, which is further discussed in the next section 5.2. However, the numerical aperture occurs squared in equation 2.7 (via the angle Ω), whereas the efficiency (T) appears linear. Therefore, the zone plate design should be optimized in order to maximize the product $\eta \times NA^2$.

Contrast Besides optimizing the flux, one should also consider the absorption properties of a sample (see Fig. 4.18). When a feature gets smaller, it typically also gets thinner; thus, the absorption length decreases. Therefore, the energy of 9 keV - which is for larger low Z-objects more or less "soft" (*i.e.* gets strongly absorbed) - becomes too hard (*i.e.* gets weakly absorbed) in an x-ray microscope. For instance, the absorption contrast of wood gets very low in a 9 keV

microscope.

To overcome this limitation, phase contrast acquisition modes have been demonstrated as efficient tool: while the absorption gets reduced with $1/E^3$ (E: energy of the x-rays), the phase contrast only gets reduced with $1/E$ [12, 137]. For Zernike phase contrast, the illumination is adjusted as a narrow hollow cone, which is transmitted by a phase ring placed between zone plate and detector [24]. The phase contrast develops due to an interference between scattered light from the dark-field and light which has passed the phase ring, which is shifted by $\pi/2$.

Resolution The obtainable resolution in TXM depends on the *NA* of the magnifying optics and can be slightly improved by a convergent illumination of the sample [29]. In the case of first order operation, the resolution is given by $d_{\text{min}} = \frac{p\lambda}{NA}$ with $p \in [0, 1]$, where p depends on the illumination. For the here-described setup, the illumination is incoherent, corresponding to $p = 0.61$. For partially coherent illumination (*i.e.* *NA* of the condenser is smaller than the objective *NA*), the resolution is reduced [138].

Since the numerical aperture is $NA = m\lambda/2\Delta r$ (see equation 2.59), the resolution is inversely proportional to the order of diffraction m used for imaging. Therefore, in principle a higher resolution can be achieved by using higher orders m. However, in view of the efficiency of the higher orders, this is no option for laboratory microscopes.

Beam path A simulation of the TXM microscope beam intensity along the direction of propagation is depicted in Fig. 5.3 for the typical illumination mode, where the condenser casts an image of a light source onto the sample plane[1]. This mode is called "critical illumination", since any inhomogeneity in the light source shape is reproduced in the image.

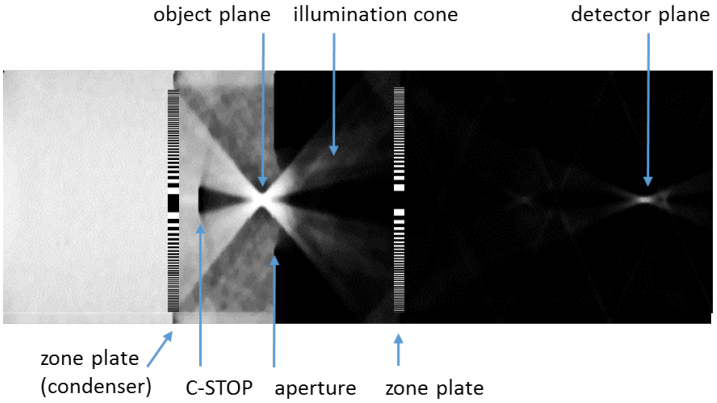

FIGURE 5.3: Beampath simulated with Fresnel propagation, to visualize the illumination profile. In the simulation, a second zone plate is used as condenser, because the model does not include total external reflection.

[1]Figure 5.3 is simulated using the Fresnel propagation formalism as described in Ref. [27]. Since this kind of simulation does not include total external reflection, a zone plate is used as condenser instead of a capillary utilized in the experiment.

Köhler illumination overcomes this by casting a defocused image of the light source onto the sample. This evenly distributed illumination is required for phase contrast measurements. In visible light microscopes, Köhler illumination is implemented by using a collector lens to image the source onto the front focal plane of the condenser. However, the usage of such a relay optics is not suitable for x-ray microscopes. Instead, several different approaches were developed to get evenly distributed illumination, like grating condensers [139]. In the framework of this thesis, always critical illumination was used, since for absorption contrast uneven illumination can be flat-field corrected.

5.2 Magnification by Fresnel zone plates

In order to enable high-resolution imaging with laboratory sources, the optical elements need to provide a sufficient numerical aperture and efficiency. Otherwise, exposure times are too long for any reasonable alignment procedure. In numbers, this means that the outermost zone width should be at least smaller than 70 nm. In combination with the required thickness, zone plates are still a very challenging task for micro-fabrication. Here, three types of zone plates were investigated for the imaging proposes. While the first type is based on electron lithography, the second type is based on atomic layer deposition (ALD) combined with focused ion beam (FIB), and the third one is directly written with FIB. A major difference is their direction of fabrication, which appears in the first and third case in the direction along the optical path, and in the second case orthogonal to the optical path. This has consequences for the specifications of the optics.

5.2.1 Zone plate types and efficiency measurements

To efficiently focus hard x-rays, a phase shift of π would be necessary. For 9.25 keV and tungsten, the required thicknesses is $\sim$ 1700 nm. Together with an outermost zone width of for example 50 nm, this means that the required aspect ratio needs to be roughly 35.
The zone plates which were available in the framework of this thesis are listed in table 5.2. Whereas the e-beam based zone plates are commercially accessible either from *Applied Nano Tools, Canada* or *Zone plates Ltd., UK*, ALD- and FIB-based zone plates were provided from the working group of *C. Grevent* from the *MPI Stuttgart*.

From table 5.2, one can summarize that the commercial zone plates reach aspect ratios of about 20. The zone plate fabricated by ion-beam lithography *ZP12F* possesses an aspect ratio of one; it is thus only useful in the soft x-ray range and listed here just for completeness. The ALD lens possesses an aspect ratio of 100.

Name fabricated	Δr [nm]	thickness [nm] material	focal length [nm]	zones	diameter [μm]	*NA*
ZP5W e-beam	50	1000 W	67.108	900	180	0.00134
ZP6W e-beam	50	1000 W	52.18	700	140	0.00134
ZP-1W e-beam	65	1500 W	87.3	693	180	0.0011
ZP11A ALD	35	3500 Al_2O_3-Ta_2O_5	9.925	60	30-38	0.0019
ZP12F FIB	300	300 Au	157.1	59	70	0.00022

TABLE 5.1: List of utilized zone plates. While the zone plates fabricated by e-beam lithography are bought from *Zone plates Ltd., UK*, ALD- and FIB-based zone plates were provided from the working group of *C. Grevent* from the *MPI Stuttgart*. Besides the fabrication technique, the diameter of the outer zone Δr, the thickness, the material, the focal length, the number of zones, the total diameter and the resulting *NA* are listed. All values are calculated for 9.25 keV.

Fabrication The first type of utilized zone plates is fabricated as depicted in Fig. 5.4. A subtractive method is applied, where first all necessary layers are deposited on the substrate. As substrate, a 200 nm thick Si_3N_4 membrane is used, which provides sufficient x-ray transparency. On top, tungsten as zone plate material, Ni as a primary mask and PMMA are deposited. After e-beam lithography which etches the principle structure into the PMMA top layer, the pattern is transferred into the underlying Nickel layer via argon sputtering. With fluorine-based reactive ion etching (RIE), the final zone plate is created from the tungsten layer. One critical point in this procedure is that the tungsten films need to be deposited with low stress to avoid collapsing of the thin zones [140].

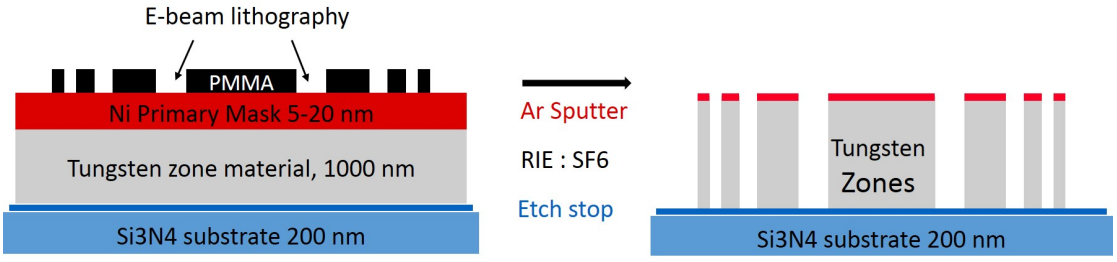

FIGURE 5.4: Zone plate fabrication principle. First, all necessary layers are deposited on a Si_3N_4 substrate. On top, tungsten as zone plate material, Ni as a primary mask and PMMA follows. After e-beam lithography which etches the principle structure in the PMMA top layer, the pattern is transferred into the underlying Nickel layer. With fluorine based reactive ion etching (RIE), the final zone plate is created from the tungsten layer.

The second utilized zone plate type is fabricated via atomic layer deposition (ALD) and focused ion beam (FIB) (see Fig. 5.5). Beginning with a glass fiber, alternately strong and weak absorbing materials are deposited by ALD. Subsequently, the resulting cylinder is sectioned by focused ion beam to obtain the zone plate. ALD as deposition method shows here very good

results due to the high quality of the deposited layers and the accurate thickness control, but it is very slow [141]. Because of the long deposition times, the fabricated number of zones is usually small. For the zone plate investigated in the framework of this thesis, a glass wire of 30 μm thickness was chosen and 4 μm zones were deposited. As materials, Al_2O_3 and Ta_2O_5 were used. In contrast to the e-beam based zone plates with free standing zones, here the x-rays have to transmit through both, opaque and transparent materials. This has the disadvantage that due to refraction in both zones, higher aspect ratios are needed; on the other hand, also much higher aspect ratios can be reached. Moreover, since absorption occurs in both zone layers, the detailed material composition needs to be considered.

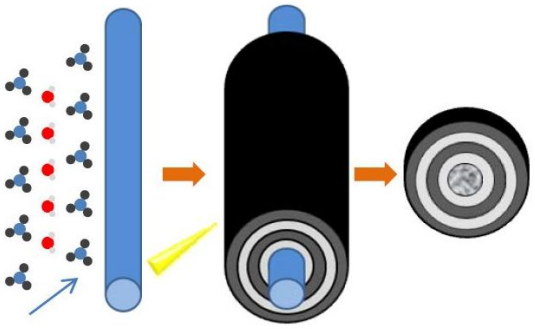

FIGURE 5.5: Zone plate fabrication principle using atomic layer deposition (ALD) and focused ion beam (FIB) [141]. A glass wire is coated by alternating absorbing and transparent layers via ALD. Afterwards, the coated wire is sectioned with FIB to produce the Fresnel zone plate.

Efficiency measurements First measurements to get an estimate of the zone plate's efficiencies were done at the *BAMline* Beamline at the *BESSY*[2] *2*. At this synchrotron, the nearly parallel beam enables much easier scans through the zone plate's focal point. Besides that, the high brightness allows for short exposure times and quick alignments. Moreover, the available Si (111) double-crystal monochromator provides narrow bandwidth radiation with a tunable energy.

To find the focus position, a scan was performed for each zone plate along the optical axis. Figure 5.6 shows the comparison of a simulated and measured intensity profile. From this, the 2D intensity profile (see Fig. 5.7) was obtained by re-slicing the 3D data set. In the measurement, the broader first order focus results from the blurring of the detector, as well as from a different scaling in the plot, which is needed to see the third order.

From the scan, the obtained best focus position was used to determine the efficiencies η of the zone plates:

$$\eta = \frac{I_{\text{focused}} A_{\text{focus}}}{I_{\text{incoming}} A_{\text{zp}}} \tag{5.4}$$

with the intensities I and areas A. Experimentally, since the incoming and focused intensities I_{incoming} and I_{focused}, respectively, cannot be measured simultaneously, the image at the focus

[2]Berlin Electron Storage Ring Synchrotron

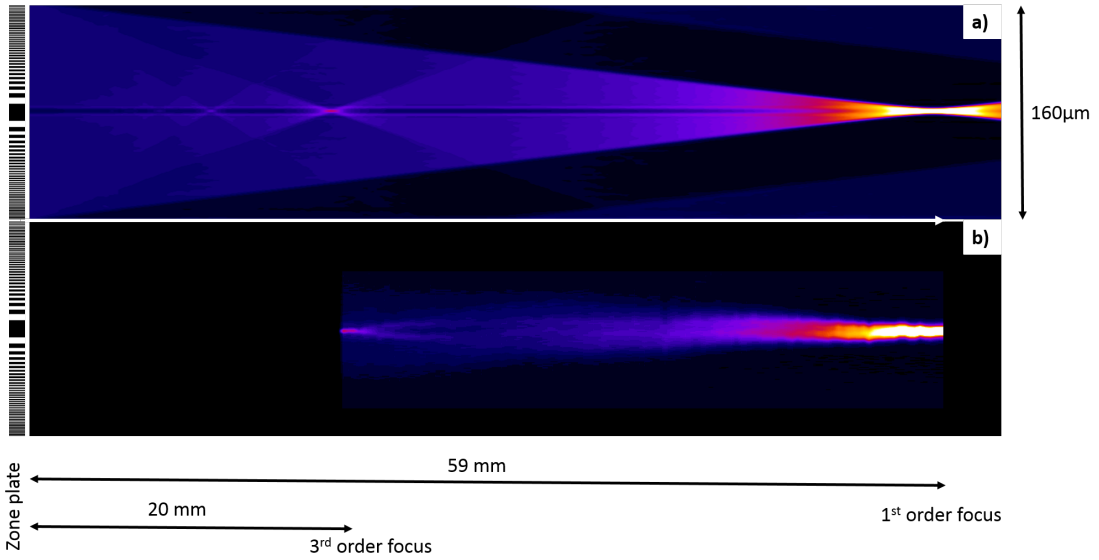

FIGURE 5.6: Intensity propagation of a zone plate. a) Simulated data with Fresnel propagation, as well as b) measured data with 120 steps of 250 μm width and an exposure time of 500 ms at the *BAMline BESSY 2*, starting at the position of the third order focus.

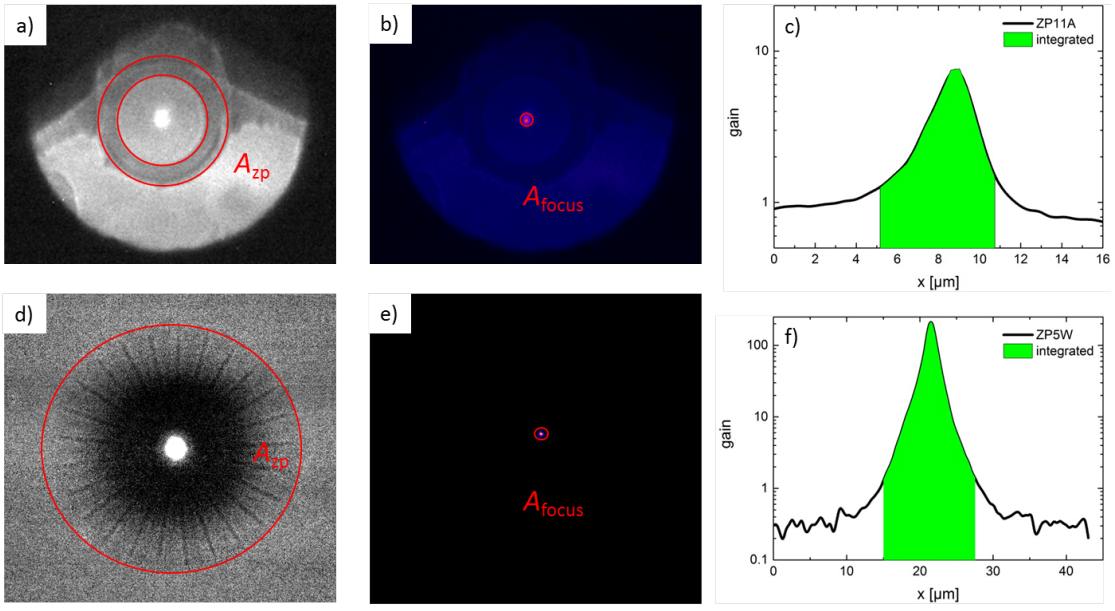

FIGURE 5.7: Exemplary determination of a zone plate's efficiency for the *ZP11A* (a-c) and *ZP5W* (d-f). a,b,d,e) X-ray images of the zone plates with different scalings. Red circles mark the area A_{zp}, where zones are present, as well as the focal area A_{focus}. From these areas and c,f) the integral of the gain $I_{focused}/I_{incoming}$, the efficiency can be calculated according to equation 5.4.

plane was flat-field corrected and I_{focused} was calculated by integrating over the gain as shown in Fig. 5.7. The resulting values are summarized in table 5.2.

Name fabricated	theoretical efficiency first order η_{theo}	measured efficiency first order η	$\eta \times (NA)^2$	
ZP5W e-beam	21.15%	6.6%	$1.18 \cdot 10^{-7}$	
ZP6W e-beam	21.15%	4.9%	$0.88 \cdot 10^{-7}$	
ZP11A ALD	7% [141]	4.4%	$1.59 \cdot 10^{-7}$	
ZP-1W e-beam	30.4%	2.8%	$0.3338 \cdot 10^{-7}$	
ZP8W e-beam	21.15%	8.8%	$1.58 \cdot 10^{-7}$	equal design to ZP5W
ZP2W e-beam	21.15%	5.2 %	$0.93 \cdot 10^{-7}$	equal design to ZP5W
ZP3W e-beam	13.2%	2.9%	$0.52 \cdot 10^{-7}$	thickness 700 nm

TABLE 5.2: Theoretical and measured efficiencies of the first order focus η_{theo} and η, respectively, together with the product $\eta \times (NA)^2$ of the utilized zone plates. All values are determined for 9.25 keV

From the experimentally determined efficiencies, one would conclude that the best performance can be reached by the ALD zone plate. However, magnifying imaging was not possible with this lens. Possibly, the lack of larger zones with smaller radii prohibits the use of these lenses, as it causes the low spatial frequencies to remain unresolved by the lens. In order to overcome this problem, currently ALD zone plates with more zones are in production. Besides a smaller central substrate fiber as a starting point, smaller outer zone widths are planned. If this can be realized, good imaging results are to be expected.

The resulting efficiencies for the e-beam zone plates show that despite similar design parameters, each zone plate possesses an individual performance which is typically well below the theoretical efficiency; the reason is most likely a limited fabrication quality. As acquisition speed relies on the product of NA^2 and η, while at the same time the quality decreases with smaller Δr, one always finds a trade-off between efficiency (related to the thickness) and *NA*. Therefore, for imaging, a zone plate should be always chosen according to the real efficiency values, not the design parameters. This can be seen for example from the comparison of *ZP5W* with *ZP-1W*, where the higher aspect ratio leads in reality for the latter case to much smaller efficiencies due to the inferior fabrication quality.

In all cases, the $\eta \times NA^2$-product is in the range of 10^{-7}. In comparison, for visible light this product is around 10^{-1}, meaning that it differs by six orders of magnitude. This clearly illustrates why x-ray microscopy is so difficult and time consuming.

However, today very active research is done to enhance the efficiency and the smallest outer

width of zone plates. Responsible for big achievements is - besides progresses with more accurate machines - the application of new techniques. In terms of lithography, stacking two or more zone plates to a combined optic is a promising path. Based on this, Mohacsi *et al.* reported zone plates with a smallest zone width of 50 nm and efficiencies of 30% [142, 143]. Using atomic layer deposition, lenses were fabricated with a smallest zone width of 35 nm and efficencies around 15% [144, 145]. Similar to ALD, sputtering techniques can be also employed, yielding lenses with 2.8 nm smallest zone width and 27% efficiency [146]. As soon as such fantastic lenses will also achieve good imaging properties (*e.g.* not too big aberrations) with a stable production quality, this will boost laboratory microscopes to a performance which is nowadays only possible at synchrotron sources.

5.2.2 Condenser

As described in chapter 5.1, the condenser has the aim to illuminate the object with low loss of brightness and filling the *NA* of the objective (*i.e.* the zone plate). In the course of the project, first a polycapillary was used, later a monocapillary. While the monocapillary is theoretically more efficient, it is also less flexible in terms of design (see also chapter 2.3.1). The polycapillary with the full and large cone angle can be used for many different optics (with different numerical apertures) and was therefore used as a "universal" condenser.

Polycapillary Although the polycapillary is in principle designed to match the *NA* of the zone plate (see table 5.3), it possesses in reality larger convergence angles due to local divergencies. Therefore, in the experiment the non-convergent part of the beam should be removed by a pinhole and beamstop.

parameter	
input focal distance	25 mm
output focal distance	60 mm
system length	155 mm
output convergence angle	0.33°
input convergence angle	0.9°

TABLE 5.3: Design properties of the polycapillary.

The polycapillary is fabricated out of 5 μm glass channels. To get the pores in the desired shape, the glass tube bundles are heated and pulled [54]. For production, it is necessary to meet an exact combination of force and heat. Afterwards, the bundle is cut at a certain position to adjust input and output focal distance.
The efficiency of capillaries is usually given as a "gain". It denotes the photon flux in the secondary focal plane of the capillary compared to the photon flux without optic. This measure is

only useful for imaging, when the angular distribution of the flux is known. For the polycapillary, the simulated gain is 60 compared to a 200 μm pinhole at 155 mm. The experimentally determined value is 105; this is not surprising, since the gain depends on the brightness and was simulated for a standard source. Indeed, the real gain is even higher, since in the measurement of the reference (without optics) also photons with higher energies were counted, which can not pass the optical elements.

Monocapillary In contrast to the polycapillary, the design of the monocapillary requires a much more accurate fabrication due to the single reflection of each ray. As a first step, a design was chosen which illuminates only a small field of view, in order to keep reflection angles small and thus reach a high efficiency. For a circular source of 20 μm diameter, the illuminated area at the specimen plane is circular with a *FWHM* of about $\sim$ 30 μm (see Fig. 5.8b). Therefore, the optical element corresponds to the ellipsoid equation: $y^2 = 0.48 \cdot x - 2.407510^{-6} \cdot x^2$, given for x in mm. From this equation, a 200 mm source-focus length results. The manufacturer specified that the monocapillary meets this equation in the produced subpart of the ellipse between 104 mm and 174 mm at all positions better than 1 μm. Here, x = 0 mm corresponds to the sample position; thus, there is approximately 100 mm space between sample and edge of the optical element. The input distance is nearly equal to that of the polycapillary to allow simple switching between both.
This type of capillary was invented by Balaic *et al.* [147, 148] from *AXCO Australia*, who has also fabricated the here utilized capillary. Since the glass reacts very strong on clamping forces, the optical element is housed for better handling in a steel tube of 6.25 mm diameter. Exact knowledge about the fabrication steps is not provided by the manufacturer, but an accurate description about general production techniques can be found in Ref. [149].

Figure 5.8 shows a simulation of the resulting illumination intensity at the position of the zone plate and the sample, together with the corresponding measurements. As described already in Fig. 5.3, the illumination profile at the zone plate position should be a hollow cone. In the simulation, the outer red line indicates the diameter of the zone plate, the inner one the diameter typically illuminated at other microscopes about 0.7 to 1 of the *NA* [150]. If ever a second monocapillary was bought, illuminating more of the inner part might help to gain flux.
Indeed, the measured intensity distribution shows in principle a good agreement with the simulations. However, when removing the pinhole, the hollow shape smears significantly out and is not as symmetric as one would expect (see Fig. 5.9b). One obvious reason for the discrepancies might be problems with the alignment, since the parameter space is very large. The alignment is further complicated by the fact that it is easier without pinhole (as the position of the pinhole has to be adapted iteratively); however, to see the resulting illumination at the sample position, the pinhole should be used, as it is part of the measurement beam path. Anyway, although we

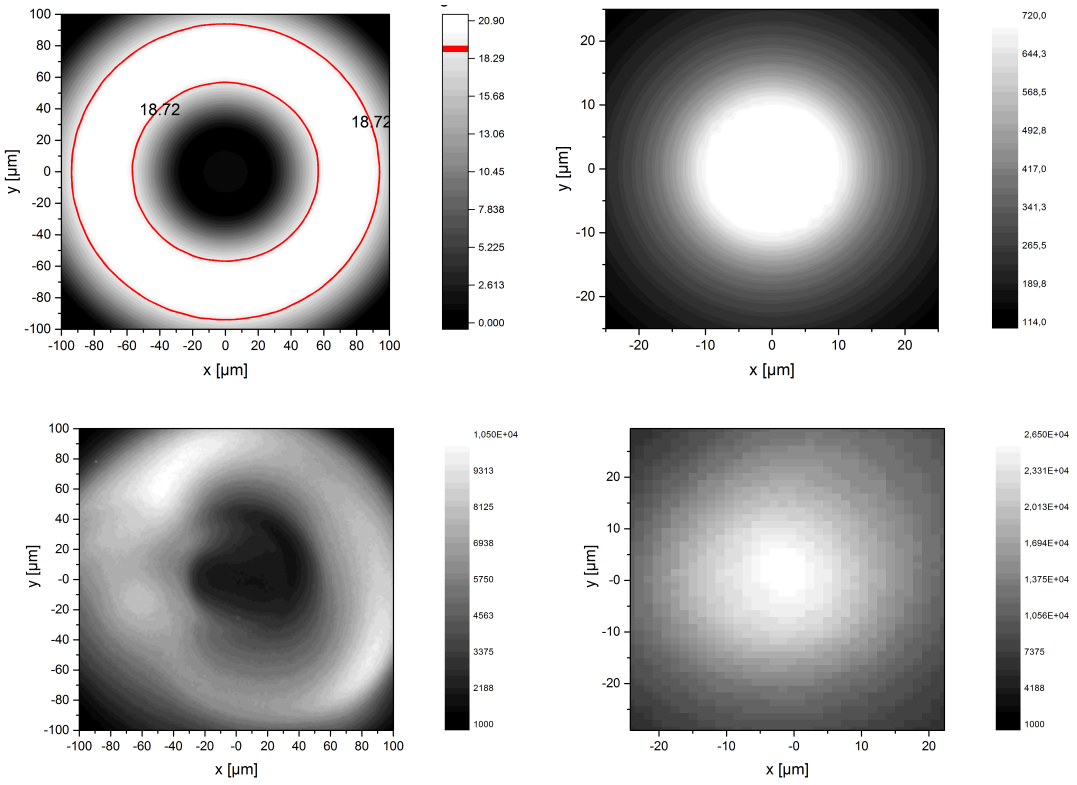

FIGURE 5.8: Simulated (top) and measured (bottom) intensity distribution of the monocapillary at *SDD* = 274 mm (plane, where the zone plate is placed) with an additional pinhole placed slightly before the sample position. Red lines indicate the area, where the zone plate should be illuminated. c) Simulated and d) measured intensity distribution at *SDD* = 200 mm. The simulations were done with ray tracing by *D. Balaic* from *AXCO Australia*.

tried to improve the alignment over days, it was never perfect; therefore, probably other reasons play an important role for the smeared-out light cone. One other possible reason is the shape of the real source with a long tail (see Fig. 3.1), which differs from the assumed circular shape in the simulation. Furthermore, the source has a finite extension in x-direction (*i.e.* the beam direction). Finally, also inaccuracies in the fabrication process or a locally reduced surface reflectivity might be the reason for the deviations. Figure 5.8 also shows a qualitatively good agreement between simulation and measurement at the sample position, where the full field of view is illuminated. However, the measured gain at the object position is about a factor of 3.3 smaller than expected from the simulations.

The experimental illumination profile is further displayed in Fig. 5.9 for different source spots, showing that a source with higher brilliance leads to higher intensities at the sample position. Clearly the larger spot with 30 μm and 300 W produces less intensity than the 20 μm spot with 200 W.

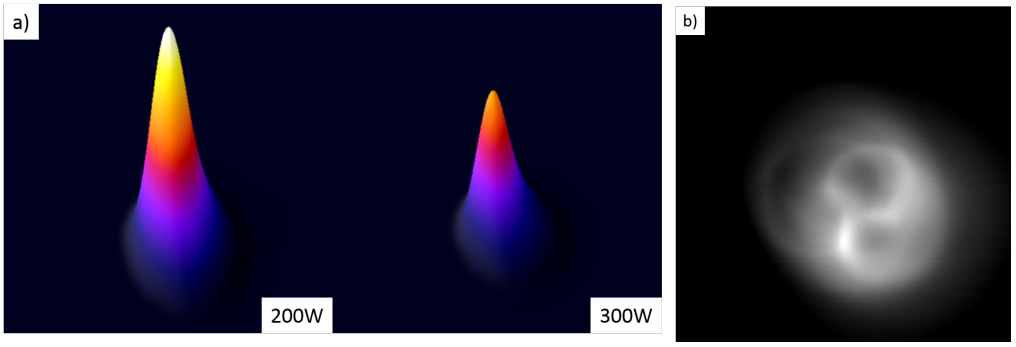

FIGURE 5.9: Intensity distributions measured with a monocapillary. a) Surface plot of the measured intensities at the sample position *SDD* = 200 mm for a source spot of 20 μm with 200 W (left) and 30 μm with 300 W (right). The left spot with higher brightness leads to a higher intensity. b) Intensity distribution of the monocapillary at the zone plate position *SDD* = 274 mm measured without pinhole. The resulting shape is asymmetric.

5.2.3 Alignment and further optical parts

Further optical elements like the central beam stop (C-stop) and pinholes with different sizes were either home-made with FIB or - if bought for larger diameters - produced by laser cutting. For the elements made with FIB, opaque gold foils with 20 μm thickness were used. This thickness is high enough to absorb nearly all 9 keV X-rays, while the milling process is still reasonable in the range of a few hours.

Figure 5.10 shows a schematic drawing of the microscope setup, which can be compared to a photograph of the experimental setup in Fig. 5.11. The instrument is equipped with a laser for pre-alignment, which is capable of measuring distances with a precision of 0.5 mm. The alignment of the optical elements follows the steps described in Fig. 5.10. It starts with an accurate positioning of the detector in z-y-direction. This is realized by placing a sample with small features in the beam while taking images at two different x-positions of the detector (along the beam path). From the offset of the sample, the z-y-position of the sample is determined, where the image of the sample does not longer move when the detector distance varies. Afterwards, the detector stage is adjusted in z-y-direction to place the sample in the center of the image. By this procedure, the later optical axis is chosen parallel to the mechanical x-axis of the detector. This is essentially important to ensure that the beam path is not lost when focusing. Since the beam is narrow and the total x-distance is in the range of one meter, this alignment has to be done in a way that the total deviation is below 100 μm.

In the next step, the condenser has to be aligned. For both, mono- and poly-capillary, the procedure is in principle similar. First of all, the pivot point is set on the entrance of the capillary. This enables the user to perform all translations and rotations with respect to the capillary's entrance. Afterwards, the entrance needs to be aligned to transmit light. This can be done by using a large area detector like the *Medipix* or *Rad-icon*, where the optic is scanned in vertical (y) and horizontal (z) direction until a reflection is found. Then, iterative small translations and

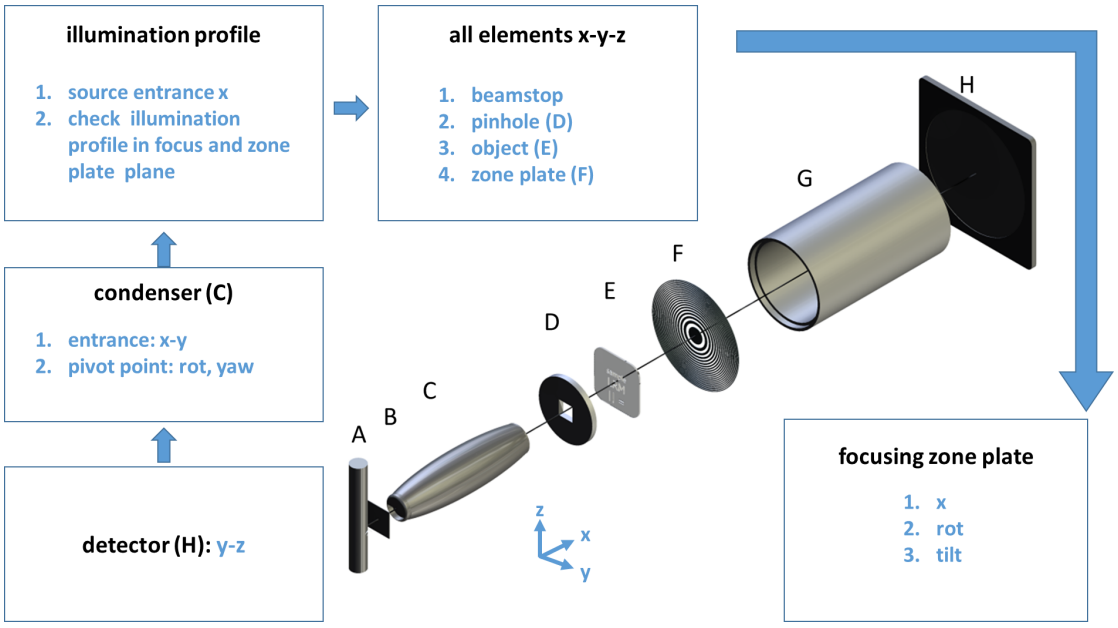

FIGURE 5.10: Schematic drawing of the microscope setup, together with the alignment scheme. The microscope consists of A) source, B) Zn foil as K_β-blocker, C) condenser, D) pinhole, E) sample, F) zone plate, G) vacuum pipe and H) detector. For alignment, first the detector is adjusted in the y-z-plane with respect to the source and an accuracy of 10 μm. Afterwards, the condenser is placed with the pivot point at the entrance of the capillary and aligned to deliver a uniform beam profile. The fine-tuning follows together with beamstop and pinhole, before the object and the zone plate are placed. Finally, the position of the zone plate is optimized.

rotations are made without loosing the reflection, until the beam is focused on the center of the detector. After this rough alignment, the beam direction x is adjusted by scanning through the focal planes with the detector, while varying the condenser's input distance. The aim of this step is to maximize flux with respect to a uniform angular distribution and maximum flux at the sample position. Finally, pinhole and beam stop are placed in the beam and the illumination is again optimized iteratively to obtain the profile as shown in Fig. 5.8. The optimization of the illumination has to be completed before the object is placed into the beam path, because then the detector cannot reach any more the specimen plane.

The next step is the vertical and horizontal alignment of the sample, and afterwards of the zone plate. For this, condenser and beam stop are removed to be able to see the object. The x-position of the zone plate is set according to the lens equation and condenser, before the condenser and beam stop are placed again in the beam path. The focus is found by scanning back and forward with the detector. This kind of focusing has the disadvantage that the magnification can not be set exactly, but the scanning is done on the "less" sensitive side of the lens equation; therefore, the image can be seen over a long distance. As a last step, rot and tilt of the zone plate is adjusted, in order to reach a homogeneous resolution in all directions. One should note that the last steps are very time-consuming, since the exposure times are long. Finally, the energy filter and the vacuum pipe are placed in the beam.

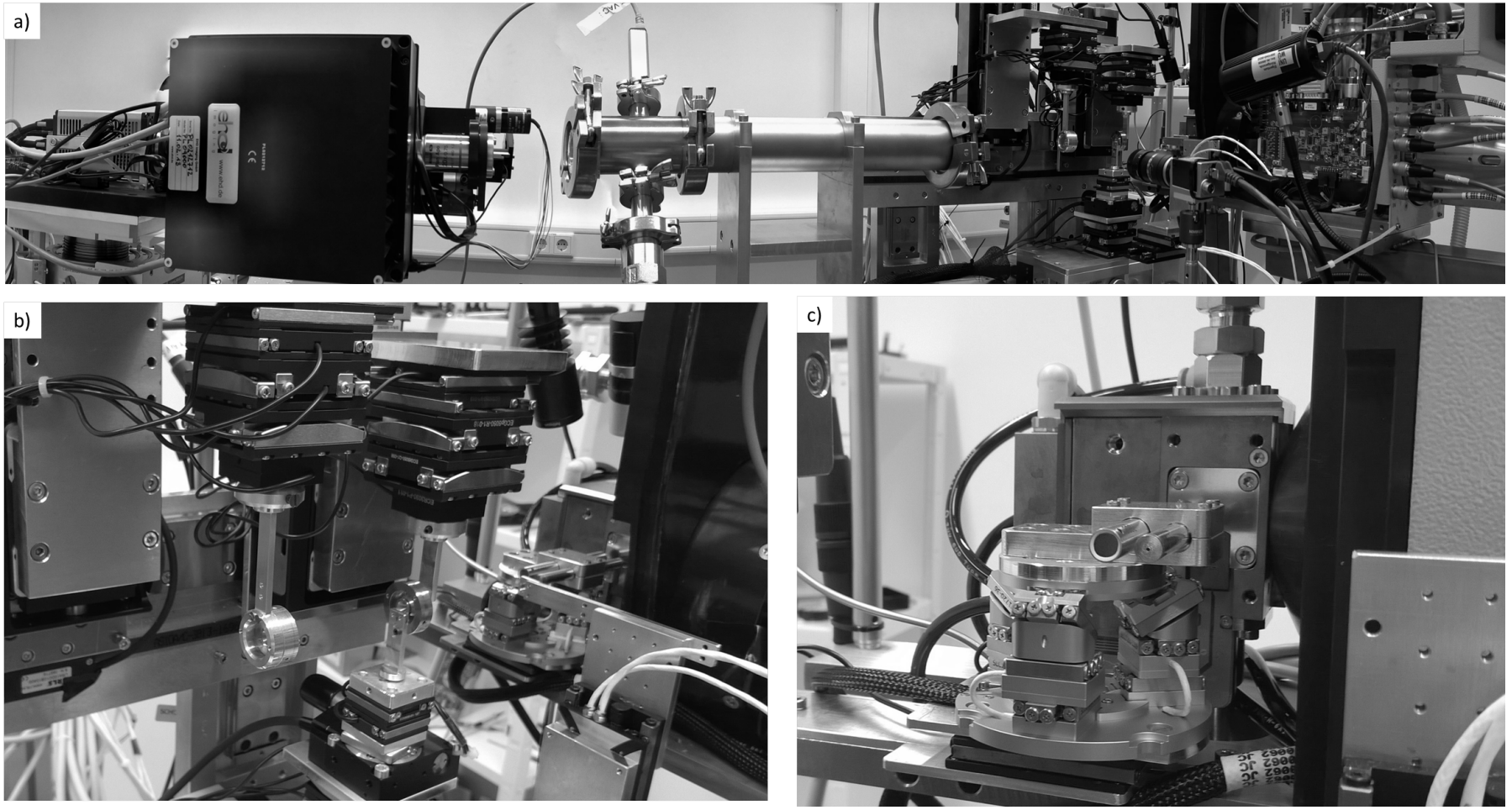

FIGURE 5.11: Pictures of the setup. a) Complete optical path, b) mounting of the zone plate, object, pinhole and beamstop, as well as c) poly- and monocapillary mounted on a hexapod.

5.2.4 Results

In order to demonstrate the capabilities of the here developed X-ray microscope, in this section X-ray images of resolution targets are presented, together with a CT scan of a real sample. Afterwards, also possible future optimization steps are discussed.

Resolution targets Figure 5.12 shows a comparison between X-ray images of a resolution target, recorded with and without magnification (see also chapter 4). The object is a commercially available Siemensstar, which is fabricated similarly to the zone plates with e-beam lithography. It consists of 1.5 μm thick tungsten and has a diameter of $\sim$52 μm. The features in the center have a width of 500 nm. On the first view, it can be clearly seen that while the small structures are blurred in the image without optics, they can be resolved when using optical elements.
For imaging with the zone plate, the magnification is $\sim$11, leading in combination with the 1.332 μm pixel width to a sampling of 122 nm. The 600 s exposure time results in a *SNR* of about 50-80; the variation in the determination of the *SNR* results due to long exposure times from the non-uniform illumination and dark noise.

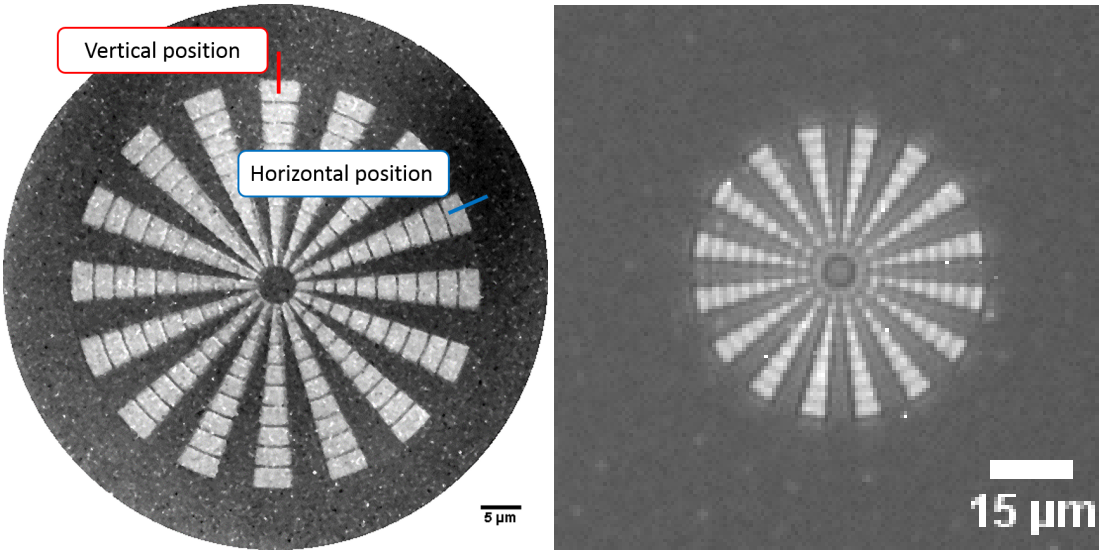

(A) (B)

FIGURE 5.12: Comparison of two images taken from a Siemensstar. a) Image taken with a magnification of 11 due to the usage of a zone plate. b) Image of the same object taken with the highest resolution ($\sim$1 μm) without X-ray optics. The Siemensstar posseses a diameter of 52 μm and finest features of 500 nm in the center.

From the image, line plots and the corresponding *MTF* can be extracted, as depicted in Fig. 5.13 exemplarily for two positions and different directions (marked in Fig. 5.12a). Following the scheme given in section 4, first the derivative of the gray values along the line profiles is calculated; the Fourier transform of the derivative (or of its Gaussian fit) then shows the *MTF*. The resolution along the horizontal and vertical direction differs, which can be also seen directly

in the image. Along the horizontal direction, the 10% *MTF* is 2900 lp/mm; this corresponds to 344 nm per line pair or 172 nm per pixel, which is close to the sampling of 122 nm. Therefore, the blurring is around 1.4 pixel. For the vertical direction, the *MTF* delivers a value of 2200 lp/mm or 454 nm per line pair, corresponding to ~ 1.8 pixel. One possible reason for the different resolution along the two directions might be a one-dimensional movement or vibration during the exposure. Moreover, the reason might be also a weak tilt of the zone plate, leading in one direction to an effectively smaller *NA* as the outer zones get inefficient.

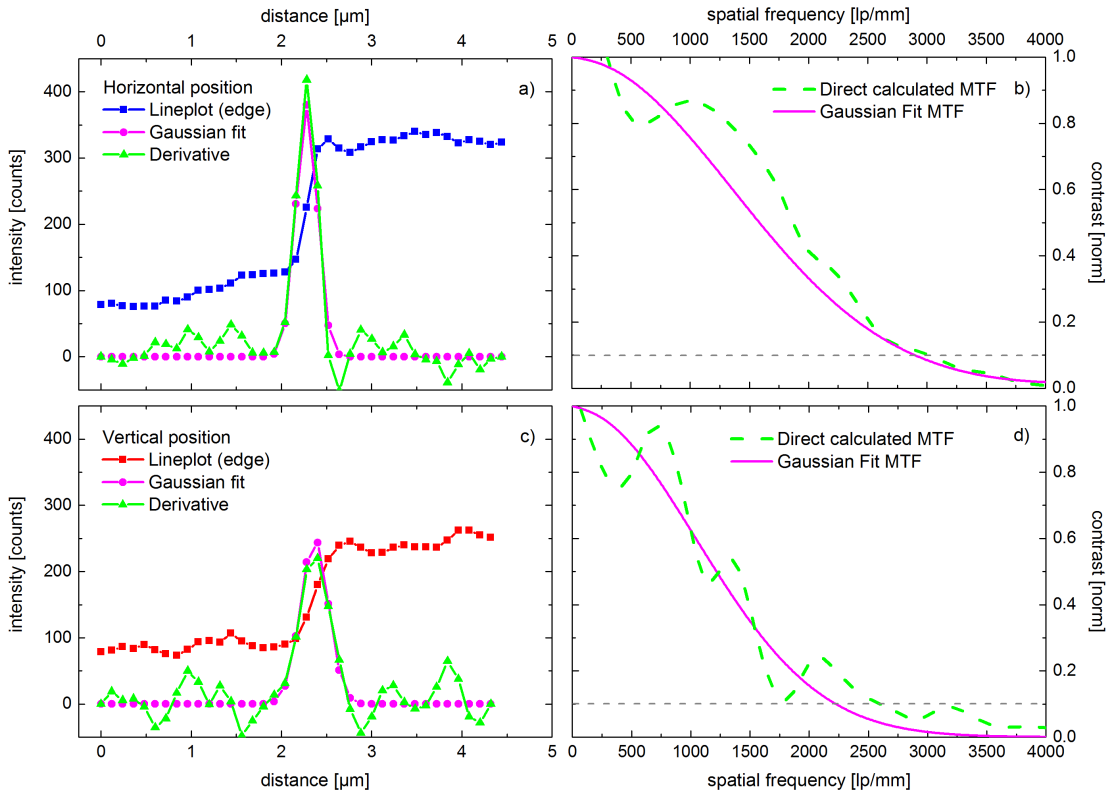

FIGURE 5.13: Line profiles of the gray values marked in Fig. 5.12 along a) the horizontal and c) the vertical direction. From this, the derivative (green) and its corresponding Gaussian fit (pink) are calculated. Their Fourier transform denotes the *MTF*, shown in b) and d), respectively. For the horizontal direction, one obtains a resolution of 2900 lp/mm; for the vertical direction of 2200 lp/mm.

The estimation of the resolution in Fig. 5.13 was not done for the smallest pixel sampling, because the edge fit requires sufficient contrast or a good enough *SNR*. Since the *SNR* scales linearly with pixel-size, at a certain point the edge fit shows values which deviate too strongly to deliver a reliable value. Nevertheless, despite the high noise level, the eye can still distinguish small features.

To overcome this, Fig. 5.14 shows X-ray images of a high-resolution Siemensstar with 150 nm center bars, together with SEM images. The smallest, inner structures can be still resolved in the X-ray images. Thus, Fig. 5.14 shows the highest resolution so far achieved with the here presented setup, sampled with 61 nm on the object. Fig. 5.14a and c depict uncorrected raw

images with an exposure time of 600 s and 3600 s respectively. For longer acquisition times, the *SNR* is enhanced. Meanwhile, asymmetries in the intensity distribution and weak tangential smearings become more pronounced, which are caused probably by slight movements of one or more elements.

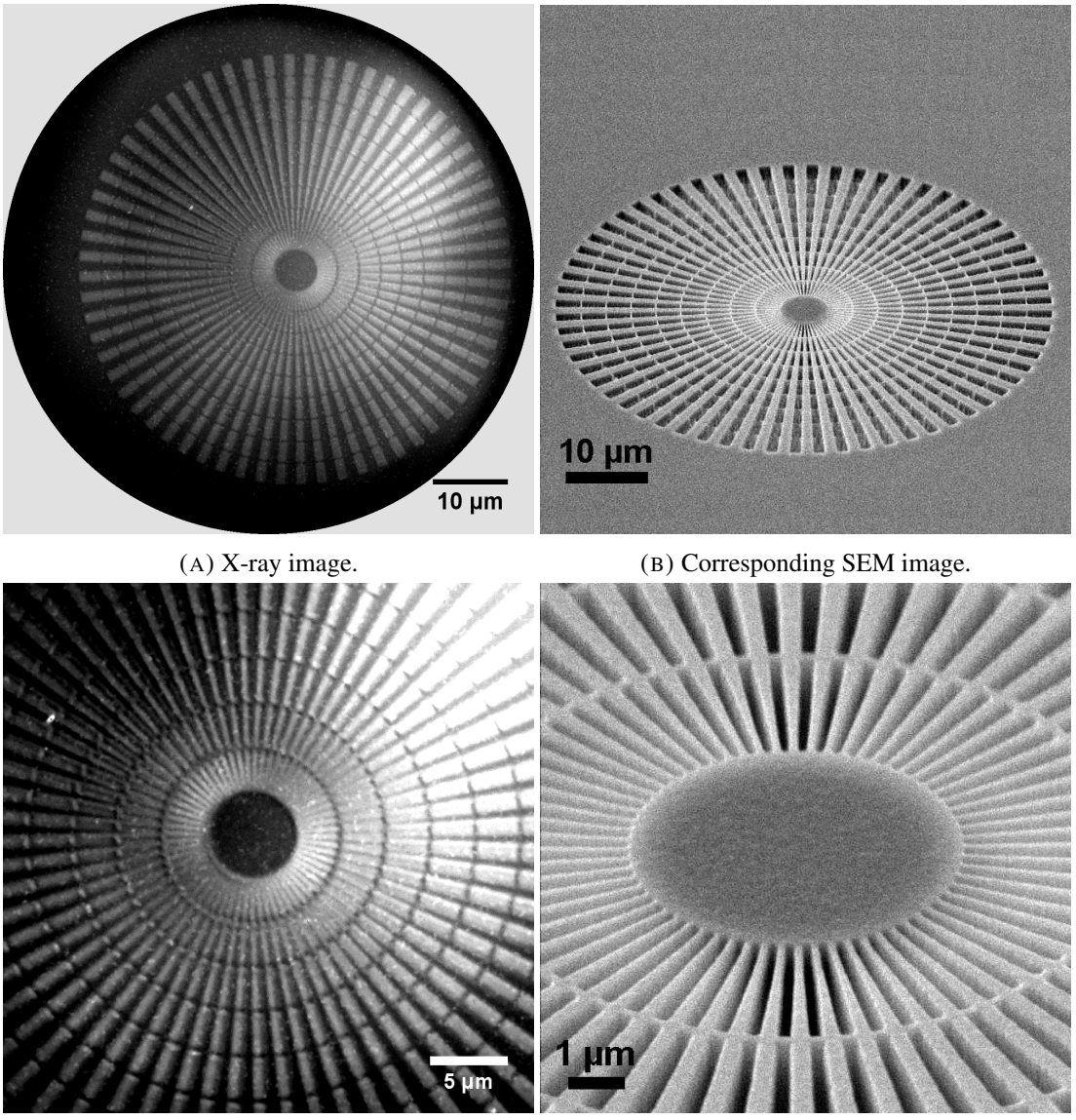

(A) X-ray image. (B) Corresponding SEM image.

(C) Zoomed X-ray image. (D) Corresponding zoomed SEM image.

FIGURE 5.14: X-ray and SEM images of a Siemensstar with 150 nm center bars. The smallest, inner structures can be still resolved in the X-ray images with a) 600 s and c) 3600 s acquisition time.

As mentioned in section 5.2.2, the illumination characteristic of poly- and monocapillary differs in the illuminated area, flux and angular distribution. While for the monocapillary a smaller area is illuminated and the blocking of the background intensity is more efficient, the polycapillary delivers a larger and more homogeneous area at the sample plane. However, the exposure time for the same signal (*i.e.* intensity minus background) is a factor of 2-4 longer; the factor varies between 2 and 4, because the illumination for the monocapillary is inhomogeneous. Thus,

higher acquisition times are needed when working with the polycapillary and slight instabilities play a bigger role.

Thus, it is not surprising that the resolution obtained with the polycapillary is sightly lower, as shown on the basis of Fig. 5.15: with the polycapillary, the inner 150 nm bars of the Siemensstar are not resolved, although in principle the resolution should not depend on the condenser. Despite the reduced resolution, a positive side effect is that the field of view is enlarged from approximately 50 μm to 100 μm.

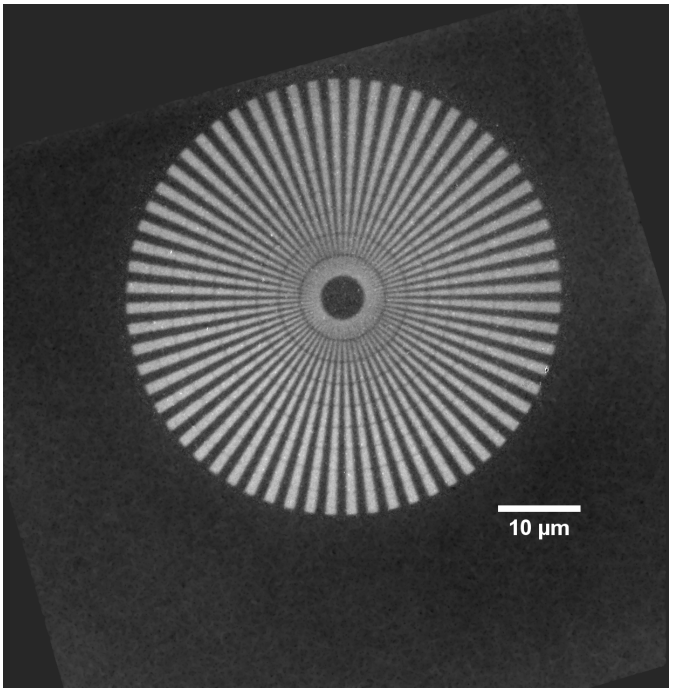

FIGURE 5.15: Siemensstar imaged with the polycapillary as condenser. The illumination is much more homogeneous, although the field of view is larger than 100 μm (the tilted rectangle is a 100 μm aperture in front of the object). In comparison to the monocapillary (see Fig. 5.14), the signal (contrast) is around 2-4 times smaller for the same acquisition time of 3600 s, although the images where taken with a similar object sampling (66 nm and 61 nm) and with the same zone plate.

Real samples Besides the resolution targets with their nearly ideal structures, also real samples were imaged using the X-ray microscope. Figure 5.16a shows the edge of a thin section of human tooth dentin. One can clearly see the tubular structure, where the tubes measure between 1-2 μm in diameter. Moreover, Fig. 5.16b depicts a ternary mixture of aluminium, germanium and silicon. The different phases of the mixture are clearly visible. The image was taken with an object sampling of 135 nm, an X-ray magnification of 4.5, and 620 nm detector pixel size. In total, twenty 30 s images were averaged, resulting in a total exposure time of 600 s with the Zyla camera. The source was set for both images to a 80 μm$\times$20 μm spot with an electron power of 200 W.

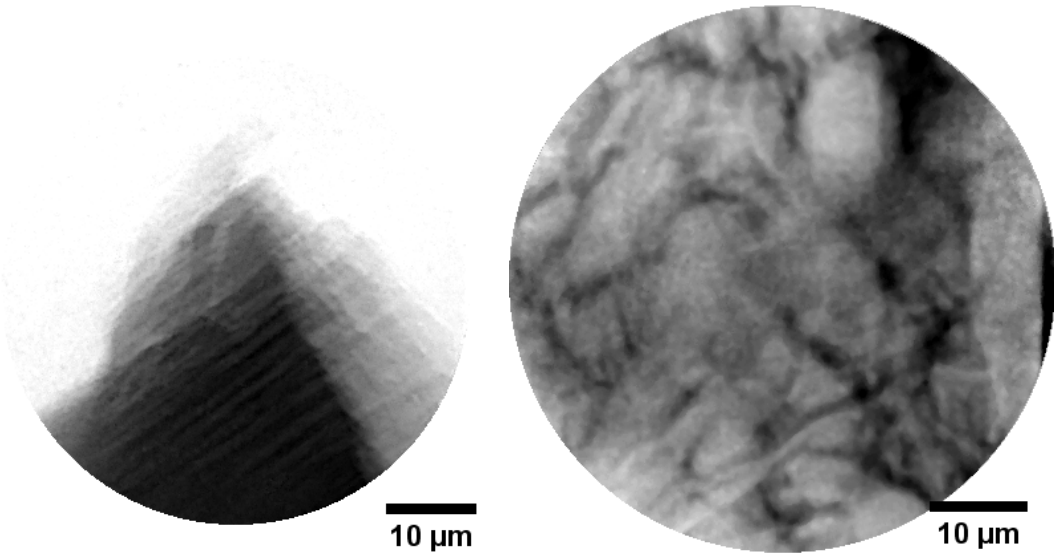

(A) (B)

FIGURE 5.16: Examples for X-ray TXM images showing real samples. a) Edge of a thin section of human tooth dentin. The small features are the tubular structure, where the tubes measure between 1-2 μm in diameter. The exposure time here was 1800 s for a pixel sampling of 147 nm. b) Tertiary mixture of aluminium, germanium and silicon. The pixel sampling on the sample is around 135 nm with an X-ray magnification of 4.5 and a pixel size of 620 nm at the detector; the exposure time was 600 s, using the Zyla camera. The source was set for both images to a 80 μm$\times$20 μm spot with an electron power of 200 W.

Already in the case of the two-dimensional resolution target, the depth of focus (*DOF*) of the zone plate has to be considered. For imaging a 3D object, this expansion in beam direction is even more important. For a parallel beam focused by a zone plate, the intensity is decreasing with increasing distance Δz from the focal plane. The distance, where the intensity is 80% of the maximum intensity in the focal plane can be calculated as [29]:

$$\Delta z = \pm \frac{1}{2} \frac{\lambda}{(NA)^2}. \tag{5.5}$$

This intensity gradient induces a broadened focus, and thus a reduced resolution when using the zone plate for magnification. Therefore, the thickness of the sample should stay below this *DOF*; otherwise, outer parts of the sample blur the image. This effect dramatically limits the size of samples for tomography. For the zone plates currently used for imaging with 50 nm outermost zone width, one can calculate $2\Delta z \cdot DOF = 74.6\,\mu$m.

It should be noted that this limit cannot be extended via region of interest (ROI) scans like in projection geometry, as these scans for samples larger than the field of view differ fundamentally concerning the collected data. Although here parts move out of the *FOV* for different angles, in each single projection the imaged parts of the sample are superimposed, but not blurred. Instead, several approaches exist to overcome the problem of a finite zone plate *DOF*. They are all based

on the fact that the signal created out of focus is weaker; this allows the reconstruction of a partial volume out of a stack of different focal planes [12, 151].

To validate the full functionality of the setup, a CT scan of the tip of a damaged injection cannula was used. As at the time of this test the FIB was not available to cut a sample to the desired shape, the needle was one of the few available objects which matches the *FOV* of the microscope. Figure 5.17 shows exemplarily a single projection, together with the reconstructed volume. The exposure time was set to 360 s per image with a pixel sampling of ∼147 nm. The pixel size on the detector was 1.33 μm (2 × 2 binning), the X-ray magnification ∼9. The measured *SNR* in the flat-field region of the projections is ∼ 75. This was possible by running the source with 200 W on a 46 μm × 16 μm X-ray spot, which is above the manufacturer's recommendations. For the CT scan, 432 projections, as well as 4 flat-field and 2 dark images were recorded, leading to a total acquisition time of 44 hours. It should be noted that the spatial stability was very good, so that only small corrections with auto-correlation were needed for reconstruction. The flat-field correction worked quite good for all projections, meaning that the changes of the illumination profile was weak during the whole acquisition time; this further proofs sufficient thermal and source stability. Since the object consists of steel, the reconstruction shows metal artifacts, which were corrected numerically.

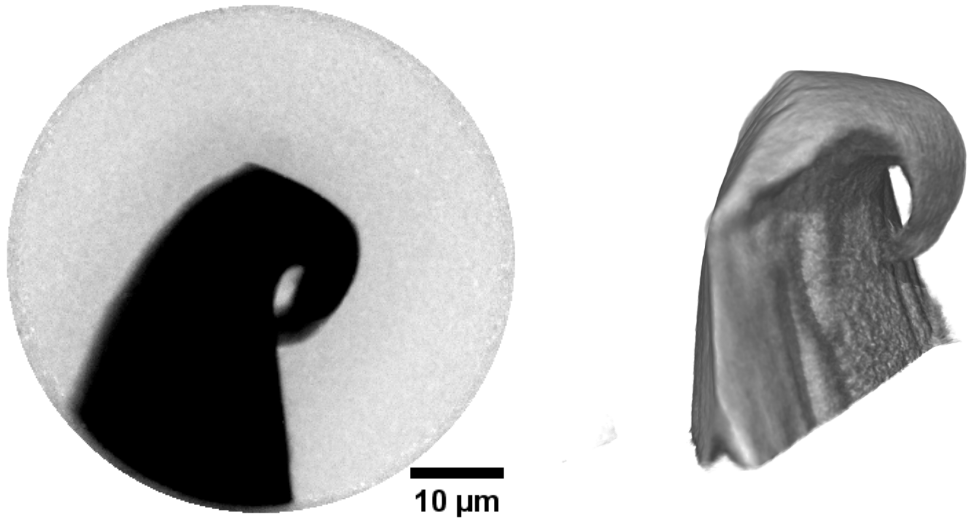

(A) (B)

FIGURE 5.17: Bent tip of a cannula imaged with the X-ray microscope. Both, a) radiograph and b) 3D rendering clearly show the twisted steel cannula tip. The tip diamater is in the range of 4 μm. The sampling was set to 147 nm at the object plane; the acquisition time for a single projection was 360 s, leading with 432 projections as well as 4 flat-field and 2 dark images to 44 hours total acquisition time.

The result demonstrates a clear twist of the cannula's tip, which occurred when the needle dropped once on the floor. On the one hand, the mechanical damage is remarkable and clearly

shows why cannulas should be replaced each time they sensed even small forces. On the other hand, this CT scan demonstrates the full functionality of the X-ray microscope.

5.2.5 Discussion

In this section, the results obtained so far are first discussed in the context of other microscopes based on laboratory sources and zone plates. Afterwards, the exposure time is compared to the non-optic mode.

Rating The *800 Ultra microscope* from *Zeiss* (former *Xradia*) which is commercially available for approximately 2 Mio US$ works on basis of the same principle as the here presented setup, using a monocapillary and a zone plate. The main difference is the source, which is an 8 keV rotating anode *rigaku micro max 007* [35]. The following comparison is based on reported values in Refs. [24, 151, 152].
Despite the higher brightness of the liquid-metal-jet source, the exposure times are longer and the resolution is lower for the here-built instrument (150 nm compared to 50 nm). The reason for this is mainly the quality of the optical elements, especially their accessibility and their costs. The zone plates used by *Zeiss* possess a smaller outermost zone width $\Delta r = 35\,\mathrm{nm}$; moreover, they are stacked and reach a thickness of 1400 nm. This leads to about twice the *NA* and an efficiency of $>12\ \%$ [151], resulting in a flux which is enhanced by a factor of 6. Furthermore, their condenser possesses an efficiency of up to 90%, and thus a further gain of flux by a factor of 3-4. Moreover, their detector performs with a sightly higher *DQE*, mainly because of the lower X-ray energy of 8 keV. Summing up, these advantages overcompensate the higher brightness of the liquid-metal-jet source. Comparing however the financial restrictions, the here-built setup yields good results.
Another microscope developed by Baumbach *et al.* [153, 154] outlines the importance of the liquid-metal-jet source for this success. While similar optics are used compared to our polycapillary setup, their source possesses a lower brightness (by approximately a factor of 10). However, their detector has a much higher *DQE*, namely $>80\%$ compared to 54%. Nevertheless, the better detector can not compensate the advantage of our highly brilliant source, leading to the need of very high exposure times around 6 hours for a single image.

Outlook With the here presented X-ray microscope based on Fresnel zone plates, it was demonstrated that structures with a size of 150 nm can be well resolved. However, the resolution reached so far is still below the theoretical value. In principle, three reasons might be responsible: most likely, mechanical vibrations and a thermal drift limit the resolution in reality; both influences become less critical for shorter exposure times. Secondly, it is likely that the outer zones of the utilized zone plate do not contribute at all or at least less efficiently for the

image formation. Therefore, novel fabrication techniques (as discussed in section 5.2.1) are very important for further improvements. Finally, also spectral blurring due to the influence of radiation at other wavelengths should be considered. For an optimal imaging, in principle radiation of a single energy would be desirable; other parts of the spectrum - such as the Bremsspectrum or fluorescence lines (tungsten: 8.4 keV and 9.6 keV) - blur the image. In this regard, the narrow natural width of the Ga K_α-line is favorable. Moreover, the Ga K_β-line can be in principle blocked using the absorption edge of a Zn filter; however, this appears also on the expense of an intensity loss of the K_α-line. The problem of spectral blurring could be overcome when using multilayers as condenser.

Comparison Finally, the two modes of the setup - with and without optical elements - can be also compared quantitatively in order to visualize the principal differences of the two approaches. In table 5.4, the photon flux per pixel of both acquisition modes is first estimated from the brightness of the source, the geometry and the total transmission of the beam path (efficiency and absorption) by using equation 2.7; afterwards, also the measured photon flux is given.

For the estimation of the projection-based setup, the relevant area is the source size; the solid angle is given by the *SDD* and the detector pixel size. In contrast, the limiting area for the estimation of the optics-based approach is given by the object pixel size and the solid angle of the zone plate. Additionally, the solid angle is reduced by the hollow cone of the condenser illumination. The transmission T is the product of absorption in air and the efficiency of the optical elements. While the efficiency for the projection-based setup (without any optical element) is one, for the optics-based setup it is composed of 6.7% efficiency of the zone plate (measured) and 30% of the condenser (estimated from the comparison with the simulation). Moreover, for the absorption in air, the shorter distance of the projection-based setup is favorable; thus, to reduce the length of the optics-based setup, a flight tube was utilized, which possesses 20 μm windows that further need to be considered.
In total, this estimation yields for the projection-based setup 770 photons, which reach per second and pixel the detector; for the optics-based setup, only 35 photons reach a detector pixel per second. One should note that the pixel size utilized for this estimation is the real size, which is roughly 9 times larger for the optics-based setup (1330 nm vs. 150 nm).

To verify this estimation, the photons were determined in two ways from recorded images. On the one hand, the counts (minus background) per second and pixel were determined and converted to photons by the factor 0.8, as described in chapter 4.1.1. On the other hand, the number of photons were calculated indirectly by measuring the *SNR* and dividing its squared value by the exposure time. In both cases, the thus detected number of photons was then divided by the *DQE* to obtain the number of photons which reach the detector. For the optics-based setup, both methods yield values which are in good agreement with the estimation; for the

	Projection-based without optic	**Optics-based** with zone plate
Pixel size	$(1330\,\text{nm})^2$	$(150\,\text{nm})^2$
Brightness	$2.6 \times 10^{10} \frac{N}{\text{mm}^2 \cdot \text{mrad}^2 \cdot \text{line} \cdot \text{s}}$	
Solid angle Ω	$2 \cdot \tan^{-1}(\frac{0.00066}{136})$ $= 9.43 \times 10^{-5}\,\text{mrad}^2$	$2 \cdot \arctan(\frac{0.09}{72}) = 6.2\,\text{mrad}^2$ $6.2\,\text{mrad}^2 - 1.2\,\text{mrad}^2 = 5\,\text{mrad}^2$
Area A	$(10\mu\text{m})^2\pi = 3.142 \cdot 10^{-4}\text{mm}^2$	$(150\text{nm})^2 = 2.25 \times 10^{-8}\text{mm}^2$
Efficiency η	1	$0.067 \cdot 0.3$
Absorption b	0.9	0.6
	136 mm air	600 mm air + 20 μm PET
Photon flux estimated	**770 N/s**	**35 N/s**
DQE	0.54 @ 9.25 keV	
(i) Detected counts	7850 / 15 s = 523 /s	4800 / 360 s = 13 /s
Detected photons	654 N/s	16 N/s
Photon flux	**1211 N/s**	**30 N/s**
(ii) *SNR*	95	76
Detected photons	602 N/s	16 N/s
Photon flux	**1115 N/s**	**30 N/s**

TABLE 5.4: Comparison of the photon flux between projection- and optics-based acquisition mode of the here-presented setup: estimation (top) based on the brightness of the source, the geometry (solid angle and area) and the total transmission of the beam path (efficiency and absorption), as well as measurements (bottom) based on (i) the detected counts and (ii) the *SNR* of recorded images. For (i), the counts (minus background) per second and pixel were converted to photons by the factor 0.8 (see chapter 4.1.1). For (ii), the number of photons were calculated indirectly by measuring the *SNR* and dividing its squared value by the exposure time. The photon flux then originates from a division with the *DQE*.

projection-based setup, the underestimation of 35% results from the other parts of the spectrum (besides the Ga K_α-line), which also contribute to the spectrum.

In total, the photon flux per second and pixel is roughly a factor of 40 higher for the projection-based setup. However, this does not take into account the size of the pixel areas, which differ by a factor of about 80. Therefore, the optics-based setup is in total more efficient. This means that the low efficiency of the optical elements can be overcompensated by a large solid angle. Thus, there is still room for improvement for the projection-based setup, for instance by reducing the *SDD* to enlarge the solid angle.

5.3 Magnification by compound refractive lenses

Using compound refractive lenses (CRLs) is the second approach to produce magnified images, which was investigated in the framework of this thesis. In the 9 keV energy range, CRLs which are fabricated today can not compete in terms of resolution and related throughput with zone plates, with the latter being more prominent for laboratory microscopes. However, at larger energies - *e.g.* 24 keV for an indium rich alloy - the CRLs overcome the performance of zone plates. Furthermore, their fabrication is much more reproducible and faster than for zone plates, in particular with high aspect ratios. In this context, "faster" means that X-ray lithography is a fabrication technology, where once the absorbing mask is produced, many lens stacks can be fabricated in parallel. Thus, the here-presented measurements can be used as an estimate for the performance and exposure times which could be reached by a liquid alloy with high indium content. Such an alloy would require to heat the liquid metal jet cycle, which was already successfully tested at the *KTH* without general problems.

The use of this second class of optical elements was possible due to a granted proposal at the *Karlsruhe Nano Micro Facility (KMNF)*. The CRLs are fabricated with X-ray LIGA by *A. Last* from the *Institute of Microstructure Technology* at the *KIT*. LIGA is the German acronym for "Lithography Galvanise and Abformung" (*i.e.* casting). For the here used CRLs, only the first step was used (*i.e.* lithography with X-rays), since the resist SU-8 itself is the material of which the lens consists. For the fabrication process, first a mask has to be produced by electron lithography. After developing the resist, it is galvanised with some micrometer gold to provide a sufficiently thick absorber for the X-ray exposure.
In order to show that SU-8 is the right choice for refractive lenses, Fig. 5.6 displays the real and imaginary part of its refractive index, which is related to the numerical aperture of the CRL via:

$$NA = \frac{D_{\text{eff}}}{2f} = \sqrt{\frac{\delta}{f\beta}\pi\lambda} = \sqrt{2\pi\frac{\delta^2\lambda}{R\beta}} \tag{5.6}$$

Thus, to reach a sufficient numerical aperture, the fraction of δ/β should be large and the radius R should be small. Therefore, a material with low Z is favorable and one should be able to fabricate lenses with small R as well as a parabolic shape to avoid aberrations. The first criterion is best fulfilled by Beryllium [155], however, this is a highly toxic material which can not be fabricated with small radii. Besides this, a suitable material should also provide a small angle scattering cross section [69], a good chemical and mechanical stability, as well as a high persistence when being exposed to the X-ray beam (which is relevant for high flux synchrotron measurements). Since for the here investigated CRLs a negative resist is used, the stability is in principle given, although SU-8 can not reach thermal stability like beryllium or diamond. Moreover, it was tested to be stable up to radiation doses of 10 MJ/cm [156].

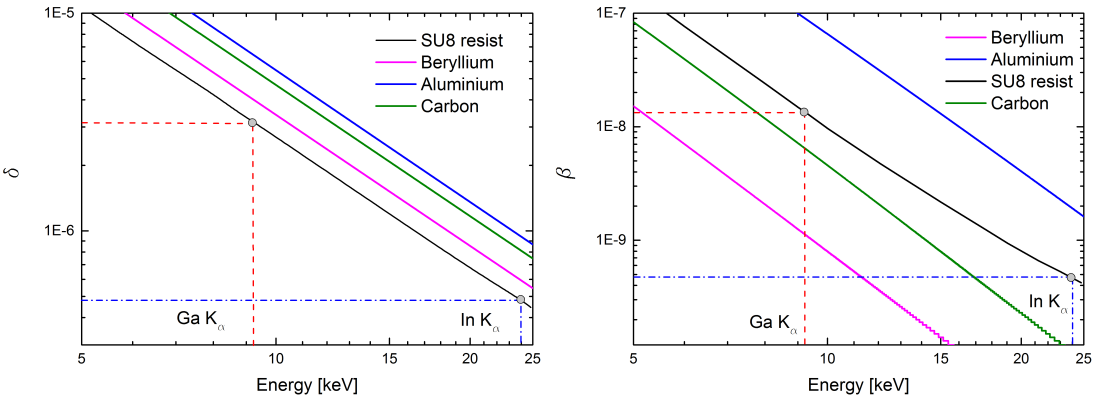

FIGURE 5.18: a) Real and b) imaginary parts of the complex refractive index of SU-8 resist and alternative materials (aluminum, beryllium, carbon).

The lenses fabricated for the here presented experiments are listed in table 5.5. Key design parameters are their smallest radius and the number of elements. Here, the smallest radius of 6 μm is given by the LIGA process; for smaller radii, the quality decreases. From this radius, the number of elements is set to 15 to reach the desired focal length. Therefore, the optimal design for a 9 keV SU-8 CRL is relatively fixed. CRL 1 and CRLs 2-3 differ by the first and last lens, which are optimized in the latter cases to compensate for aberrations. This compensation is necessary due to the two combined 1D stacks. The focal length was chosen to be able to magnify in a compact setup, as well as to have comparable length scales to the zone plates.

	Radius R	Efficiency η (theo)	Lenses N	Focal length f	Eff. aperture D_{eff}	Length L
CRL 1	6 μm	28%	15	62.5 mm	60 μm	5.4 mm
CRL 2	6 μm	28%	15	64.6 mm	60 μm	6 mm
CRL 3	6 μm	28%	15	64.6 mm	60 μm	6 mm

TABLE 5.5: Parameters of the used CRLs. CRL 1 and CRLs 2-3 differ by the first and last lens, which are optimized in the latter cases to compensate for aberrations.

5.3.1 Prism condenser

The condenser originally intended to be used for the CRLs setup is a so-called X-ray prism condenser (XPL) [157]. It consists of thousands of small prisms which are arranged in a V-shape to focus light. The focusing is one-dimensional. Thus, similar to the CRLs, two XPLs need to be placed behind each other in a crossed configuration.

However, the prism condenser designed and fabricated for the setup does not provide sufficient flux. Fig. 5.19c shows the resulting illumination profile at the sample position. The intensity is too low for any full-field imaging. Furthermore, the *FOV* or illuminated area was smaller than expected from the design. It is not clear why the flux is too low. One reason might be that some of the prisms appear damaged and misplaced, as can be seen by light microscopy: whereas the

center part shows a regular shape (see Fig. 5.19a), at the outer regions without metal stabilizers the prisms are displaced (see Fig. 5.19b).

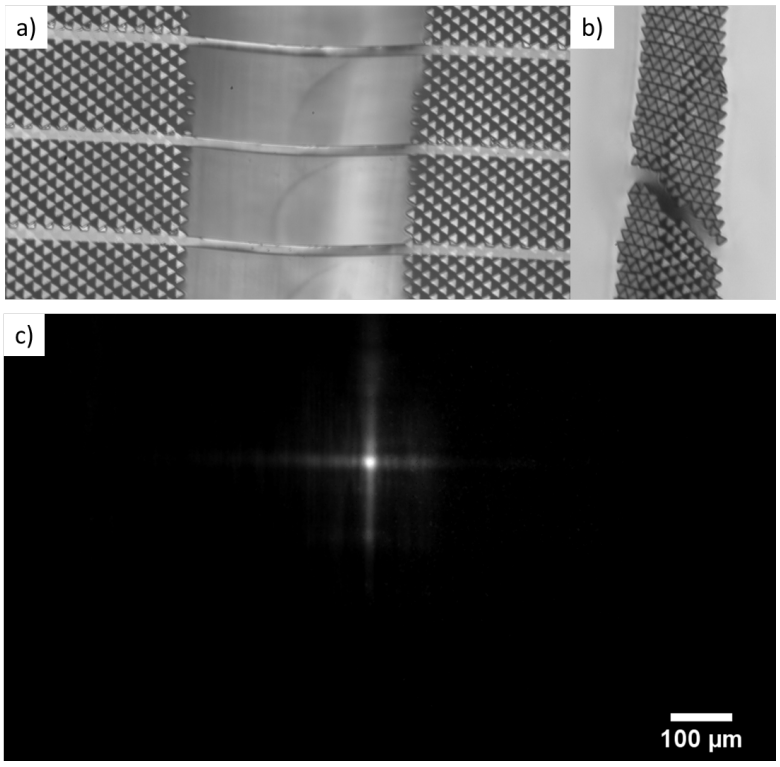

FIGURE 5.19: Light microscope images of the prism condenser produced for the setup: a) center part and b) end part with displaced prisms. c) Illumination profile at the sample position. The intensity was too low for any full-field imaging.

To demonstrate nevertheless a pure refractive microscope, a second CRL was used as condenser. However, as this possesses a smaller field of view, also the polycapillary was used for imaging. Both results are presented in the following.

5.3.2 Results with compound refractive lenses

The alignment of the refractive lens stack differs from that of the zone plate, as the CRLs are extended along the beam direction. When placing the detector close to the lens, the outer sidewall can be used for alignment, until the edges of the single lenses overlap and do not longer show up separately as stripes (see Fig. 5.23). Further fine-alignment can be done by maximizing the flux without the condenser at a detector position, where the lens demagnifies the source.

Efficiencies In order to provide - besides the measurement of images (*e.g.* of a resolution target) - an absolute comparison of the performance of the CRLs to the zone plates, the direct imaging of the source spot was done without condenser. This rules out the effect of a differently aligned condenser or a different matching of the illumination profile to the optical element. For

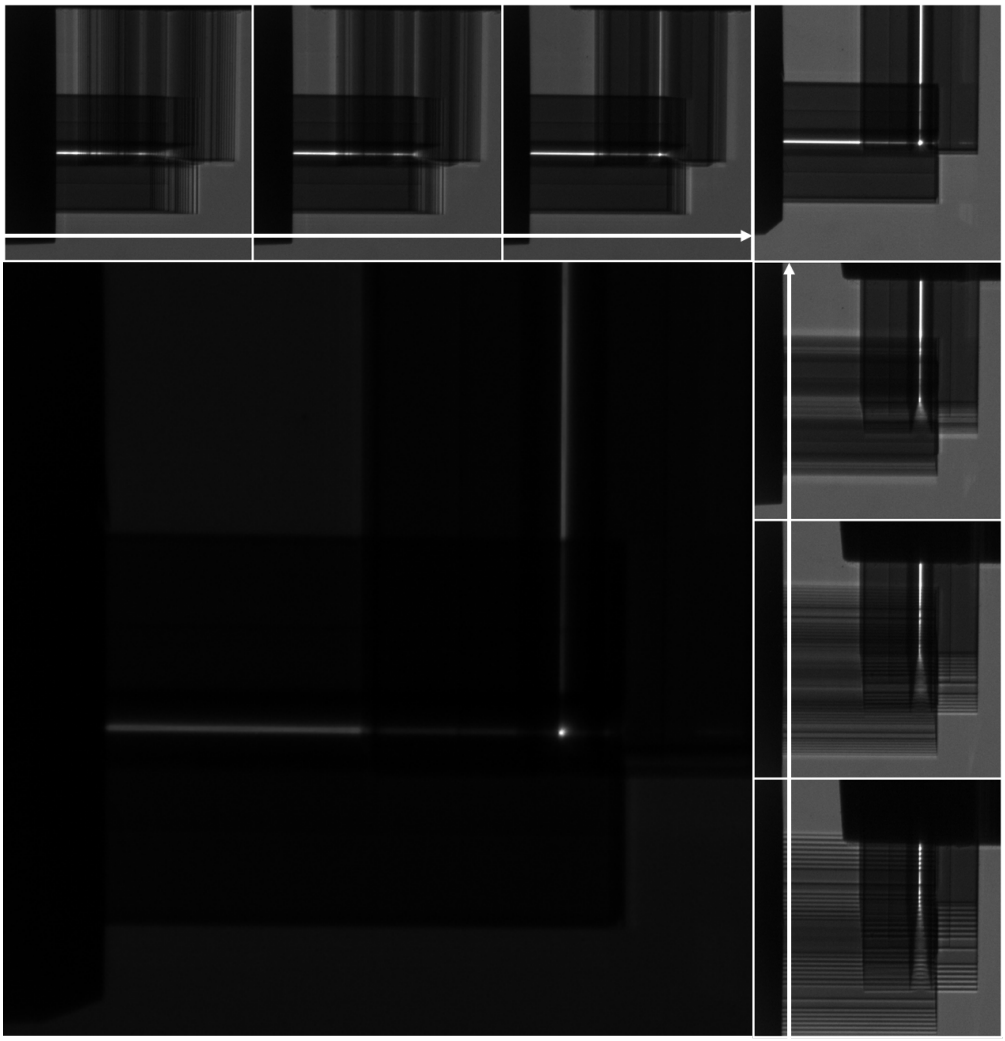

FIGURE 5.20: CRL alignment. When placing the detector close to the lens, the outer sidewall can be used for alignment, until the edges of the single lenses overlap and do not longer show up separately as stripes. While the upper images display the influence of rotating the lens holder in 0.3° steps (in the experiment, usually 0.05° steps are chosen), the side images depict the effect of misaligning the yaw of the holder.

instance, the zone plate works good with hollow cone illumination, whereas the CRLs should be illuminated with a full cone.

For imaging the spot, equal magnifications and source settings were used for CRLs and zone plates. As due to different focal lengths the total sample-detector distance differs, also the absorption in air varies. However, this effect is below 5% and hence does not change the qualitative result. The measured values are summarized in table 5.6, with the first row giving the maximum intensity in counts. Already from the counts, one can see that the performance of the zone plates in terms of flux is around a factor of two better. From the well-known product of efficiency and squared *NA* of the zone plates, these counts can be used to calculate this product also for the CRLs. With knowing the *NA* of the CRLs, finally their efficiencies are estimated (see table 5.6). Indeed, the thus determined experimental values are close to the theoretical ones. While the

CRLs possess a small *NA*, they possess (in theory as in reality) a high efficiency which can partially compensate for the smaller *NA*. Such a combination of high efficiency and small *NA* can be useful for reaching low resolutions (*e.g.* 200 nm - 500 nm). Moreover, with the here utilized CRLs, larger samples can be imaged, since their *DOF* is more extended than for the zone plate. Finally, for the CRLs no beam stop is needed (in contrast to the zone plates); thus, the full cone can be used, leading to a higher total flux.

	CRL1	**CRL2**	**ZP5W**	**ZP6W**
measured counts	13450	12180	22891	19120
$NA^2 \times \eta$	$5.8 \cdot 10^{-8}$	$5.29 \cdot 10^{-8}$	$1.18 \cdot 10^{-7}$	$0.88 \cdot 10^{-7}$
NA	0.00048	0.00046	0.00134	0.00134
fill factor	100%	100%	∼80%	∼80%
measured efficiency	25.4 %	25 %	6.6%	4.9%
theoretical efficiency	28%	28%	21.5%	21.5%

TABLE 5.6: Comparison of the performance of CRLs and zone plates at 9.25 keV, based on direct imaging of the source spot. As can be seen from the measured counts (first row), the flux is around a factor of two better for the zone plates. From the well-known $NA^2 \times \eta$ - product of the zone plates, these counts can be used to calculate this product also for the CRLs. With knowing the *NA* of the CRLs, finally their efficiencies result, which are very close to the theoretical ones. One further difference between both lens types is the fill factor: while for CRLs, the full cone can be used for illumination, ZPs need a central beam stop.

Imaging with refractive elements The first imaging of a sample by using only refractive optical elements was done via two similar CLRs, which were used as condenser and magnifying lens. This has naturally the disadvantage that for optimum illumination - which matches the *NA*, *i.e.* the beam path is symmetric with respect to the sample position - the *FOV* is reduced by the magnification factor. For larger *FOV*s, the illumination is not optimal.

In the experiment, such non-optimal illumination was used to image a Au grating with 2.4 μm period; the results are shown in Fig. 5.21. The measurement parameters were a sampling of 200 nm and a 3× magnification by the CRLs. Moreover, the condenser lenses were placed to refocus the source with a magnification of one; thus, the field of view corresponds to the source size of around 20 μm. The exposure time was set to 600 s for a source power of 200 W and 70 keV maximum acceleration voltage.

Furthermore, by translating and rotating the objective lenses out of the direct beam (with the CRL still being aligned with the sample), it was possible to demonstrate the appearance of a so-called darkfield image [153]; it results from the fluorescence of the Au L_α-line at 9.71 keV. In this image, the grating appears inverted, since the origin of the radiation is the grating itself. The reason for the surprisingly high intensity is that the energies of the Au L_α- and Ga K_α-lines

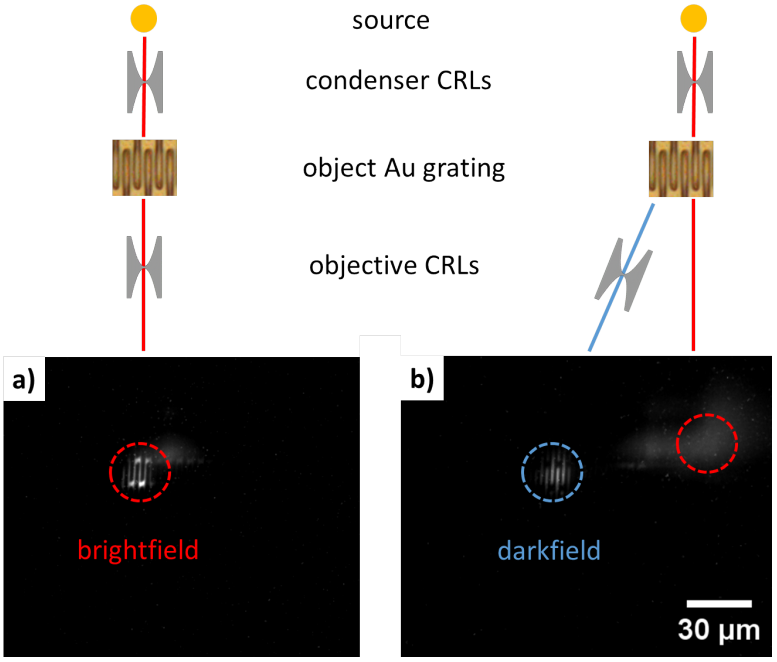

FIGURE 5.21: a) Bright- and b) dark images of a Au grating with 2.4 μm period, taken with a sampling of 200 nm, a 3$\times$ magnification by the CRLs, and a 1$\times$ magnification of the condenser lenses. The exposure time was set to 600 s for a source power of 200 W and 70 keV maximum acceleration voltage.

are very close to each other, corresponding to similar geometrical distances such as the focal length. Unfortunately, such strong fluorescence might have a negative impact on the resolution of the standard (brightfield) image.

Imaging with CRLs and polycapillary To overcome the small *FOV*, for the next images the polycapillary was used as condenser, leading to a large *FOV* of approximately 100 μm. Fig. 5.22 shows a gold test pattern (produced with LIGA) used for determining the *MTF* with bars down to 1 μm, together with the light microscope image of the used CRL stack with alternating crossed lenses. The object sampling was set to 150 nm with an exposure time of 1800 s. The resolution obtained for 10% contrast is with 1150 lp/mm (corresponding to 434 nm per pixel) lower than expected: the measured blurring is around 3 pixel.

However, focusing is always difficult with a test pattern which possesses larger features than the desired resolution. Therefore, the Siemensstar with the smallest features of 150 nm was imaged with a pixel sampling of 55 nm, an exposure time of 2400 s and the CRLs magnification of 12. Indeed, even the inner features can be still resolved. Thus, the here presented setup shows in combination with CRLs much higher resolutions than published up to now [158–161]. For instance, the microscope of Gary *et al.* [158] uses a multilayer condenser and a CRL made of 92 plastic elements (containing only hydrogen and carbon) for 8 keV radiation; they demonstrate a best resolution of around 1.1 μm.

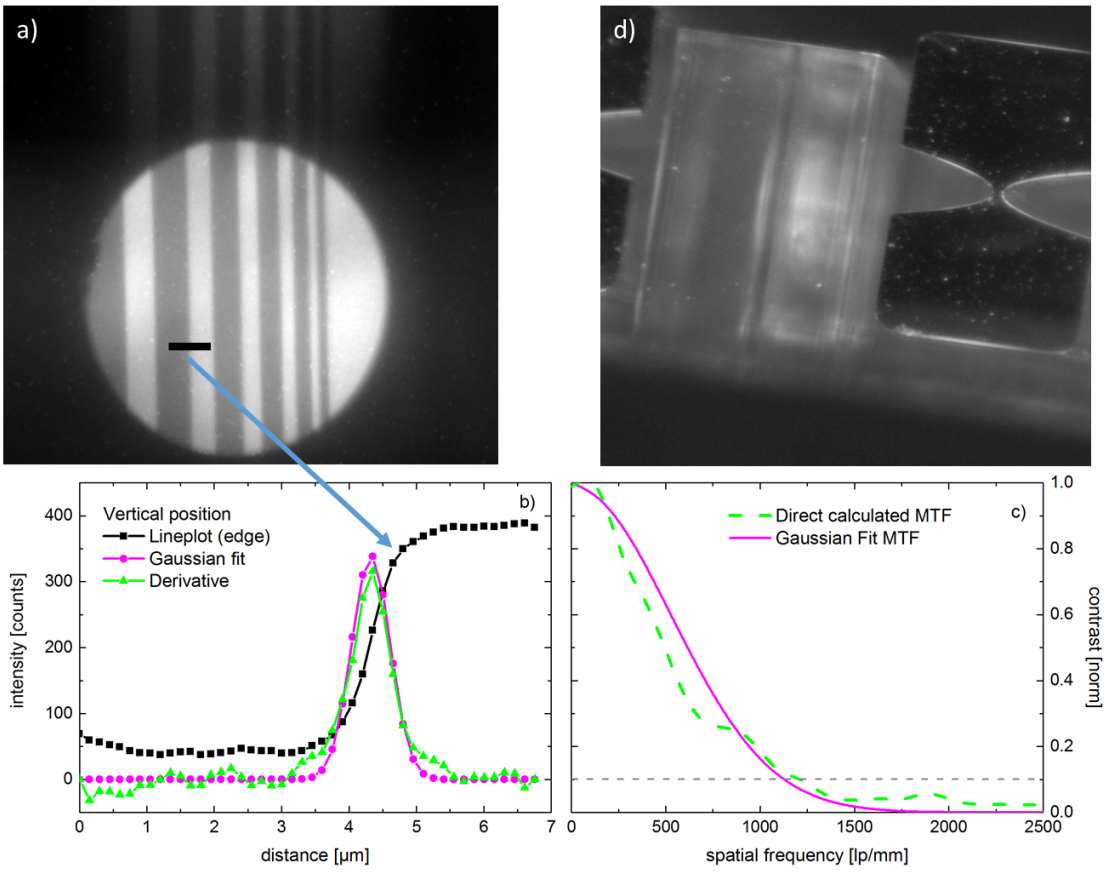

FIGURE 5.22: a) Image of a gold resolution target made with LIGA. The exposure time was set to 1800 s with a magnification of 4.44 and an object sampling of 150 nm. b) Lineplot through the edge marked in a), together with c) the corresponding *MTF*. d) Light microscope image of the used stack of alternating CRLs.

For a quantitative analysis, Fig. 5.23b also shows line plots through 300 nm as well as 200 nm

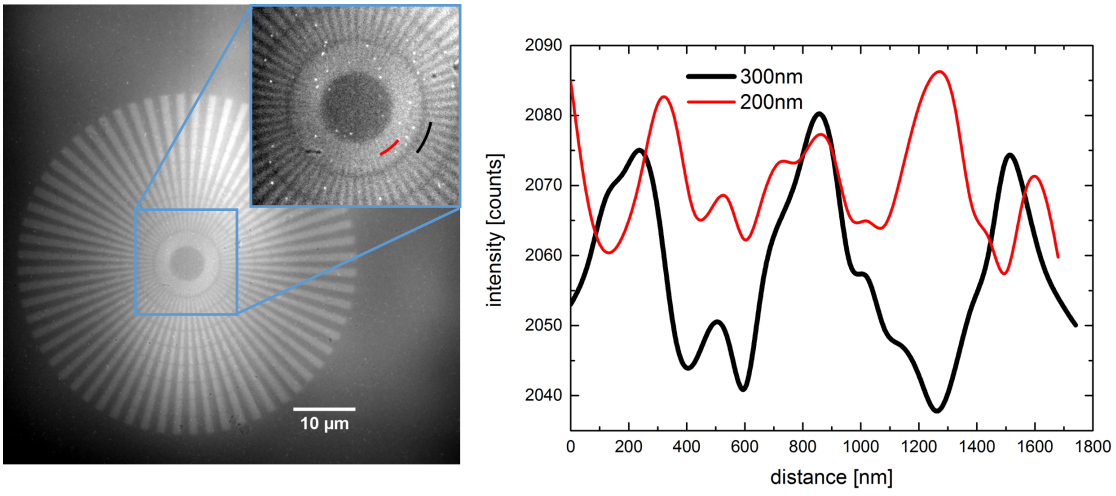

FIGURE 5.23: a) Image of a Siemensstar, which was taken via CRLs and the polycapillary (as condenser) with an exposure time of 2400 s and an object sampling of 55 nm. b) Lineplots through the red and black bars depicted in a), corresponding to 300 nm and 200 nm structures. Due to the low contrast and high noise level in the image, no *MTF* can be determined.

bars, respectively. Due to the low contrast and high noise level in the image, unfortunately, no useful *MTF* can be determined. On the other hand, the visibility of the inner features outlines the capability of higher resolutions, once a higher throughput can be reached.

5.4 Comparison with nanofocus setups

As the LRM also developed a setup (*LRM-XRM-II*), where a high resolution is reached by shadow imaging, using a small X-ray source, a comparison of this setup with the here presented microscope is interesting. At the alternative setup, to reach resolutions down to 100 nm, the electron spot of a scanning electron microscope is focused on the tip of a needle, which has the size of some tens of nanometers [162]. Thus, the beampath of the nanofocus setup is based on projection geometry. As detector, either a Si *Medipix* can be used, or a morpe efficient direct converting CdTe *Pixirad*, which is also sensitive to photons of higher energies. In the next paragraphs, first the two existing X-ray microscopes of the *LRM* are compared, followed by a more general discussion of the principle techniques.

Comparison of the LRM X-ray microscopes In order to compare the two setups quantitatively, Fig. 5.24 shows a resolution target measured with the nanofocus setup and the *Medipix* detector. On the one hand, structures down to 100 nm can be resolved. Thus, both setups are capable to resolve features in the range of 100-150 nm. While the air-damped housing and vacuum of the nanofocus source prevents this system nicely from external disturbance, this also requires a sample which can be handled in vacuum and which is conducting.

On the other hand, the photon flux is rather low for the nanotube-based setup, namely 0.028 N/s (see table 5.7). In contrast, the optics-based microscope shows a photon flux of 16 N/s (see table 5.4), corresponding to 1.8 N/s for the same object sampling as with the nanofocus tube. Thus, even if the approximately three-times more sensitive CdTe *Pixirad* detector is used, the photon flux of the nanofocus setup is still a factor of $\sim$ 20 lower. This leads to very long exposure times.

SDD	420 mm
SOD	0.4 mm
Pixel size	52 nm
Exposure time	60 min
Power	0.009 W
Spectrum	30 keV max , polychromatic
Solid angle	$4.72228 \cdot 10^{-9}$ sr
Photons	0.028 N/s

TABLE 5.7: Nanofocus-based acquisition and image parameters of Fig. 5.24b. The low photon flux is the main disadvantage of the nanofocus-based setup.

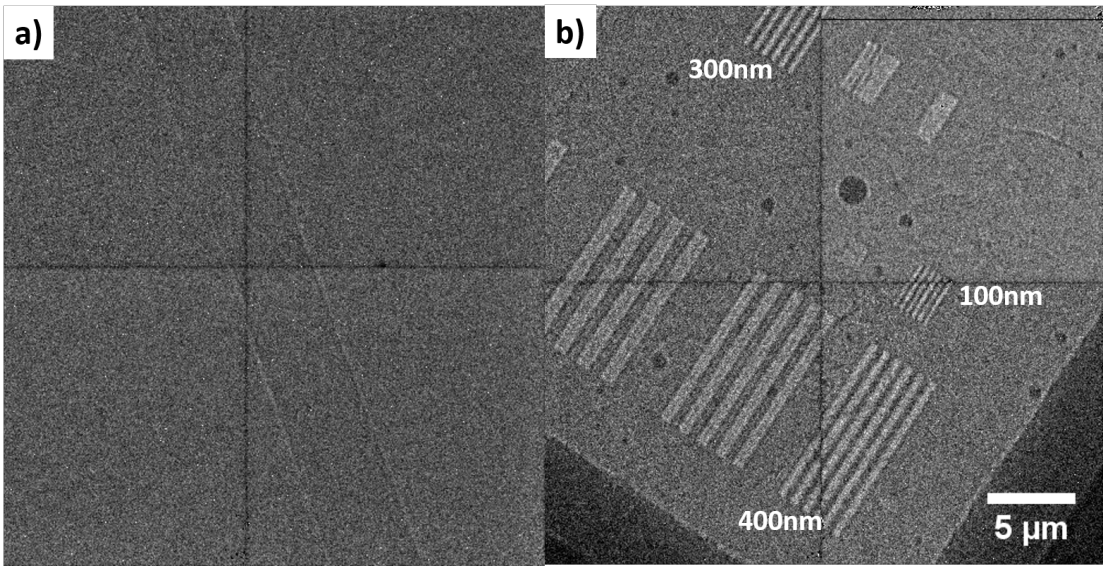

FIGURE 5.24: Images obtained with the nanofocus setup [162]. a) Carbon fiber with a diameter of approximately 5 μm as an extreme example that phase contrast allows to image interfaces, although the *SNR* is below 5 (30 min acquisition time). b) Au resolution target, containing several structures produced by FIB. Features down to 100 nm can be still resolved. The acquisition parameters are given in table 5.7.

However, weakly absorbing objects with sharp interfaces can be still imaged with the nanofocus setup, as with the small source, strong inline phase contrast is present. An example for this effect is shown in Fig. 5.24a, where a 5 μm carbon fiber is visible although the *SNR* is below 5. As noted earlier, in lens-based microscopes this is also possible using Zernike phase contrast, but with much more effort.

General comparison of X-ray microscopes Different, more general parameters are further considered based on table 5.8:

	Optics-based	**Nanofocus-based**
Resolution	+++	++
Exposure time	++	+
Stability	+++	++
Energy	++	++
Phase contrast	++	+++
Complexity / costs	+	+++
Development potential	+++	+

TABLE 5.8: Comparison between optics-based and nanofocus-based X-ray microscopes.

- First of all, the **resolution** which can be reached is in principle high for both approaches; in literature, up to now higher resolutions were demonstrated for the optics-based configuration [152].

- Another important parameter is the **exposure time**, which is related for both setups to the photon flux. In the case of the nanofocus setup, for the same resolution (*i.e.* object sampling), this flux (*i.e.* the solid angle) can be increased by decreasing the *SOD*, but this distance is limited by the finite size of source and object. However, when intermediate resolutions (*i.e.* 300-400 nm) are sufficient, the source size can be increased, increasing the flux. Additionally, as the target thickness scales with the effective source size, then also the target thickness can be increased; this increases further the flux. Thus, while the optics-based setup is in principle superior for low resolutions, the nanofocus setup wins at intermediate resolutions.

- When judging the **stability**, in the case of an optics-based setup mainly the positionability of sample, optical element and detector has to be considered. In contrast, for the nanofocus-based setup, the hot source spot needs to be kept constant, which is more difficult.

- Concerning the usable **energy** range, there is no big difference between both approaches. While for zone plates, the energy is limited to approximately 9 keV (problematic for samples bigger than 100 μm), CRLs are capable for 25 keV measurements. Indeed, higher energies can be only reached with nanofocus tubes. However, for most samples the energy range of the optics-based setup is enough.

- Considering resolution-enhancing inline **phase contrast**, the nanofocus setup is superior, as the phase contrast is automatically supplied by the high coherence of the small source. For the optics-based setup, specific illumination and a phase ring are needed, leading to a loss of flux.

- Comparing the **costs**, the nanofocus system is clearly cheaper due to a smaller amount of parts and a less complex beam path.

- However, the latter point is somehow counteracting the **development potential**. For reaching very high resolutions at low exposure times, the optics-based approach is clearly preferable: both, the optics as well as the source provide room to boost the system's performance. Concerning the optical elements, a larger *NA* allows not only a higher resolution, but also keeps the flux per pixel on the detector constant. In this regard, one can observe an ongoing progress, as the optic development profits from a large community which constantly makes progress. In contrast, for a higher resolution of the nanofocus setup, the solid angle and thus also the flux is decreased due to a limited *SOD*. This can be only compensated by increasing the brightness of the source, which is limited by the danger of evaporating the anode material. Therefore, the development potential of nanofocus-based microscopy is mainly limited to resolutions above 200 nm.

Summing up, both techniques have their irrespective advantages and disadvantages. From an industrial perspective of costs and complexity, the nanofocus-based setup is clearly preferable for samples which can be placed close to the source. However, from a developer's or researcher's point of view, the optics-based setup bears a greater potential to overcome nowaday's limits of microscopy based on compact X-ray tubes.

6 Further experiments

In the last chapter, two topics are briefly introduced, where the liquid-metal-jet based setup shows promising results. In the first case, its high brilliance is exploited for waveguide-based imaging (see section 6.1). The second case shows high-speed imaging results (see section 6.2).

6.1 Imaging by waveguides

The first side-projects carried out on the here-presented setup is the realization of waveguide-based imaging in cooperation with Daniele Pelliccia from the *Monash University, Australia*. While he and his group fabricated the waveguides, characterized them and performed measurements on a rotating anode source, additional measurements with the highly brilliant liquid-metal-jet source where performed in Würzburg. The results are published in Ref. [163] and will be briefly summarized in the following.

Motivation One possible method for laboratory-based X-ray microscopy is phase contrast microscopy which uses X-ray waveguides to produce a secondary source [164, 165]. Hereby, the small size of this secondary source provides a spatially coherent X-ray signal, which is very important for phase contrast measurements. Additionally, small detector pixel sizes also enhance the phase contrast signal. As already discussed in chapter 4.1.2, the here presented setup with the highly brilliant liquid-metal-jet source fulfills also this second criteria and is therefore suited for phase-contrast measurements with waveguides.

Setup For the investigations, two one-dimensional waveguides were used in crossed configuration, leading to a two-dimensional focal point. They were fabricated at the *Monash University* by first etching 0.2-2 mm channels in a silicon wafer; afterwards, a second wafer was bonded to the etched one, leading to channels as depicted in Fig. 6.1b. Moreover, as a major challenge for imaging with waveguides is the small solid angle from which light is coupled into them, we have added pre-focusing optics into the beam path in order to increase the flux density at the entrance of the waveguide (see Fig. 6.1). As optical elements, Montel multilayer mirrors were utilized,

which were provided by the *Axo Dresden GmbH*; the waveguides were placed symmetrically around their focal spot and needed to be fine-adjusted by five-axial piezo-electrical stages. For detection, the macroscope was used.

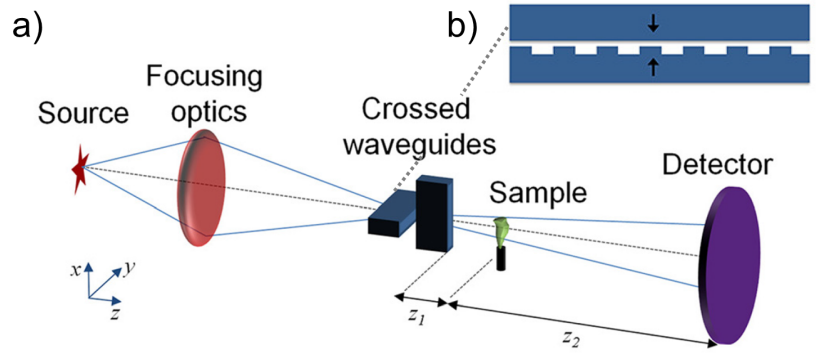

FIGURE 6.1: Schematic drawing of the setup with waveguides. The source is pre-focused via Montel mirrors on two waveguides, which are placed symmetrically around the focal spot. They produce a quasi-pointlike secondary source. Afterwards, the sample is fixed at a distance z_1 from the exit of the second waveguide, and the macroscope detector follows at distance z_2 from the sample.

Experimental results: high magnification Due to the usage of two one-dimensional waveguides which are arranged behind each other, the beam size gets non-uniform. The resulting astigmatism is the stronger, the smaller the waveguide and the higher the magnification is. The resulting difference in magnification can be seen when imaging a gold mesh with a periodicity of 12.5 μm, as depicted in Fig. 6.2a. A further challenge is the non-uniform beam profile at the sample position which stems from diffraction effects at the waveguide edge [166], leading to distortions in the image.

Experimental results: low magnification Both, astigmatism and aberration can be reduced for lower magnifications, as depicted in Fig. 6.2b for the image of an ant's antenna. Besides a good attenuation contrast, which is typical for insect exoskeletons, one also clearly observes a strong phase contrast, evident from the elevated signal at the edges. The high sensitivity to phase contrast allows also to image lower absorbing plants, as further discussed in Ref. [163].

Besides an improved fabrication process of waveguides which is also presented in the manuscript, Ref. [163] demonstrates that the here presented setup is capable to image low absorbing organic material via a waveguide-based phase contrast microscope. Thus, this method allows for achieving high resolutions with relatively simple production methods. A further reduction of exposure time is only possible for sources with even higher brightness, since the maximum *NA* is limited by the total reflection angle.

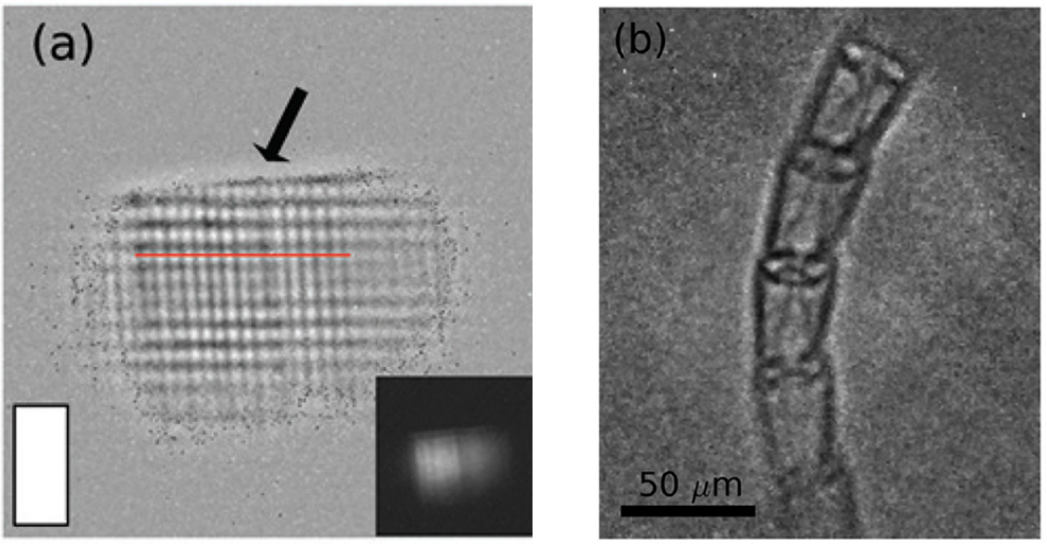

FIGURE 6.2: Flatfield-corrected images taken with waveguides with 200 nm width and a) high magnification, b) low magnification. a) Image of a gold mesh with a periodicity of 12.5 μm and the measurement parameters: exposure time 45 s, $z_1 = 35$ mm, $z_2 = 355$ mm. Due to a strong astigmatism, the mesh is distorted; the white rectangle in the bottom left corner represents a scale of $50 \times 50\,\mu$m. The arrow highlights abberration effects. b) Image of an ant's antenna, with the measurement parameters: total exposure time 7.5 min, $z_1 = 155$ mm, $z_2 = 235$ mm. Phase contrast is evident from the elevated signal at the edges.

6.2 High-speed imaging

In scientific as well as industrial research, there is a general interest in examining the time-dependent behavior of dynamical systems or changes of samples over lifetime. For this, a typical experiment is in-situ fatigue of mechanical parts such as dental implants [167]. However, these studies are nowadays typically restricted to synchrotron beamlines, as here the high brightness allows sufficiently low exposure times and fast enough imaging. Therefore, this topic is also another interesting application for the liquid-metal-jet source. As the exposure time is indirect proportional to the square of the resolution, we concentrated on high-speed imaging with acquisition times of 10 ms and a moderate resolution around 10-20 μm. In comparison, at synchrotron beamlines such as $ID19$, frame-rates of 1000 fps or even higher are nowadays performed routinely at the same resolution. However, here beamtime is limited, which is not the case for laboratory-based setups. One possibility to yield higher frame-rates also in the laboratory is the combination of several sources, as demonstrated in Ref. [168]; there, a combination of three liquid-metal-jet sources and detectors are used for gaining time-resolved lung CTs.

Proof of concept In the framework of this thesis, also a detector capable for high-speed imaging was built (see chapter 3.2). A first example which demonstrates the capability of the LMJ-setup for high-speed imaging is a matchstick which gets inflamed by a soldering iron. Fig. 6.3

shows a CT scan before inflaming, together with a time series of the in-flaming process in 10 ms steps. The latter images are subtracted from the first one to enhance contrast, and thus display the lost (*i.e.* burnt) material.

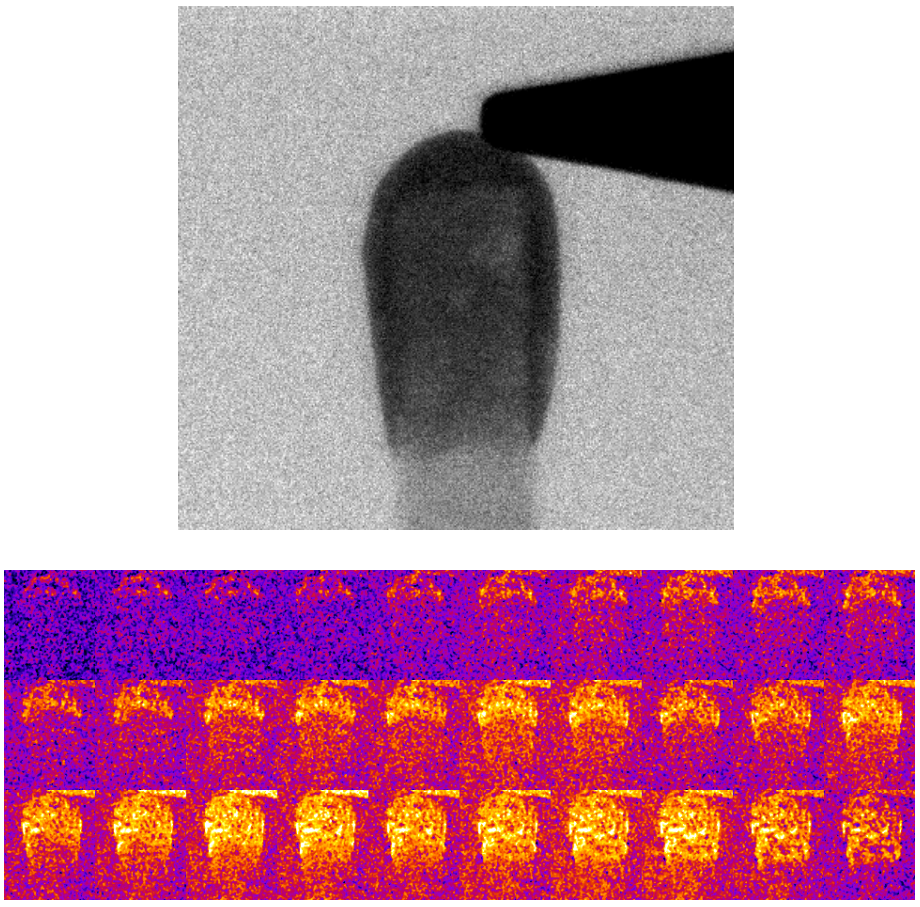

FIGURE 6.3: Soldering iron to remotely inflame the matchstick. The montage shows the in-flaming of a matchstick during 300 ms in 10 ms steps (bottom). To intensify the contrast, the image of the original matchstick (bottom) is subtracted.

Foams Since the possible frame-rate is a function of the pixel sampling, for fast acquisition the sample has to be relatively large. Moreover, as most of the intensity of the liquid-metal-jet source is emitted at 9 keV, the sample needs to be based on a material with a relatively low Z number and density. Thus, together with the moderate frame-rate - *e.g.* one CT scan every 5 s - the choice of possible sample systems is limited. One good candidate are foams, where the statistic distribution of pores can be evaluated by high-speed CTs. This is used to investigate how parameters like the pH influence the stability of the foam.

Fig 6.4 shows CT scans of a milk foam used in food industry, taken with different frame-rates. As one can see directly, the signal-to-noise ratio decreases with increasing frame-rate, meaning that smaller air bubbles can be only resolved for high frame-rates.

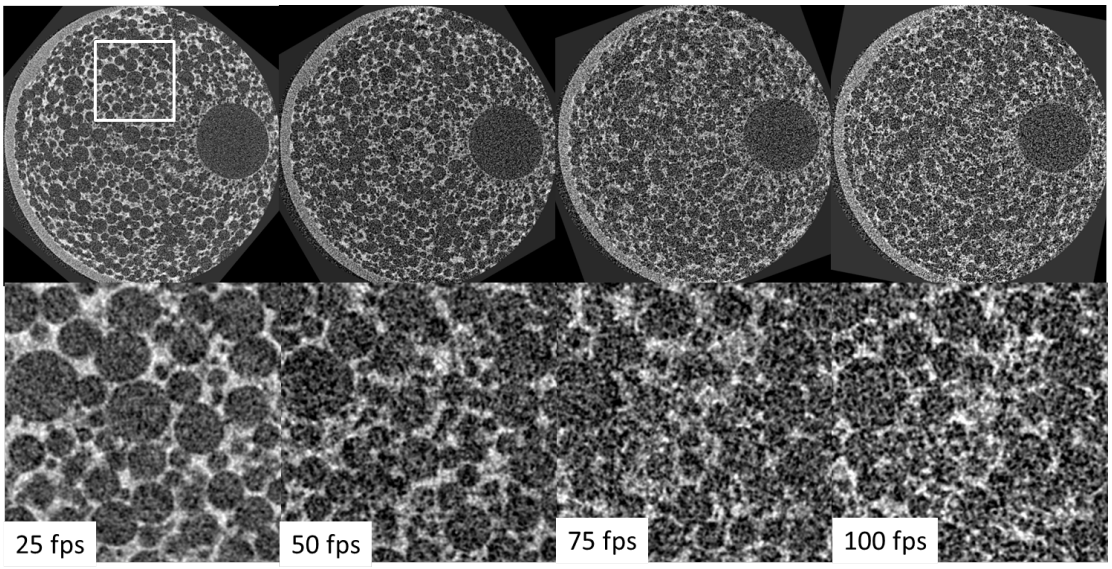

FIGURE 6.4: Slice of the reconstructed volume of a milk foam, with frame rates varying from the left to the right. The voxel sampling is around 11 μm; each reconstruction was done with 500 projections. The source was set to 270 W with an effective 27 μm source spot diameter at 70 kV maximum acceleration voltage.

Another example where the coarsening of protein foams was investigated at the *LRM* is presented in Ref. [169]. Here, pores were individually tracked over time to evaluate their growth behavior. So far, the measurements were carried out only at the synchrotron, which allowed a full CT scan in 1 s. However, this project could be also extended in future to the liquid-metal-jet setup, where a larger variety of different proteins could be investigated.

Outlook In principle, without further optimizing the source, the only possible improvement of the setup with respect to high-speed imaging concerns the detector. At the time the setup was built, only indirect detectors with fast enough readout were available. However, for such detectors, a large field of view leads to a loss of efficiency, as the coupling of the optical lenses to the camera is relatively inefficient (see chapter 3.2). Nowadays, also fast enough direct converting detectors with *DQE*s up to 100% exist [82].

7 | Summary and outlook

In this last chapter, the thesis and the status of the built X-ray microscope is summarized. Finally, possible further improvements of the instruments, as well as interesting future projects are discussed.

7.1 Summary

The scope of this thesis was the development, creation and characterization of an *X-ray microscope* with *CT capabilities* in the *hard X-ray range* based on a novel X-ray tube - namely the *liquid-metal-jet source*. By creating X-rays with a conventional electron impact source, most of the electronic power is converted to heat. This limits the electron current and thus also the brightness, as otherwise the anode will melt and be destroyed. To overcome this limit, in the case of the here utilized source a fast flowing liquid metal jet is formed, consisting of gallium and indium. By this, the anode is continuously replaced and a higher brightness than with conventional X-ray tubes can be reached[1].

Design goal Two imaging modes were set in the focus of development, which take advantage of the highly brilliant source[2]. In the first mode, the instrument should serve as micro-CT scanner, which is able to scan routinely and fast samples of different size. In order to increase the signal-to-noise ratio, this mode exploits the effect of *inline phase contrast*, where interference fringes at edges or interfaces are detected. This is implemented in the current setup via the long propagation distance, the small source size ($\sim 10\mu$m $\times 10\mu$m) and the small pixel pitch on the detector. The second mode of the instrument should use *X-ray optics* to magnify the sample and therefore reach higher resolutions.

[1] Of course, by raping up the electron power, at some point the liquid alloy will also start to evaporate, and evaporated ions will degrade the cathode; therefore, the gain of brightness is limited.

[2] In the case of low-brightness sources, these modes are either not possible to be implemented, or lead to unreasonable high exposure times.

When designing the X-ray microscope, particular focus was set on flexibility in order to allow the simple integration of various measurement methods. Therefore, the setup was built in a relative large hutch, which allows further installations for other experiments, *e.g.* sample treatment, spectrometer, optics or special detectors.
In general, various detectors are available to serve the demands for different samples and acquisition modes. Most are indirect converting, home-built ones, using optical cameras which are coupled by relay optics to the scintillator. For this, two cameras are used: a cooled CCD for long exposure times and a low read-out noise sCMOS for a fast acquisition up to 200 fps.

Since the two modes differ in terms of resolution, exposure time, handling and field of view, they are separately discussed in the following.

Micro-CT mode The standard mode of the instrument uses the shadow projection geometry with small detector pixels, allowing stable CT scans with good signal-to-noise ratio and contrast (see chapter 4.1)).

- In order to achieve a high *resolution* also without using optical elements, the thickness of the scintillator needs to be thin. As a compromise between resolution and efficiency, here a 5.5 μm thick LSO:tb szintilator was chosen. The best resolution obtained so far with the 10% MTF criterion is 1 μm (see chapter 4.1.3).

- Additionally, the geometry can be set in a way that images show strong *inline phase contrast*, which can be converted to a better signal-to-noise ratio with the help of a phase retrieval algorithm (see chapter 4.1.2).

- The energy spectrum given by the source with a maximum acceleration voltage of 70 keV and the most intense Ga K_α-line defines especially for the micro-CT mode - where the samples are larger - the kind of sample material which can be imaged (see Fig. 4.18)[3]. For the here presented setup, especially carbon-based samples are suitable for fast scans, taking advantage of the highly brilliant 9 keV line. In chapter 4.2.3, various *successful CT scans* of samples such as carbon-reinforced plastics and wood were presented, proofing the versatile applicability of the instrument. Furthermore, thicker samples and higher Z materials (such as a cochlea implant) were also successfully imaged by exploiting the Bremsspectrum, although here the exposure times become longer by approximately a factor of five.

Nano-CT mode The second mode corresponds to a transmission X-ray microscope, which uses X-ray optics for illumination and magnification of the specimen. For both, reflective

[3] Of course, it also depends on the sample's density.

(mono- and polycapillary), diffractive (zone plates) and refractive elements (prism condenser, compound refractive lenses) were investigated.

Indeed, several combinations of optical elements were tested. The combination with the shortest exposure time - and therefore also the highest resolution - is a monocapillary together with a tungsten zone plate, which possesses a thickness of 1000 nm and a smallest zone width of 50 nm. With this combination, 150 nm features of a Siemensstar were clearly resolved (see chapter 5.2.4). A sightly lower resolution was obtained in combination with a polycapillary as condenser. The use of zone plates produced by a novel fabrication technique via atomic layer deposition failed for full-field imaging. However, it is likely that the next generation of this kind of zone plates will show up good results.
Moreover, also compound refractive lenses produced by LIGA were successfully utilized for imaging (see chapter 5.3.2). Here, also the 150 nm bars of the Siemensstar were resolved, which is much better than comparable results published so far in literature (around 1.1 μm [158]).

Alternative modes As one side project, imaging with a secondary source created by sub-μm waveguides was demonstrated (see chapter 6.1). Indeed, the high brightness of the source and the produced small light spot lead to a high inline phase contrast, which allows imaging even low-absorbing organic material [163].

Moreover, the high brightness of the source supports also high-speed imaging, which is interesting for instance when investigating foams (see chapter 6.2). Here, a medium resolution of $\sim 10\,\mu$m was demonstrated for a CT scan with total exposure time of 5 s, with 10 ms for a single exposure.

Summary In the framework of this thesis, a very versatile imaging system was built, which covers sample sizes from 50 μm to 50 mm at object samplings between 50 nm and 50 μm, respectively. With the micro-CT mode, samples can be scanned fast and routinely with a resolution of 1-2 μm and a total exposure time of 1-3 hours. For the nano-CT mode, the user still needs a lot of experience to guarantee a proper alignment and stability for good results, *i.e.* for resolving features in the range of 150 nm at acquisition times for CT scans of more than two days. Moreover, the flexibility of the setup was demonstrated by measurements with waveguides and time-instable samples.

7.2 Outlook

When characterizing the here presented instrument, we got aware of further possible improvements of the current setup, which could not be implemented so far either due to a lack of time or financial resources.

Micro-CT mode As the results presented in chapter 4 show, the optic-less setup already fulfills all target specifications. However, there is still room for improvement, concerning not the general acquisition settings, but possible add-on's:

- Due to the flexible instrumentation, there is enough space for *in-situ sample preparation*, such as humidity chambers to avoid drying of the samples and devices that allow pressure or fatigue studies.
- Since for most samples, the challenge is to achieve a good enough contrast, the high potential of using different sources for *multimodal imaging* is a very interesting extension.
- As stages and optics are already present, it would be relatively simple to implement *fluorescence imaging* by adding a spectrometer. In this case, the condenser can be used in combination with a pinhole for scanning the sample point by point. Together with staining and markers, this is especially interesting for biological samples.

Nano-CT mode As can be seen in chapter 5, the nano-CT setup already yields high resolutions in the range of 150 nm for both, zone plates and compound refractive lenses. In principle, there exist two possible directions for further improving the nano-CT setup:

- On the one hand, one could focus on the optimization at the current energy of 9.25 keV, corresponding to the Ga K_α-line. This requires the implementation of *zone plates with a higher numerical aperture* and a *more efficient condenser*. For such an optimization, a close collaboration with the supplier will be important: one needs access to a certain number of optical elements, test them, give feedback to the supplier, who afterwards can adapt his production technique and deliver new parts.
- On the other hand, one could move to a higher energy, namely the *In K_α line at 24 keV*. At this energy, the performance of compound refractive lenses is better. However, the detection gets more difficult and the source has to be re-engineered to a heated liquid-metal cycle, in order to allow a higher indium content.

Although samples which are small enough for the accessible field of view (100-150 μm) typically will not require a higher energy than 9 keV, for region-of-interest scans (*e.g.* when small

structures are placed on a thicker substrate), the higher penetration depth can be very useful. Additionally, there exist also relevant, high Z materials such as gold, iron or steel, where also for small sample sizes around 50 μm, X-rays with an energy of 9 keV are not transmitted, while 24 keV would be sufficient.
In both cases, a multilayer as condenser would also block the broadband Bremsspectrum, which acts now as a background radiation, since the optical elements are optimized for a certain energy. This gets more important in the case of the 24 keV line, where the Bremsspectrum is more intense due to the higher excitation energy.

Finally, a very general improvement would be also a further *increase of stability*, meaning a reduction of movements and vibrations. However, when keeping the requirement of a flexible two-mode system, the setup is already quite optimized in this regard; otherwise, a more compact, single nano-CT setup would be an option. In the present case, rather *novel cameras* with lower dark noise and higher quantum efficiency could further reduce the acquisition time and thus lead to an increase of resolution.

A Appendix

A.1 Description of the mechanical system

The system consists of various manipulators, whose names and specifications are listed in the following; X corresponds to the beam path direction, Y to the perpendicular direction also parallel to the table, and Z to the direction vertical to the optical table. While the JFA axes are integrated in the granite table, all other stages are mounted on these axes (despite the condenser axes, which are directly mounted on the source).
Most stages operate in closed loop (CL) configuration, using an optical encoder. Additionally, the microscope detector is equipped with three open loop *New-Focus 8742* picomotors to align the scintillator and adjust the focal distance; the scintillator of the macroscope detector is equipped with one linear piezo from *Attocube ECS3030*.

name supplier	travel	load	resolution	direction	comment
JFA	1000 mm	800 N	0.05 mm	X	sample
JFA	1000 mm	800 N	0.05 mm	X	detector
5101.30 xhuber	155mm	1500 N	0.0005 mm	Y	detector
5103.A20 xhuber	40 mm	1500 N	0.0005 mm	Z	detector
5103.A20 xhuber	90 mm	1500 N	0.0005 mm	Z	optics stage

TABLE A.1: Overview of the detector, sample and optics stage manipulators, corresponding to the main axes at the bottom of the stages shown in Fig. 3.13.

name supplier	travel	load	resolution	direction	comment feedback
ECS5050 *Attocube*	30 mm	150 N	1 nm	X	In-Out CL
SmarPod 70.42 *Smaract*	$\pm$ 2 mm	5 N	2 nm	XYZ $\theta\ \phi\ \alpha$	Hexapod CL

TABLE A.2: Condenser manipulator with freely selectable pivot point. The travel of the SmarPod depends on its actual position.

name supplier	travel	load	resolution	direction	comment
PLS85 *PiMicos*	157 mm	150 N	50 nm	X	OL
5103.A10 *xhuber*	15 mm	150 N	50 nm	Z	OL
ECS5050 *Attocube*	30 mm	150 N	1 nm	X	In-Out CL
ECGt5050 *Attocube*	10°	10 N	0.0001°	θ	yaw CL
ECGp5050 *Attocube*	10°	10 N	0.0001°	ϕ	tilt CL
RS40 *PImicos*	360° ∞	5 N	0.005°	α	OL
ECS3030 *Attocube*	20 mm	90 N	1 nm	y'	OL
ECS3030 *Attocube*	20 mm	90 N	1 nm	x'	OL

TABLE A.3: Object manipulator, which positions the sample. For performing CTs, additional axis on top of the rotating plate allow moving the sample exactly in the center of rotation.

name supplier	travel	load	resolution	direction	comment
PLS 85 *Micos*	157 mm	50 N	50 nm	Z	CL
ECS5050 *Attocube*	30 mm	150 N	1 nm	X	CL
ECS5050 *Attocube*	30 mm	150 N	1 nm	Y	CL
ECGt5050 *Attocube*	10°	10 N	0.0001°	θ	yaw CL
ECGp5050 *Attocube*	10°	10 N	0.0001°	ϕ	tilt CL
ECR30 *Attocube*	30 mm	150 N	0.0004°	X	CL

TABLE A.4: Optics manipulator I with six degrees of freedom; while five of them are covered by piezos, a vertical movement is executed by a stepper motor due to the needed load.

name supplier	travel	load	resolution	direction	comment
PLS 85 *Micos*	52 mm	50 N	50 nm	Z	 CL
ECS5050 *Attocube*	30 mm	150 N	1 nm	X	 CL
ECS5050 *Attocube*	30 mm	150 N	1 nm	Y	 CL
ECGt5050 *Attocube*	10°	10 N	0.0001°	θ	yaw CL
ECGp5050 *Attocube*	10°	10 N	0.0001°	ϕ	t ilt CL
ECR30 *Attocube*	30 mm	150 N	0.0004°	X	 CL

TABLE A.5: Optics manipulator II, which is based on the same principle as the optics manipulator I, but possesses a shorter vertical travel distance.

name supplier	travel	load	resolution	direction	comment
LPS45 *PiMicos*	26 mm	8 N	6 nm	Z	 CL
LPS45 *PiMicos*	26 mm	10 N	6 nm	X	 CL
LPS45 *PiMicos*	26 mm	10 N	6 nm	Y	 CL

TABLE A.6: Pinhole manipulator, consisting of three piezo axes.

A.2 Description of the software and electronic components

The software is programmed in *National Instruments LabView*. A schematic of the complete system is depicted in Fig. A.1, and further described in the following.

1. **PC Control**: computer, where the main application runs, controlling all the components.
2. **PC Cameralink**: computer used for recordings of the cameras. It was necessary to separate this PC from the Control PC, since full-speed 10-Tap Cameralink only supports short cables; therefore, the PC is located as close as possible to the detectors.
3. **PC Monitoring**: host for webcams to enable a visual feedback of the axis positions to avoid (expensive) collisions. Due to the high degree of freedom, there exist many possibilities for such collisions and they need to be avoided manually.
4. **PC Source**: connected to the X-ray tube.
5. **CRIO NI I**: embedded PC which measures cooling water, status of the chiller, temperatures and provides these values to the source and the control PC.
6. **CRIO NI II**: embedded PC which is used to trigger and read the exposure status of the detectors; during exposure, the light of the hutch is switched on by its relays.

The software of the Control PC collects the data from the other devices for logging their status and stores this information. Controlling of the scans is done with sequences which can be created either with an built-in tool or by a text file.

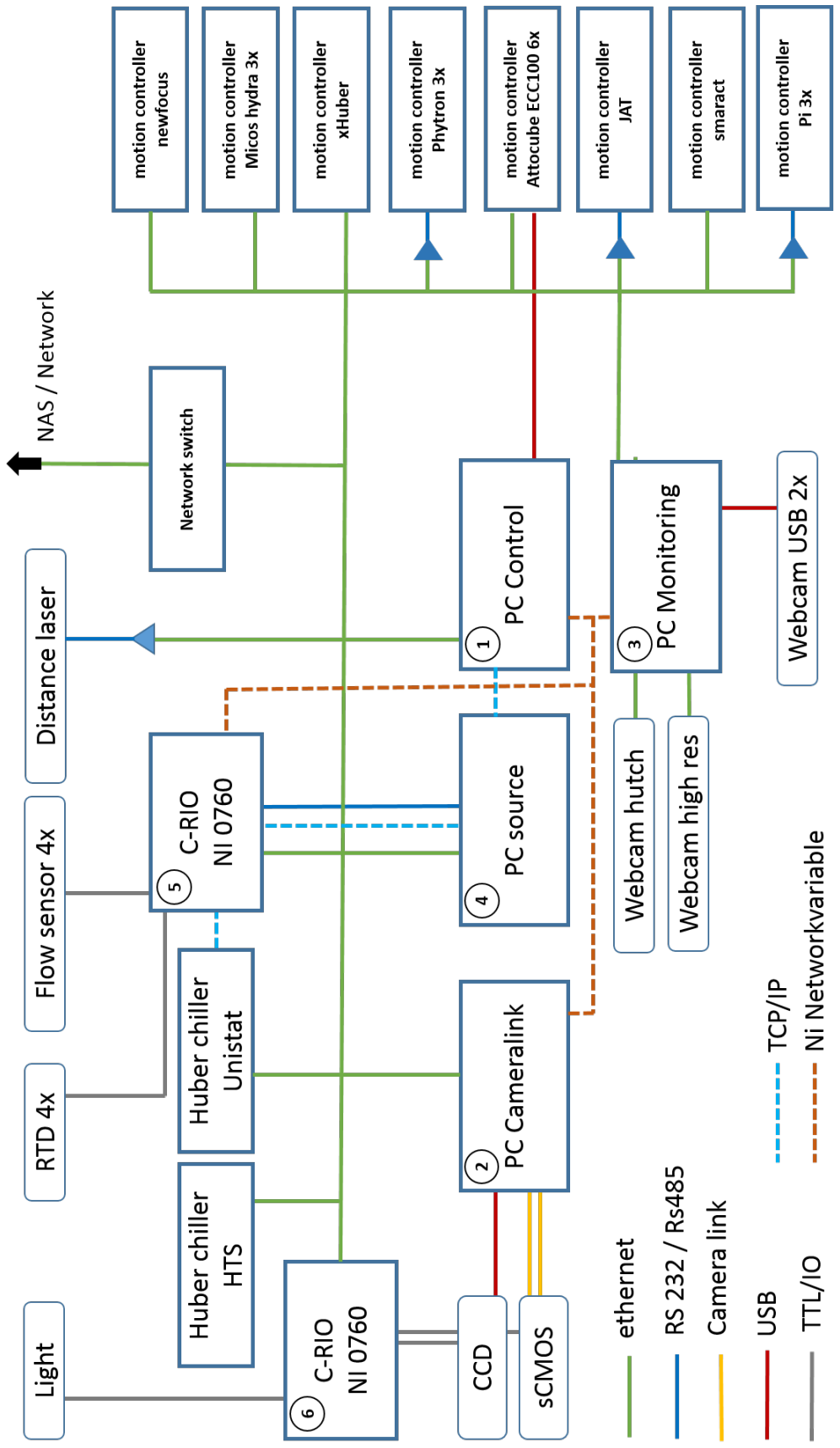

FIGURE A.1: System overview.

A.3 Additional Figures

In addition to the spectrum of the alloy with 95% gallium and 5% indium content which is shown in Fig. 3.6, Fig. A.2 shows the spectrum of galinstan. The spectra are very similar, but the distribution changes in the latter case to the benefit of the In line and the Bremsspectrum.

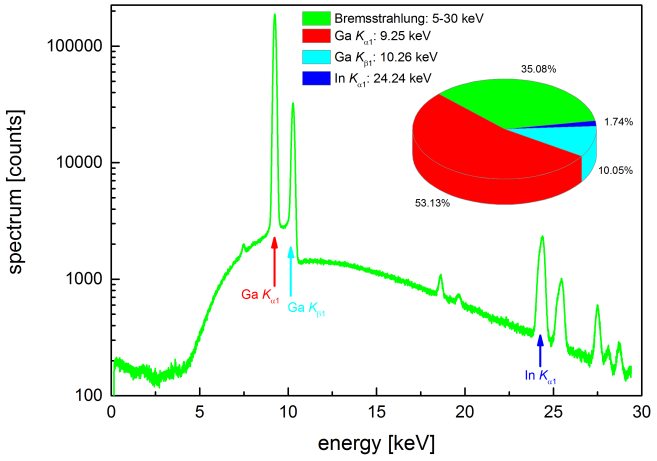

FIGURE A.2: Spectrum of galinstan.

Fig. A.3 shows the spectrum of the source, together with the energy-dependent absorption of the scintillators. Only where *both* possess significant intensity, the detection process is efficient. Therefore, when using the thin scintillators (Gadox and LSO:TB), higher energies are rarely used for imaging. Moreover, for the lutetium based scintillators, the L_3-edge is positioned at 9.244 keV. Thus, it separates the Ga $K_{\alpha1}$- and the $K_{\alpha2}$-line. This is especially effective for the thinner LSO:TB, where it induces an absorption difference of around 50%. On the one hand, such suppression is good for microscopy with optical elements to avoid chromatic blurring; on the other hand, this leads also to a loss of photon flux. Therefore, it is a disadvantage for the shadow-projection geometry.

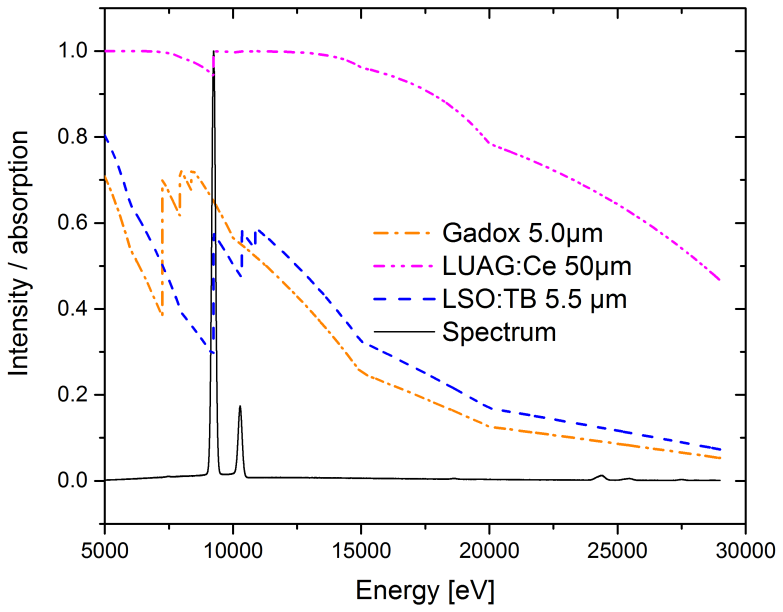

FIGURE A.3: Spectrum of the source (solid black line), together with the energy-dependent absorption of the utilized scintillators (dashed curves).

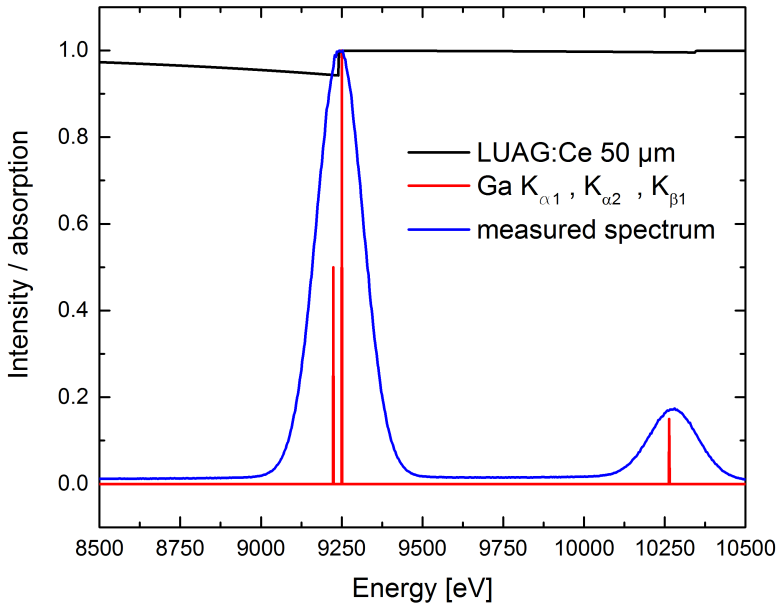

FIGURE A.4: Absorption of the LUAG:Ce scintillator, together with the measured spectrum of the source and the theoretical Ga $K_{\alpha 1}$-, $K_{\alpha 2}$- and K_{β}-lines, which are much more narrow than the resolution of the spectrometer.

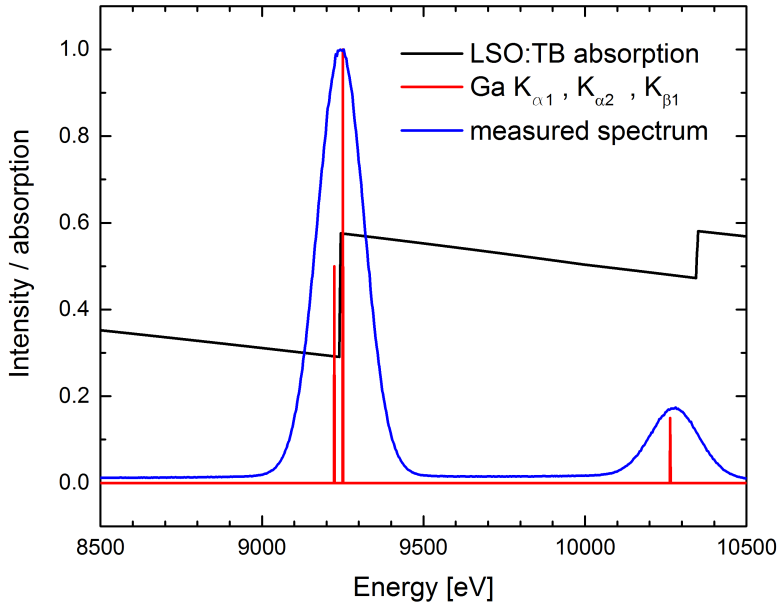

FIGURE A.5: Absorption of the LSO:TB scintillator, together with the measured spectrum of the source and the theoretical Ga $K_{\alpha1}$-, $K_{\alpha2}$- and K_{β}-lines, which are much more narrow than the resolution of the spectrometer.

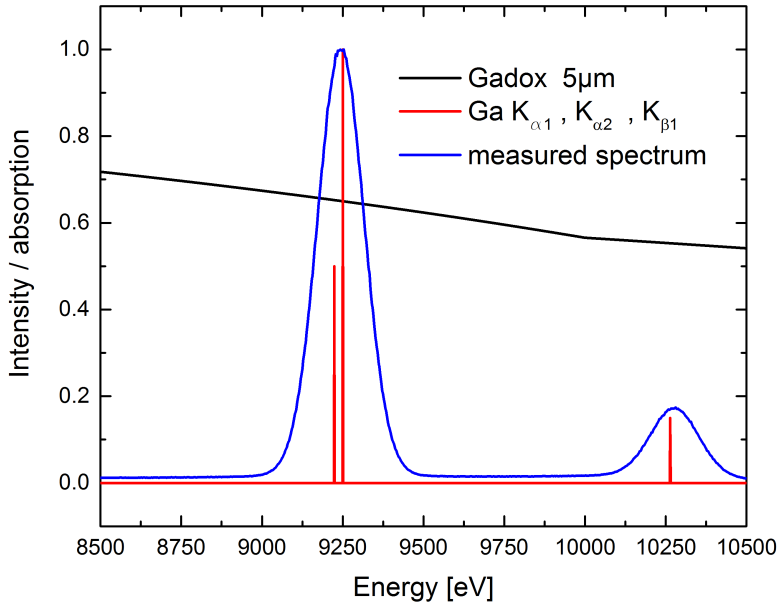

FIGURE A.6: Absorption of the Gadox scintillator, together with the measured spectrum of the source and the theoretical Ga $K_{\alpha1}$-, $K_{\alpha2}$- and K_{β}-lines, which are much more narrow than the resolution of the spectrometer.

B Publications

B.1 Directly related to this project

C. Fella, A. Balles, S. Zabler, A. Last and R. Hanke. Hybrid setup for micro- and nano-computed tomography in the hard x-ray range. In preparation for *Review of Scientific Instruments*.

C. Fella, A. Balles, W. Wiest, S. Zabler and R. Hanke. Laboratory Source Based Full-Field X-Ray Microscopy at 9 keV. *AIP Conf. Proc.*, 1696:020025, 2016.

C. Fella, A. Balles, S. Zabler, R. Hanke, R. Tjeung, S. Nguyen, and D. Pelliccia. Laboratory x-ray microscopy on high brilliance sources equipped with waveguides. *Journal of Applied Physics*, 118(3):034904, 2015.

A. Balles, S. Zabler, T. Ebensperger, C. Fella, and R. Hanke. Propagator based formalism for optimizing in-line phase contrast imaging at laboratory X-ray setups. *Review of Scientific Instruments*, 87(9):093707, 2016.

A. Balles, C. Fella, J. Dittmann, W. Wiest, S. Zabler, and R. Hanke. X-ray grating interferometry for 9.25 keV design energy at a liquid-metal-jet source. *AIP Conf. Proc.*, 1696:020043, 2016.

S. Zabler, T. Ebensperger, C. Fella, and R. Hanke. High-resolution X-ray imaging for lab-based materials research. *Conference on Industrial Computed Tomography, Wels, Austria*, 2012.

S. Zabler, C. Fella, A. Dietrich, F. Nachtrab, M. Salamon, V. Voland, T. Ebensperger, S. Oeckl, R. Hanke, and N. Uhlmann. High-resolution and high-speed CT in industry and research. *Proc. SPIE 8506, Developments in X-Ray Tomography VIII*, 850617, 2012.

B.2 Related to other projects

W. Wiest, S. Zabler, A. Rack, C. Fella, A. Balles, K. Nelson, R. Schmelzeisen, and R. Hanke. In situ microradioscopy and microtomography of fatigue-loaded dental twopiece implants. *Journal of Synchrotron Radiation*, 22:1492–1497, 2015.

K. Blum, W. Wiest, C. Fella, A. Balles, J. Dittmann, A. Rack, D. Maier, R. Thomann, B. C. Spies, R. J. Kohal, S. Zabler, and K. Nelson. Fatigue induced changes in conical implant-abutment connections. *Dental Materials*, 31(11):1415-1426, 2015.

List of Figures

List of Tables

Abbreviations

ALD	**A**tomic **L**ayer **D**eposition
BESSY	**B**erlin **E**lectron **S**torage **R**ing **S**ynchrotron
CAD	**C**omputer **A**ided **D**esign
CNR	**C**ontrast-to-**N**oise **R**atio
CRL	**C**ompound **R**efractive **L**ens
CT	**C**omputed **T**omography
DOF	**D**epth **O**f **F**ield
DQE	**D**etective **Q**uantum **E**fficiency
FBP	**F**iltered **B**ack **P**rojection
FEM	**F**inite **E**lement **M**ethod
FEL	**F**ree **E**lectron **L**aser
FIB	**F**ocused **I**on **B**eam
FOV	**F**ield **O**f **V**iew
FWHM	**F**ull **W**idth at **H**alf **M**aximum
FZP	**F**resnel **Z**one **P**late
ILST	**I**terative **L**east **S**quares **T**echnique
LIGA	**LI**thography **G**alvanik **A**bformung
LMJ	**L**iquid-**M**etal-**J**et
LRM	**L**ehrstuhl für **R**öntgen**M**ikroskopie
LSF	**L**ine **S**pread **F**unction
MLL	**M**ultilayer **L**aue **L**enses
MTF	**M**odulation **T**ransfer **F**unction
NA	**N**umerical **A**perture
ODD	**O**bject-**D**etector **D**istance
PSF	**P**oint **S**pread **F**unction

RIE	**R**eactive **I**on **E**tching
SART	**S**imultaneous **A**lgebraic **R**econstruction **T**echnique
SDD	**S**ource-**D**etector **D**istance
SEM	**S**canning **E**lectron **M**icroscope
SIRT	**S**imultaneous **I**terative **R**econstruction **T**echnique
SNR	**S**ignal-to-**N**oise **R**atio
SOD	**S**ource-**O**bject **D**istance
STXM	**S**canning **T**ransmission **X**-ray **M**icroscope
TXM	**T**ransmission **X**-ray **M**icroscope
QE	**Q**uantum **E**fficiency
XPL	**X**-ray **P**rism **C**ondenser

Bibliography

[1] J. van Zuylen. The microscopes of Antoni van Leeuwenhoek. *Journal of microscopy*, 121(3):309–328, 1981.

[2] E. Abbe. Beiträge zur Theorie des Mikroskops und der mikroskopischen Wahrnehmung. *Archiv für Mikroskopische Anatomie*, 9(1):413–418, 1873.

[3] M. Knoll and E. Ruska. Das Elektronenmikroskop, 1932.

[4] P. J. de Veen, C. Bos, D. R. Hoogstede, C. T. A. Revenberg, J. Liljeholm, and T. Ebefors. High-resolution X-ray computed tomography of through silicon vias for RF MEMS integrated passive device applications. *Microelectronics Reliability*, 55(9-10):1644–1648, 2015.

[5] S. W. Hell and J. Wichman. Breaking the diffraction resolution limit by stimulated emission: stimulated-emission-depletion fluorescence microscopy. *Optics Letters*, 19(11):780 – 782, 1994.

[6] L. Novotny and B. Hecht. *Principles of Nano-Optics*. Cambridge University Press, 2012.

[7] L. Reimer. *Scanning Electron Microscopy: Physics of Image Formation and Microanalysis, Vol. 11*. Springer, 2013.

[8] D. B. Williams and C. B. Carter. *Transmission Electron Microscopy: A Textbook for Materials Science, Vol. 2*. Springer Science & Business Media, 2009.

[9] V. E. Cosslett and W. C. Nixon. X-Ray Shadow Microscopy. *Nature*, 170(4324):436–438, 1952.

[10] W. C. Nixon. High-resolution X-ray projection microscopy. *Proceedings of the Royal Society of London*, 232(1191):475–485, 1955.

[11] W. L. Wolfe. *Introduction to Radiometry*. SPIE, 1998.

[12] P. W. Hawkes and J. C. H. Spence. *Science of microscopy*. Springer, 2007.

[13] W. Chao, P. Fischer, T. Tyliszczak, S. Rekawa, E. Anderson, and P. Naulleau. Real space soft x-ray imaging at 10 nm spatial resolution. *Optics Express*, 20(9):9777, 2012.

[14] S. Rehbein, P. Guttmann, S. Werner, and G. Schneider. Characterization of the resolving power and contrast transfer function of a transmission X-ray microscope with partially coherent illumination. *Optics express*, 20(6):5830–9, 2012.

[15] F. Doering, A. L. Robisch, C. Eberl, M. Osterhoff, A. Ruhlandt, T. Liese, F. Schlenkrich, S. Hoffmann, M. Bartels, T. Salditt, and H. U. Krebs. Sub-5 nm hard x-ray point focusing by a combined Kirkpatrick-Baez mirror and multilayer zone plate. *Optics express*, 21(16): 19311–23, 2013.

[16] A. Ruhlandt, T. Liese, V. Radisch, S. P. Krueger, M. Osterhoff, K. Giewekemeyer, H. U. Krebs, and T. Salditt. A combined Kirkpatrick-Baez mirror and multilayer lens for sub-10 nm x-ray focusing. *AIP Advances*, 2(1):012175, 2012.

[17] G. Schneider, P. Guttmann, S. Heim, S. Rehbein, F. Mueller, K. Nagashima, J. B. Heymann, W. G. Müller, and J. G. McNally. Three-dimensional cellular ultrastructure resolved by X-ray microscopy. *Nature methods*, 7(12):985–7, 2010.

[18] M. Holler, A. Diaz, M. Guizar-Sicairos, P. Karvinen, E. Färm, E. Härkönen, M. Ritala, A. Menzel, J. Raabe, and O. Bunk. X-ray ptychographic computed tomography at 16 nm isotropic 3D resolution. *Scientific reports*, 4:3857, 2014.

[19] J. Miao, P. Charalambous, J. Kirz, and D. Sayre. Extending the methodology of X-ray crystallography to allow imaging of micrometre-sized non-crystalline specimens. *Nature*, 400(6742):342–344, 1999.

[20] D. A. Shapiro, Y.-S. Yu, T. Tyliszczak, J. Cabana, R. Celestre, W. Chao, K. Kaznatcheev, A. L. D. Kilcoyne, F. Maia, S. Marchesini, Y. S. Meng, T. Warwick, L. L. Yang, and H. A. Padmore. Chemical composition mapping with nanometre resolution by soft X-ray microscopy. *Nature Photonics*, 8(10):765–769, 2014.

[21] M. Dierolf, A. Menzel, P. Thibault, P. Schneider, C. M. Kewish, R. Wepf, O. Bunk, and F. Pfeiffer. Ptychographic X-ray computed tomography at the nanoscale. *Nature*, 467 (7314):436–439, 2010.

[22] M. Dierolf, O. Bunk, S. Kynde, P. Thibault, I. Johnson, A. Menzel, K. Jefimovs, C. David, O. Marti, and F. Pfeiffer. Ptychography & lensless x ray imaging. *Europhysics News*, 39 (1):22–24, 2008.

[23] K. A. Nugent. Coherent methods in the X-ray sciences. *Advances in Physics*, 59(1):1–99, 2009.

[24] A. Tkachuk, F. Duewer, H. Cui, M. Feser, S. Wang, and W. Yun. X-ray computed tomography in Zernike phase contrast mode at 8 keV with 50-nm resolution using Cu rotating anode X-ray source. *Zeitschrift für Kristallographie*, 222(11):650–655, 2007.

[25] A. Sakdinawat and D. Attwood. Nanoscale X-ray imaging. *Nature Photonics*, 4(12): 840–848, 2010.

[26] M. Dressel, G. Grüner, and G. F. Bertsch. *Electrodynamics of Solids: Optical Properties of Electrons in Matter, Vol. 70*. 2002.

[27] J. Als-Nielsen and D. McMorrow. *Elements of Modern X-ray Physics: Second Edition*. Wiley, 2011.

[28] J. A. Seibert. X-ray imaging physics for nuclear medicine technologists. Part 1: Basic principles of x-ray production. *Journal of nuclear medicine technology*, 32(3):139–147, 2004.

[29] D. Attwood. *Soft X-Rays and Extreme Ultraviolet Radiation: Principles and Applications*. Cambridge University Press, 2007.

[30] R. E. van Grieken and A. A. Markowicz. *Handbook of X-ray spectrometry*. Marcel Dekker, 2002.

[31] J. H. Ryu, J. S. Kang, and K. C. Park. Carbon nanotube electron emitter for X-ray imaging. *Materials*, 5(11):2353–2359, 2012.

[32] YXLON. *Mikrofokus-Röntgensysteme Y.FXE*. Datasheet, 2015.

[33] A. Sasov. Laboratory X-Ray Nano-CT System. *Ecndt*, 1:4–6, 2006.

[34] F. Nachtrab, T. Ebensperger, B. Schummer, F. Sukowski, and R. Hanke. Laboratory X-ray microscopy with a nano-focus X-ray source. *Journal of Instrumentation*, 6(11):C11017, 2011.

[35] Rigaku. *Micro Max 007HF*. Datasheet, 2011.

[36] V. Malka, J. Faure, Y. A. Gauduel, E. Lefebvre, A. Rousse, and K. T. Phuoc. Principles and applications of compact laser–plasma accelerators. *Nature Physics*, 4(6):447–453, 2008.

[37] T. Tajima and J. M. Dawson. Laser electron accelerator. *Physical Review Letters*, 43(4): 267–270, 1979.

[38] S. Corde, K. Ta Phuoc, G. Lambert, R. Fitour, V. Malka, A. Rousse, A. Beck, and E. Lefebvre. Femtosecond x-rays from laser-plasma accelerators. *Reviews of Modern Physics*, 85(1):1–48, 2013.

[39] J. Schwinger. On the classical radiation of accelerated electrons. *Physical Review*, 75 (12):1912–1925, 1949.

[40] J. D. Jackson. *Classical Electrodynamics, Third Edition, Vol. 67*. Wiley, 1999.

[41] V. A. Bordovitsyn. *Synchrotron Radiation Theory and Its Development*. World Scientific, 1999.

[42] B. W. J. McNeil and N. R. Thompson. X-ray free-electron lasers. *Nature Photonics*, 4 (12):814–821, 2010.

[43] Z. Huang and R. D. Ruth. Laser-Electron Storage Ring. *Physical Review Letters*, 80(5): 976–979, 1998.

[44] Z. Huang. Brightness and Coherence of Synchrotron Radiation and FELs. *International Particle Accelerator Conference*, page 16, 2013.

[45] G. Williams. *X-ray data booklet*. 2001.

[46] J. T. J. Cremer. *Neutron and X-ray Optics*. Newnes, 2013.

[47] W. Demtröder. *Experimentalphysik 2*. Springer, 2013.

[48] W. Bragg and S. Peirce. LXIV. The absorption coefficients of X-rays. *Philosophical Magazine Series 6*, 28(166):626–630, 1914.

[49] Erko. *Modern developments in x-ray and neutron optics*. Springer, 2008.

[50] R. Huang and D. H. Bilderback. Single-bounce monocapillaries for focusing synchrotron radiation: modeling, measurements and theoretical limits. *Journal of synchrotron radiation*, 13(1):74–84, 2006.

[51] M. R. Howells, D. Cambie, R. M. Duarte, S. Irick, A. Macdowell, H. A. Padmore, T. Renner, S. Rah, and R. Sandler. Theory and Practice of Elliptically-Bent X-Ray Mirrors. *Optical Engineering*, 39(10):2748–2762, 2000.

[52] M. A. Kumakhov and F. F. Komarov. Multiple reflection from surface X-ray optics. *Physics Reports*, 191(5):289–350, 1990.

[53] C. A. MacDonald. Focusing Polycapillary Optics and Their Applications. *X-Ray Optics and Instrumentation*, 2010(1):1–17, 2010.

[54] D. H. Bilderback. Review of capillary x-ray optics from the 2nd International Capillary Optics Meeting. *X-Ray Spectrometry*, 32(3):195–207, 2003.

[55] V. G. Kohn. On the Theory of Reflectivity by an X-Ray Multilayer Mirror. *Phys. stat. sol.*, 61(187):61–70, 1995.

[56] M. Bass, E. V. Stryland, D. Williams, and W. Wolfe. *Handbook of optics, 3rd edition*. McGraw-Hill, 2001.

[57] R. D. Dietsch. *Applied X-ray Optics and High Precision Deposition*. Prospectus, 2015.

[58] G. C. Yin, Y. F. Song, M. T. Tang, F. R. Chen, K. S. Liang, F. W. Duewer, M. Feser, W. Yun, and H. P. D. Shieh. 30 nm resolution x-ray imaging at 8 keV using third order diffraction of a zone plate lens objective in a transmission microscope. *Applied Physics Letters*, 89(22):2004–2007, 2006.

[59] J. W. Goodman. Introduction to Fourier Optics. *Optical Engineering*, 35(5):1513, 1996.

[60] J. Kirz. Phase zone plates for X-rays and the extreme UV. *Journal of the Optical Society of America*, 64(3):301–309, 1974.

[61] H. C. Kang, J. Maser, G. B. Stephenson, C. Liu, R. Conley, A. T. Macrander, and S. Vogt. Nanometer Linear Focusing of Hard X-Rays by a Multilayer Laue Lens. *Physical Review Letters*, 96(12):127401, 2006.

[62] X. Huang, H. Yan, E. Nazaretski, R. Conley, N. Bouet, J. Zhou, K. Lauer, L. Li, D. Eom, D. Legnini, R. Harder, I. K. Robinson, and Y. S. Chu. 11 nm hard X-ray focus from a large-aperture multilayer Laue lens. *Scientific reports*, 3:3562, 2013.

[63] A. J. Morgan, M. Prasciolu, A. Andrejczuk, J. Krzywinski, A. Meents, D. Pennicard, H. Graafsma, A. Barty, R. J. Bean, M. Barthelmess, D. Oberthuer, O. Yefanov, A. Aquila, H. N. Chapman, and S. Bajt. High numerical aperture multilayer Laue lenses. *Scientific reports*, 5:9892, 2015.

[64] S. Niese, P. Krüger, A. Kubec, S. Braun, J. Patommel, C. G. Schroer, A. Leson, and E. Zschech. Full-field X-ray microscopy with crossed partial multilayer Laue lenses. *Optics Express*, 22(17):20008–13, 2014.

[65] H. Yan, R. Conley, N. Bouet, and Y. S. Chu. Hard x-ray nanofocusing by multilayer Laue lenses. *Journal of Physics D: Applied Physics*, 47(26):263001, 2014.

[66] S. Suehiro, H. Miyaji, and H. Hayashi. Refractive lens for X-ray focus. *Nature*, 352 (6334):385–386, 1991.

[67] B. X. Yang. Fresnel and refractive lenses for X-rays. *Nuclear Instruments and Methods in Physics, Research Section A*, 328:578–587, 1993.

[68] A. Snigirev, V. Kohn, I. Snigireva, and B. Lengeler. A compound refractive lens for focusing high-energy X-rays. *Nature*, 1996.

[69] P. Boye. *Nanofocusing refractive X-ray lenses*. PhD thesis, 2010.

[70] B. Lengeler, C. Schroer, J. Tummler, B. Benner, M. Richwin, A. Snigirev, I. Snigireva, and M. Drakopoulos. A microscope for hard X-rays based on refractive optics. *Synchrotron Radiation News*, 12(5):45–45, 1999.

[71] K. Evans-Lutterodt, J. Ablett, A. Stein, C.-C. Kao, D. Tennant, F. Klemens, A. Taylor, C. Jacobsen, P. Gammel, H. Huggins, G. Bogart, S. Ustin, and L. Ocola. Single-element elliptical hard x-ray micro-optics. *Optics Express*, 11(8):919, 2003.

[72] V. Aristov, M. Grigoriev, S. Kuznetsov, L. Shabelnikov, V. Yunkin, T. Weitkamp, C. Rau, I. Snigireva, A. Snigirev, M. Hoffmann, and E. Voges. X-ray refractive planar lens with minimized absorption. *Applied Physics Letters*, 77(24):4058, 2000.

[73] B. Cederström, C. Ribbing, and M. Lundqvist. Generalized prism-array lenses for hard X-rays. *Journal of synchrotron radiation*, 12(3):340–4, 2005.

[74] R. Accorsi. *Design of near-field coded aperture cameras for high-resolution medical and industrial gamma-ray imaging*. PhD thesis, 2001.

[75] M. Matsuoka and Y. Kohmura. A New Concept of X-Ray Microscopes with a Coded Aperture Imaging Mask. *Japanese Journal of Applied Physics*, 34(1):372–373, 1995.

[76] M. Osterhoff and T. Salditt. Real structure effects in X-ray waveguide optics: The influence of interfacial roughness and refractive index profile on the near-field and far-field distribution. *Optics Communications*, 282(16):3250–3256, 2009.

[77] C. Fuhse, C. Ollinger, and T. Salditt. Waveguide-based off-axis holography with hard X-rays. *Physical Review Letters*, 97(254801), 2006.

[78] G. F. Knoll. *Radiation Detection and Measurement, Vol. 3*. Wiley, 2010.

[79] G. Blasse and B. C. Grabmaier. *Luminescent Materials*. Springer, 1994.

[80] S. E. Derenzo, M. J. Weber, E. Bourret-Courchesne, and M. K. Klintenberg. The quest for the ideal inorganic scintillator. *Nuclear Instruments and Methods in Physics Research, Section A: Accelerators, Spectrometers, Detectors and Associated Equipment*, 505(1-2): 111–117, 2003.

[81] P. A. Rodnyi, P. Dorenbos, and C. W. E. van Eijk. Energy Loss in Inorganic Scintillators. *Physica Status Solidi (B)*, 187(1):15–29, 1995.

[82] C. Ponchut, J. M. Rigal, J. Clément, E. Papillon, A. Homs, and S. Petitdemange. MAXIPIX, a fast readout photon-counting X-ray area detector for synchrotron applications. *Journal of Instrumentation*, 6(01):C01069, 2011.

[83] S. Kasap and J. Rowlands. Direct-conversion flat-panel X-ray image detectors. *IEE Proceedings - Circuits, Devices and Systems*, 149(2):85, 2002.

[84] O. Hemberg, M. Otendal, and H. M. Hertz. Liquid-metal-jet anode electron-impact x-ray source. *Applied Physics Letters*, 83(7):1483, 2003.

[85] D. H. Larsson, H. Hertz, and U. Lundström. Bio-Imaging with Liquid-Metal-Jet X-ray Sources. *International Conference on X-Ray Microscopy*, 2014.

[86] T. Tuohimaa. *Liquid-Jet-Target Microfocus X-Ray Sources: Electron Guns, Optics and Phase-Contrast Imaging*. PhD thesis, 2008.

[87] N. Nakamor, K. Yamano, M. Yamada, and H. Kanamori. Effect of Electron Energy Distribution on Bremsstrahlung Spectrum. *Japanese Journal of Applied Physics;*, pages Japanese Journal of Applied Physics; ISSN:0021–492, 1993.

[88] T. R. C. Johnson. Dual-energy CT: general principles. *AJR. American journal of roentgenology*, 199(5 Suppl), 2012.

[89] O. Hemberg, M. Otendal, and H. M. Hertz. Liquid-metal-jet anode electron-impact x-ray source. *Applied Physics Letters*, 83(7):1483–1485, 2003.

[90] J. Brown and E. Graves. Comprehensive Biomedical Physics. *Comprehensive Biomedical Physics*, pages 97–119, 2014.

[91] U. Lundström, D. H. Larsson, a. Burvall, P. a. C. Takman, L. Scott, H. Brismar, and H. M. Hertz. X-ray phase contrast for CO2 microangiography. *Physics in medicine and biology*, 57(9):2603–17, 2012.

[92] A. Olivo and O. Heid. *The New X-Ray Revolution*. Siemens.com, 2015.

[93] V. Nagarkar, T. Gupta, S. Miller, Y. Klugerman, M. Squillante, and G. Entine. Structured CsI(Tl) scintillators for X-ray imaging applications. *IEEE Transactions on Nuclear Science*, 45(3):1–5, 1998.

[94] M. Nikl. Scintillation detectors for x-rays. *Measurement Science and Technology*, 17(4): R37–R54, 2006.

[95] M. J. Yaffe and J. A. Rowlands. X-ray detectors for digital radiography. *Physics in Medicine and Biology*, 42(1):1–39, 1997.

[96] Proxivision. *Phosphor Screens*. Prospectus, 2013.

[97] A. Koch, C. Raven, P. Spanne, and A. Snigirev. X-ray imaging with submicrometer resolution employing transparent luminescent screens. *JOSA A*, 15(7):1940–1951, 1998.

[98] M. Stampanoni, G. Borchert, and P. Wyss. High resolution X-ray detector for synchrotron-based microtomography. *Nuclear Instruments and Methods in Physics, Research Section A: Accelerators, Spectrometers, Detectors and Associated Equipment*, 491:291–301, 2002.

[99] T. Martin and A. Koch. Recent developments in X-ray imaging with micrometer spatial resolution. *Journal of synchrotron radiation*, 13(2):180–94, 2006.

[100] H. Graafsma and T. Martin. *Detectors for synchrotron tomography*. Oxford, 2008.

[101] P. A. Douissard, A. Cecilia, T. Martin, V. Chevalier, M. Couchaud, T. Baumbach, K. Dupré, M. Kühbacher, and A. Rack. A novel epitaxially grown LSO-based thin-film scintillator for micro-imaging using hard synchrotron radiation. *Journal of Synchrotron Radiation*, 17(5):571–583, 2010.

[102] Crytur. *LuAG : Ce Scintillation Material*. Datasheet, 2014.

[103] J. T. Bushberg, J. A. Seibert, E. M. Leidholdt, and J. M. Boone. *The Essential Physics of Medical Imaging*. Lippincott Williams & Wilkins, 2011.

[104] J. Beutel and H. Kundel. *Handbook of medical imaging*. SPIE Press, 2000.

[105] I. A. Cunningham, M. S. Westmore, and A. Fenster. A spatial-frequency dependent quantum accounting diagram and detective quantum efficiency model of signal and noise propagation in cascaded imaging systems. *Medical physics*, 21(3):417–27, 1994.

[106] G. Turrell and J. Corset. *Raman Microscopy: Developments and Applications*. Elsevier, 1996.

[107] Finger Lakes Instruments. *ProLine PL09000*. Datasheet, 2014.

[108] C. Coates, B. Fowler, and Gerhard Holst. *sCMOS Scientific CMOS Technology*. Prospectus, 2009.

[109] G. C. Holst. *CMOS/CCD Sensors and Camera Systems, Second Edition*. SPIE, 2011.

[110] G. C. Holst. *CCD arrays, cameras, and displays*. SPIE, 1996.

[111] T. M. Buzug. *Einführung in die Computertomographie*. RheinAhrCampus, 2004.

[112] A. Rose. Quantum and Noise Limitations of the Visual Process. *J. Opt. Soc. Am.*, 43(9): 715, 1953.

[113] M. Ando, N. Sunaguchi, Y. Wu, S. Do, Y. Sung, A. Louissaint, T. Yuasa, S. Ichihara, and R. Gupta. Crystal analyser-based X-ray phase contrast imaging in the dark field: implementation and evaluation using excised tissue specimens. *European radiology*, 24 (2):423–33, 2014.

[114] A. Balles, S. Zabler, T. Ebensperger, C. Fella and R. Hanke. Propagator based formalism for optimizing in-line phase contrast imaging at laboratory X-ray setups . *Review of Scientific Instruments*, 2016.

[115] A. Snigirev, I. Snigireva, V. Kohn, S. Kuznetsov, and I. Schelokov. On the possibilities of x-ray phase contrast imaging by coherent high-energy synchrtron radiation. *Review Sci. Inst.*, 66(12):5486–5492, 1995.

[116] S. Zabler, P. Cloetens, J.-P. Guigay, J. Baruchel, and M. Schlenker. Optimization of phase contrast imaging using hard x rays. *Review of Scientific Instruments*, 76(7):073705, 2005.

[117] T. Weitkamp, D. Haas, D. Wegrzynek, and A. Rack. ANKAphase: Software for single-distance phase retrieval from inline X-ray phase-contrast radiographs. *Journal of Synchrotron Radiation*, 18(4):617–629, 2011.

[118] D. Paganin, S. C. Mayo, T. E. Gureyev, P. R. Miller, and S. W. Wilkins. Simultaneous phase and amplitude extraction from a single defocused image of a homogeneous object. *Journal of Microscopy*, 206(1):33–40, 2002.

[119] M. Ullherr and S. Zabler. Correcting multi material artifacts from single material phase retrieved holo-tomograms with a simple 3D Fourier method. *Optics Express*, 23(25): 32718–27, 2015.

[120] A. Burvall and U. Lundström. Phase retrieval in X-ray phase-contrast imaging suitable for tomography. *Optics Express*, 19(11):6355–6367, 2011.

[121] G. Schneider. Cryo X-ray microscopy with high spatial resolution in amplitude and phase contrast. *Ultramicroscopy*, 75(2):85–104, 1998.

[122] B. Kantor, S. M. Jorgensen, P. E. Lund, M. S. Chmelik, D. A. Reyes, and E. L. Ritman. Cryostatic micro-computed tomography imaging of arterial wall perfusion. *Scanning*, 24 (4):186–90, 2002.

[123] Degenhardt. Rapid Three-Dimensional Phenotyping of Cardiovascular Development in Mouse Embryos by Micro-CT with Iodine Staining. *Circ Cardiovasc Imaging*, 2010.

[124] H. Turbell. *Cone-Beam Reconstruction Using Filtered Backprojection*. PhD thesis, 2001.

[125] R. Gordon, R. Bender, and G. T. Herman. Algebraic reconstruction techniques (ART) for three-dimensional electron microscopy and x-ray photography. *Journal of theoretical biology*, 29(3):471–481, 1970.

[126] A. Andersen. Simultaneous Algebraic Reconstruction Technique (SART): A superior implementation of the ART algorithm. *Ultrasonic Imaging*, 6(1):81–94, 1984.

[127] P. Gilbert. Iterative methods for the three-dimensional reconstruction of an object from projections. *Journal of Theoretical Biology*, 36(1):105–117, 1972.

[128] M. Goitein. Three-dimensional density reconstruction from a series of two-dimensional projections. *Nuclear Instruments and Methods*, pages 509–518, 1972.

[129] X. Pan, E. Y. Sidky, and M. Vannier. Why do commercial CT scanners still employ traditional, filtered back-projection for image reconstruction? *Inverse Problems*, 25(12): 123009, 2009.

[130] J. Dittmann. *Tomographische Rekonstruktion aus wenigen Röntgenprojektionen auf Grundlage der Compressed Sensing Theorie*. Master thesis, 2013.

[131] A. Rack. *Untersuchung komplexer Materialsysteme mittels Synchrotron-Tomographie und 3D-Bildanalyse*. PhD thesis, 2006.

[132] J. Kastner, B. Plank, and D. Salaberger. High resolution X-ray computed tomography of fibre- and particle filled polymers. *18th World Conference on Nondestructive Testing*, pages 16–20, 2012.

[133] M. Vincent, A. Redjeb, P. Laure, and T. Coupez. Injection Moulding of Short Fibre Reinforced Thermoplastics: a Comparison Between Experimental Results and Numerical Simulation. *ECCM 12, Biarritz (France)*, pages 1–7, 2006.

[134] M. Gupta and K. K. Wang. Fiber orientation and mechanical properties of short-fiber-reinforced injection-molded composites: Simulated and experimental results. *Polymer Composites*, 14(5):367–382, 1993.

[135] L. Gold. *Study of cycling behavior of lithium-ion batteries using micro-CT*. Master thesis, 2015.

[136] A. Paul van de Heyning. *Cochlear Implants and Hearing Preservation*. Karger Medical and Scientific Publishers, 2010.

[137] C. Holzner, M. Feser, S. Vogt, B. Hornberger, S. B. Baines, and C. Jacobsen. Zernike phase contrast in scanning microscopy with X-rays. *Nature Physics*, 6(11):883–887, 2010.

[138] L. Jochum and W. Meyer-Ilse. Partially coherent image formation with x-ray microscopes. *Applied optics*, 34(22):4944–4950, 1995.

[139] U. Vogt, M. Lindblom, P. Charalambous, B. Kaulich, and T. Wilhein. Condenser for Koehler-like illumination in transmission x-ray microscopes at undulator sources. *Optics Letters*, 31(10):1465, 2006.

[140] P. Charalambous. Fabrication and characterization of Tungsten zone plates for multi KeV X-rays. *AIP Conference Proceedings*, 507(1):625–630, 2000.

[141] M. W. R. Mayer. *A new production method for Fresnel zone plates for high-resolution X-ray microscopy and investigation of their imaging properties*. PhD thesis, 2011.

[142] I. Mohacsi, P. Karvinen, I. Vartiainen, V. a. Guzenko, A. Somogyi, C. M. Kewish, P. Mercere, and C. David. High-efficiency zone-plate optics for multi-keV X-ray focusing. *Journal of synchrotron radiation*, 21(3):497–501, 2014.

[143] I. Mohacsi, I. Vartiainen, M. Guizar-Sicairos, P. Karvinen, V. A. Guzenko, E. Müller, E. Färm, M. Ritala, C. M. Kewish, A. Somogyi, and C. David. High resolution double-sided diffractive optics for hard X-ray microscopy. *Optics Express*, 23(2):776, 2015.

[144] U. Tunca Sanli, K. Keskinbora, C. Grévent, and G. Schütz. Overview of the multilayer-Fresnel zone plate and the kinoform lens development at MPI for intelligent systems. *SPIE Optics + Optoelectronics*, page 95100U, 2015.

[145] M. Mayer, K. Keskinbora, C. Grévent, A. Szeghalmi, M. Knez, M. Weigand, A. Snigirev, I. Snigireva, and G. Schütz. Efficient focusing of 8 keV X-rays with multilayer Fresnel zone plates fabricated by atomic layer deposition and focused ion beam milling. *Journal of synchrotron radiation*, 20(3):433–40, 2013.

[146] X. Huang, R. Conley, N. Bouet, J. Zhou, A. Macrander, J. Maser, H. Yan, E. Nazaretski, K. Lauer, R. Harder, I. K. Robinson, S. Kalbfleisch, and Y. S. Chu. Achieving hard X-ray nanofocusing using a wedged multilayer Laue lens. *Optics express*, 23(10):12496–507, 2015.

[147] D. X. Balaic, Z. Barnea, K. A. Nugent, R. F. Garrett, J. N. Varghese, and S. W. Wilkins. Protein Crystal Diffraction Patterns Using a Capillary-Focused Synchrotron X-ray Beam. *Journal of synchrotron radiation*, 3(6):289–95, 1996.

[148] D. X. Balaic, K. A. Nugent, Z. Barnea, R. Garrett, and S. W. Wilkins. Focusing of X-rays by Total External Reflection from a Paraboloidally Tapered Glass Capillary. *Journal of synchrotron radiation*, 2(6):296–9, 1995.

[149] Cornaby W. *The handbook of x-ray single-bounce monocapillary optics, including optical design and synchrotron applications*. PhD thesis, 2008.

[150] X. Zeng, M. Feser, E. Huang, A. Lyon, W. Yun, M. Denecke, and C. T. Walker. Glass Monocapillary X-ray Optics And Their Applications In X-ray Microscopy. *AIP Proceedings*, 41:41–47, 2010.

[151] Y. J. Liu, J. Y. Wang, Y. L. Hong, Z. L. Wang, K. Zhang, P. A. Williams, P. P. Zhu, J. C. Andrews, P. Pianetta, and Z. Y. Wu. Extended depth of focus for transmission x-ray microscope. *Optics Letters*, 37(17):3708–3710, 2012.

[152] Q. Yuan, K. Zhang, Y. Hong, W. Huang, K. Gao, Z. Wang, P. Zhu, J. Gelb, A. Tkachuk, B. Hornberger, M. Feser, W. Yun, and Z. Wu. A 30 nm-resolution hard X-ray microscope with X-ray fluorescence mapping capability at BSRF. *Journal of synchrotron radiation*, 19(6):1021–8, 2012.

[153] S. Baumbach, B. Kanngiesser, W. Malzer, H. Stiel, and T. Wilhein. A laboratory 8 keV transmission full-field x-ray microscope with a polycapillary as condenser for bright and dark field imaging. *Review of Scientific Instruments*, 86(8), 2015.

[154] S. Baumbach, B. Kanngiesser, W. Malzer, H. Stiel, S. Bjeoumikhova, and T. Wilhein. Setup of an 8 keV laboratory transmission x-ray microscope. *Journal of Physics: Conference Series*, 499:012005, 2014.

[155] B. Lengeler and J. Tümmler. Transmission and gain of singly and doubly focusing refractive x-ray lenses. *Journal of Applied Physics*, 84(11):5855–5861, 1998.

[156] A. Last. *User Manual: Planare, refractive X-ray lenses*. User manual, 2014.

[157] M. Simon. *Röntgenlinsen mit großer Apertur*. PhD thesis, 2010.

[158] C. K. Gary, H. Park, L. W. Lombardo, M. a. Piestrup, J. T. Cremer, R. H. Pantell, and Y. I. Dudchik. High resolution x-ray microscope. *Applied Physics Letters*, 90(18):3–5, 2007.

[159] L. Sveda, J. Marsik, M. Horvath, L. Pina, Y. I. Dudchik, V. Semencova, R. Havlikova, and V. Jelinek. Laboratory X-ray microscopy with reflective – refractive lens system. *Journal of Physics: Conference Series*, 186:012037, 2009.

[160] L. Pina, Y. Dudchik, V. Jelinek, L. Sveda, J. Marsik, M. Horvath, and O. Petr. X-ray imaging with compound refractive lens and microfocus X-ray tube. *Advances in X-ray/EUV Optics and Components III*, 7077:70770H–2–7, 2008.

[161] M. A. Piestrup, C. K. Gary, H. Park, J. L. Harris, J. T. Cremer, R. H. Pantell, Y. I. Dudchik, N. N. Kolchevsky, and F. F. Komarov. Microscope using an x-ray tube and a bubble compound refractive lens. *Applied Physics Letters*, 86(13):131104, 2005.

[162] P. Stahlhut, T. Ebensperger, S. Zabler, and R. Hanke. A laboratory X-ray microscopy setup using a field emission electron source and micro-structured reflection targets. *Nuclear Instruments and Methods in Physics Research, Section B: Beam Interactions with Materials and Atoms*, 324:4–10, 2014.

[163] C. Fella, A. Balles, S. Zabler, R. Hanke, R. Tjeung, S. Nguyen, and D. Pelliccia. Laboratory x-ray microscopy on high brilliance sources equipped with waveguides. *Journal of Applied Physics*, 118(3):034904, 2015.

[164] D. Pelliccia, A. Sorrentino, I. Bukreeva, A. Cedola, F. Scarinci, M. Ilie, A. M. Gerardino, M. Fratini, and S. Lagomarsino. X-ray phase contrast microscopy at 300 nm resolution with laboratory sources. *Optics Express*, 18(15):15998–6004, 2010.

[165] C. J. Blackhall, K. S. Morgan, and D. Pelliccia. Dual scanning and full-field hard x-ray microscopy with a laboratory source. *Optics Express*, 22(13):15437–46, 2014.

[166] H. Neubauer, S. Hoffmann, M. Kanbach, J. Haber, S. Kalbfleisch, S. P. Krüger, and T. Salditt. High aspect ratio x-ray waveguide channels fabricated by e-beam lithography and wafer bonding. *Journal of Applied Physics*, 115(21):214305, 2014.

[167] W. Wiest, S. Zabler, A. Rack, C. Fella, A. Balles, K. Nelson, R. Schmelzeisen, and R. Hanke. In situ microradioscopy and microtomography of fatigue-loaded dental two-piece implants. *Journal of Synchrotron Radiation*, 22:1492–1497, 2015.

[168] S. Dubsky, J. Thurgood, Y. Henon, and A. Fouras. A Low Dose, High Spatio-Temporal Resolution System For Real-Time Four-Dimensional Lung Function Imaging. *American Thoracic Society International Conference Meetings Abstracts*, 2014.

[169] J. Dittmann, A. Eggert, M. Lambertus, J. Dombrowski, A. Rack, and S. Zabler. Finding robust descriptive features for the characterization of the coarsening dynamics of three

dimensional whey protein foams. *Journal of Colloid and Interface Science*, 467:148–157, 2015.

Acknowledgements

First of all, I would like to thank my doctoral adviser Prof. Randolf Hanke for always supporting me. I appreciated a lot the familiar atmosphere at your institute.
Furthermore, I would like to thank my supervisor Simon Zabler who introduced me to the field of X-ray imaging and computed tomography. I learnt a lot from our discussions.
I would also thank Prof. Jakob for co-refereeing this thesis.

Furthermore, I want to acknowledge all my collaboration partners, especially:

- Arndt Last from the *KIT* for fabricating the CRLs and sharing your interesting knowledge about refractive optics and LIGA.
- Reiner Dietsch and Sven Niese from *Axo Dresden* for supporting us with multilayers.
- Kahraman Keskinbora and Corinne Grevent from the *MPI-IS Stuttgart* for providing us the ALD zone plates.
- Heinrich Riesemeier from the *BAMline* for supporting our synchrotron measurements.
- Daniele Pelliccia from the *RMIT University* for the fruitful cooperation and sharing your knowledge about waveguide optics.
- Pambos Charalambos from *Zoneplates Ltd.* for the very nice beam time in July 2014.
- Semfira Bjeoumikhova from the *IFG* for borrowing us polycapillaries.
- David Balaic from *Axco* for simulating the monocapillary.
- Per Takman and Tomi Tuohimaa from *Excillum* for support with the source.

However, the whole thesis would not have been possible without my great colleagues at the *Lehrstuhl für Röntgenmikroskopie* and the *Fraunhofer IIS*, especially the 0.308-Lab-Team Andi and Wolfram - it was a pleasure to work with you. Moreover, I would like to thank Jonas and Kilian for the support at various reconstuction issues, as well as Markus for the IT support. Thanks also to Phillip for sharing your knowledge about the XRM, to Astrid for joining the beamtime in Berlin, as well as Britta for all the organizational support.

Moreover, I also want to acknowledge the help of many other people from the *University of Würzburg*, especially Rainer Brauner, Ralf Müller and all the others from the electronics and mechanical workshop, as well as Monika Emmerling for introducing me at the *Helios Nanolab* and supporting me with the sample preparation.

Finally, I want to thank my family and friends for all the support during the years, especially Sina for never losing the patience.